

ISSN 2189-6909  
September 2016

# LASTI

# Annual Report

Laboratory of Advanced Science and Technology for Industry  
University of Hyogo

Vol.17 (2015)



## PREFACE

This annual report reviews the research activities of the Laboratory of Advanced Science and Technology for Industry (LASTI) in the academic year of 2015 which is from April 2015 to March 2016) including research activities using NewSUBARU light source at the site of SPring-8 and other research activities of the micro and nanoscale are carried out energetically in the building of Center for Advanced Science and Technology (CAST) II.

The annual report describes that topics of the NewSUBARU research activities of this year including research and development of gamma ray application at BL2 beamline, the next generation lithography using Extreme Ultraviolet at BL3, BL9B, BL9C, and BL10 beamlines, and Nanoimprint Lithographic Technology at CAST, LIGA process technology at BL2 and BL11 beamlines, and chemical analysis using soft X-ray absorption fine structure at (BL5, BL9A, and BL7 beamlines and soft X-ray emission spectroscopy at BL5 and BL9A beamlines in soft x-ray energy region.

Most of our research activities are being conducted in collaboration research works with industries, government research institutes, and other universities.

We will continue to respond to the community's demand by offering new science and technology.



Takeo Watanabe

A handwritten signature in black ink that reads "Takeo Watanabe". The signature is written in a cursive, flowing style.

Director of Laboratory of  
Advanced Science and  
Technology for Industry,  
University of Hyogo



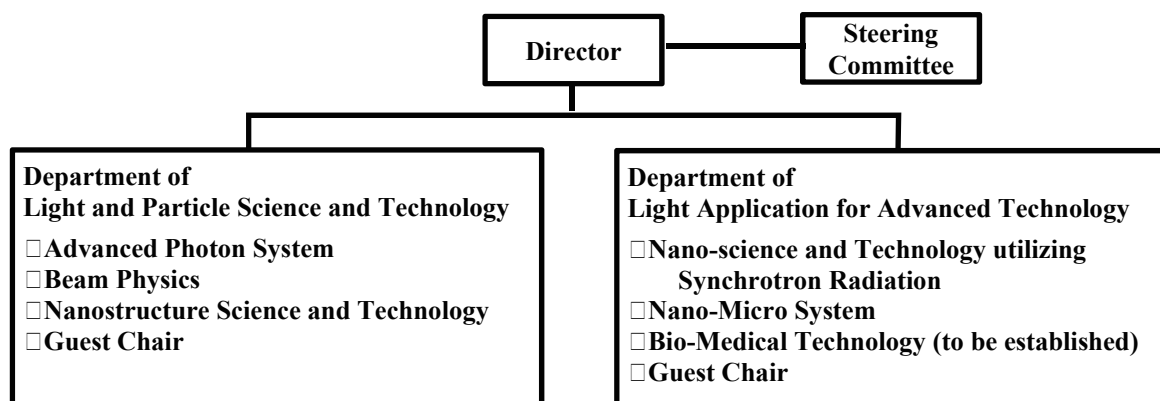


Staff of LASTI  
(In front of Advanced Research Building)



# The Organization of Laboratory of Advanced Science and Technology for Industry University of Hyogo

## The organization



## Staff (FY 2015)

### Research and faculty staff

MIYAMOTO Shuji, Professor, Director  
 MATSUI Shinji, Professor  
 KANDA Kazuhiro, Professor  
 UTSUMI Yuichi, Professor  
 WATANABE Takeo, Professor  
 NIIBE Masahito, Associate Professor  
 SHOJI Yoshihiko, Associate Professor  
 HARUYAMA Yuichi, Associate Professor  
 YAMAGUCHI Akinobu, Associate Professor  
 AMANO Sho, Research Associate  
 HASHIMOTO Satoshi, Research Associate  
 HARADA Tetsuo, Research Associate  
 OKADA Makoto, Research Associate

### Specially appointed staff

MOCHIZUKI Takayasu, Professor  
 KINOSHITA Hiroo, Professor  
 KUDOU Hiroto, Associate Professor  
 NAGATA Yutaka, Assistant Professor  
 IYOSHI Syuzou, Resercher

### Guest staff

OHKUMA Haruo, Professor  
 ASANO Yoshihiro, Professor  
 FUKUSHIMA Sei, Professor

### Administrative staff

HAMAGAMI Akiyuki, General Manager  
 KOBORI Kazuyuki, Manager  
 KURODA Takashi, Chief  
 KAMIYA Miki, CAST  
 KANATANI Naoko, NewSUBARU  
 YAMAMOTO Keiko, CAST  
 YOKOYAMA Yuka, CAST  
 YANO Ayumi, CAST  
 FUJIMAKI Hisae, CAST  
 YAMADA Miki, CAST  
 YAMAMOTO Mako, NewSUBARU  
 KUSUMOTO Kumi, CAST  
 MORIGUCHI Miyuki, Harima Forum of  
 Science and Technology for 21st Century

### Liaison staff

FUKADA Noboru, NewSUBARU  
 UMESAKI Masanori, NewSUBARU  
 ISHIKAWA Kazuko, NewSUBARU  
 MINAMIYAMA Yasuto, NewSUBARU  
 KOTAKA Takuya, NewSUBARU

## Contact address

### Advanced Research Building

3-1-2 Kouto, Kamigori-cho, Ako-gun, Hyogo, 678-1205 JAPAN.  
 T:+81-791-58-0249 F:+81-791-58-0242

### NewSUBARU Synchrotron Radiation Facility

1-1-2 Kouto, Kamigori-cho, Ako-gun, Hyogo, 678-1205 JAPAN.  
 T:+81-791-58-2503 F:+81-791-58-2504

**Web URL** <http://www.lasti.u-hyogo.ac.jp/>, <http://www.lasti.u-hyogo.ac.jp/NS/>

**e-Mail** [lasti@lasti.u-hyogo.ac.jp](mailto:lasti@lasti.u-hyogo.ac.jp)

**Access** <http://www.lasti.u-hyogo.ac.jp/NS-en/access/>

# CONTENTS

## PREFACE

## ORGANIZATION of LASTI

### Part 1. Current Status of NewSUBARU and Other Light Source

<b>NewSUBARU Storage Ring</b> .....	1
Shuji Miyamoto ( <i>LASTI/University of Hyogo</i> )	
<b>NewSUBARU Beamlines</b> .....	3
Kazuhiro Kanda ( <i>LASTI/University of Hyogo</i> )	
<b>Recent Improvements on the Beam Operation of the NewSUBARU Electron Storage Ring</b> .....	10
S. Hashimoto, Y. Takemura <sup>1</sup> , H. Takeuchi <sup>1</sup> , K. Morisato <sup>1</sup> , and S. Miyamoto ( <i>LASTI, University of Hyogo, <sup>1</sup>JASRI SPring-8</i> )	
<b>Simulation Study on Optimization of the Beam Dynamics at LEENA Accelerator</b> .....	11
Satoshi Hashimoto, Karin Kobayashi, and Shuji Miyamoto ( <i>LASTI, University of Hyogo</i> )	
<b>High Average Power Soft X-ray in the Water Window from Ar Laser Plasma</b> .....	14
Sho Amano, ( <i>LASTI/Univ. Hyogo</i> )	
<b>Present Status of BL05A performance</b> .....	16
T. Hasegawa <sup>1</sup> , S. Fukushima <sup>2,3</sup> , T. Kotaka <sup>3</sup> and K. Kanda <sup>3</sup> ( <sup>1</sup> <i>Synchrotron Analysis L.L.C.</i> , <sup>2</sup> <i>NIMS</i> , <sup>3</sup> <i>LASTI/University of Hyogo</i> )	
<b>Development of the Control System of Double Multilayers monochromator in NewSUBARU BL07A</b> .....	18
M. Okui <sup>1,2</sup> , I. Kikuchi <sup>2</sup> , N. Yano <sup>2</sup> , A. Watanabe <sup>2</sup> , N. Murayama <sup>2</sup> , S. Fukushima <sup>1,3</sup> and K. Kanda <sup>1</sup> ( <sup>1</sup> <i>LASTI/Univ. Hyogo</i> , <sup>2</sup> <i>Kohzu Precision Co., Ltd.</i> , <sup>3</sup> <i>NIMS</i> )	
<b>Performance of BL07A Installed New Multilayered-Mirror Monochromator</b> .....	20
S. Tanaka <sup>1</sup> , N. Yato <sup>2</sup> , M. Okui <sup>1,2</sup> , S. Fukushima <sup>1,3</sup> , and K. Kanda <sup>1</sup> ( <sup>1</sup> <i>LASTI/Univ. Hyogo</i> , <sup>2</sup> <i>Kohzu Precision Co., Ltd.</i> , <sup>3</sup> <i>NIMS</i> )	
<b>Adjustment of the Equipment for the measurement of Ultra-soft X-ray Fluorescence Spectrum on BL07A</b> .....	22
S. Fukushima <sup>1,2</sup> , H. Takamatsu <sup>1</sup> , S. Tanaka <sup>1</sup> , K. Kanda <sup>1</sup> ( <i><sup>1</sup>LASTI/Univ. Hyogo, <sup>2</sup>NIMS</i> )	
<b>Installation of Silicon Drift Detector for PFY-XAFS measurement of insulating materials in BL-09A</b> .....	25
Shigeaki Uemura <sup>1</sup> , Junji Iihara <sup>1</sup> , Takashi Yajima <sup>2</sup> , Masahito Niibe <sup>2</sup> ( <sup>1</sup> <i>Sumitomo Electric Industries, <sup>2</sup>Ltd., Sumitomo Riko Co. Ltd.</i> , <sup>3</sup> <i>LASTI/Univ. Hyogo</i> )	

<b>Development of an Analysis Station for Soft X-ray Absorption Spectroscopy in BL10</b> .....	27
Y. Muramatsu <sup>1</sup> , A. Tueda <sup>1</sup> , T. Uemura <sup>1</sup> , K. Nambu <sup>1</sup> , T. Ouchi <sup>1</sup> , T. Harada <sup>2</sup> , T. Watanabe <sup>2</sup> , H. Kinoshita <sup>2</sup> ( <sup>1</sup> Eng./Univ. Hyogo, <sup>2</sup> LASTI/Univ. Hyogo)	
<b>Soft X-ray Absorption Spectroscopy (XAS) and X-ray reflectivity (XRR) analysis system in BL10</b> .....	29
Y. Muramatsu <sup>1</sup> , A. Tueda <sup>1</sup> , T. Uemura <sup>1</sup> , K. Nambu <sup>1</sup> , T. Ouchi <sup>1</sup> , T. Harada <sup>2</sup> , T. Watanabe <sup>2</sup> , H. Kinoshita <sup>2</sup> ( <sup>1</sup> Eng./Univ. Hyogo, <sup>2</sup> LASTI/Univ. Hyogo)	
<b>Part 2. Research Activities</b>	
<b>Development of LCS Gamma-Ray Simulation Code and GUI Application</b> .....	33
Satoshi Hashimoto, Takuya. Matsumoto, and Shuji Miyamoto ( <i>LASTI/University of Hyogo</i> )	
<b>Measurements of Neutron Energy Spectra Depending on the Emission Angle due to Photo-nuclear reaction using LCS photons</b> .....	34
Y. Asano, T. Sanami, H. Nakashima, Y. Kirihara, T. itoga, Y. Namito, A. Takemoto, M. Yanaguchi, S. Miyamoto ( <i>RIKEN SPring-8 Center, High Energy Accel. Res. Org., JAEA, JASRI, LASTI/Univ. Hyogo</i> )	
<b>Photoneutron Reactions in Nucleosynthesis</b> .....	37
Hiroaki Utsunomiya ( <i>Konan Univ.</i> )	
<b>Total and Partial Photoneutron Cross Section Measurements by Direct Neutron-multiplicity Sorting</b> .....	39
Hirokaki Utsunomiya, and the Phoenix Collaboration ( <i>Konan Univ.</i> )	
<b>First Characterization of Time Projectionchamber as a High-performance Gamma-ray Pair Creation Telescope and Polarimeter</b> .....	41
Denis Bernard ( <i>LLR, Ecole Polytechnique &amp; CNRS/IN2P3, France</i> )	
<b>Measurements of Nuclear Resonance Fluorescence on <sup>52</sup>Cr with a Linearly Polarized Photon Beam at BL01</b> .....	45
T. Shizuma <sup>1</sup> , T. Hayakawa <sup>1</sup> , F. Minato <sup>2</sup> , I. Daito <sup>3</sup> , H. Ohgaki <sup>3</sup> , S. Miyamoto <sup>4</sup> ( <sup>1</sup> National Inst. Quantum & Radiol. Sci. & Technol., <sup>2</sup> JAEA, <sup>3</sup> Kyoto Univ., <sup>4</sup> LASTI/Univ. Hyogo)	
<b>Azimuthal Anisotropy of Neutrons in <sup>56</sup>Fe(polarized <math>\gamma</math>, n) <sup>57</sup>Fe Reactions at BL01</b> .....	47
T. Hayakawa <sup>1</sup> , T. Shizuma <sup>1</sup> , S. Miyamoto <sup>2</sup> , S. Amano <sup>2</sup> , A. Takemoto <sup>2</sup> , M. Yamaguchi <sup>2</sup> , K. Horikawa <sup>2</sup> , H. Akimune <sup>3</sup> , S. Chiba <sup>4</sup> , K. Ogata <sup>5</sup> , M. Fujiwara <sup>5</sup> ( <sup>1</sup> National Inst. Quantum & Radiol. Sci. & Technol., <sup>2</sup> LASTI/Univ. Hyogo, <sup>3</sup> Konan Univ., <sup>4</sup> Tokyo Instit. Technol., <sup>5</sup> Osaka Univ.)	
<b>The film modification of Si-containing hydrogenated DLC films by the soft X-ray irradiation</b> .....	49
Shotaro Tanaka <sup>1</sup> , Ryo Imai <sup>1</sup> , Takayuki Hasegawa <sup>2</sup> and Kazuhiro Kanda <sup>1</sup> ( <sup>1</sup> LASTI/Univ. of Hyogo, <sup>2</sup> Synchrotron Analysis L.L.C.)	

<b>Surface modification Processes of Highly Hydrogenated Diamond-Like Carbon Thin Films by Soft X-ray Irradiation</b> .....	52
K. Kanda <sup>1</sup> , R. Imai <sup>1</sup> , K. Komatsu <sup>2</sup> , H. Saitoh <sup>2</sup> ( <sup>1</sup> LASTI/Univ. Hyogo, <sup>2</sup> Nagaoka Univ. of Technol.)	
<b>Refractive-index Modifications in Silica-Bases Films by Undulator Radiation with Multilayer Spectrometer</b> .....	55
K Moriwaki <sup>1</sup> , G. Kimura <sup>1</sup> , K. Kanda <sup>2</sup> and S. Matsui <sup>2</sup> ( <sup>1</sup> Kobe Univ., <sup>2</sup> LASTI/Univ. of Hyogo,)	
<b>Effect of the Soft-X-ray on the Surface of Fluorinated DLC Film</b> .....	57
H. Takamatsu, M. Okada, M. Niibe, and K. Kanda (LASTI/ Univ. Hyogo)	
<b>Evaluation of Damage in an Organic Thin Film with Cluster Ion Sputtering</b> .....	59
S. Fujita, Y. Nohara, M. Ohno, Y. Haruyama (Nissan Chemical Industries, Ltd., LASTI/Univ. Hyogo)	
<b>Molecular Orientation in Photoreactive Liquid Crystalline Polymer Films Observed by NEXAFS</b> .....	62
Y. Haruyama, Y. Taniguchi, M. Kondo, N. Kawatsuki, M. Okada, S. Matsui (LASTI/Univ. Hyogo, Eng./Univ. Hyogo)	
<b>A large Takeoff-angle Dependence of C-K Emission Spectra Observed in Highly Oriented Pyrolytic Graphite</b> .....	64
Noritaka Takehira <sup>1</sup> , Masahito Niibe <sup>1</sup> , Yuma Araki <sup>1</sup> , Takasshi Tokushima <sup>2</sup> , ( <sup>1</sup> LASTI/Univ. of Hyogo, <sup>2</sup> RIKEN Spring-8 Center)	
<b>Irradiation Effect of Oxygen Plasma to TiO<sub>2</sub> Thin Films</b> .....	67
Yuma Araki <sup>1</sup> , Masahito Niibe <sup>1</sup> , Retsuo Kawakami <sup>1</sup> , Noritaka Takehira <sup>1</sup> , Yoshitaka Nakano <sup>3</sup> ( <sup>1</sup> LASTI/Univ. of Hyogo, <sup>2</sup> Tokushima Univ. <sup>3</sup> Chubu Univ.)	
<b>Modification of Horizontally Aligned Multi-walled Carbon Nanotube Films by Ar Ion beam Irradiation and Its Characterization by Soft X-ray Spectroscopy</b> .....	69
S. Honda <sup>1,7</sup> , M. Niibe <sup>2</sup> , M. Terasawa <sup>2</sup> , R. Hirase <sup>3</sup> , H. Yoshioka <sup>3</sup> , H. Izumi <sup>3</sup> , K. Niwase <sup>4</sup> , E. Taguchi <sup>3</sup> , T. Harada <sup>2</sup> , Y. Muramatsu <sup>1</sup> , K.-Y. Lee <sup>6</sup> and M. Oura <sup>7</sup> ( <sup>1</sup> Eng./Univ. Hyogo. <sup>2</sup> LASTI/Univ. Hyogo, <sup>3</sup> Hyogo Pref. Instit. Technol., <sup>4</sup> Hyogo Univ. Teacher Education, <sup>5</sup> Osaka Univ. <sup>6</sup> Taiwan Univ. Sci. & Technol., <sup>7</sup> RIKEN SPring-8 Center)	
<b>Development of High-Reflective W/Si-multilayer Diffraction Grating for the Analysis of Fluorine Materials</b> .....	71
M. Kuki <sup>1</sup> , T. Uemura <sup>1</sup> , M. Yamaguchi <sup>1</sup> , T. Harada <sup>1</sup> , T. Wtanabe <sup>1</sup> , Y. Muramatsu <sup>2</sup> , and H. Kinoshita <sup>1</sup> ( <sup>1</sup> LASTI/Univ. Hyogo, <sup>2</sup> Eng./Univ. Hyogo)	
<b>Development of the Molecular Orientation Analysis by Soft X-ray Absorption Spectroscopy</b> .....	77
E. Takahashi <sup>1</sup> , K. Imanishi <sup>1</sup> , S. Suehiro <sup>1</sup> , Y. Suzuki <sup>2</sup> , Y. Ota <sup>3</sup> , Y. Muramatsu <sup>3</sup> ( <sup>1</sup> Sumika Chem. Anal. Service Ltd., <sup>2</sup> Yamagata Univ. <sup>3</sup> Eng./Univ. Hyogo)	
<b>Local Structure Analysis of Graphitic Carbon Materials by X-ray Absorption Spectroscopy</b> .....	79
K. Murayama <sup>1</sup> , T. Haruyama <sup>1</sup> , R. Kazihara <sup>1</sup> , Y. Muramatsu <sup>2</sup> ( <sup>1</sup> MIKUNI COLOR, Ltd. <sup>2</sup> Univ. Hyogo)	

<b>Soft X-ray Absorption Spectroscopy of Oxygen in Rubber-Brass Adhesive Layer</b> .....	81
T. kakubo <sup>1</sup> , N. Amino <sup>1</sup> , K. Nanbu <sup>2</sup> , Y. Muramatsu <sup>2</sup> ( <sup>1</sup> <i>Yokohama Rubber Co. Ltd.</i> , <sup>2</sup> <i>Univ. Hyogo</i> )	
<b>Analyses of Surface State of Detonation Nanodiamond</b> .....	83
M. Nishikawa <sup>1</sup> , M. Liu <sup>1</sup> , A. yamakawa <sup>1</sup> , Y. Muramatsu <sup>2</sup> ( <sup>1</sup> <i>Daicel Corporation</i> , <sup>2</sup> <i>Eng./Univ. Hyogo</i> )	
<b>Analysis of the Carbon Black by Soft X-ray Absorption Spectroscopy</b> .....	85
A. Inoue <sup>1</sup> , M. Fujisue <sup>2</sup> , T. Hattori <sup>1</sup> , T. Takakura <sup>1</sup> , T. Inoue <sup>1</sup> , K. Murayama <sup>3</sup> , Y. Mutamatsu <sup>3</sup> (Mitsubishi Chemical Corp., Mitsubishi Rayon Co. Ltd, Univ. Hyogo)	
<b>Development of Transmission Grating for EUV Interference Lithography of 1X nm HP</b> .....	87
T. Hukui, H. Tanino, Y. Fukuda, M. Kuki, T. Watanabe, H. Kinoshita, and T. Harada ( <i>LASTI/University of Hyogo</i> )	
<b>Trial Fabrication of PTFE-filled E-plane Waveguide Coupler using SR Etching Process</b> .....	92
Mituyoshi. Kakeuchi <sup>1</sup> , Akinobu. Yamaguchi <sup>2</sup> , Yuichi. Utsumi <sup>2</sup> , Isao. Ohta <sup>3</sup> ( <sup>1</sup> <i>Okayama Pref. Univ.</i> , <sup>2</sup> <i>LASTI/Univ. Hyogo</i> , <sup>3</sup> <i>Univ. Hyogo</i> )	
<b>Lab-on-a-CD to Implement High Precise Unit Chemical Operation for Immunoassay</b> .....	94
M. Takeuchi <sup>1</sup> Y. Arisue <sup>1</sup> , Y. Ukita <sup>2</sup> , C. Kataoka <sup>3</sup> , T. Kobayashi <sup>4</sup> , A. Yamaguchi <sup>1</sup> , Y. Utsumi <sup>1</sup> ( <sup>1</sup> <i>LASTI/Univ. Hyogo</i> , <sup>2</sup> <i>Univ. Yamanashi</i> , <sup>3</sup> <i>Carbuncle Bio Sci. Tech. LLC</i> , <sup>4</sup> <i>National Institute Technol. Tsuyama College</i> )	
<b>Proposal of Direct Digital Manufacturing Approach for Production of Microfluidic Devices</b> .....	98
Yoshiaki Ukita <sup>1</sup> , Akinobu Yamaguchi <sup>2</sup> , Yuichi Utsumi <sup>2</sup> ( <sup>1</sup> <i>Univ. Yamanashi</i> , <sup>2</sup> <i>LASTI/Univ. of Hyogo</i> )	
<b>Synthesis of Particles Extracted from Aqueous Solution Induced by X-ray Radiolysis Using Synchrotron Radiation</b> .....	100
Akinobu Yamaguchi <sup>1</sup> , Ikuo Okada <sup>2</sup> , Takao Fukuoka <sup>1</sup> , Yuichi Utsumi <sup>1</sup> ( <sup>1</sup> <i>LASTI/Univ. Hyogo</i> , <sup>2</sup> <i>SR Research Center Nagoya Univ.</i> )	
<b>Negative Tone 50 nm Line and Space Pattern Fabrication by Electron Lithography using NEB-22</b> .....	102
Makoto Okada and Shinji Matsui ( <i>LASTI/Univ. Hyogo</i> )	
<b>List of publications</b>	
<b>(1) Papers</b> .....	107
<b>(2) International meetings</b> .....	112
<b>(3) Academic degrees</b> .....	118

## **Part 1. Current Status of NewSUBARU and Other Light Source**



Memorial tree planting for Prof. Ainosuke Ando



# NewSUBARU Storage Ring

Shuji Miyamoto

## Storage Ring Parameters

Figure 1 shows the layout of NewSUBARU Synchrotron Light Facility and the electron injection linac of SPring-8. NewSUBARU is installed in square building of 63m×85m. Electron beams are injected through the transport line L4BT. The machine parameters of the NewSUBARU storage ring are listed in Table I. Although the machine condition remains the same, some of the values are revised according to the new model calculation.

Table I Main parameters of the NewSUBARU storage ring.

Circumference	118.73 m	
Lattice	DBA+Inv. bending	
Number of bending mag.	12	
Radius of curvature	3.217m	
RF frequency	499.955 MHz	
Betatron tunes	H: 6.30, V:2.23	
Bunch length (sigma)	33ps (normal operation)	
Harmonic number	198	
Radiation loss per turn	33.4 keV (@1GeV)	
Electron energy	1.0GeV	1.5GeV
	Mode	TopUp Decay
Natural energy spread	0.047%	0.072%
Natural emittance	50 nm	112 nm
Storage current	300 mA	350mA

## Operation Status

The ring has two user-time operation modes, 1.0 GeV top-up operation mode and 1.5 GeV current decay operation mode. The basic operation time is 9:00 - 21:00 of weekdays. Monday is used for machine R&D, Tuesday is for 1.5 GeV user time, Wednesday and Thursday are for 1.0 GeV top-up user time, Friday is for 1.0 GeV or 1.5 GeV user time. Night period or weekend is used for machine study and user time with the special mode, such as a single bunch operation and a changing the electron energy, if necessary.

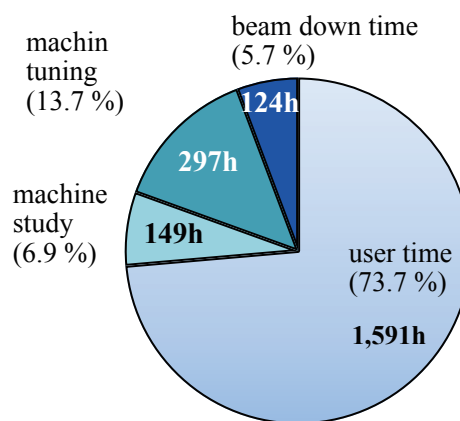


Figure 2 Operating time breakdown of NewSUBARU in FY2015.

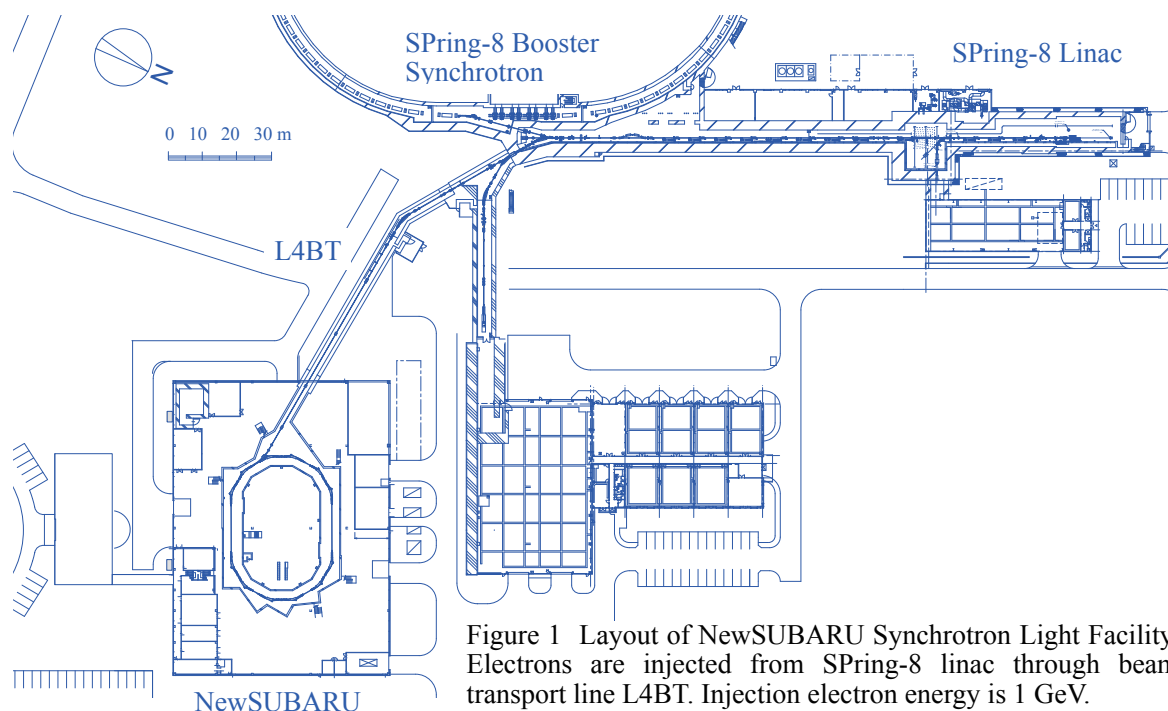


Figure 1 Layout of NewSUBARU Synchrotron Light Facility. Electrons are injected from SPring-8 linac through beam transport line L4BT. Injection electron energy is 1 GeV.

The total machine time in FY2015 was 2161 hrs, 97% of that of FY2014, including the beam down time. Figure 2 shows the breakdown. The beam down time includes not only the down by a failure, but also off-beam periods by a beam abort or others due to the beam instability. The down time due to the machine trouble was 5.7 %, is long comparing with recent years. Main cause of this is the aging of the equipment such as electronic components of control devices.

### Machine Trouble

The machine troubles in FY2015 are listed in Table II. The rate of hardware troubles were increasing due to the aging.

### Machine Study and Special User Time

Table III shows the list of machine studies in FY 2013. Most of the study reports are open to the public on the home page of NewSUBARU.

([http://www.lasti.u-hyogo.ac.jp/beam\\_physics/NewSUBARU.html](http://www.lasti.u-hyogo.ac.jp/beam_physics/NewSUBARU.html)).

### Accelerator Improvements

Figure 3 shows recent filling pattern of the electron bunch in the storage ring. (a) is a filling model for high current long life operation and (b) is an example of measured filling pattern. Lowest current bunch relative to the model filling is selected as a injection bucket at top-up operation. (c) is a single bunch operation at special user time.

Table II Machine troubles in FY2016.

Group	Failure / trouble	beam down time (hr)
Operation	Beam loss by an instability	3.65
RF	Circulator arc & Tuning	8.57
Magnet	Magnet interlock failure	102.65
Electrosity	power cubicle failure	3.3
	lightning power failure	5.3

Table III List of machine studies and special user mode in FY2016.  
(unit is an operation shift = 12 hrs)

R & D theme and special user mode	responsible person	operation shifts
Laser Compton scattering $\gamma$ -ray	S.Miyamoto	58
Commissioning of beam profile monitor port SR2	Y.Shoji	3
Tuning of 1.5 GeV acceleration	S.Hashimoto & M Niibe	10
Beam measurements by AC sextapole magnet	Y.Shoji	5

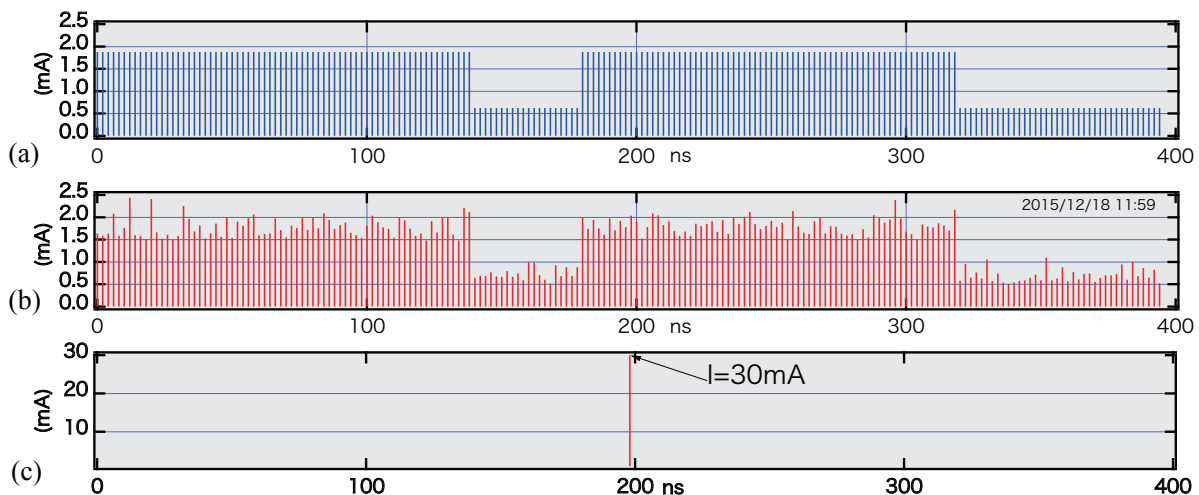


Figure 3 Filling pattern of the electron bunch in the storage ring. Horizontal axis shows a lap time of electron circulation. (a) Model of filling pattern at user time. (b) Measured filling pattern at user time. (c) Single bunch operation at special user time.

## Beamlines

Kazuhiro Kanda  
LASTI, University of Hyogo

Total nine beamlines are operating in the NewSUBARU synchrotron facility. Four beamlines of BL01, BL03, BL06 and BL11 were constructed until 1999. Three beamlines of BL07, BL09 and BL10 were started the operation from 2000.

BL03B beamline branched from the BL03 beamline propose for the usage of the EUVL (extreme ultraviolet lithography) microscope for the EUVL finished mask inspection.

BL09B beamline branched from BL09 beamline for the usage of the usage of the EUV interference lithography to evaluate. And BL09C beamline branched from BL09B

beamline for the usage of the thickness measurement of the carbon contamination originated to the resist outgassing during the EUV exposure.

BL02 beamline was constructed for the usage of LIGA in 2003.

BL05 beamline was constructed in response to a demand in the industrial world in 2008, which is the enhancement of the analysis ability in the soft X-ray region with the development of nanotechnology.

The arrangement of the beamlines in the NewSUBARU synchrotron radiation facility is shown in Fig.1.

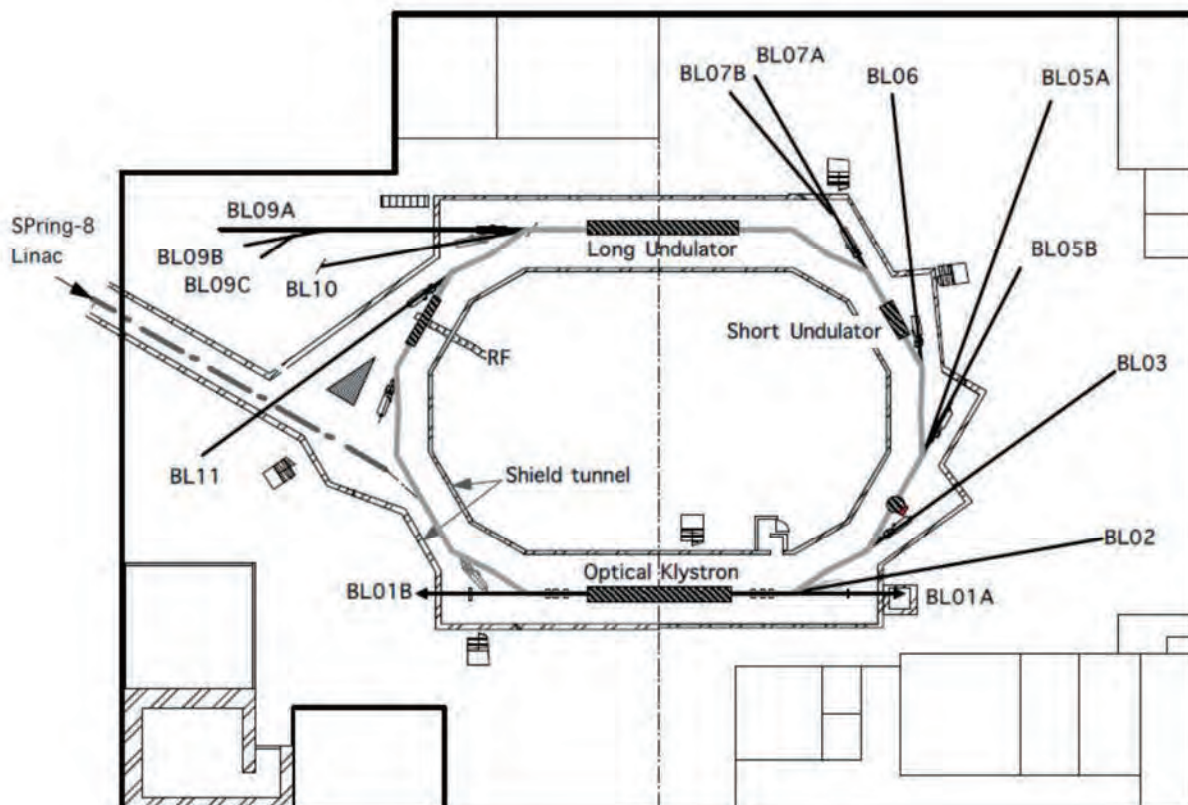


Fig. 1 Beamline arrangement in NewSUBARU.

## I. BL01

BL01 is a beamline for research and developing new light sources. This beamline is one of two long straight section on NewSUBARU. Optical klystron was installed at this straight section. Upstream side of this beamline (BL01B) is intended to be used for visible and infrared light generated from free electron laser (FEL) or synchrotron radiation (SR). Downstream side of this beamline (BL01A) is used for laser Compton scattering gamma-rays source. Gamma-ray beamline hutch just outside of the storage ring tunnel was constructed in 2004 for gamma-ray irradiation experiments. Specification of this gamma-ray sources are listed in Table 1.

**Table 1.** Specification of BL01 gamma beam

CO <sub>2</sub> laser 10.52 μm 5W	Gamma energy : 1.7 - 4 MeV Gamma flux* : 9 x10 <sup>6</sup> γ/s : 6 x10 <sup>5</sup> γ/s (1.5-1.7 MeV) (with 3mmφ collimator)
Nd laser 1.064 μm 0.532 μm 5 W	Gamma energy : 17 - 40 MeV Gamma flux* : 7.5 x10 <sup>6</sup> γ/s : 3 x10 <sup>5</sup> γ/s (15-17 MeV) (with 3mmφ collimator)

\*Electron beam energy : 1-1.5 GeV

\*Electron beam current : 250 mA

## II. BL02

The LIGA (abbreviated name of Lithographic, Galvanofarming and Abfarming) process which consists from deep x-ray lithography, electroforming, and molding process is one of the promising candidates for such 3D microfabrication. More than hundreds aspect ratio for microstructure can be attained by the usage of the higher energy x-rays (4-15 keV) from synchrotron radiation (SR) with deeper penetration depth to the photosensitive resist. In this system we have succeeded to enlarge the exposure area up to A4 size and the fabrication dimension from submicron to millimeter by varying the energy of the x-ray source in accordance with the size of desired microparts. Microstructure with high aspect ratio over several hundred will be achieved using the x-rays over 10 keV since high energy x-ray has deep penetration depth to the photosensitive resist materials. Whereas, in the case of lithography for low energy x-rays from 1 keV to 2 keV, submicron structures with high aspect ratio will be achieved using the x-rays mask with precise line-width and thinner absorber, since low energy x-rays has low penetration depth. Based on this principle, the beamline for x-ray exposure have constructed with continuous selectivity of x-rays from 100 eV to 15 keV by using the x-ray mirrors (plane and

\*Gamma-ray beam divergence : 0.5 mrad

New gamma-ray irradiation hutch "GACKO" was installed at BL01A, collaborating with Konan University. Table 2 shows the specification of "GACKO".

**Table 2.** Specification of "GACKO"

Maximum gamma-ray power	0.33 mW
Maximum gamma-ray energy	1.7 MeV - 73 MeV
CO <sub>2</sub> laser, wavelength/power	10.59 μm / 10W
1-1.7MeV gamma-ray flux	2×10 <sup>7</sup> γ/sec@10W/300mA
Nd:YVO <sub>4</sub> laser, wavelength/power	1.064 μm/ 30W, 0.532 μm/20W
10-17 MeV gamma-ray flux	5×10 <sup>7</sup> γ/sec@30W/300mA

cylindrical mirror) and Be film filters. The horizontal angle of the outgoing SR could be obtained up to 12.5 mrad, which corresponds to the horizontal size of 220 mm (A4 horizontal size) at the exposure position. The second characteristic performance of the beamline is the high efficiency differential pumping system. This was necessary for maintain the vacuum difference between the storage ring (<10<sup>-9</sup> Pa) and the end-station (<10<sup>-9</sup> Pa) at which gasses for substrate cooling will be introduced in the exposure apparatus.

The flexibility for the shapes and functions of microstructure will be enlarged by achieving 3D microfabrication process using multi step exposure at various configuration between x-ray mask and substrates. The relative positions between x-ray mask and substrates, tilt and rotation angle to the SR incident direction can be moved simultaneously during SR exposure using 5 axis stages. The movement of each axis is controlled by the PC in terms of the scanning speeds, scanning length, and repetition number. In order to decrease the heat load of sample substrate suffered during SR irradiation helium introduction and substrate cooling mechanism were also equipped. Specification of spectrometer is listed in Table 3.

**Table 3.** Specification of the LIGA exposure system

Optics	Plane and cylindrical mirror, Be filters
Exposure energy	100 - 2 keV, and 4 – 15 keV
Exposure method	Proximity and multi-step exposure
Wafer size	A4 or 8 inch
Exposure area	230 mm(H) × 300 mm(V)
Exposure environment	< 1 atm (He-gas)

### III. BL03

BL03 is a beamline for the developing the next generation lithographic technology so called extreme ultraviolet lithography (EUVL). The exposure tool is installed at the end station. Using this exposure tool, the research and development of the next generation lithography such as the less than 70 nm node is going on process. The exposure wavelength is 13.5 nm.

The semiconductor industry plays a very important role in the information technology (IT). In 2006, 256 Gbit DRAM with a gate length of 70 nm will be demanded in the IT industry. The extreme ultraviolet lithography (EUVL) is a promise technology for fabricating a fine pattern less than

70 nm. To meet this schedule, this technology has to be developed in the pilot line until 2004. As for the practical use, it is very important that both to achieve large exposure area and to fabricate fine patterns. Therefore, at Himeji Institute of Technology, large exposure field EUV camera consists of three aspherical mirrors was developed. First in the world, we fabricated 60 nm line and space pattern in the large exposure area of 10 mm×10 mm on a wafer. Furthermore, BL03B beamline branches from the BL03 beamline propose for the usage of the EUVL microscope for the EUVL finished mask inspection. Table 4 shows the specification of ETS-1.

**Table 4.** Specification of the exposure tool (ETS-1)

Imaging optics	Three aspherical mirrors
Exposure wavelength	13.5 nm
Numerical aperture	0.1
Demagnification	1/5
Resolution	60 nm
Depth of focus	0.9 μm
Exposure area (static)	30 mm × 1 mm
Exposure area (scanning)	30 mm × 28 mm
Mask size	4 inch, 8 inch, and ULE 6025
Wafer size	8 inch
Exposure environment	In vacuum

### IV. BL05

BL05 was constructed in response to a demand in the industrial world, which is enhancement of the analysis ability in the soft x-ray region with the development of nanotechnology. BL05 consists of two branch lines for use in the wide range from 50 eV to 4000 eV. BL05A and BL05B are designed to cover the energy range of 1300-4000 eV and 50-1300 eV, respectively. The incident beam from the bending magnet is provided for two branch lines through different windows of a mask. Therefore, these two branch lines can be employed simultaneously. At the end stations of each branch, the transfer vessel systems were mounted for the measurements of sample without exposure to air. In

addition, globe box was placed for the preparation of samples into transfer vessel.

1) The double crystal monochromator was installed at the BL05A. InSb, Ge, Si, SiO<sub>2</sub>, Beryl and KTP crystals are prepared for a double-crystal monochromator. Toroidal mirrors are used as a pre-mirror and a focusing mirror of BL05A. XAFS measurement in the total electron yield mode and fluorescence XAFS measurement using SSD (SII Vortex) can be performed. The fluorescence XAFS spectra can be measured for samples at the end station filled with He gas. Table 5 shows the specification of monochromator.

**Table 5.** Monochromator specification

Monochromator	Double crystal monochromator
Monochromator crystals	SiO <sub>2</sub> ( 1010 ), InSb ( 111 ), Ge ( 111 ), Beryl ( 1010 ), KTP ( 110 ), Si ( 111 )
Energy range	1300-4000 eV
Resolution	$E/\Delta E=3000$

2) The constant-deviation monochromator consisting of a demagnifying spherical mirror and a varied-line-spacing plane grating (VLSPG), which can provide high resolution, simple wavelength scanning with fixed slits, was mounted on BL05B. The optical system consists of a first mirror (M0), a second mirror (M1), an entrance slit (S1), a pre-mirror (M2), and three kinds of plane grating (G), an exit slit (S2) and a focusing mirror (M3). The including angle of the monochromator is 175°. Two measurement chambers are

prepared at the end station of BL05B. The XAFS spectra in the total electron yield mode and fluorescence XAFS spectra using SDD (Ourstex) can be measured in a high vacuum chamber. In addition, the photoelectron spectrum can be measured using spherical electron analyzer (VG Sienta, R3000) in an ultrahigh-vacuum chamber. The chambers can be replaced by each other within 1 hour. Table 6 shows the specification of the monochromator.

**Table 6.** Monochromator specification

Monochromator	Varied-line-spacing plane grating monochromator
Grating	100 l/mm, 300 l/mm, 800 mm/l
Energy range	50-1300 eV
Resolution	$E/\Delta E=3000$

## V. BL06

BL06 has been mainly developed for irradiation experiments such as photochemical reaction, SR-CVD, photo-etching, surface modification. The white radiation beam from bending magnet is introduced to the sample stage using a pair of mirror, whose incident angle was 3°. The SR at BL06 sample stage had a continuous spectrum from IR to soft x-ray, which was lower than 1 keV. A differential

pumping system can be utilized for experiments in a gas atmosphere, which is difficult in the soft x-ray region. A sample holder can install four pieces of samples at a time. By using heater set in the sample holder, the sample can be heated from room temperature to 220°C. The temperature of sample is monitored using a Cr-Al thermocouple mounted on the sample holder.

## VI. BL07A and BL07B

This beamline was designed for the development of new materials by SR technology. This beamline consists of two branch lines, which are provided with an incident beam from a 3-m-long undulator by switching the first mirror. One of them is a high photon-flux beamline with a multilayered-mirror monochromator for the study of SR-process (BL07A) and another is a high-resolution beamline with a varied line spacing grating monochromator for the evaluation of nano-structure characteristics by SR-spectroscopy (BL07B). The useful range of emitted photons from 50 to 800 eV is covered at both beamlines. The light source of BL07 is a 3-m length planar undulator, which consists of 29 sets of permanent magnets, a period length of which is 76 mm. The incident beam from the undulator is provided for two branch lines by translational switching of first mirror.

### 1) BL07A

The multilayered-mirror (MLM) monochromator, which has high reflectivity in the soft X-ray region, was installed at the BL07A. It consists of a switching mirror chamber, a

slit chamber, a MLM monochromator, a filter chamber and a reaction chamber. To obtain a large photon flux, we decided to use only first mirror (switching mirror), M0, for focusing. The MLM monochromator is designed to cover an energy range of up to about 800 eV by combination of three kinds of mirror pairs with 4 kinds of filter. The flux deliver by this design is estimated to be between a maximum of  $10^{17}$  photons/s at 95 eV and a minimum  $2 \times 10^{14}$  photons/s at 300 eV for a 500 mA ring current. Table 7 shows the summary of BL07A. In addition, X-ray fluorescence (XRF) apparatus using spherical varied line spacing grating was mounted at the downstream of irradiation chamber. The poly capillary was used to enhance beam-condensing efficiency. Measurement energy range was from 30 eV to 450 eV. This XRF apparatus was expected to utilize the chemical analysis on the light metals, Li and Be, and light elements, B, C and N.

**Table 7.** Summary of BL07A.

Energy range (eV)	Multilayer mirror					Filter	
	Material	spacing	Thickness Ratio	number of layers	$\Delta E/E$	material	Thickness
50-60	Mo/Si	20 nm	0.8	20	6.2 %	Al	100 nm
60-95						None	—
90-140	Mo/B <sub>4</sub> C	11 nm	0.5	25	3.3 %	Ag	100 nm
140-194						Cr	500 nm
190-400	Ni/C	5 nm	0.5	60	2.5 %	Ni	500 nm
400-560							
550-800							

## 2) BL07B

The constant-deviation monochromator consisting of a demagnifying spherical mirror and varied line spacing plane grating (VLSPG), which can provide to high resolution, simple wavelength scanning with fixed slits, was mounted on BL07B. The optical system consists of a first mirror (M0), an entrance slit (S1), a premirror (M1), and three kinds of plane grating (G), an exit slit (S2) and a focusing mirror

(M2). The monochromator is designed to cover the energy range 50-800 eV with three gratings, of which including angle are 168°. The VLSPG has been well known to obtain high resolution in extreme ultraviolet region by diminishing various kinds of aberration. The total resolving power about 3000 can be realized in the whole energy region. Table 8 shows the specification of the monochromator.

**Table 8.** Monochromator specification

Mount type	Hetrick-Underwood type
Grating G1, G2, G3	Plane VLS (600 l/mm, 1200 l/mm, 2400 l/mm)
Energy range	50-150 eV, 150 – 300 eV, 300-800 eV
Resolving power ( $E/\Delta E$ )	~3000

**VII. BL09**

A purpose of this beamline is studies on a soft x-ray interferometry or a holographic exposure experiment with making use of highly brilliant and coherent photon beams radiated from 11 m long undulator in NewSUBARU.

BL09 consists of M0 mirror, M1 mirror, G grating and M2 and M3 mirror. M0 and M3 mirrors are used for horizontal deflection and beam convergence, M1 is used for vertical beam convergence at the exit slit, and M2 is used for vertical deflection and beam convergence. A monochromator is constructed by M1 and a plane grating. The maximum acceptance of the undulator beam is 0.64 mrad in horizontal and 0.27 mrad in vertical. The acceptance can be restricted by 4-jaw slits equipped at upstream of the M0 mirror.

BL09A beamline is used for material analysis: X-ray

absorption spectroscopy (XAS) and X-ray photoelectron spectroscopy (XPS). In 2013, X-ray emission spectrometer (XAS) was introduced at the endstation of the BL09A. The energy range and resolution of the XAS was designed to be about 50-600 eV and 1500, respectively.

BL09B beamline branched from BL09 beamline for the usage of the EUV interference lithography for the evaluation of the exposure characteristics of EUV resist. Coherence length of 1 mm at the resist exposure position was achieved using BL09B beamline. And BL09C beamline branched from BL09B beamline for the usage of the thickness measurement of the carbon contamination originated to the resist outgassing during the EUV exposure. Table 9 shows the specification of the monochromator.

**Table 9.** Monochromator specification

Mount type	Monk-Gillieson type
Grating	Plane VLS (300, 900, 1200 l/mm)
Energy range	50 – 750 eV
Resolving power ( $E/\Delta E$ )	~3000

### VIII. BL10

BL10 is for the global use in the Himeji Institute of Technology. M0 mirror is used for horizontal deflection and beam convergence, M1 is used for vertical beam convergence at the exit slit, and M2 is used for vertical deflection and beam convergence. A monochromator is constructed by M1 and a plane grating. At the beginning, the multiplayers reflectivity measurement was carried out at this beamline. The characteristics of this beamline and the result of the Mo/Si multiplayers measurement are carried out for the development of the EUV- mask technology.

BL10 utilizes a monochromator of the varied line spacing plane grating monochromator (VLS-PGM). The line density of the monochromator in central region of the gratings were 600, 1800 and 2,400 lines/mm. The reflectometer is a two axis vacuum goniometer using two Huber goniometers. One axis carries the sample, which may for example be a mirror at the center of the reflectometer vacuum tank ( $\theta$ -motion). The other ( $\phi$ -motion) carries the detector on a rotating arm.

In addition there are through-vacuum linear motions to translate the sample in two orthogonal directions ( $x,y$ ). All motors are controlled by computer. The sample itself is mounted on a kinematic holder. The control stage monochromator rotation, and data analysis were program using LABVIEW software. The reflectivity result obtained at BL10 has a good agreement with that at LBNL. Table 10 shows the specification the monochromator.

The micro-CSM tool was adapted at the most downstream of the BL10 beamline for the EUV mask defect inspection. This too is very effective for the inspection of the actinic patterned mask.

A large reflectometer was installed in a branch line for large EUV optical component including EUV collector mirrors. The reflectometer has a sample stage with  $y, z, \theta, \phi$ , and Tilt axis, which can hold large optical elements with a maximum weight of 50 kg, a diameter of up to 800 mm, and a thickness of 250 mm. The entire sample surface is able to be measured.

**Table 10.** Monochromator specification

Mount type	Hettrick-Underwood type
Grating	Plane VLS (600, 1800, 2400 l/mm)
Energy range	50 – 1,000 eV
Resolving power ( $E/\Delta E$ )	$\sim 1000$

### IX. BL11

A beam line BL11 is constructed for exposure Hard X-ray Lithography (DXL) in the LIGA (German acronym for Lithographie Galvanoformung and Abformung) process. LIGA process, that utilizes a useful industrial application of SR, is one of the promising technologies for fabrication of extremely tall three-dimensional (3D) microstructures with a large aspect ratio. This process was invented at the Institut Fur Mikrostrukturtechnik (IMT) of the Karlsruhe Nuclear Center (KfK) in 1980. Microstructures with height of over a few hundreds  $\mu\text{m}$  have been widely applied to various fields such as micro-mechanics, micro-optics, sensor and actuator technology, chemical, medical and biological engineering, and so on. This beam line was designed by the criteria ; photon energy range from 2 keV to 8 keV, and a density of total irradiated photons  $\geq 10^{11}$  photons/cm<sup>2</sup>. The BL11 can provide the most suitable photon energy for microfabrication in X-ray lithography, while the BL2 is equipped for fabricating fine pattern submicron-scale structure and microstructure with high aspect ratio by

selectivity of X-rays using movable mirror system. That is, LIGA process in NewSUBARU can provide the best 3D microfabrication because the BL11 and BL2 are complementary. The beamline BL11 is consisting of an absorber chamber, a first-mirror chamber (M1), a 4-way slit chamber, a Be and polyimide window chamber, and an exposure chamber. The horizontal angle of the outgoing SR could be obtained up to 17.8 mrad, providing a beam spot size on the exposure stage  $\geq 80 \times 10 \text{ mm}^2$ . The micron-scale structure with high aspect ratio will be achieved using the toroidal typed mirror M1 which can produce a parallel collimated beam of X-rays. In addition, the homogeneity of the beam is excellently controlled by a novel adding system.

Using the precision stage in the exposure chamber, the flexibility for the shaped and functions of microstructure will be enlarged by achieving 3D microfabrication process using multi step exposure at various configuration between x-ray mask and substrates. The exposure area of 200 mm  $\times$  200 mm is brought to fruition. In order to decrease the

heat load of sample substrate suffered during SR irradiation, helium introduction and substrate cooling system were also

equipped. The specification of the LIGA exposure system is listed in Table 11.

**Table 11.** Specification of the LIGA exposure system

Exposure method	Proximity exposure
Wafer size	8 inch
Exposure area	200 mm(H) × 200 mm(V)
Exposure environment	< 1atm (He-gas)

### Acknowledgement

We would like to thank all the staff who work at NewSUBARU synchrotron light facility for their help to describe the update details of the beamlines.

# Recent Improvements on the Beam Operation of the NewSUBARU Electron Storage Ring

S. Hashimoto, Y. Takemura<sup>#</sup>, H. Takeuchi<sup>#</sup>, K. Morisato<sup>#</sup> and S. Miyamoto  
LASTI,<sup>#</sup>JASRI

## Abstract

Recent improvements on the operation of NewSUBARU electron storage ring are reported. The stored energy is stably ramped from 1.0 to 1.5 GeV without any beam loss. The minimum gap of the long undulator becomes under 30 mm.

## Introduction

Recent synchrotron radiation users at the NewSUBARU facility [1] desire the higher brightness, the higher stability of synchrotron radiation, and the operation at narrower gap of insertion devices. In order to respond to these requests, we have performed machine studies. In this paper we report recent improvements on the beam operation of the NewSUBARU ring including (1) the stable energy ramping, (2) the shortening of the time for the energy ramping, and (3) the operation with 10.8m-long undulator with a gap narrower than before.

## Stabilization of 1.5GeV energy ramping

Electron beams are injected at the energy of 1.0 GeV from the SPring-8 Linac. In the case of 1.5 GeV, the stored energy is ramped up. The former ramping parameter sometimes caused beam loss during the energy ramping because of annual drifts of temperatures, beam instabilities and so on. Thus we re-adjusted the new ramping parameter including fine-tuning of quadrupole, sextupole and steering magnets at the each energies. By using the new parameter, the beam loss or the deterioration of the beam lifetime hardly occurs. Fig.1 shows typical variation of the stored beam current and energy during the energy ramping.

Our ring usually stops an operation at night. Every morning, electromagnets are initialized after power-on. By optimizing and automating the operation procedure for stable energy ramping, the time required until the start of the 1.5 GeV user experiment becomes shorter than before.

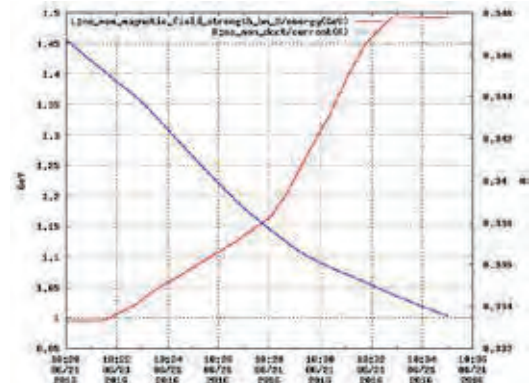


Fig.1 Beam energy and current during the energy ramp

## Operation with narrower gap of 10.8m-long undulator (LU)

The gap length is narrower, the effects of the nonlinear magnetic field of insertion devices on the electron beams is stronger. For compensation of these disturbances, the strength of several kinds of magnets is adjusted according to the gap length. The minimum gap length that can be realized in the previous was 34.8 mm. Recently some users requests lower energy range of LU. After machine studies, the present minimum gap becomes 26mm at 1.5 GeV operation. This is almost same as the physically possible minimum value. At the energy of 1.0 GeV, injection efficiency is somewhat lower (~50%) than the required value 80% at the top-up operation. Further tunings of sextupole and skew quadrupole magnets are being performed toward the realization of the top-up operation with LU gap 26mm at 1.0GeV.

## References

[1] <http://www.lasti.u-hyogo.ac.jp/NS-en/>

# Simulation Study on Optimization of the Beam Dynamics at LEENA Accelerator

Satoshi Hashimoto, Karin Kobayashi, and Shuji Miyamoto  
LASTI

## Abstract

By simulation, we studied the beam dynamics of the 15MeV electron linear accelerator LEENA and calculated the optimized parameters for short bunching of electron beams to generate the high power coherent radiation in the terahertz region.

## Introduction

We have been researching the generation of the terahertz light using relativistic electron beams of the 15MeV electron linear accelerator LEENA [1]. The general layout of LEENA is shown in Fig.1. The terahertz lights by synchrotron radiation (SR), Smith-Purcell radiation, and transition radiation have been successfully observed [2].

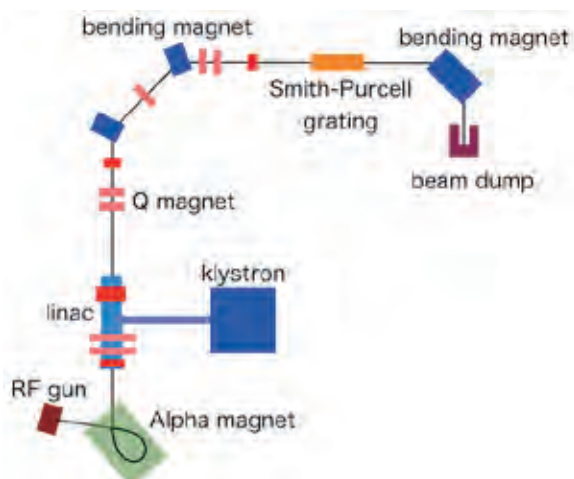


Fig.1 General layout of LEENA.

The intensity spectrum of the SR light from a bending magnet of LEENA is shown in Fig. 2, where Coherent SR (CSR) is plotted in addition to “usual” SR. The CSR is generated from an electron bunch shorter than the radiation wavelength. The radiated power of CSR is proportional to the square of the number of electron  $N$  in a bunch and is  $N$ -times higher than “usual” SR.

In this paper, an electron beam dynamics at RF-gun, solenoid coil, alpha magnet is calculated using simulation codes and the optimum parameters for the short bunching to generate the CSR in terahertz region are shown.

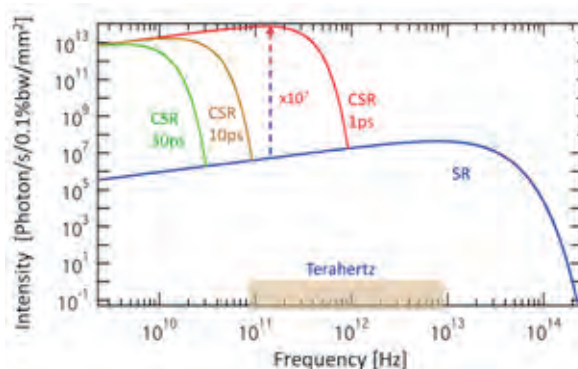


Fig.2 Intensity of coherent and incoherent synchrotron radiation from a bending magnet of LEENA (calculation). Bunch lengths are 1, 10, 30 ps.

## Forming electron bunches in the RF-gun

Electrons are continuously supplied from a thermal  $\text{LaB}_6$  cathode and are accelerated by the RF electric field in the gun cavity (Fig.3). RF frequency is 2856 MHz.

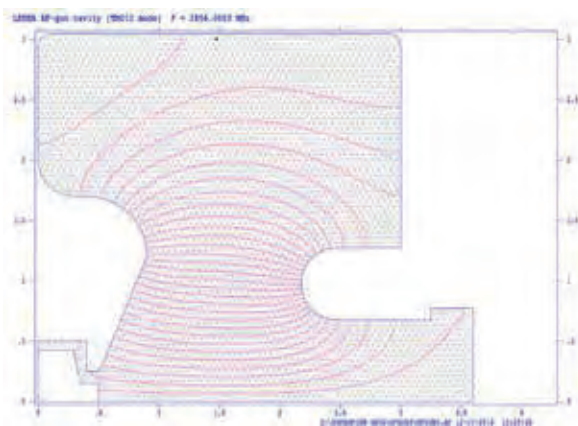


Fig. 3 Electric fields in the axially symmetric RF-gun cavity of LEENA calculated with SUPERFISH [3]

Electrons in the accelerating phase of the RF field are drawn out from the cathode. While these electrons travel through a drift space, the velocity modulation is converted to the density

modulation and electron bunches are formed. The electron number distribution calculated using GPT [4], 3D particle tracking code with space charge, is shown in Fig.4.

Fig.5 shows the energy (Lorentz factor) of electrons. The energy is almost linear with respect to the direction of travel and the gradient of three bunches are 15, 11, 9.4 MeV/m from left to right. As the drift space is longer, the energy gradient becomes gentle.

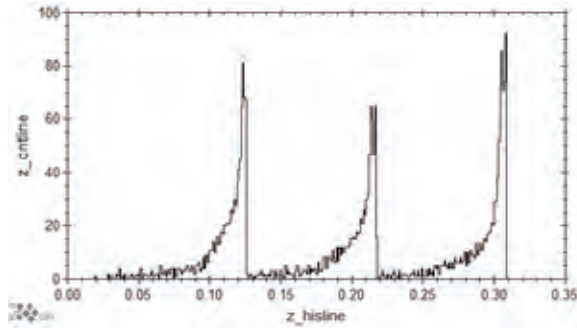


Fig.4 Electron number distribution along the longitudinal direction  $z$  after three periods of RF.

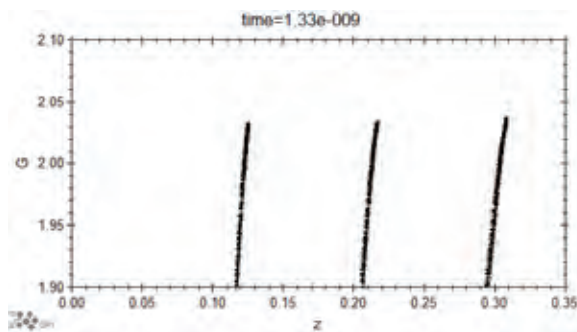


Fig.5 Electron energy (Lorentz factor) distribution along  $z$  after three periods of RF.

### Focusing electron beams by the solenoid coil

An electron beam diverges in radial direction due to its space charge effect. To compensate this, the water-cooled solenoid coil (300 A, 75 turn, 0.37 Tesla) is placed in about 40cm downstream of the cathode.

Fig. 6 shows the time evolution of electron radial distributions in the case of no solenoid field, where the radius of bunched beams is diverged. When a solenoid coil current is set to the optimum value that depends on the beam current, beams are well focused as shown in Fig. 7. Fig. 8 shows the solenoid coil current dependence of calculated beam profiles at the entrance of the alpha magnet. This result qualitatively agrees to the experimental results measured by the screen monitor placed at the entrance of alpha magnet.

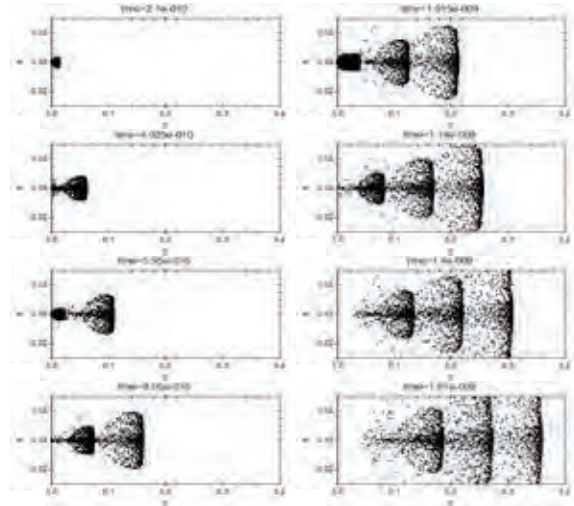


Fig.6 Time evolution of radial distribution of electrons without solenoid field.

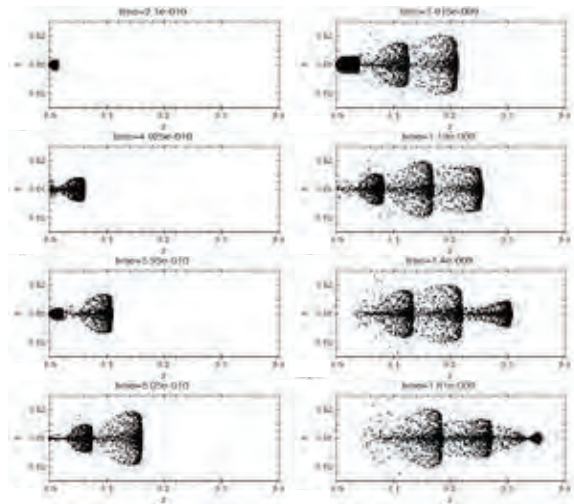


Fig.7 Time evolution of radial distribution of electrons with solenoid field.

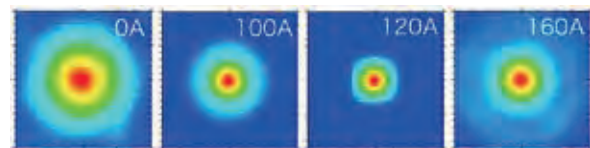


Fig.8 Calculated electron beam profile at the entrance of the alpha magnet when the solenoid coil current is varied.

### Bunching in Alpha magnet

In an alpha magnet, electron trajectory is like the Greek letter alpha, where the faster (slower) electron passes through the outer (inner) trajectory. As a result, at the exit of the alpha magnet, a bunch length is shortened. Cross-sectional view of the upper half of the alpha magnet and the magnetic lines of force calculated using POISSON [3] are shown in Fig. 9.

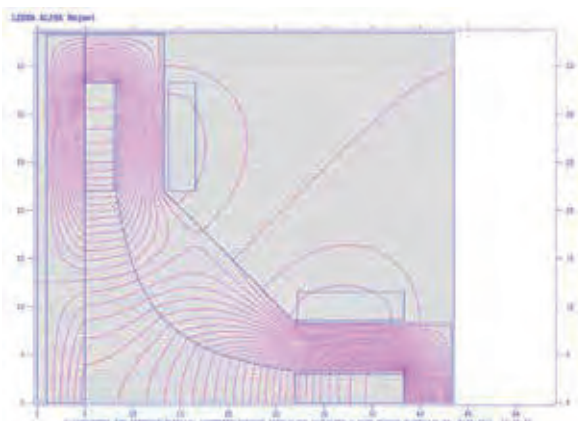


Fig.9 The cross-sectional view of the upper half of the alpha magnet and its magnetic lines of force.

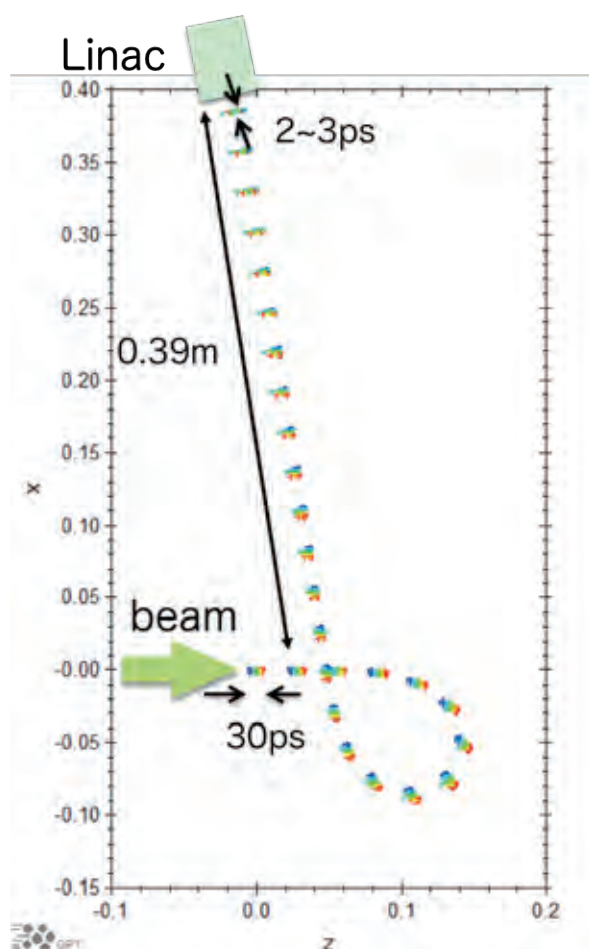


Fig.10 Bunching process of an electron beam in the alpha magnet calculated using GPT.

The particle tracking calculation with 3D space charge effects in the alpha magnet is carried out, where magnetic field data is converted from POISSON to GPT format. The bunching process is shown in Fig. 10. Using the typical

bunch length of 30 ps at the entrance of the alpha magnet, the shortest bunch length at the entrance of the linear accelerating tube that is 0.39m downstream to the alpha magnet is found to be 2 ~ 3 ps. This bunch length corresponds to a wavelength in terahertz region.

In order to realize the above condition, the required energy gradient at the entrance of the alpha magnet is 20 MeV/m. However, as shown in Fig. 5, the typical energy gradient is less than 10 MeV/m and is insufficient for achieving the shortest bunch length.

Three solutions to this problem can be considered; (1) increase the RF power introduced to the RF gun to steep the energy gradient, or (2) shorten the distance between the RF gun and the alpha magnet, and (3) shorten the distance between the alpha magnet and the accelerating tube. It is effective to shorten the drift space in order to prevent the bunch length is extended. We are now preparing to modify the experimental setup.

### Summary

For the generation of the high power radiation in terahertz using relativistic electrons, the bunch length of an electron beam should be under about a few ps. By simulation studies, we calculated and visualized the beam dynamics at the RF gun, solenoid and alpha magnets of LEENA.

As a simulation result, it is found that the minimum bunch length that can be possible at LEENA is about 2 ps. But some modifications of devices may be required for achieving it. We are now considering and preparing the modification of the machine.

### References

- [1] <http://www.lasti.u-hyogo.ac.jp/NS-en/facility/leena/>
- [2] LASTI Annual Report, Special Issue: The 20<sup>th</sup> Anniversary vol.16, ISSN 2189-6909 (2014), in Japanese
- [3] POISSON/SUPERFISH codes, [http://laacg.lanl.gov/laacg/services/download\\_sf.phtml](http://laacg.lanl.gov/laacg/services/download_sf.phtml)
- [4] GPT, <http://www.pulsar.nl/gpt/index.html>

# High average power soft X-ray in the water window from Ar laser plasma

Sho Amano  
LASTI/ UH

## Abstract

High average power of 140 mW and high conversion efficiency of 14% were demonstrated in “water window” soft X-rays generated by a laser plasma source that was developed in-house, when a commercial Nd:YAG Q-switched laser was used to irradiate a solid Ar target with energy of 1 J at a repetition rate of 1 Hz. The source has a translating substrate system with a cryostat that can continuously supply the solid Ar target for repetitive laser pulses, and continuous and stable output power is achieved from the Ar plasma emission.

## Introduction

Soft X-rays (SXR) in the “water window” region between the K absorption edges of oxygen at 2.3 nm and carbon at 4.4 nm are used for high contrast SXR microscope imaging studies of live biological samples because of the different absorption lengths of water and the proteins in biological specimens. We considered the development of a continuous laser plasma X-ray (LPX) source in the water window using a solid Ar plasma target. Ar is considered to be ideal deposition-free targets because it is formed from inert gas rather than metals, and will thus be chemically inactive and will not be deposited on the mirrors near the plasma. This reduction in plasma debris is a major advantage in continuous operation. We decided to use a cryogenic Ar solid target to provide both higher conversion efficiency and higher brightness because of the target’s high solid density. In addition, a smaller gas load for evacuation by the exhaust pump system was expected from the solid state target when compared with gas and liquid jets. We originally developed a cryogenic translating target system to supply the solid Ar target continuously. Using this system, we successfully produced a continuous supply of Ar solid targets and demonstrated the continuous generation of LPX emissions at repetition rates of up to 10 Hz produced by a commercial Nd:YAG Q-switched rod laser. In this paper, we report the plasma SXR emission characteristics in the water window of a solid Ar plasma target supplied by the developed system [1].

## Experiments

Figure 1 shows the side view of the developed LPX source, including the system used for continuous supply of the cryogenic targets. The target system is described in detail in [2]. A copper substrate was attached to the tip of a cryostat head with a He gas closed loop, enabling the substrate surface to be

cooled to a temperature of 15 K. The Ar target gas is blown on to the substrate surface and is thus condensed to form a solid layer. The substrate that was coated with the solid Ar layer translates up and down, with movement in only one dimension, which means that a fresh target surface is supplied for each laser shot. In this experiment, the Ar gas flow rate and the target speed were set to be 250 mL/min and either 3 or 4 mm/s, respectively. Wipers are used to adjust the Ar solid layer thickness to 500  $\mu\text{m}$ , which is sufficient to prevent a 1 J laser shot from damaging the substrate surface, and these wipers also assist in re-covering the laser craters on the target. The entire vacuum chamber was evacuated using a 190 l/s turbo molecular pump, and the vacuum is maintained at less than 1 Pa.

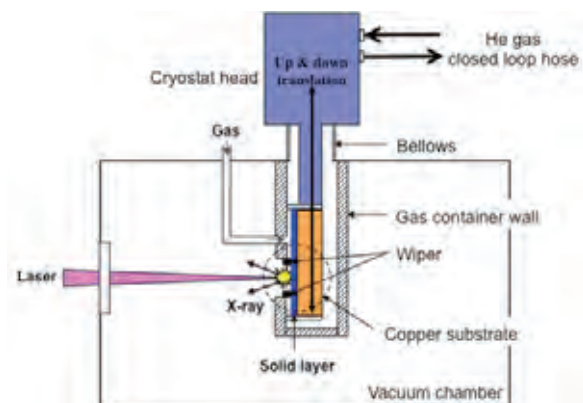


Fig. 1. Side view of the LPX source, including the translating cryogenic target system.

A conventional Q-switched Nd:YAG rod laser (Spectra-Physics, PRO-230) was used as a pump source and could deliver pulses at a wavelength of  $1\omega$  (1064 nm) with a pulse width of 10 ns. The maximum pulse energy and the repetition rate are 1.2 J and 10 Hz, respectively. The pulses were expanded using a

beam expander before passing through a window, and were then focused perpendicularly on the target via a lens with a focal length of 500 mm; as a result, plasmas were produced and SXR radiations were emitted.

### Results & Discussion

To measure the generated SXR energy, an absolutely calibrated X-ray diode (XRD) with 200 nm titanium and 50 nm carbon filters (Opto Diode, AXUV100Ti/C2) was used. The XRD's specifications state that it has a detection range of 1–12 nm. By measuring the SXRs using the XRD located at 45° to the axis of laser beam incidence, we were able to optimize the operating conditions in terms of laser intensity and energy to maximize the CE. By changing the position of the focusing lens to vary the laser spot, the laser intensity on the target could be adjusted to determine the optimum intensity. Figure 2(a) shows the CE per unit solid angle as a function of the lens position (laser intensity). The laser pulse energy used was 0.5 J at 1 Hz. We denote the lens position (LP) using a zero at the best focus position, a negative number when in-focus (where the laser spot is in the target before the best focus) and a positive number for out-of-focus (beyond the best focus). Figure 2(a) shows the maximum CE at the best focus of LP = 0 mm, at which the laser spot diameter was 50  $\mu\text{m}$ . Next, the lens position was fixed at LP = 0 mm and the dependences of the laser pulse energy were investigated. Figure 2(b) shows the CE per unit solid angle as a function of the laser energy. This indicates that the CE was maximized at a laser energy of 1 J. From the above results, we concluded that the maximum CE per unit solid angle was achieved at LP = 0 mm and at a laser energy of 1 J, and the laser intensity was estimated to be  $5 \times 10^{12} \text{ W/cm}^2$ .

The spatial distributions of the SXR emissions were measured by scanning the XRD on a rotating stage around the plasma. The measurements showed that these distributions could be expressed using a fitting curve of  $(\cos\theta)^{0.41}$ . Taking this distribution into account, we obtained a maximum spatially integrated CE of 19% over the full XRD detection range (1–12 nm). With regard to the CE in the “water window” region, it can be calculated from the ratio of the area in the water window to the full range of the Ar spectrum shape. This ratio was calculated to be 0.76 and we concluded that the maximum spatially integrated CE was 14% in the water window (2.3–4.4 nm) with a laser energy of 1 J.

We then tested for repetitive generation of the plasma SXR pulses by focusing laser pulses with energy of 1 J at 1 Hz on the Ar target surface. The combination of the Ar gas flow rate and the target speed enable a re-covered target surface to be supplied for each laser pulse. The continuously generated repetitive SXR pulses were obtained successfully. In this experiment, we achieved continuous SXR generation with a high average power of 140 mW (=

1 J  $\times$  1 Hz  $\times$  14%) in the water window (2.3–4.4 nm). We expect our LPX source to offer a powerful alternative to the use of SR facilities for the development of various applications, including SXR microscopy.

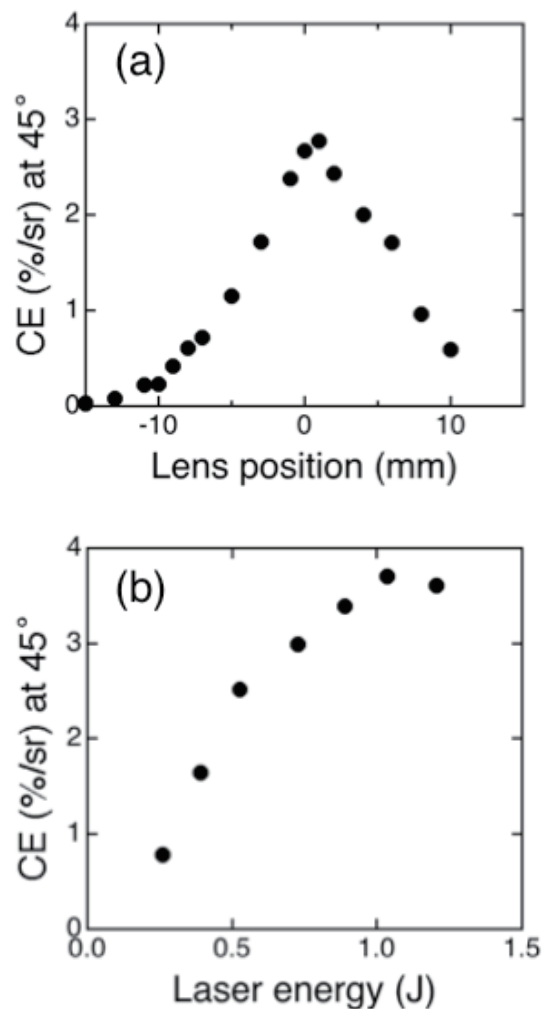


Fig.2. (a) CE per solid angle in full detection range (1–12 nm) as a function of lens position (LP). The laser energy was 0.5 J. (b) CE per solid angle at LP = 0 mm as a function of laser energy.

### Acknowledgments

This work was supported by JSPS KAKENHI (Grant No. 23654204 & 26390113) and Hyogo Science and Technology Association (Grant No.26049).

### References

- [1] S. Amano, Appl. Phys. Exp. **9**, 076201 (2016).
- [2] S. Amano, Rev. Sci. Instrum. **85**, 063104 (2014).

# Present Status of BL05A Performance

T. Hasegawa<sup>1,4</sup>, S. Fukushima<sup>2,4</sup>, T. Kotaka<sup>3</sup> and K. Kanda<sup>4</sup>

1 Synchrotron Analysis L.L.C., 3-2-24 Wadamia-dori, Hyogo-ku, Kobe-shi, Hyogo 652-0863 Japan

2 National Institute for Materials Science, 1-2-1 Sengen, Tsukuba-shi, Ibaraki 305-0047 Japan

3 New SUBARU, 1-1-2, Koto, Kamigori-cho, Ako-gun, Hyogo 678-1205 Japan

4 LASTI, University of Hyogo, 3-1-2 Koto Kamigori-cho, Ako-gun, Hyogo 678-1205 Japan

## Abstract

A renewed double crystal monochromator (DCM) improved performance of BL05A for X-ray absorption fine structure (XAFS) measurements in the soft X-ray region. We were successful in obtaining the extended X-ray absorption fine structure (EXAFS) spectrum owing to the stability of the exit X-ray beam intensity of the new DCM. In addition, we succeeded to obtain the aluminium *K*-edge X-ray absorption near edge structure (XANES) spectra because of the increased photon intensity in the aluminium *K*-edge region by replacing the beryllium filter (45  $\mu\text{m}$  thickness) with previous one (25  $\mu\text{m}$  thickness).

## Introduction

BL05 is constructed on the basis of strong demand of industrial users for X-ray absorption fine structure (XAFS) spectroscopy. This beamline consists of two branch lines, one is a double crystal monochromator (DCM) beamline (BL05A) for the use in the higher-energy region (1300-4000 eV) and the other is a varied line spacing plane grating (VLSPG) monochromator beamline (BL05B) for the use in the lower-energy region (50-1300 eV) [1, 2]. An angle that accepts X-rays exiting from the storage ring is different in BL05A and BL05B respectively, and so these branches can be operated simultaneously. BL05 is managed and maintained by the Synchrotron Analysis L.L.C. (SALLC), which is composed of the industrial companies, in cooperation with the staffs of the Laboratory of Advanced Science and Technology for Industry in University of Hyogo. We replaced the DCM in BL05A to corresponding to the user's demands for high-precision EXAFS measurements. In this paper, we describe improved performance of BL05A for XAFS measurements in the soft x-ray region.

### 1. EXAFS measurements using a renewed double crystal monochromator

In BL05A, a Golovchenko-type DCM has been used from 2008, the operation for public use of BL05 has started. The stability of the DCM is the most important factor in beamline performance. The DCM is mounted two parallel crystals to each other to produce a monochromatic exit beam which is running parallel with the incident white synchrotron radiation beam. But there was a problem with stability of the exit X-ray beam intensity, caused by deterioration of a driving mechanical

translating system of the crystals on the DCM. Therefore, It was difficult for the extended X-ray absorption fine structure (EXAFS) measurement, such as the bragg angle was varied widely, due to excessive attenuation of the monochromatic exit beam intensity. And so a renewed DCM, calculation and combination-type, was installed in 2014 (Fig.1). This new DCM is designed to maintain a good parallelism between crystals and stability of the exit X-ray beam position when scanning over a large energy range by moving all axes of crystals controlled by computer. Fig.2 shows the measured silicon *K*-edge EXAFS spectra of silicon dioxide ( $\alpha$ -quartz) using the previous DCM and the new one, respectively. We found out that high-quality EXAFS spectrum was obtained in the new DCM.

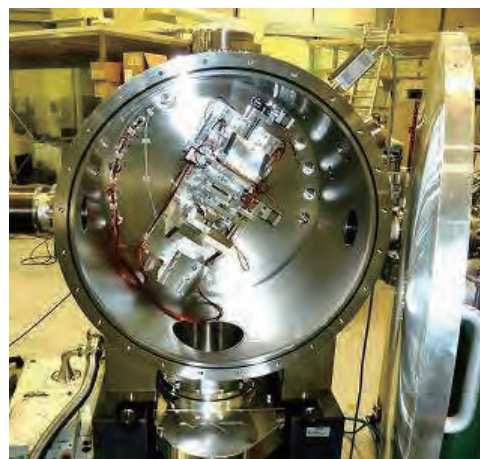


Fig.1 Inside of a renewed DCM.

### 2. Evaluation of an improved beryllium filter

In the soft X-ray beamlines, a beryllium filter is often used to protect the vacuum within

the storage ring from contamination because of providing a vacuum isolation and transmitting the X-ray beam. The beryllium filter in BL05A is installed to separate the ultra-high vacuum in the storage ring with the front-end from the high vacuum in the beamline, which is bonded to mounting flange. For the purpose of improving the transmission factor of X-rays at the lower-energy region (e.g., the  $K$  absorption edges of elements with atomic numbers less than silicon), we succeeded to make the filter of thickness from 45  $\mu\text{m}$  down to 25  $\mu\text{m}$  and obtain the magnesium  $K$ -edge XANES spectra in the past [3]. Then we tried to measure the aluminium  $K$ -edge XANES spectrum using the new filter. In Fig.3, the measured aluminium  $K$ -edge XANES spectra of several aluminium compounds are shown. We verified that there is enough photon intensity in these lower-energy region and can be obtained high-precision XANES spectra, which provide a detailed information related to chemical bond.

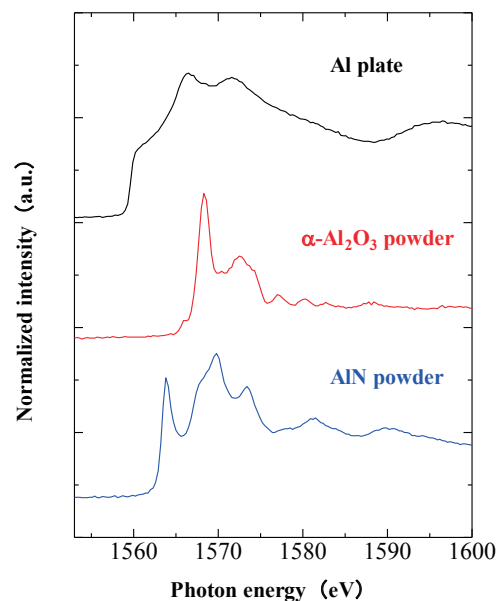


Fig.3 Al  $K$ -edge XANES spectra of aluminium compounds.

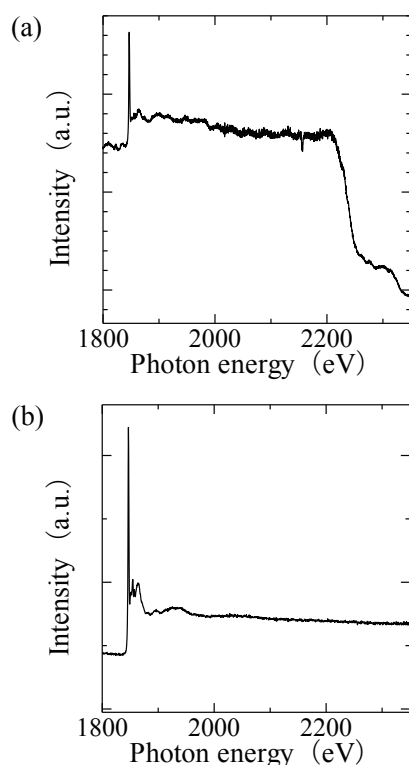


Fig.2 Si  $K$ -edge EXAFS spectra of silicon dioxide ( $\alpha$ -quartz) powder, (a) Golovchenko-type DCM and (b) calculation and combination-type DCM.

#### References

- [1] T. Hasegawa *et al.*, *Advances in X-ray Chem. Anal. Jpn.*, **41**, pp.99-106 (2010) [in Japanese].
- [2] K. Kanda *et al.*, *J. Phys.: Conf. Ser.*, **425**, 132005/1-4 (2013).
- [3] T. Hasegawa *et al.*, *LASTI Annual Report*, **vol.16**, pp.73-74 (2014).

# Development of the control system of double multilayers monochromator in New SUBARU BL07A

Masato Okui<sup>1,2</sup>, Isao Kikuchi<sup>2</sup>, Naoki Yato<sup>2</sup>, Akinobu Watanabe<sup>2</sup>, Norio Murayama<sup>2</sup>, Sei Fukushima<sup>1,3</sup> and Kazuhiro Kanda<sup>3</sup>

<sup>1</sup>LASTI, University of Hyogo, <sup>2</sup>Kohzu Precision Co., Ltd., and <sup>3</sup>National Institute of Material Sciences  
E-mail: okui@kohzu.co.jp

## Abstract

The upgrade project of New SUBARU BL07A began on 2013. In this project, a new double multilayers monochromator MKZ-7NS controlled by integrated computing was installed on the beamline. The features of the monochromator are shown from the point of view of the optical geometry in this report. A new control system using electronic cam algorithm on PC software was introduced since 2016 Spring. The software in this control system could scan with wave length continuously that was conventionally thought to be difficult using a computing type monochromator.

## Introduction

It is clear that a double crystal / multilayers monochromator plays an important role in many experiments using synchrotron radiation. The following two types of monochromator have been adopted widely in order to keep the fixed beam position on their downstream experimental equipment. One is a cam-actuated monochromator that the slave axes are connected mechanically to the main axis e.g. [1], and the other is a monochromator controlled each mechanically independent axes by computing e.g. [2].

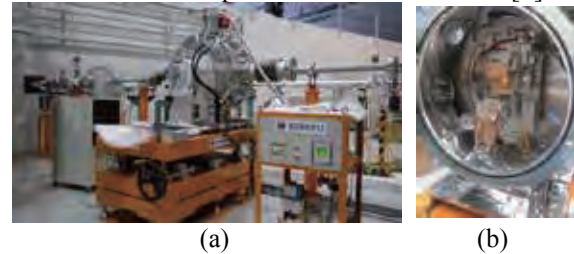
BL07 in New SUBARU is a beamline whose an insertion light source is a 3m undulator. This beamline is composed of two branch lines BL07A and BL07B [3]. The upgrade project of this beamline began on 2013. In this project, a new double multilayers monochromator Kohzu MKZ-7NS controlled by integrated computing was installed on BL07A [4].

In this report, the authors shall describe the features of the this new monochromator, MKZ-7NS. Additionally, they shall describe our new control system using electronic cam algorithm on the control software. The software in this control system shall be able to scan with wave length continuously that was conventionally thought to be difficult using the computing type monochromator.

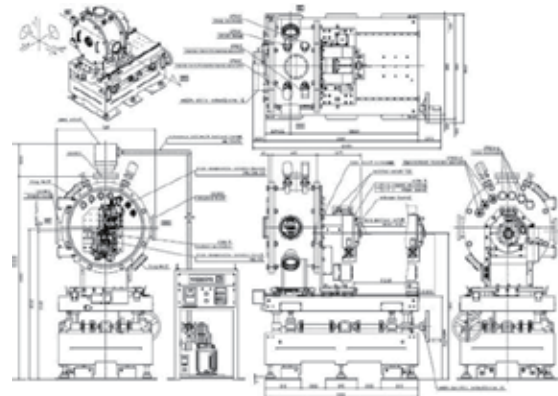
## The feature of MKZ-7NS

Fig. 1 shows the photograph of MKZ-7NS and its inside of their chamber. Fig.2 shows outline drawing of MKZ-7NS. The optical geometry using offset along the optical axis direction of the second monochromatic multilayers was adopted in MKZ-7NS as with the geometry of Kohzu KHL-3 in KEK PF [5]. A slave axis synchronized with main axis for emitting to fixed exit position is only Z2 axis. X axis used for switching of monochromatic crystals is

outside of the vacuum chamber. Thus, numbers of axes inside of the vacuum chamber are decreased to 5 axes less than the previous monochromator [2].



**Fig. 1.** Photograph of MKZ-7NS, (a) MKZ-7NS on BL07A in New SUBARU; (b) Inside of the Monochromator



**Fig. 2.** Outline drawing of MKZ-7S monochromator

## New control system for MKZ-7NS

Motor controllers, motor drivers and their control software was included in this control system. This motor controller was customized on the basis of Kohzu ARIES/LYNX multi-axis controller. The customized controller is able to change arbitrarily target position and speed during driving a motor without stopping movement. The optional function

of this controller make an electronic cam on the following control system practicable. The optical geometry is shown as Fig. 3 [4].

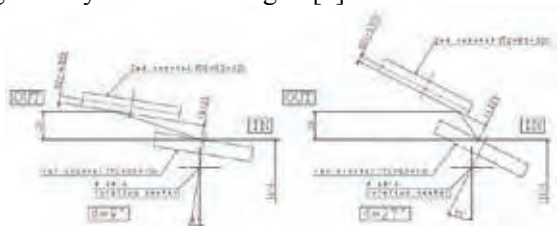


**Fig. 3.** Optical geometry of MKZ-7NS monochromator

$Z_2$  position of the slave axis synchronized to main axis is expressed by the following equation (1), where  $D$  is the offset of the monochromatic crystals,  $\theta$  is the Bragg angle, and  $D_0$  is the distance of the monochromatic crystals when the Bragg angle is the origin [4].

$$Z_2 = \frac{D}{2 \cos \theta} - D_0 \quad (1)$$

### Electronic Cam

The series of function of electronic cam shall be provided by the control software that remote-controls the motor controller on Windows PC. The flow chart of the algorithm of the electronic cam used in the control software is shown in Fig. 4. In this algorithm, the  $Y_2$  position is always corrected automatically to new position that is calculated by equation (1) each time when the control software gets newly the main axis position without stopping their movement even if the slave axis is moving.

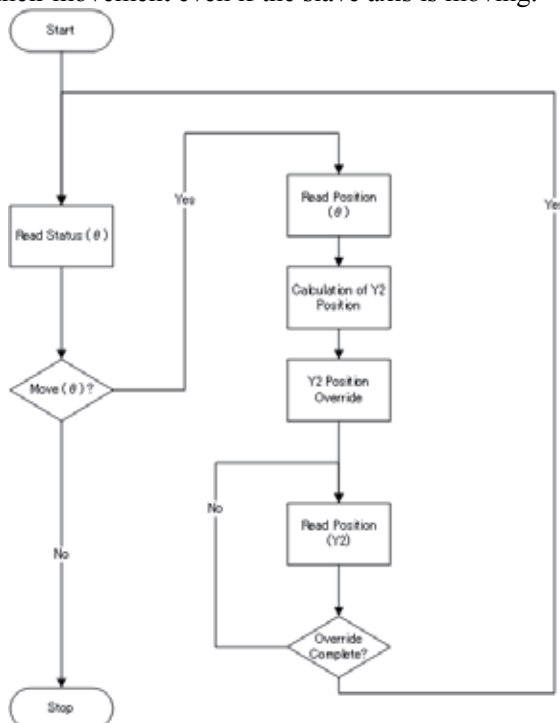


**Fig. 4** Flow chart of electronic cam

### Experimental results

New control software with electronic cam algorithm was installed to Windows PC that has been used for controlling its monochromator in BL07A. Since 2016 Spring, some verification experiments was performed in this beamline.

$Z_{2calc}$  that is calculated  $Z_2$  position by equation (1) and  $Z_{2act}$  that is actual position controlled by this electronic cam control algorithm are shown in Fig. 5 with regards to  $\theta$  angle, respectively. In Fig. 5, the difference between calculated position and actual position is also shown as  $\Delta Z_2$ , together.

In this experiment, 130eV was used as photon energy from its undulator in this experiment. And the main axis theta was driven from 14.6661deg to 20.7469deg.

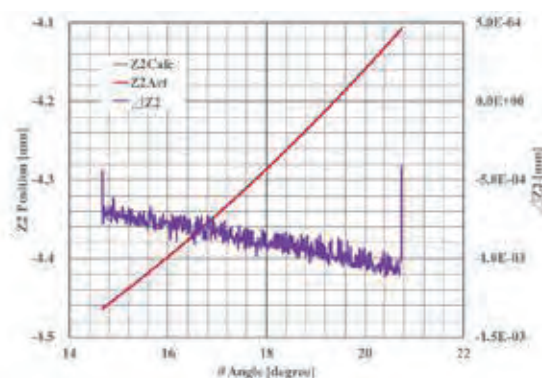


**Fig. 5**  $Z_2$  position regards to  $\theta$  angle and the difference between  $Z_{2act}-Z_{2calc}$ ,  $\Delta Z_2$

In Fig. 5 the line of actual  $Z_2$  position controlled by the algorithm of the electronic cam would be almost similar to it of calculated ideal  $Z_2$  position. The maximum difference between the calculated  $Z_2$  and the actual  $Z_2$  is approximately  $1.1 \mu\text{m}$ .

This result shows the electronic cam algorithm would be able to provide permissible fixed exit position of monochromatized radiation from the monochromator for almost user experiment in BL07A.

This electronic cam algorithm shall be able to scan with wave length continuously by a computing type monochromator as well as a mechanical cam-actuated type monochromator.

### References

- [1] M. Yabashi *et al.* Proc SPIE, **3773**, pp.2-13, (1999).
- [2] A. Nisawa *et al.* Nucl. Inst. & Meth. In Phys. Res. A, **497**, pp.563–568 (2003).
- [3] K. Kanda *et al.* Nucl. Inst. & Meth. In Phys. Res. A, **467–468**, pp.500–503 (2001).
- [4] M. Okui *et al.*, AIP Conf. Proc., in press.
- [5] H. Kawada *et al.*, AIP Conf. Proc., **705**, pp.663–666 (2004).

# Performance of BL07A installed new multilayered-mirror monochromator

Shotaro TANAKA<sup>1</sup>, Naoki YATO<sup>2</sup>, Masato OKUI<sup>1,2</sup>, Sei FUKUSHIMA<sup>1,3</sup> and Kazuhiro KANDA<sup>1</sup>

1. LASTI, University of Hyogo

2. Kohzu Precision Co., Ltd.

3. National Institute for Materials Science.

## Abstract

New integrated computing multilayered-mirror monochromator (MLMM) was installed at BL07A to eliminate unnecessary harmonic light from an undulator. BL07A is 3-m undulator beamline for high photon-flux irradiation with monochromatized light. These characters satisfy for SR stimulation process experiments such as single excitation process experiments and low temperature process. We measured intensity at irradiation chamber using photodiode. As a result intensity of incident beam was more than  $10^{14}$  photons/s·cm<sup>2</sup> at the energy range of 80-560 eV at irradiation chamber of BL07A.

## Introduction

New MLMM was installed at BL07A. BL07A is 3-m undulator beamline. It is designed for high photon-flux irradiation. Energy of incident light can be selected because of quasi-monochromatized light. But unnecessary harmonic light is also irradiated, and it becomes hard to study single excitation process.

Recently, single excitation process experiments are required. For example, Si crystallization at low temperature is utilized for flexible display and molecular knife can be studied for modification of materials. For experiments of single excitation process, integrated computing multilayered-mirror monochromator (MLMM) was installed at BL07A.

In soft X-ray region, the reflectance of many materials is very small. However energy resolution is high, intensity used normal double crystal monochromator is decreased. Multilayered mirror is fitted for improvement of reflectivity index in soft X-ray region. Incident light is reflected by many interfaces on multilayered mirror, and there are interfered. Thus, higher reflectance can be gained using multilayered mirror. Therefore, multilayered mirror was selected as monochromatic devices instead of crystal.

In this report, the intensity of incident beam at irradiation chamber of BL07A was measured using photodiode.

## Multilayered mirror

Monochromator, MKZ-7NS designed and fabricated by Kohzu Precision Co. Ltd was constructed at BL07A [1]. MKZ-7NS is controlled by integrated computing. The Bragg angle can be from 9° to 65°. Detailed information on MKZ-7NS was reported on ref. [2].

Table 1. Multilayer mirrors.

Energy (eV)	multilayer	Spacing
80-200	Mo/Si	20 nm
125-360	Mo/B <sub>4</sub> C	11 nm
260-800	Ni/C	5 nm

Three kinds of multilayered mirror were used for covering an energy range from 80 to 800 eV. Table 1 shows used multilayered mirrors. However reflection of multilayered mirror is higher, harmonic light is also occurred. For elimination of harmonic light from multilayered mirror, three kinds of filter were mounted. Table 2 shows detail

Table 2. Filters.

Energy (eV)	Filter	Thickness
140-400	Ag	100 nm
400-560	Cr	500 nm
560-800	Ni	500 nm

of filters. Combinations of mirrors and filters could be realized high intensity monochromatized light.

The intensity of incident beam at irradiation chamber of BL07A was measured by a photodiode (AXUV-100). Light reception area of this photodiode was  $1 \text{ cm}^2$ . Intensity unit was defined photons/s $\cdot$ cm $^2$ .

### Result and discussion

Figure 1 shows intensity of incident beam at irradiation chamber of BL07A. During this experiment, the electron energy of NewSUBARU storage ring was 1.0 GeV. In the energy range of 80-200 eV, maximum of intensity was more than  $10^{15}$  photons/s $\cdot$ cm $^2$ , and in the energy range from 200-560 eV, maximum of intensity was more than  $10^{14}$  photons/s $\cdot$ cm $^2$ . This intensity can be used for irradiation experiments sufficiently. But, in the energy range of up to 800 eV, the intensity was drastically decrease. This is considered the intensity of monochromatized light is cut by Ni filter. 7th harmonic light was the highest intensity at the range of 200-560 eV. But 7th harmonic light was not ensured monochromatized condition. Therefore, when this beamline was used, 1st-5th harmonic lights should be used.

### Conclusion

The intensity of incident beam at irradiation chamber of BL07A was measured using photodiode. As a result, the intensity was more than  $10^{14}$  photons/s $\cdot$ cm $^2$  at the range from 80-560 eV. This intensity can be used for irradiation experiments sufficiently, and ionized energy of useful light elements, such as C, Si was covered.

### Reference

- [1] K. Kanda *et al.*, Nucl. Inst. Meth. A, 467-468 (2001)500.
- [2] M. Okui *et al.*, Proc. SRI2015, (2015).

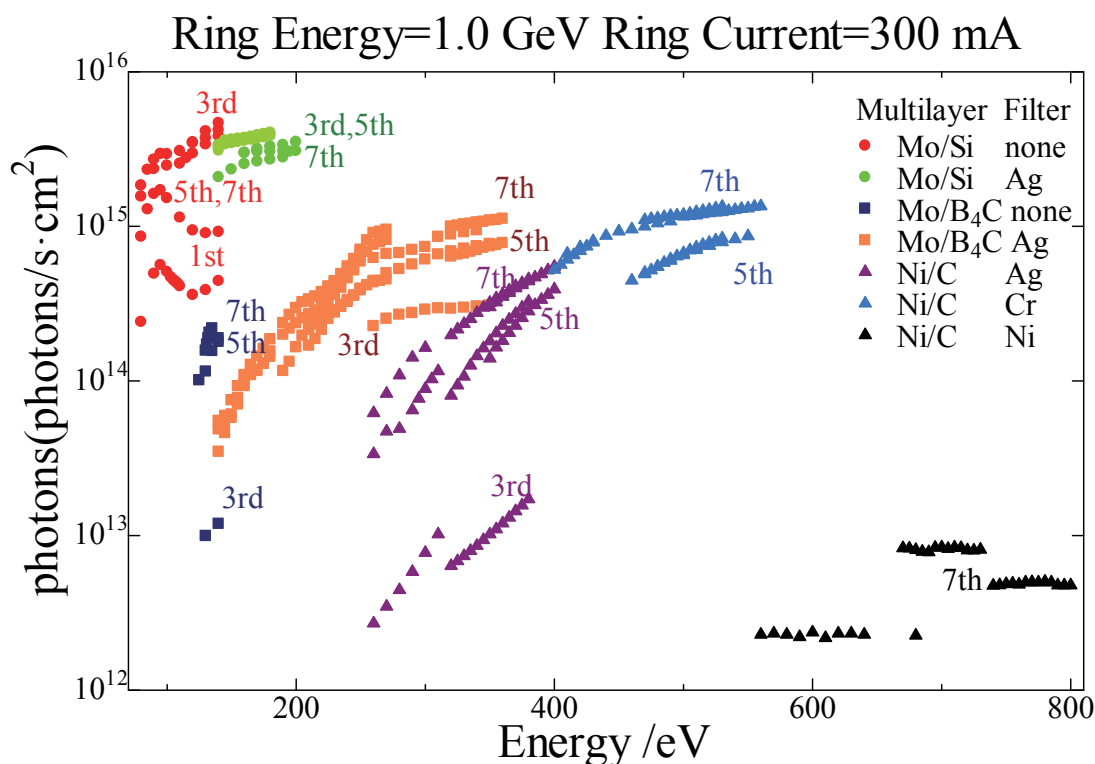


Figure 1. Intensity of incident beam at irradiation chamber at 1.0 GeV operation mode.

# Adjustment of the equipment for the measurement of Ultra-soft X-ray Fluorescence Spectrum on BL07A

Sei Fukushima<sup>1,2</sup>, Hiroki Takamatsu<sup>1</sup>, Shotaro Tanaka<sup>1</sup>, Kazuhiro Kanda<sup>1</sup>

1: LASTI, University of Hyogo, 3-1-2 Koto Kamigori-cho, Ako-gun, Hyogo 678-1205 Japan

2: National Institute for Materials Science, 1-2-1 Sengen, Tsukuba-shi, Ibaraki 305-0047 Japan

## Abstract

For the development and investigation of ultra-soft X-ray fluorescence spectroscopy for the non-destructive chemical state analysis of ultra-light elements in several advances materials, the equipment with high-performance type spectrometer had been installed at the end of BL07A in 2014FY. However, the existence of some items on which countermeasures should be required was revealed in last FY. In this report, tow of countermeasures is presented.

## Introduction

For analyzing the chemical state or the electronic structure of valence band, one of the most popular methods is XAFS (X-ray absorption fine structure) measurement, and NewSUBARU has been already executed and obtained many remarkable results in the field of ultra-light elements such as Li, C and so on. However, one of the disadvantage points of XAFS measurement is the necessity of sweep the energy of incident X-rays. As known well, the efficiency of excitation for core level of such ultra-light element is so low, thus highly condensed

monochromatized X-ray beam with high photon flux should be necessary for measurement.

In contrast, the energy sweep of incident X-rays are not necessary for obtaining any fluorescent X-rays (characteristic X-rays) from the samples. Thus, the examination about the possibility of application of fluorescent X-rays of ultra-light elements is important as a practical meaning.

Instead of the X-rays for excitation, electron beam is also available for obtaining characteristic X-rays, and this manner is already widely used as the EPMA (electron probe micro analyzer) analysis. This manner is also efficient for the ultra-light elements, and, some of these members have already fabricated EPMA system for the chemical state analysis of ultra-light elements [1]. As already shown in the Annual report in last FY, the spectrometer for fluorescent X-rays was already confirmed its specification, and has been continue to adjustment at BL07A.

In last FY, the existence of some items in both beamline and this spectrometer was revealed, and the countermeasures against these items had been executed. In this report, two of these countermeasures are presented.

## Re-adjustment of spectrometer

Just before and after stopping of the storage ring, the signal strength of the spectrometer had become weak. The overview and schematic illustration of this spectrometer is shown in Fig.1. The important points of adjustment of

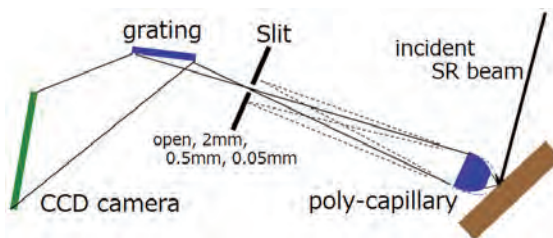


Fig.1  
The overview and the schematic illustration of the ultra-soft X-ray spectrometer.

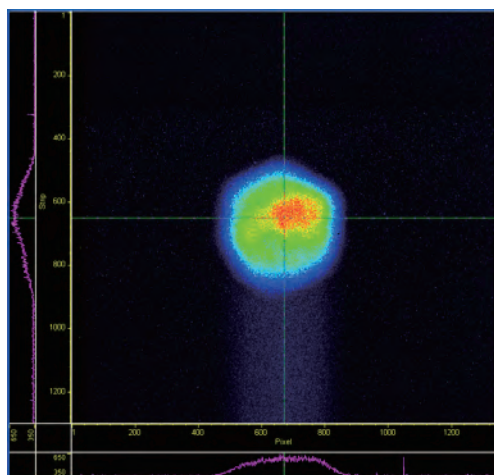


Fig.2 The CCD camera image of the scattered X-rays at the sample surface path through the poly-capillary and slit directly.

this spectrometer are the alignment with poly-capillary, slit and grating. Thus, before the adjustment of direction of poly-capillary, the alignment of the position of slit against the emission point of fluorescent X-rays on the sample surface path through the top of poly-capillary should be adjusted.

For this aim, whole of the part just after the slit system had been removed for the first. And, CCD camera was connected for observing the beam position which came from the sample surface after the direction of poly-capillary was set beside the optical axes mechanically. Then, introducing the SR beam to sample surface, and the slit holder was adjusted using micro movement mechanism of the holder when the brightest spot image on CCD camera was observed. The spot image just after the adjustment is shown in Fig.2.

After the adjustment of slit position and the re-construction of the spectrometer, the rough alignment of the direction of poly-capillary was executed using the zero-order light beam of the grating till obtaining the most homogeneous and bright image on CCD camera. In Fig.3, the camera image of the zero-order light just after the adjustment is shown.

Finally, using the micro movement mechanism of poly-capillary and the scattered X-rays from the sample surface, the alignment of whole system was adjusted.

After the all of above process, the normal movement of this spectrometer was confirmed, because the almost same bright image of scattering X-rays was obtained.

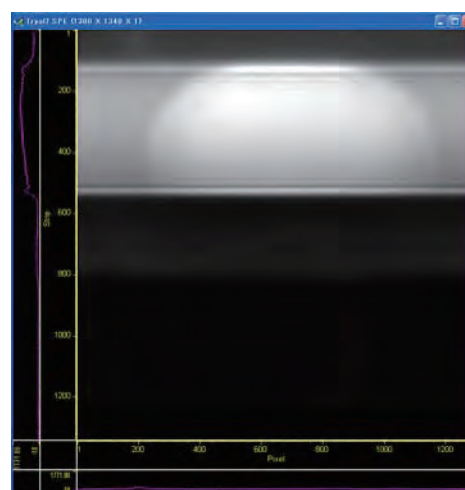


Fig.3 The CCD camera image of the zero-order light just after the adjustment.

### Cleaning multi-layer mirror

In parallel with the adjustment of alignment of spectrometer, the lowering of the strength of the incident beam was also investigated. There are two possible causes of the lowering; one is the carbon fouling on the surface of switching mirror at the end of the front-end system of BL07, and the other is the same fouling on the multi-layer mirror (Mo/Si, Mo/B<sub>4</sub>C and Ni/C ; these were fabricated on the one piece of Si substrate.) of the beamline monochromator.

The cleaning of switching mirror was carried out by plasma ashing process aided by the SPring-8.

On the other hand, there had been hard to find any report about the cleaning of the surface of such kind of the multi-layer flat mirror for beamline monochromator. Fortunately, Dr.T. Harada (LASTI, Univ. Hyogo) et al. had reported the cleaning process of the multi-layer mirror surface of the reduction optical system using the combination of ozone and the excimer ultraviolet light source. So, the cleaning process two multi-layer mirror of BL07 was also carried out by cleaning system set at BL03 with the great support of Dr. Harada.

In Fig.4, the comparison of surface of the mirror between just before and just after of cleaning process is shown. In Fig.4(b), the surface of mirrors just after about 10hrs processing is shown. The foot print of the incident beam is clearly observed as the carbon fouling. Fig.4(c) is just after about 20hrs. No

fouling can be seen on the surface.

#### Present state and future

During 2015FY, as shown above, almost all of the machine time had to be consumed for the adjustment and treatment of beamline components and equipment. Almost items against which required any countermeasure was seemed to be disappeared.

In this FY, all of the adjustment will make to be finished, and e-started, the examination of measurement condition of

the fluorescent X-rays will be re-started as soon as possible.

#### Acknowledgement

The authors thank gratefully Dr. Tetsuo Harada (LASTI, Univ. Hyogo) for the cleaning of multi-layer mirror, and Kazunori Tsukamoto and Dr. Toyohiko Tazawa (JEOL Ltd.) for the adjustment of the equipment.

#### References

[1] S. Fukushima *et al.* *Microchim. Acta* **161** pp.399-404 (2007)

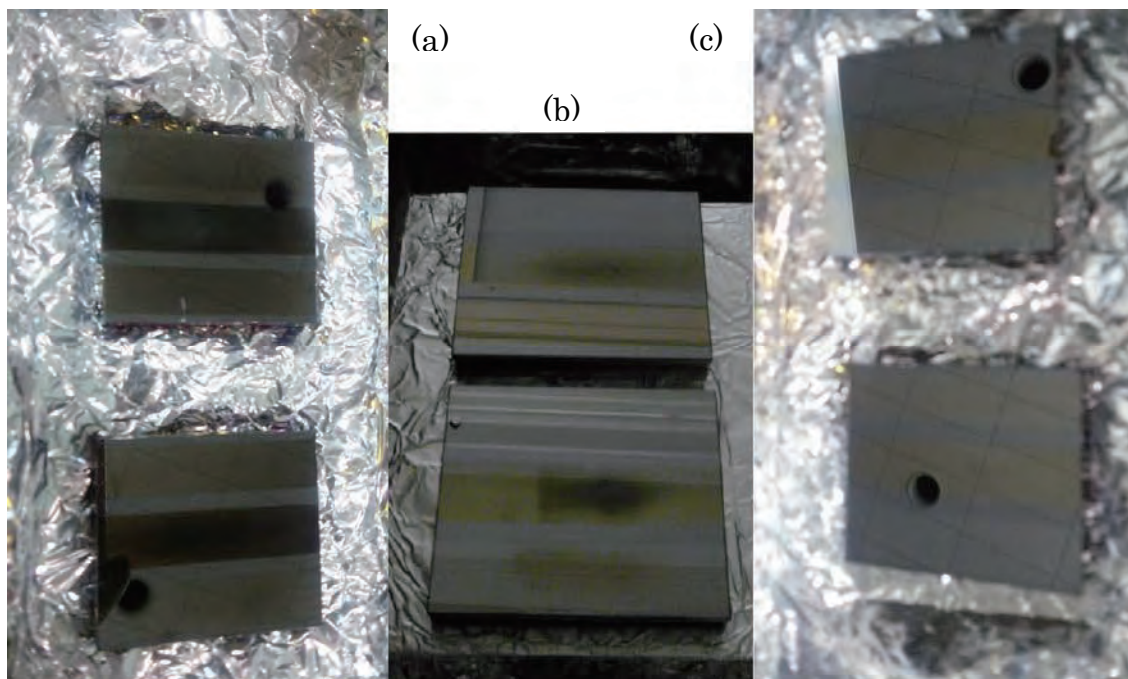


Fig.4 The aspect of the multi-layer mirror surface.

- (a) Just before cleaning.
- (b) After about 10hrs. Lower is the 1st mirror of the beamline monochromator, and the foot print of incident beam is clearly recognized.
- (c) Just after cleaning (about 20hrs).

The black small solid circle images are the reflected images of the ceiling air duct.

# Installation of Silicon Drift Detector for PFY-XAFS Measurement of Insulating Materials in BL-09A

Shigeaki Uemura<sup>1</sup>, Junji Iihara<sup>1</sup>, Takashi Yajima<sup>2</sup>, Masahito Niibe<sup>3</sup>

<sup>1</sup>Sumitomo Electric Industries, Ltd., <sup>2</sup>Sumitomo Riko Company Limited, <sup>3</sup>University of Hyogo

## Abstract

We installed a silicon drift detector at BL-09A in NewSUBARU, in order to perform PFY-XAFS measurements for insulating materials. We applied this technique to h-BN and polyimide and succeeded to obtain good spectra.

## Introduction

We are developing XAFS measurement techniques for insulating materials such as ceramics and resins. Last year, we succeeded in the TEY-XAFS measurement for hexagonal boron nitride (h-BN) with evaporated gold stripe, which was very effective to reduce charge up [1].

In this study, we developed the TFY-XAFS technique for the resin materials, whose thermal stability is so poor that the gold stripe evaporation cannot be used. Instead of the conventional photo diode detectors, we attempted to utilize a silicon drift detector (SDD), which enables us to obtain XAFS spectra even from charged up specimens, realizing a superior energy resolution, signal to background ratio, and sensitivity.

## Installation of SDD

We installed an SDD of AMPTek, Inc. (Type: X123SDD) at an ICF port of the analyzing chamber in BL9A. The distance between the SDD and sample is variable from 50 to 250 mm (Fig. 1).

We modified the control program of BL9A to obtain spectrum by the SDD at each energy of the incident x-ray, which enabled us to optimize the region of interest (ROI) for PFY-XAFS after the measurement. This was very useful to separate the fluorescence signal from elastic scattering signal.

Figure 2 shows a distribution of the fluorescence intensity that was obtained from a highly oriented pyrolytic graphite (HOPG) sample. The PFY-XAFS spectrum, which is extracted with the ROI indicated by the blue line, is shown in Fig. 3.

## Application of PFY-XAFS for insulating materials

We applied the newly developed PFY-XAFS measurement technique to the h-BN sample. Figure 4 shows the obtained spectrum, which was found to be very similar

to the one that had been obtained by the TEY-XAFS technique using gold stripe [1]. This result demonstrates that the PFY-XAFS technique is very useful to measure insulating materials.

Then, we applied the PFY-XAFS technique to poly imide (PI) films. We prepared following two specimens: one is processed by a special surface treatment and the other not processed.

Figure 5 shows the PFY-XAFS spectra of the two PI films. There are four prominent peaks, A, B, C and D, which are assigned to C=C, C=O in pyromellitic anhydride (PMDA), O-C=O, and C=C in the 4,4-diamino diphenyl ether (ODA), respectively [2]. We found that peak A and C became larger while peak B became smaller by the surface treatment process. Peak D showed no significant change by the treatment. As a possible mechanism, the increase of peak B (O-C=O) and decrease of peak C (C=O) may suggest that the imide rings cleave by the surface treatment, as shown in Fig. 6. Regarding the increase of peak A, further investigation will be required.

## References

- [1] T.Yonemura, J.Iihara, S.Uemura, K.Yamaguchi and M.Niibe, 2014 New Subaru Annual report p.106-107
- [2] T. Tanaka, K. K. Bando, N. Matsubayashi, M. Imamura and H. Shimada, *Physica Scripta*. Vol. T115, 412-414 (2005)



Fig. 1 Attached SDD in an analyzing chamber at BL9A.

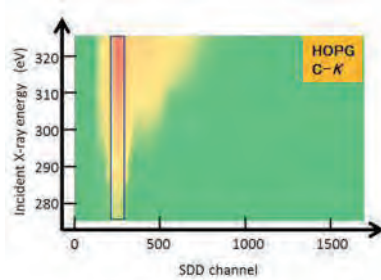


Fig. 2 Distribution of fluorescence intensity obtained from HOPG.

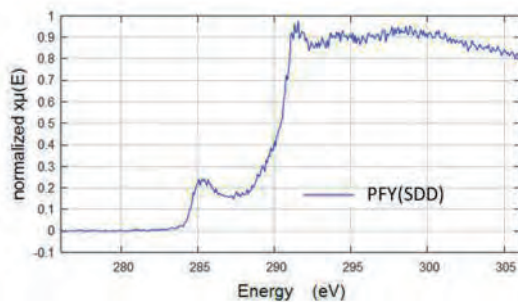


Fig. 3 C-K XAFS spectrum of HOPG.

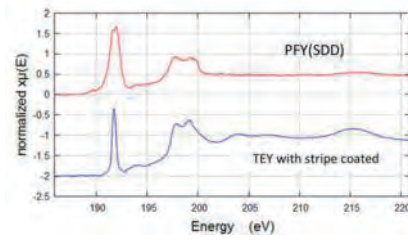


Fig. 4 B-K XAFS spectrum of h-BN. (upper) PFY-XAFS (lower) TEY-XAFS.

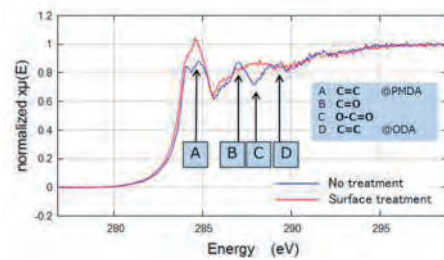


Fig. 5 C-K XAFS spectrum for Polyimides with/without surface treatment

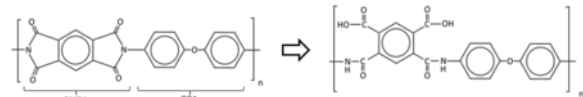


Fig. 6 Cleaving of imide ring.

# Development of an analysis station for soft X-ray absorption spectroscopy in BL10

Yasuji Muramatsu, Akinobu Tsueda, Tomoyuki Uemura, Keita Nambu, Takahito Ouchi, Tetsuo Harada, Takeo Watanabe, and Hiroo Kinoshita  
University of Hyogo

## Abstract

A measurement station for X-ray absorption spectroscopy (XAS) has been developed and installed in BL10 at the NewSUBARU. The XAS station enables the soft X-ray absorption measurements in 70 – 1100 eV region with a total electron yield (TEY) method. The station will be widely utilized for chemical and/or local-structure analyses of light element materials.

## Introduction

A beamline BL10 has been developed as a multi-purpose soft X-ray beamline in NewSUBARU (NS) [1]. Especially, it has been mainly used for optical evaluation of multilayer mirrors. However, optical properties of BL10 is suitable for X-ray absorption spectroscopy (XAS) in soft X-ray region, because BL10 has a potential to utilize soft X-rays ranging from several tens eV to 1000 eV emitted from a bending magnet source. Additionally, an analysis station for soft X-ray absorption spectroscopy in NewSUBARU has been required by materials scientists. Hence, we have developed the soft X-ray absorption analysis station, and installed it in BL10. The present report briefly describes the design and performance of the XAS station [2-5].

## Design of the XAS station

The XAS station has been designed based on the following concepts;

- (1) Compact chamber to install the limited narrow space of BL10.
- (2) Simple and flexible chamber to easily improve the measurement functions.
- (3) Large sample plates can be loaded into the measurement chamber for the efficient measurements. Many sample plates can also be loaded in a sample-bank chamber.
- (4) High speed pumping to enable the measurements under the middle vacuum ( $\sim 10^{-6}$  Torr).
- (5) Position and angle of sample plate can be easily adjusted by a four-axis stage.

Based on the above concepts, the XAS chamber has been developed and installed in BL10 as shown in Fig. 1. The XAS station consists of a main chamber and a sample-bank chamber. A large ICF-305  $\phi$  pipe was used for the main chamber, and the chamber was sealed with an O-ring for easy access to the chamber. Size of a sample plate (Cu plate) is 70 x 25 mm<sup>2</sup>, on which

twenty samples (5 x 5 mm<sup>2</sup>) can be mounted.

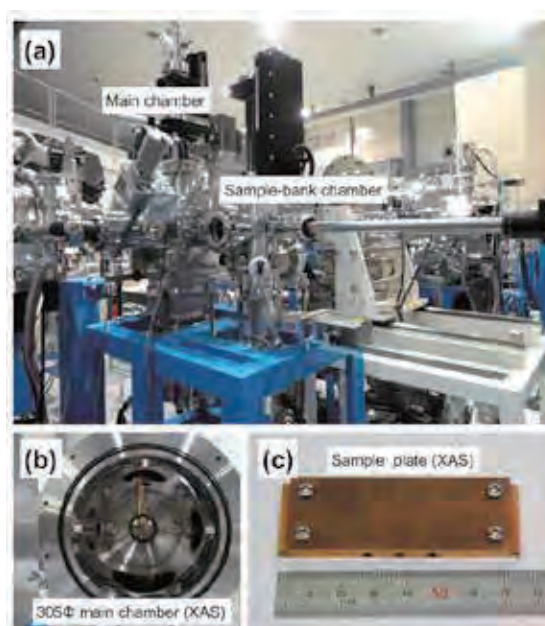


**Fig. 1** Photos of the XAS station (a), a main chamber (b), and a sample plate (c).

## Performance of the XAS station

Figure 2 shows X-ray absorption near-edge structure (XANES) of standard samples measured with three gratings (600, 1800, 2400 mm<sup>-1</sup>) of BL10 monochromator. XANES measured in BL10/NS are compared to those in BL-6.3.2 at the Advanced Light Source (ALS). The figure clearly shows that the high-resolution XANES from Al *L* edge ( $\sim 70$  eV) to Zn *L* edge ( $\sim 1100$  eV) can be obtained in BL10/NS.

Figure 3 (left panel) shows the incident-angle( $\phi$ )-dependent C *K*-XANES of the highly oriented pyrolytic graphite (HOPG) and carbon black (CB). The spectra were taken with the incident angles of 15  $\sim$  90° (normal incidence). HOPG exhibits strong incident-angle-dependence on the  $\pi^*$  peak intensity. However, carbon black exhibits little angle dependence,



# Soft X-ray absorption spectroscopy (XAS) and X-ray reflectivity (XRR) analysis system in BL10

Yasuji Muramatsu, Akinobu Tsueda, Tomoyuki Uemura, Keita Nambu, Takahito Ouchi, and Tetsuo Harada, Takeo Watanabe, and Hiroo Kinoshita  
University of Hyogo

## Abstract

A measurement station for X-ray absorption spectroscopy (XAS) has been newly installed upstream the X-ray reflectometer in BL10 at the NewSUBARU. By combination of the conventional X-ray reflectometer, XAS analysis and X-ray reflectivity (XRR) evaluation in soft X-ray region can be performed in BL10. Chemical state and layer structure analyses of organic thin films were demonstrated by using the XAS/XRR system.

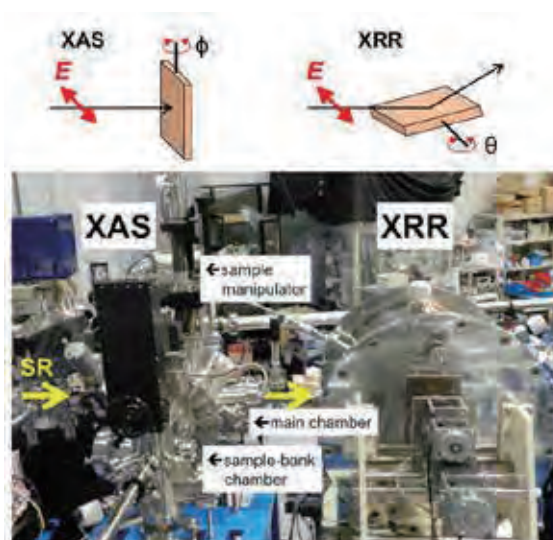
## Introduction

Recently, an analysis station for X-ray absorption spectroscopy (XAS) has been developed [1-3] and installed upstream the X-ray reflectometer in BL10 at the NewSUBARU. The XAS station enables the chemical/electronic-state analysis, and the X-ray reflectometer enables layer structure analysis from the X-ray reflectivity (XRR) measurements. Thus, the XAS/XRR system can be a nice tool for evaluation of thin films composed of light elements. The present report demonstrates the chemical and layer-structure analyses of organic thin films using the XAS/XRR system [4].

## Experiments

Figure 1 shows the XAS/XRR system composed of the XAS and XRR stations, which are installed in tandem. In the XAS station, a sample plate can be rotated around a vertical axis, which can analyze the orientation. On the other hand, a sample plate can be rotated around a horizontal axis in the XRR station, which can analyze the angle-dependent X-ray reflectivity and chemical analysis in depth direction.

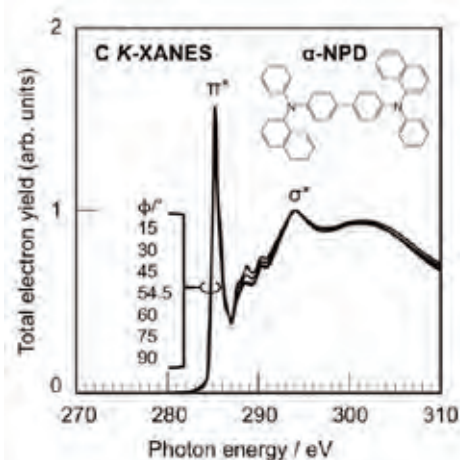
Samples were prepared by Sumika Chemical Analysis Service, Ltd. The measured organic films were vacuum deposition films of N,N'-Di (1-naphthyl)-N,N'-diphenylbenzidine ( $\alpha$ -NPD) on Si substrates. Thickness of the films can be estimated as approximately 100 nm. Orientation of the  $\alpha$ -NPD films was evaluated by the incident-angle ( $\phi$ )-dependent C K XANES (X-ray absorption near-edge structure) in the XAS station. XANES in N K edge of the films was also measured to analyze their chemical states. Incident-angle ( $\theta$ )-dependent XAS and XRR in the 200 – 600 eV region were simultaneously measured in the XRR station. XAS spectra were obtained with a total electron yield (TEY) method in both XAS and XRR stations.



**Fig. 1** Photograph of XAS and XRR stations in BL10. Upper panel shows the layout of sample rotations.

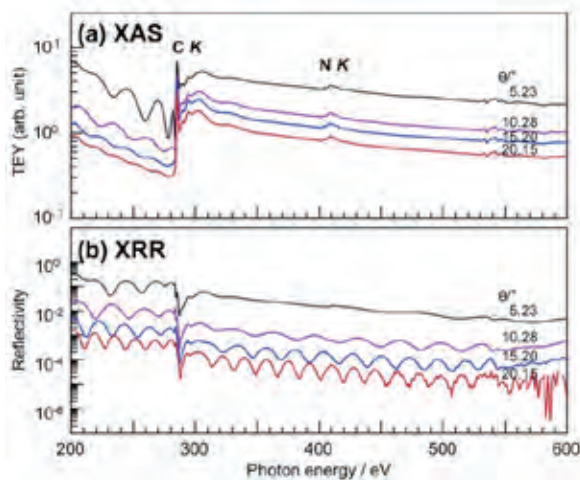
## Results and Discussion

Figure 2 shows the  $\phi$ -dependent C K-XANES of the  $\alpha$ -NPD films. It is confirmed that the  $\alpha$ -NPD films take no layer structure, because little  $\phi$ -dependence was observed.



**Fig. 2**  $\phi$ -dependent C K-XANES of the  $\alpha$ -NPD films, measured with  $\phi = 15 \sim 90^\circ$ .

Figure 3 shows the simultaneously measured TEY-XAS and XRR spectra in a 200 – 600 eV region of the  $\alpha$ -NPD films. In XAS spectra, interference structures can be clearly observed below the C K edge, which are dependent on the incident angle  $\theta$ . Absorption peaks in C K and NK regions can be clearly observed, because  $\alpha$ -NPD is composed of carbon and nitrogen atoms. Little peak can be observed in O K edge even in the shallow angle of 5.23°. This means that surface of the  $\alpha$ -NPD film is not oxidized. In XRR spectra, interference structures can be clearly observed in the 200 – 600 eV range, which depend on  $\theta$ . This clarifies that the  $\alpha$ -NPD films were deposited as uniform layers.



**Fig. 3** Simultaneously measured TEY-XAS (a) and XRR (b) spectra of the  $\alpha$ -NPD film sample, measured with  $\theta = 5.23, 10.28, 15.20,$  and  $20.15^\circ$ .

To determine the thickness of the  $\alpha$ -NPD films on Si substrates, XRR spectra taken with  $\theta = 20.15^\circ$  was simulated as shown in Figure 4. The simulations were performed by using the optical calculation software of the Center for X-Ray Optics (CXRO). Interference structures were fitted below and above the C K edge. Slight phase shift of 3.2 eV was observed at the C K edge. In the both regions, the measured interference structure can be well fitted by the simulations with parameters of 102.5 nm thickness of  $\alpha$ -NPD film on a  $\text{SiO}_2/\text{Si}$  substrate. This calculated thickness agrees to the estimated thickness of 100 nm.

In conclusion, the XAS/XRR system in BL10 is a powerful tool to evaluate chemical/electronic-states and layer structures of organic thin film samples.

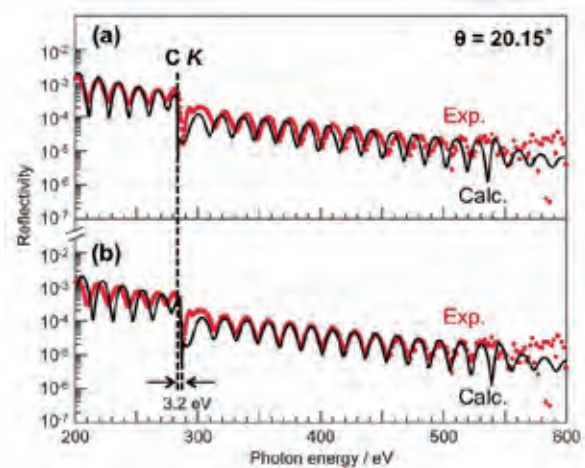


**Fig. 4** Upper panel (a) shows the calculated XRR spectrum (solid line) of the  $\alpha$ -NPD/ $\text{SiO}_2/\text{Si}$  system, compared to the measured XRR spectrum (dotted line) of the  $\alpha$ -NPD film sample. Lower panel (b) shows the calculated XRR spectrum shifted with +3.2 eV.

#### Acknowledgements

We would like to express thanks to Dr. Shogo Suehiro of Sumika Chemical Analysis Service, Ltd for his preparation of the  $\alpha$ -NPD film samples.

#### References

- [1] Y. Muramatsu, A. Tsueda, T. Harada, and H. Kinoshita, *Adv. X-ray Chem. Anal., Japan*, 43, 407-414 (2012).
- [2] Y. Muramatsu, A. Tsueda, T. Uemura, T. Harada, and H. Kinoshita, *Adv. X-ray Chem. Anal., Japan*, 44, 243-251 (2013).
- [3] T. Uemura, Y. Muramatsu, K. Nambu, T. Harada, and H. Kinoshita, *Adv. X-ray Chem. Anal., Japan*, 45, 269-278 (2014).
- [4] T. Uemura, Y. Muramatsu, K. Nambu, D. Fukuyama, M. Kuki, T. Harada, T. Watanabe, and H. Kinoshita, *Adv. X-ray Chem. Anal., Japan*, 46, 317-325 (2015).

## Part 2. Research Activities



Workshop of synchrotron radiation usage



# Development of LCS Gamma-Ray Simulation Code and GUI Application

Satoshi Hashimoto, Takuya Matsumoto, and Shuji Miyamoto  
LASTI

## Abstract

We are developing a simulation codes on Laser Compton Scattering Gamma-Ray generation and its Graphical User Interface application. These codes can make possible the numerical reproduction of the complex LCS experiments, the easy execution of the simulation for users, and the data visualization.

## Introduction

The beamline BL01 of NewSUBARU synchrotron light facility [1] is one of the few Laser Compton Scattering (LCS) Gamma-ray facilities in the world. Using LCS Gamma-ray at the NewSUBARU, user experiments such as HARPO project [2] have been performed.

The LCS Gamma-ray source is composed from many systems such as an electron accelerator, laser systems, optical components, collimators, detectors.

We are developing the LCS simulation code that can reproduce the realistic experiments. And also we have developed the useful GUI program for easy execution of the simulation. These codes can run in cross-platform environments (Linux, OSX, Windows).

## LCS Gamma-ray Simulation code

The simulation code we are developing is basically based on theoretical works [3,4] and is coded with Fortran. At first we developed the code according to a simple 1D model approximately including the effects of finite emittances of the electron and laser beams. Intensity graphs of gamma photons when a horizontally polarized laser beam with finite radius collides with an electron beam with finite emittance are shown in Fig.1. Simulation result agrees well with measurement.

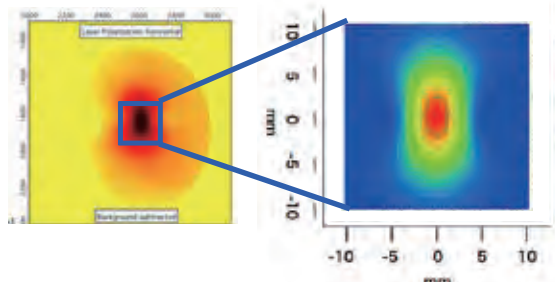


Fig.1 Intensity plots of LCS gamma-ray by the horizontally polarized laser photons. Measured by an imaging plate (left) and simulation (right).

Further upgrade of the code is in progress, that is, a code due to the Monte-Carlo method with many numerical particles in order to be closer to reality.

## GUI Application

The Fortran simulation code reads lots of parameters from input files and writes the huge numerical data to output files. For easy execution by users, we also developed a Graphical User Interface (GUI) program. The GUI program is separated from the simulation code and written using Python and its graphical toolkit, WxPython. Users can easily edit, load and save input parameters, execute the simulation code, visualize output data on the GUI panel. Typical GUI panels are shown in Fig.2.

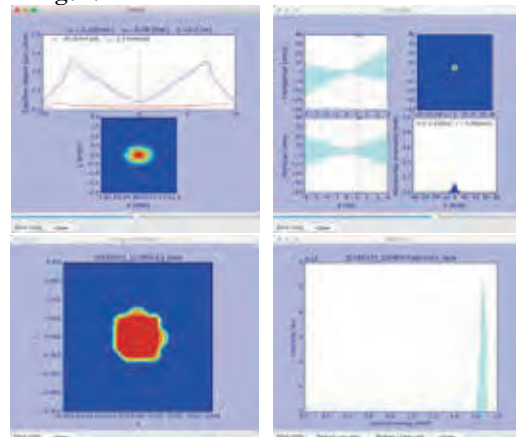


Fig.2 GUI front panels for the LCS simulation.

## References

- [1] <http://www.lasti.u-hyogo.ac.jp/NS-en/facility/bl01/>
- [2] S.Wang, D.Bernard, et al., 7<sup>th</sup> Symposium on Large TPCs for Low-Energy Rare Event Detection, Paris, 15-17 December 2014.
- [3] V.N.Litvinenko, J.Madey, SPIE vol. 2521, 55-77
- [4] C.Sun and Y.K.Wu, Phys.Rev.ST Accel. Beams 14: 044701,2011

# Measurements of neutron energy spectra depending on the emission angle due to photo-nuclear reaction using LCS photons

Yoshihiro Asano<sup>1,5</sup>, Toshiya Sanami<sup>1,2</sup>, Hiroshi Nakashima<sup>1,3</sup>,  
Yoichi Kirihara<sup>2</sup>, Toshiro Itoga<sup>4</sup>, Yoshihito Namito<sup>2</sup>,  
Akinori Takemoto<sup>5</sup>, Masashi Yamaguchi<sup>5</sup>, Shuji Miyamoto<sup>5</sup>

<sup>1</sup>RIKEN SPring-8 Center, 1-1-1 Kouto, Sayo-cho, Sayo-gun, Hyogo 679-5198, Japan,

<sup>2</sup>High Energy Accelerator Research Organization, 1-1 Oho, Tsukuba, Ibaraki 305-0801, Japan

<sup>3</sup>Japan Atomic Energy Agency, 2-4 Shirakata, Tokai-mura, Naka-gun, Ibaraki 319-1195, Japan

<sup>4</sup>JASRI, 1-1-1 Kouto, Sayo-cho, Sayo-gun, Hyogo 679-5198, Japan

<sup>5</sup>University of Hyogo, 1-1-2, Koto, Kamigori-cho, Ako-gun, Hyogo 678-1205, Japan

## Abstract

Neutron energy spectra due to photo-nuclear reactions from  $^{nat}\text{C}$  and  $^{197}\text{Au}$  targets were measured with polarized photon beams using the time of flight and pulse shape analyses methods at the NewSUBARU-BL1 beamline. The dependence on the azimuthal angle and polar angle for the neutron energy spectra was found in the photonuclear reaction for the linearly and the circularly polarized photons. The difference on the neutron yield increases with neutron energy in the azimuthal angle for linearly polarized photons and in the polar angle in comparison with linearly and circularly polarized photons.

## Introduction

To construct the high-energy electron machines, one of the crucial issues is the radiation protection such as the estimation of leakage dose distribution and induced activities. Sometimes, the design of the radiation shielding restricts the machine designs. To investigate the physical phenomena of neutrons due to photo-nuclear reaction is important because of insufficient experimental data in addition to its strong attenuation and the cause to activate the components. The double differential cross section data that fully describe energy and angle of the emitted neutrons are required to design and estimate the shielding and leakage dose distributions. However, there are few experimental data of the double differential cross section until now. In addition, the azimuthal angle dependence of emitted neutrons due to polarized photons was reported experimentally [1]. The dependence on the photon polarization for the neutron due to photo-nuclear reaction will be more important. For example, at the International Linear Collider (ILC), experiments with the polarized electron and positron beam of 250 GeV will be performed and the polarized photons are produced by the polarized electron with undulator [2] so that the shielding design of the ILC facility should consider the influence of the polarized

photons.

A linearly and circularly polarized Laser Compton Scattering (LCS)  $\gamma$ -ray beams with quasi-monochromatic energy up to 76 MeV are available at NewSUBARU-BL01 [3], [4]. To investigate the double differential cross section of neutron production due to photo-nuclear reaction systematically for giant dipole resonance (GDR) and quasi-deuteron disintegration (QDD) region, we have measured the neutron spectra at the several directions from the photonuclear reaction with the linearly and circularly polarized photon using liquid scintillation counters with gold and graphite targets[5],[6].

## Experiments and Results

Experimental set-up is shown in Photo.1 and Fig.1. Two collimators, one is 6mm diameter in upwards and the other is 4mm in downwards, were employed to define the LCS  $\gamma$ -ray spectra for the  $^{nat}\text{C}$  target experiments, and 3mm and 2mm diameters for the gold target experiments. The intensities of LCS photon were measured by GSO scintillation counters and monitored by thin plastic scintillation counter (PLS). The separation of photons and neutrons were performed by using time of flight and the pulse shape analyses methods of the liquid scintillation

counters with the size of 127mm in diameter and 127 mm long.

The photon maximum energies of 23.1 MeV and 26.6MeV were employed for the  $^{nat}C$  target experiments with the Nd:YVO<sub>4</sub> laser (wave length, 1064nm) and 1.14 GeV and 1.22GeV electrons, respectively. In the experiments, a  $\lambda/4$  wave plate of the laser was employed to avoid the polarization effect. Figs.2 and 3 show the measurement results of neutron spectra for 23.1MeV and 26.6MeV photons, respectively. In these figures, H60° and H90° means the detector positions at the polar angles of 60 and 90 degrees in the horizontal plane. V90° means the position at the azimuthal angle 90 degrees in vertical plane. As shown in figures, the neutrons due to photo-nuclear reactions seem to be an isotropic distribution over a wide energy range.

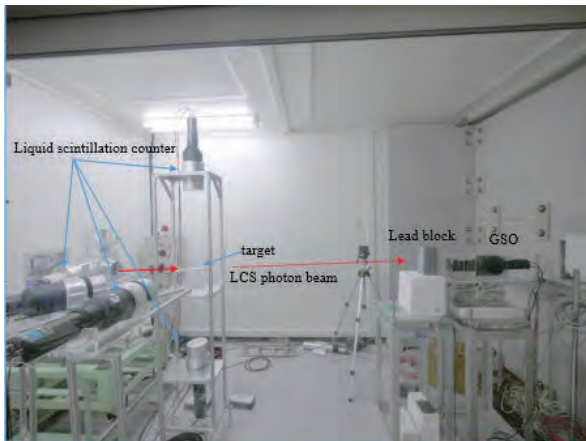


Photo.1 Experimental setup in the hutch 2 of BL1 beamline.

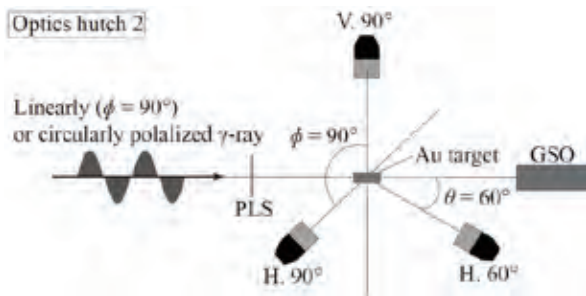


Fig.1 Illustration of the setup of experiments. V.90°,H60°,H90° means liquid scintillation counters which install in horizontal (H60° and H90°) and vertical (V90°) planes. PLS means a thin plastic scintillation counter.

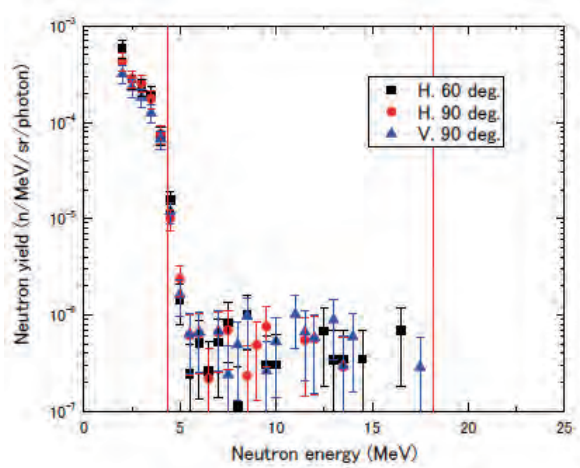


Fig.2 Neutron spectra due to  $^{nat}C(\gamma,n)$  reaction with 23.1 MeV photons. Red lines indicate the maximum neutron energy of these reactions for  $^{12}C$  and  $^{13}C$ .

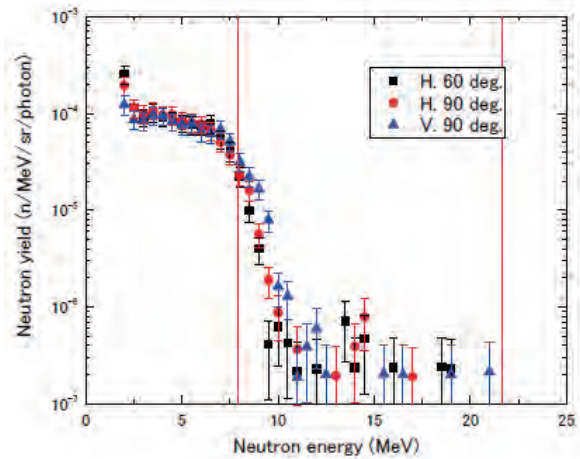


Fig.3 Neutron spectra due to  $^{nat}C(\gamma,n)$  reaction with 26.6 MeV photons. Lines and symbols are same as Fig.2.

In the case of gold target experiments, the purpose is to obtain the effect of the neutron spectrum due to photon polarization so that the gold target was employed with the electron energy of 982.4MeV and 16.95MeV of maximum LCS photon energy. The reasons are that the cross section of the gold for photo-nuclear reaction is large and the electron energy of 982.4MeV is easier to operate the single bunch mode and top-up. Fig.4 shows the energy dependence of the emitted neutrons due to linearly and circularly polarized photons. In this figure, the vertical axis shows the ratio of the neutrons in the lateral direction of 0 and 90 degrees of azimuthal angle due to linearly or circularly polarized photons. The linear polarization of the LCS photons was set at

the azimuthal angle of 90 degrees (the V90° direction). The results show that the ratio increases with neutron energy for the linearly polarized photons. On the other hand, the ratio is approximately constant for the circularly polarized photons. Figure 5 shows the ratio of the neutron yields for the linearly polarized photons to that for the circularly polarized photons. For the V90° direction, the ratio is almost constant in whole neutron energy. It indicates that there is no energy dependence on an influence of the polarization for the same direction as the linear polarization. For the H60° and H90° directions that are the right angle to the direction of the linear polarization, the ratios decrease with increasing emitted neutron energy.

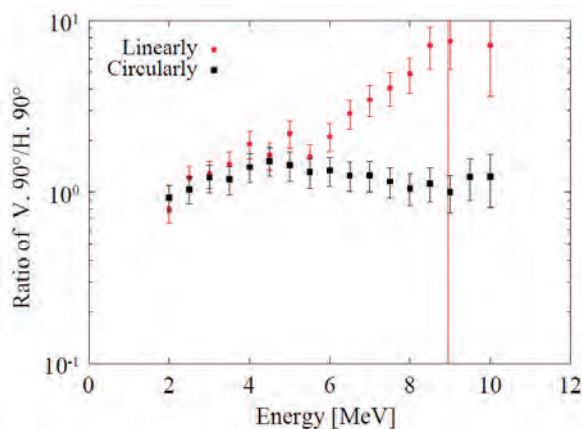


Fig.4 Energy dependence on the photon polarization for the emitted neutron due to photo-nuclear reaction. (The ratio of the neutron yields for the V90° direction to those for the H90°.)

## Conclusions

To investigate the double differential cross section of neutron emission due to photo-nuclear reaction, we measured the neutron spectra generated from the natural graphite and gold targets due to the photo-nuclear reaction by the polarized laser Compton scattering photon beams of 23.1 MeV, 26.6 MeV, and 16.95 MeV with the time-of flight and the pulse shape analysis methods at NewSUBARU-BL01 beamline. As the results, the emitted neutron spectra without polarization effect show almost isotropic distribution, and the neutron yield, which is set at the same direction as the photon linear polarization, is higher than the yields of the other directions. The

difference on the neutron yields increases with neutron energy. There is no influence of the polarization on the neutron energy spectrum for the same direction as the linear polarization. The right angle to the direction of the linear polarization, the neutron yield decreases with increasing neutron energy. The results clearly point out that the difference in neutron yield and the dependence on the neutron energy should be taken into account for shielding design of the facility with the polarized photons. However the experimental data of double differential cross section with photon polarization effect are quite insufficient so that the same experiments with different material targets and different photon energy, especially higher energies should be performed continuously.

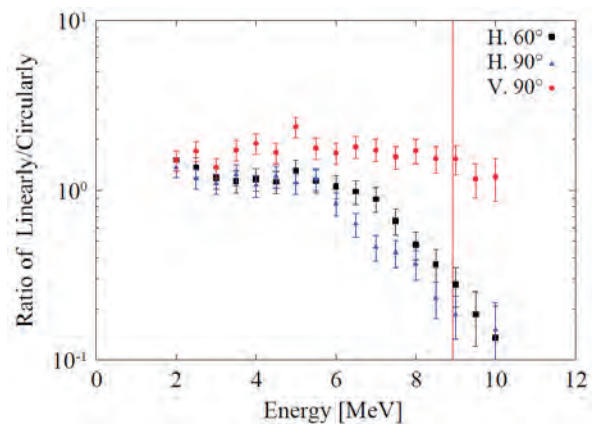


Fig.5 Energy dependence on the photon polarization for the emitted neutron due to photo-nuclear reaction. (The ratio of the neutron yields at each direction for the linearly to that for the circularly polarized photons.)

## References

- [1] K. Horikawa et al., Phys. Lett. B **737**, 109 (2014)
- [2] International Linear Collider Technical Design Report, <https://www.linearcollider.org/ILC/Publications/Technical-Design-Report>
- [3] S. Miyamoto, et al., Radiat. Meas. **41**, S179 (2007)
- [4] Y. Asano, et al., Progress in Nucl. Sci. & Tech. **4**, 254 (2014)
- [4] D. Satoh, S. Kunieda, Y. Iwamoto, N. Shigyo and K. Ishibashi, Nucl. Sci. Tech. **2** 657 (2002)
- [5] T. Itoga, et al., To be published in the proceedings of 13<sup>th</sup> International Conference on Radiation Shielding, Paris France Sep. 2016
- [6] Y. Kirihara et al., To be published in the proceedings of 13<sup>th</sup> International Conference on Radiation Shielding, Paris France Sep. 2016

# Photoneutron Reactions in Nucleosynthesis

Hiroaki Utsunomiya

Department of Physics, Konan University, Kobe, Japan

## Abstract

The development of laser Compton scattering  $\gamma$ -ray beams has highlighted the role of photoneutron reactions in the p-process, s-process, and applications to light nuclei in nucleosynthesis. Among  $(\gamma, n)$ ,  $(\gamma, p)$  and  $(\gamma, \alpha)$  photo-reactions and  $(p, \gamma)$  capture reactions complemented by  $\beta$ -transformations, neutron removal reactions play a major role in the p-process nucleosynthesis.

The development of laser Compton scattering  $\gamma$ -ray beams has highlighted the role of photo-neutron reactions in the p-process, s-process, and applications to light nuclei in nucleosynthesis. Among  $(\gamma, n)$ ,  $(\gamma, p)$  and  $(\gamma, \alpha)$  photo-reactions and  $(p, \gamma)$  capture reactions complemented by  $\beta$ -transformations, neutron removal reactions play a major role in the p-process nucleosynthesis [1].

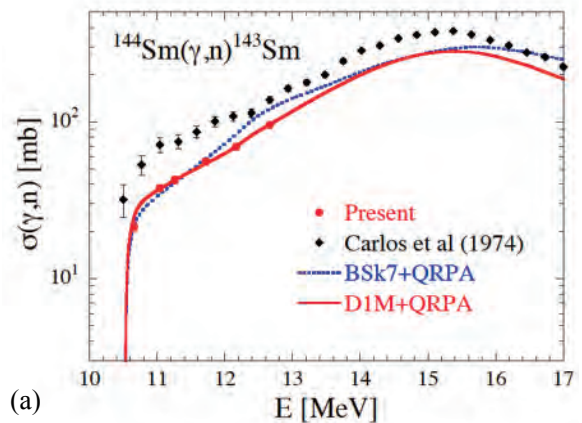
The methodology called the  $\gamma$ -ray strength function method [2] has been devised to study radiative neutron capture cross sections for unstable nuclei at the s-process branch-point based on a unified understanding of  $(n, \gamma)$  and  $(\gamma, n)$  cross sections. This method has been applied to 17 elements (Se, Ge, Mo, Zr, Pd, Sn, La, Pr, Nd, Sm, Dy, Ta, W, Re, Os, Au, Pb) and 51 isotopes including the application in the rare-earth region [3,4]. Radiative capture reactions on light nuclei are also studied by photonuclear reactions based on the reciprocity theorem. Recently, photodisintegration of  $^9\text{Be}$  was re-examined in the context of explosive nucleosynthesis of  $^9\text{Be}$  through  $\alpha + \alpha \rightleftharpoons ^8\text{Be}(n, \gamma)^9\text{Be}$  [5]. The role of photonuclear reactions in nucleosynthesis will be strengthened in the ELI-NP which is under construction in Bucharest-Măgurele. I review the latest experimental developments of photoneutron reactions in nucleosynthesis and give future prospect of the field.

## References

- [1] H. Utsunomiya, P. Mohr, A. Zilges, M. Rayet, "Direct determination of photodisintegration cross sections and the p-process", Nucl. Phys. A 777, pp. 459-478 (2006).
- [2] H. Utsunomiya, S. Goriely, M. Kamata, T. Kondo, O. Itoh, H. Akimune, T. Yamagata, H. Toyokawa, Y. -W. Lui, S. Hilaire, " $\gamma$ -ray strength function for  $^{116,117}\text{Sn}$  with the pygmy dipole resonance balanced in the photoneutron and neutron capture channels", and A. J. Koning, Phys. Rev. C 80, 055806 (2009).
- [3] D. M. Filipescu, I. Gheorghe, H. Utsunomiya, S. Goriely, T. Renstrøm, H.-T. Nyhus, O. Tesileanu, T. Glodariu, T. Shima, K. Takahisa, S. Miyamoto, Y.-W. Lui, S. Hilaire, S. Péru, M. Martini, and A.

J. Koning, "Photoneutron cross sections for samarium isotopes: Toward a unified understanding of  $(\gamma, n)$  and  $(n, \gamma)$  reactions in the rare earth region", Phys. Rev. C 90, 064616 (2014).

- [4] H.-T. Nyhus, T. Renstrøm, H. Utsunomiya, S. Goriely, D. M. Filipescu, I. Gheorghe, O. Tesileanu, T. Glodariu, T. Shima, K. Takahisa, S. Miyamoto, Y.-W. Lui, S. Hilaire, S. Péru, M. Martini, L. Siess, and A. J. Koning, "Photoneutron cross sections for neodymium isotopes: Toward a unified understanding of  $(\gamma, n)$  and  $(n, \gamma)$  reactions in the rare earth region", Phys. Rev. C 91, 015808 (2015).
- [5] H. Utsunomiya, S. Katayama, I. Gheorghe, S. Imai, H. Yamaguchi, D. Kahl, Y. Sakaguchi, T. Shima, K. Takahisa, and S. Miyamoto, "Photodisintegration of  $^9\text{Be}$  through the  $1/2^+$  state and cluster dipole resonance", Phys. Rev. C 92, 064323 (2015).
- [6] P. Carlos, H. Beil, R. Bergere, A. Lepretre, A. Deminiac, and A. Veysiere, Nucl. Phys. A 225, 171 (1974).



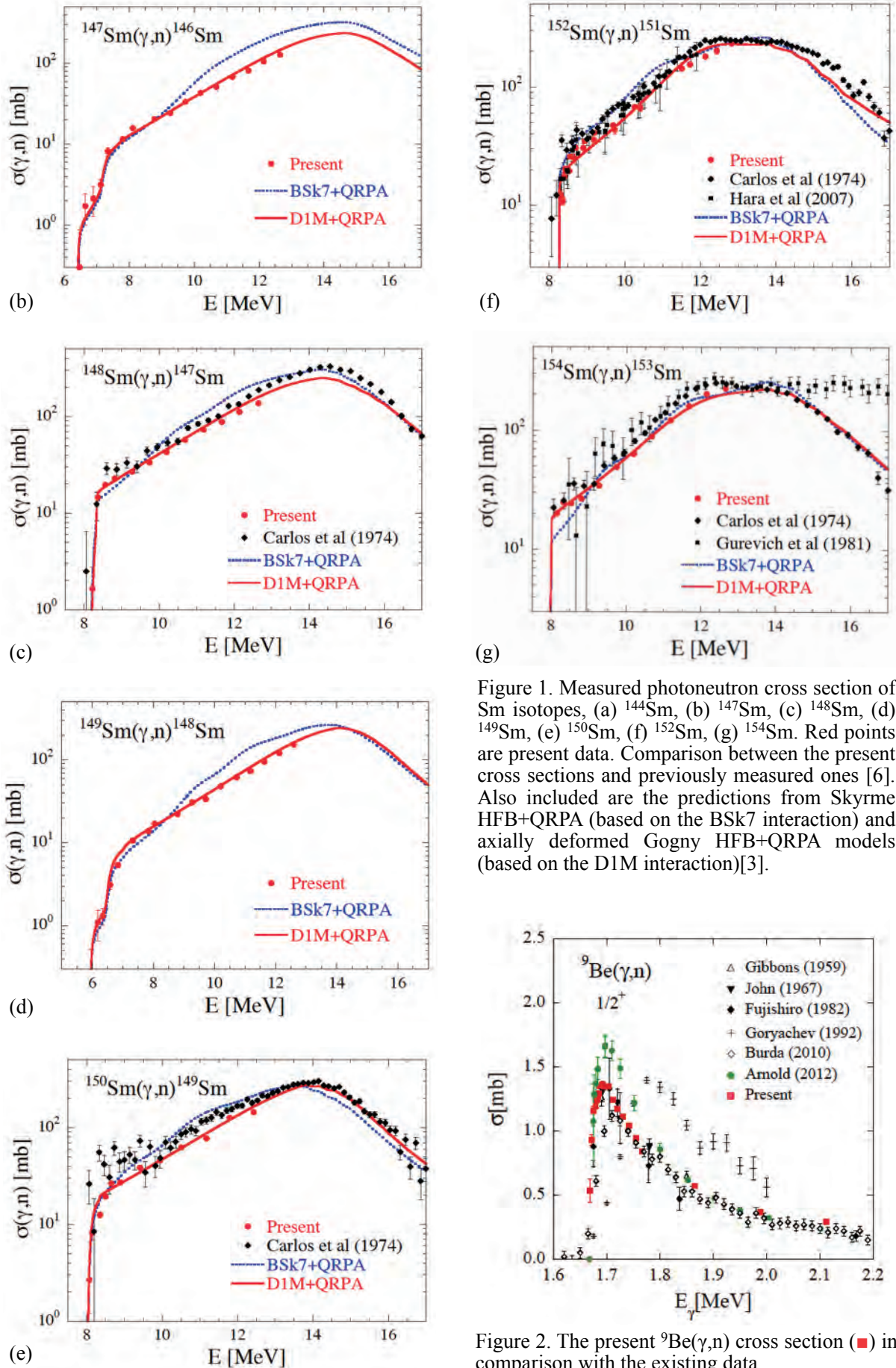


Figure 1. Measured photoneutron cross section of Sm isotopes, (a)  $^{144}\text{Sm}$ , (b)  $^{147}\text{Sm}$ , (c)  $^{148}\text{Sm}$ , (d)  $^{149}\text{Sm}$ , (e)  $^{150}\text{Sm}$ , (f)  $^{152}\text{Sm}$ , (g)  $^{154}\text{Sm}$ . Red points are present data. Comparison between the present cross sections and previously measured ones [6]. Also included are the predictions from Skyrme HFB+QRPA (based on the BSk7 interaction) and axially deformed Gogny HFB+QRPA models (based on the DIM interaction)[3].

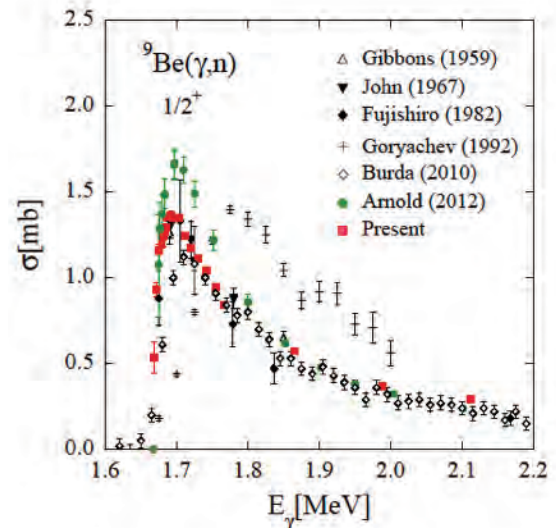


Figure 2. The present  $^{9}\text{Be}(\gamma, n)$  cross section ( $\blacksquare$ ) in comparison with the existing data.

# Total and partial photoneutron cross section measurements by direct neutron-multiplicity sorting

Hiroaki Utsunomiya, the Phoenix\* Collaboration  
Department of Physics, Konan University, Kobe, Japan

## Abstract

I coordinate the Phoenix Collaboration for the IAEA(International Atomic Energy Agency)-CRP(Cordinated Research Program) F41032 to provide new data of total and partial  $(\gamma, xn)$  cross sections with  $x=1-3$  for 11 nuclides for updating the photonuclear data library in collaboration with the Skobeltsyn Institute of Nuclear Physics of the Lomonosov Moscow State University and the Extreme Light Infrastructure-Nuclear Physics (ELI-NP) and new data of  $(\gamma, n)$  cross sections for 18 nuclides for generating a reference database for photon strength functions (PSF) in collaboration with the University of Oslo. (*\*Photoexcitation and neutron emission cross ( $x$ ) sections.*)

I coordinate the Phoenix Collaboration for the IAEA-CRP F41032. The Phoenix Collaboration Team is as Figure 1. The purposes of this research project are to provide :

1) new data of total and partial  $(\gamma, xn)$  cross sections with  $x=1-3$  for 11 nuclides from  $^{209}\text{Bi}$  to  $^9\text{Be}$  for updating the photonuclear data library in collaboration with the Skobeltsyn Institute of Nuclear Physics of the Lomonosov Moscow State University and the Extreme Light Infrastructure-Nuclear Physics (ELI-NP) and

2) new data of  $(\gamma, n)$  cross sections for 18 nuclides from  $^{205}\text{Tl}$  to  $^{58}\text{Ni}$  for generating a reference database for photon strength functions (PSF) in collaboration with the University of Oslo.

The main purpose of the Phoenix Collaboration is to resolve the long-standing problem of the

discrepancy between the Livermore and Saclay data of total and partial photoneutron cross sections and provide PSF data twofold, in the context of a unified understanding of  $(\gamma, n)$  and  $(n, \gamma)$  cross sections over isotopic chains with the  $\gamma$ -ray strength function method and a construction of the PSF by combining the  $(\gamma, n)$  data and the data obtained with the Oslo method.

The experiments will be performed at the NewSUBARU synchrotron radiation facility (Figure 2) using quasi-monochromatic  $\gamma$ -ray beams produced in the inverse Compton scattering of 1064nm and 532nm laser photons with relativistic electrons. The  $(\gamma, xn)$  data will be taken with the flat-efficiency neutron detector (Figure 3.) recently developed for direct neutron-multiplicity sorting, while the  $(\gamma, n)$  data with the high-efficiency neutron detector as long performed in the past.

The Konan, MSU, ELI-NP, and Oslo teams are

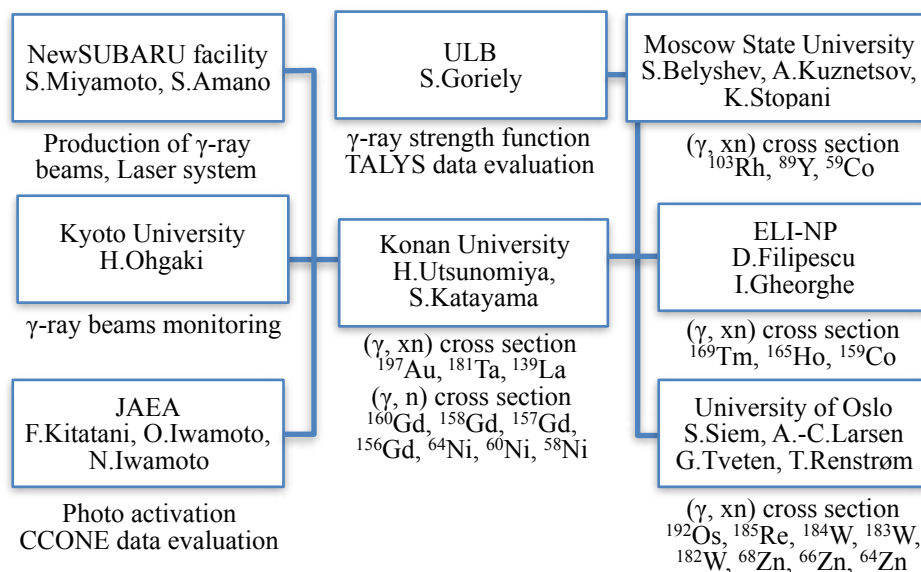
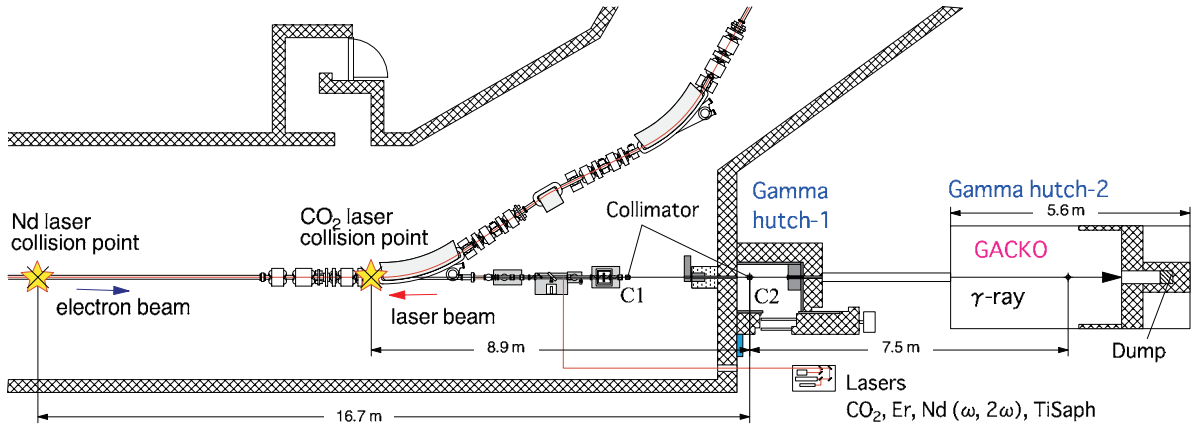


Figure 1 . Teams and members of Phoenix Collaboration.

assigned their own  $(\gamma, xn)$  and  $(\gamma, n)$  data as follows.

1.  $(\gamma, xn)$  data with  $x=1-3$  for 11 nuclei for updating the photonuclear data library
  - The Konan team:  $^{197}\text{Au}$ ,  $^{181}\text{Ta}$ ,  $^{139}\text{La}$ ,  $^9\text{Be}$
  - The ELI-NP team:  $^{209}\text{Bi}$ ,  $^{169}\text{Tm}$ ,  $^{165}\text{Ho}$ ,  $^{159}\text{Tb}$
  - The MSU team:  $^{103}\text{Rh}$ ,  $^{89}\text{Y}$ ,  $^{59}\text{Co}$

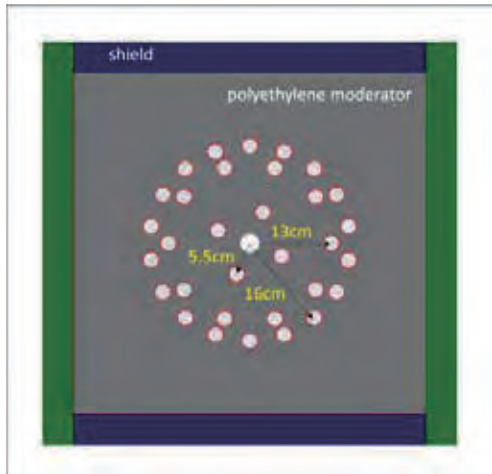
2.  $(\gamma, n)$  data for 18 nuclei for generating a reference database for photon strength functions
  - The Konan team:  $^{160}\text{Gd}$ ,  $^{158}\text{Gd}$ ,  $^{157}\text{Gd}$ ,  $^{156}\text{Gd}$ ,  $^{64}\text{Ni}$ ,  $^{60}\text{Ni}$ ,  $^{58}\text{Ni}$
  - The Oslo team:  $^{205}\text{Tl}$ ,  $^{203}\text{Tl}$ ,  $^{192}\text{Os}$ ,  $^{185}\text{Re}$ ,  $^{184}\text{W}$ ,  $^{183}\text{W}$ ,  $^{182}\text{W}$ ,  $^{89}\text{Y}$ ,  $^{68}\text{Zn}$ ,  $^{66}\text{Zn}$ ,  $^{64}\text{Zn}$



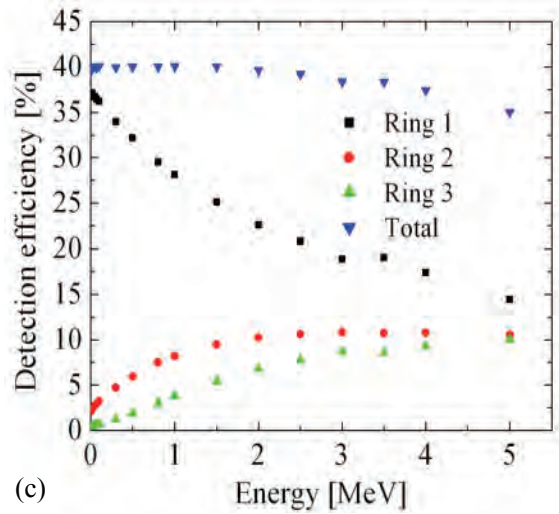
**Figure 2.** The beam-line BL01 for  $\gamma$ -ray production and the experimental hutch GACKO at NewSUBARU.



(a)



(b)



(c)

**Figure 3.** The newly developed flat efficiency neutron detector system. (a) Photograph outside. (b) Layout of the  $^3\text{He}$  detector in the polyethylene moderator. (c) The calculated neutron detection efficiency of three  $^3\text{He}$  detector rings as a function of the neutron energy.

# First characterization of a time projection chamber as a high-performance gamma-ray pair-creation telescope and polarimeter

Denis Bernard

LLR, Ecole Polytechnique & CNRS/IN2P3, France

## Abstract

We have exposed a time projection chamber (TPC) to the polarized gamma-ray beam provided by the BL01 laser Compton scattering (LCS) beam line at NewSUBARU. More than 60 million gamma-to- $e^+e^-$ -pair conversion events were taken in the gamma-energy range 1.7 – 74 MeV. Preliminary results of the on-going analysis of these data show the excellent behavior of the detector despite the high particle flux and for the first time we demonstrate high-performance polarimetry, in the MeV-GeV energy range, with a space-compatible technique such as a TPC.

Several classes of cosmic sources such as active galactic nuclei (AGN), pulsars and gamma-ray bursts (GRB) produce huge flows of gamma rays. These high-energy photons are produced by non-thermal processes such as synchrotron radiation and inverse Compton scattering, and provide insight to enable us to understand the structure of these sources and the emission mechanisms at work.

In the 0.01 – 1 MeV energy range, Compton telescopes are extremely efficient. In the 0.1 – 1000 GeV energy range, past and present pair-creation telescopes are extremely efficient. In between lies a “sensitivity gap”, namely the energy range 1 – 100 MeV, in which very few high-sensitivity observations of gamma-ray emitting cosmic sources are available. On the “pair side”, performance degrades strongly at low energy because the angular resolution is extremely low because of the multiple scattering of the pair electrons in the converter material (most often tungsten slabs): Even though the pair-creation threshold is at 1 MeV, the Fermi-LAT Collaboration, for example, has barely published any observation below 100 MeV.

Most radiation mechanisms mentioned above produce linearly polarized  $\gamma$ -rays, to some extent, while phenomena such as magnetic field turbulence tend to dilute the polarization of the overall radiation emitted by a given source. In contrast to these radiative emission mechanisms, hadronic interactions of baryonic high-energy cosmic rays (protons or ions) with matter at rest produce non-polarized photons via spin-0  $\pi^0$  decay.

The measurement of the linear polarization (fraction and angle) of the emission, which is such a powerful tool for understanding the mechanisms at work in cosmic sources at low energies (from radio to X-rays) has never been performed above 1

MeV: Compton polarimeters become ineffective at high energies not only because the cross section is decreasing but because the polarization asymmetry falls as  $1/E$  [1]. For pair telescopes, again it's multiple scattering that ruins the azimuthal information carried by the pair as soon as a few milli-radiation lengths ( $10^{-3} X_0$ ) away from the conversion point [2].

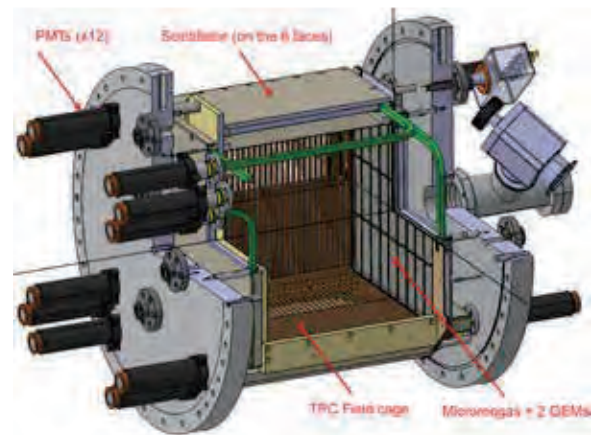


Figure 1. 3D CAD drawing of the HARPO detector.

The aim of the present work is to demonstrate the potential of a low-density (gas), homogeneous detector for high-performance (angular resolution and sensitivity) gamma-ray astronomy [3] and

<sup>1</sup>In principle the analysis of the recoil electron azimuthal angle distribution for triplet conversion events ( $\gamma e^- \rightarrow e^+ e^- e^-$ ) should enable us to perform polarimetry too [5]. In practice though, the cross section for a large enough recoil electron momentum is much too small to perform a measurement on a cosmic source [3, 4].

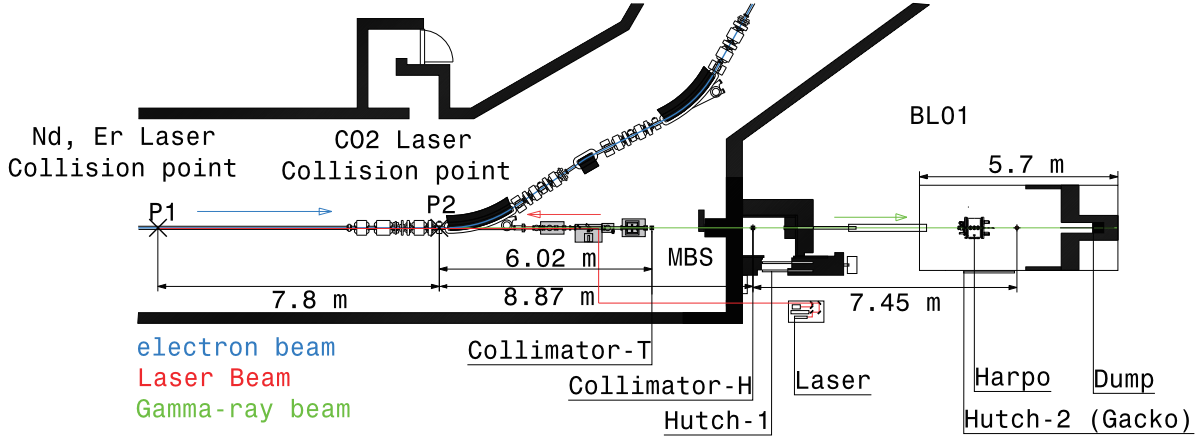


Figure 2. Layout of the HARPO detector in the GACKO experimental hutch on the BL01 beam line.

polarimetry [4] in the MeV-GeV energy range, using nuclear<sup>1</sup> conversions to pairs,  $\gamma Z \rightarrow e^+e^-Z$ .

A TPC [6, 7] is a volume filled with matter, here an argon-based gas, immersed in an electric field, here homogeneous. After a high-energy “event” has taken place in the gas, for us  $\gamma \rightarrow e^+e^-$ , the two leptons ionize the gas on their path and exit the detector<sup>2</sup> The ionization electrons drift (opposite to) along the electric field and are collected on the TPC “endplate” anode. We have segmented the endplate into two series of orthogonal strips, the charge collected by each providing two projections on the  $x$  and  $y$  “transverse” directions, respectively, of the signal that is arriving at the end-plate at a given time  $t$ . The measurement of the drift duration  $t - t_0$ , where  $t_0$  is the event time, provides the measurement of the third “longitudinal” coordinate,  $z$ . During most of the data taking at NewSUBARU we used an argon-isobutane 95-5% mixture at a pressure of  $\approx 2.1$  bar. The presence of a small amount of multi-atomic molecules limits the “heating” of the electrons by their multiple collisions during the drift and therefore decreases the value of the diffusion coefficient down to about  $0.03 \text{ cm}^2/\text{cm}$ . Figure 1 shows the layout of the HARPO detector [11].

The data taking took place in November 2014.  $\gamma$ -rays were produced by laser Compton scattering (LCS) of a laser beam on the high-energy (GeV) electrons stored in the NewSUBARU storage ring [12, 13]. Tuning the electron energy in the range 0.6 – 1.5 GeV and using lasers with various wavelengths (Nd:YVO<sub>4</sub>  $1\omega$  and  $2\omega$ , CO<sub>2</sub> and Erbium), we were able to vary the Compton-edge  $\gamma$ -energy from 1.7 to 74 MeV.

<sup>2</sup>Time projection chambers are considered also for Compton telescopes [8] and photoelectric telescopes [9, 10].

Monochromaticity was obtained by collimating the  $\gamma$  beam on axis. In that case, the polarization (fraction and direction) of the laser beam is transferred to the  $\gamma$ -beam. We took most of the data with fully polarized beams ( $P \approx 1$ ). Part of the data was also taken with an unpolarized beam ( $P \approx 0$ , which means here random linear polarization), so as to better control the possible systematic bias induced by the fact that the detector is not cylindrically symmetric: indeed the  $x, y, z$  structure of the detector was found to induce such biases. Figure 2 shows the layout of the experimental setup.

The weak point of TPCs is that they generate a huge flow of information that is incident on the digitizing electronics, in our case  $2 \times 288$  charges to be dealt with every 30 ns, with the consequence that, with a storage depth of 511 time bins, the duration of the digitization of an event can be as long as 1.7 ms. Therefore, to cope with the huge rate of background noise mainly due to tracks from  $\gamma$ -ray conversions upstream of the detector or of the detector gas, we have designed and used a sophisticated trigger system that allowed us to reject background by more than two orders of magnitude while the overall trigger efficiency on the signal (i.e.  $\gamma$  conversions to pairs in the TPC gas) was kept larger than 50 % [14].

Figure 3 shows a sample of events. The analysis of the data is well advanced [15]. Figure 4, for example, shows the distribution of the azimuthal angle,  $\omega$ , of nuclear conversions at a  $\gamma$  energy of 11.8 MeV. The ratio of the  $P \approx 1$  and  $P \approx 0$  distribution enables an almost complete cancellation of the systematic biases. A  $(1 + A \cos[2(\omega - \omega_p)])$  fit of this distribution yields a value of the polarization asymmetry of  $A = 7.4 \pm 0.6\%$ , that is lower than the value of 17% predicted by QED at that energy [4]. Monte Carlo simulations show that this dilution of the asymmetry is

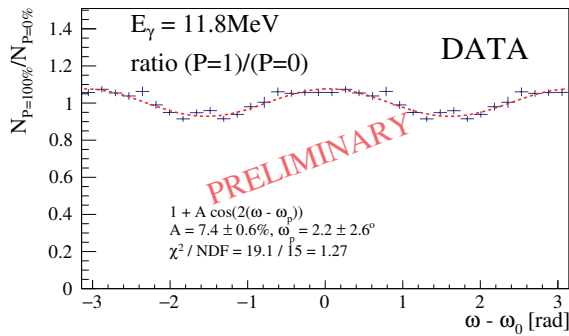


Figure 4. The ratio of the  $P \approx 1$  and  $P \approx 0$  azimuthal distributions of 11.8 MeV  $\gamma$  conversion to  $e^+e^-$  pairs in 2.1 bar argon-isobutane 95:5 gas.

compatible with that induced by the single-track resolution at that energy [15].

This work is funded by the French National Research Agency (ANR-13-BS05-0002) and was performed by using NewSUBARU-GACKO (Gamma Collaboration Hutch of Konan University). It involved contributions from members of Irfu CEA-Saclay and of LLR Ecole Polytechnique & CNRS/IN2P3 (France), and of JASRI/Spring8 and of LASTI University of Hyogo (Japan).

On behalf of the French groups of the project, “the detector team”, I would like to express my warmest gratitude to our Japanese colleagues, “the beam team”, without the dedication, the effectiveness and the efficiency of whom we couldn’t have achieved such a successful data-taking and collected such excellent quality data. I am convinced that the results of this characterization of such a high-performance MeV-GeV  $\gamma$ -ray telescope and polarimeter will set ground to the use of TPCs on board a future space mission.

## References

- [1] D. Bernard, “Compton polarimetry revisited,” Nucl. Instrum. Meth. A 799, 155 (2015) [arXiv:1507.02824 [astro-ph.IM]].
- [2] Yu. D. Kotov, “Methods of measurement of gamma-ray polarization”, Space Science Reviews 49 (1988) 185.
- [3] D. Bernard, “TPC in gamma-ray astronomy above pair-creation threshold,” Nucl. Instrum. Meth. A 701, 225 (2013) Erratum: [Nucl. Instrum. Meth. A 713, 76 (2013)] [arXiv:1211.1534 [astro-ph.IM]].
- [4] D. Bernard, “Polarimetry of cosmic gamma-ray sources above  $e^+e^-$  pair creation threshold,” Nucl. Instrum. Meth. A 729, 765 (2013) [arXiv:1307.3892 [astro-ph.IM]].
- [5] Y. Iwata et al., “New polarimeter for high-energy gamma-rays,” Nucl. Instrum. Meth. A 336, 146 (1993).
- [6] D.R. Nygren and J. N. Marx, “The Time Projection Chamber”, Physics Today 31 (1978) 46.
- [7] D. Attie, “TPC review,” Nucl. Instrum. Meth. A 598, 89 (2009).
- [8] T. Tanimori et al., “An Electron-Tracking Compton Telescope for a Survey of the Deep Universe by MeV gamma-rays,” Astrophys. J. 810, no. 1, 28 (2015) [arXiv:1507.03850 [astro-ph.IM]].
- [9] K. Jahoda et al., “Polarization from Relativistic Astrophysical X-ray Sources: The PRAXYS Small Explorer Observatory”, American Astronomical Society, AAS Meeting #225, id. 338.40.
- [10] “Design improvements and X-ray performance of a time projection chamber polarimeter for persistent astronomical sources”, J.E. Hill et al., Proc. SPIE Int. Soc. Opt. Eng. 9144, 91441N, Montreal(2014)
- [11] D. Bernard et al., “HARPO: a TPC as a gamma-ray telescope and polarimeter,” Proc. SPIE Int. Soc. Opt. Eng. 9144, 91441M, Montreal(2014) [arXiv:1406.4830 [astro-ph.IM]].
- [12] K.Horikawa et al., “Measurements for the energy and flux of laser Compton scattering  $\gamma$ -ray photons generated in an electron storage ring: NewSUBARU”, Nucl. Instrum. Meth. A 618, 209 (2010).
- [13] S. Amano et al., “Several-MeV  $\gamma$ -ray generation in NewSUBARU by laser Compton backscattering”, Nucl. Instrum. Meth. A 602, 337 (2009).
- [14] Y. Geerebaert et al., “Measurement of 1.7 to 74 MeV polarized gamma rays with the HARPO TPC,” Proceedings VCI2016, arXiv:1603.06817 [physics.ins-det], to appear in Nucl. Instrum. Meth. A, doi:10.1016/j.nima.2016.06.031.
- [15] P. Gros et al., “First measurement of polarization asymmetry of a gamma-ray beam between 1.74 to 74 MeV with the HARPO TPC”, arXiv:1606.09417 [astro-ph.IM], submitted to Proc. SPIE Int. Soc. Opt. Eng. 9905, Edinburgh (2016)

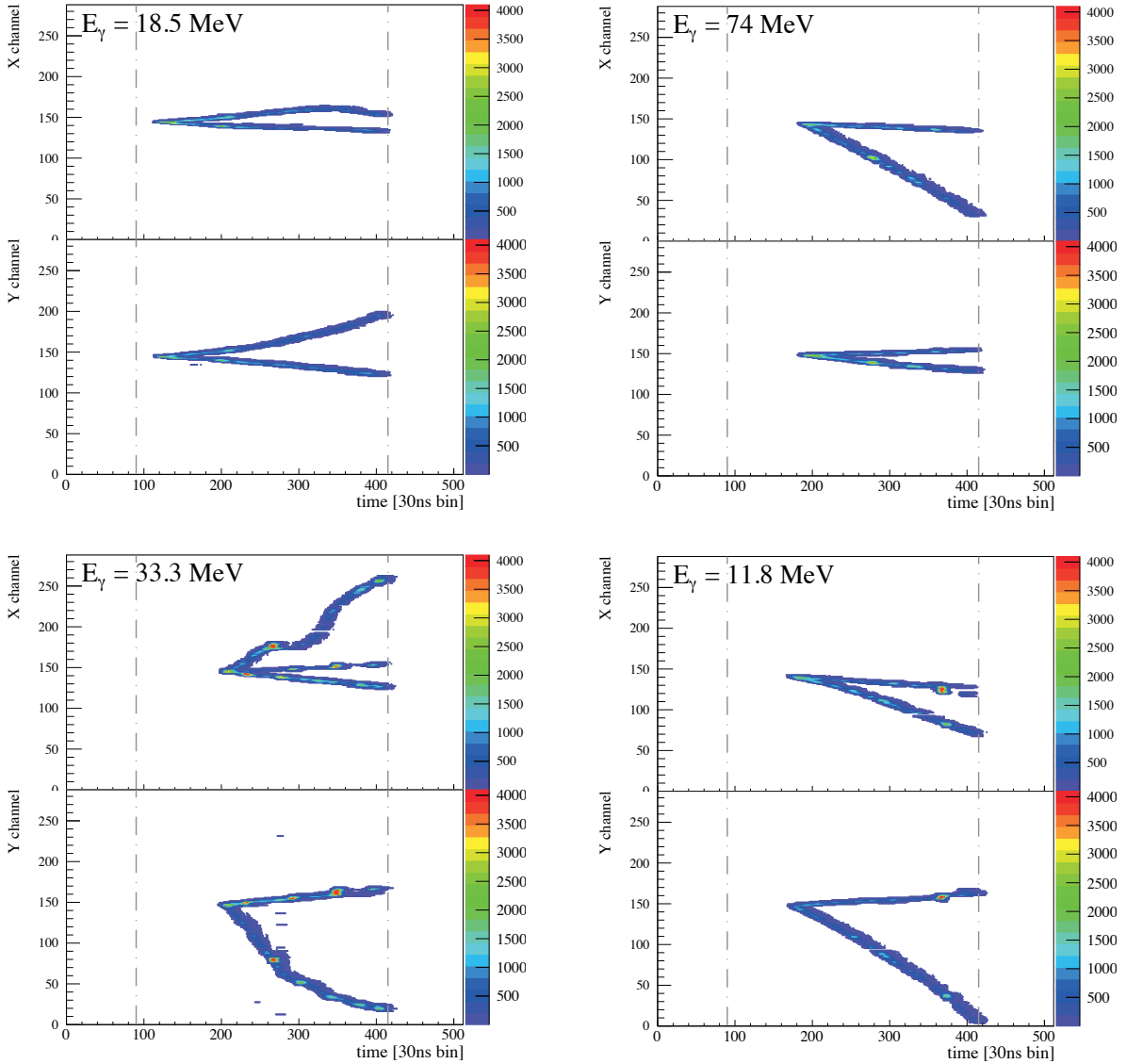


Figure 3. Four examples of  $\gamma$  rays provided by the BL01 NewSUBARU beam line, converting to an  $e^+e^-$  pair into the 2.1bar argon-isobutane gas mixture of the HARPO detector. For each event, the  $(x, t)$  and  $(y, t)$  signal “maps” are shown. The vertical lines at the  $\approx 90$  and  $\approx 410$  time bins show the event time  $t_0$  and the arrival time of the electrons that were produced very close to the cathode and had to drift over the full 30 cm of gas, respectively. All four events show a conversion point located at  $> 90$  time bin, which means that the conversion indeed took place in the gas, not in the solid material upstream of it. The 18.5 MeV event is a typical “nuclear” conversion, that is  $\gamma Z \rightarrow e^+e^-Z$ . The 33.3 MeV event is a triplet conversion, that is  $\gamma e^- \rightarrow e^+e^-e^-$ , where the large-polar-angle low-energy “recoiling” electron is clearly visible; the two leptons of the pair are seen to overlap in the  $(y,t)$  map. The 74 MeV event shows a clear indication of the momentum carried away by the unobserved recoiling nucleus as the two leptons are directed downwards in the  $(x,t)$  map, while the incident photon was directed horizontally, coming from the “left”. The 11.8 MeV event shows a strong localized energy deposit on the “upper leg”, due to a low-energy  $\delta$ -ray.

# Measurements of nuclear resonance fluorescence on $^{52}\text{Cr}$ with a linearly polarized photon beam at BL01

Toshiyuki Shizuma<sup>1</sup>, T. Hayakawa<sup>1</sup>, F. Minato<sup>2</sup>, I. Daito<sup>3</sup>, H. Ohgaki<sup>3</sup>, S. Miyamoto<sup>4</sup>

<sup>1</sup>National Institutes for Quantum and Radiological Science and Technology

<sup>2</sup>Japan Atomic Energy Agency

<sup>3</sup>Kyoto University

<sup>4</sup>LASTI, University of Hyogo

II

## Abstract

Electromagnetic dipole transitions in  $^{52}\text{Cr}$  were measured via nuclear resonance fluorescence with a linearly polarized photon beam generated by laser Compton scattering between laser light and high energy electrons. More than 40 transitions were observed at excitation energy between 7.5 and 12 MeV in  $^{52}\text{Cr}$ . Parity quantum numbers of the excited states were determined by comparison of azimuthal intensity asymmetry of scattered  $\gamma$  rays with respect to the polarization plane of the incident photon beam. Strength distribution of the dipole transitions was obtained from the measured intensity of the scattered  $\gamma$  rays. A total ground state decay width of 35.6(1.1) eV was obtained at energy region between 7.5 and 12 MeV.

## Introduction

Electric dipole (E1) and magnetic dipole (M1) excitations at low excitation energy are fundamental excitation modes of atomic nuclei. The observation of the E1 and M1 transitions provides information on the collective and single-particle motion such as pygmy E1 resonance (PDR) [1] and spin-flip M1 resonance [2]. For example, the M1 resonance is related to the spin dependent part of the nuclear excitation [3].

Nuclei in the vicinity of the closed  $N = Z = 28$  shells such as chromium, iron, and nickel exhibit one of the most favorable regions for observing both the E1 and M1 transitions at low excitation energy. However, it is difficult to distinguish E1 and M1 transitions in nuclear resonance fluorescence (NRF) measurements with unpolarized photon beam such as bremsstrahlung radiation, since both E1 and M1 transitions have same angular distribution. On the other hand, by using a linearly polarized photon beam it is possible to determine whether the transition type is E1 or M1, since E1 transitions have different angular distribution from M1 transitions with respect to the polarization of the incident photon beam. In order to measure the E1 and M1 strength distribution in  $^{52}\text{Cr}$ , we have carried NRF measurements with a linearly polarized photon beam delivered at NewSUBARU.

## Experiments and Results

A quasi-monoenergetic, linearly polarized photon beam was generated in backward Compton scattering of laser light with high energy electrons circulated in the NewSUBARU electron storage ring. A Q-switch Nd:YVO<sub>4</sub> laser with a wavelength of 1064 nm operated at a frequency of

20 kHz was used for the incident laser photons. The energy of electrons was chosen to be 683, 708, 731, 756, 792, and 828 MeV to generate quasi-monoenergetic photon beams with the maximum energy of 8.2, 8.8, 9.4, 10, 11, and 12 MeV, respectively. A 10 cm thick Pb collimator with a 3-mm aperture was used to produce a quasi-monoenergetic photon beam with  $\Delta E/E \approx 3\%$ . The average photon flux was  $6.2 \times 10^5$  photons/s which was measured by an 8"×10" NaI(Tl) scintillation detector. The target was a natural chromium with a diameter of 1 cm and a length of 3cm. Two high-purity Ge detectors with efficiencies of 120% and 140% relative to a 3"×3" NaI scintillation detector were used to observe scattered  $\gamma$  rays from the target. The 120% (140%) Ge detector was placed horizontally (vertically) at a scattering angle  $\theta$  of 90° to measure intensity asymmetry of scattered  $\gamma$  rays with respect to the polarization plane of the incident photon beam. The energy distribution of the incident photon beam was measured by a 3.5"×4" LaBr<sub>3</sub> detector. A Monte Carlo simulation code EGS-5 [4] was used to analyze the response of the LaBr<sub>3</sub> detector for extraction of the energy distribution of the incident photon beam.

Figure 1 shows a typical energy spectrum of scattered  $\gamma$  rays obtained at polar and azimuthal angles of  $(\theta, \phi) = (90^\circ, 0^\circ)$  and  $(90^\circ, 90^\circ)$  from the measurements with the maximum photon beam energy of 8.2 MeV. In the upper (lower) panel M1 (E1) transitions are shown.

The intensity asymmetry of the scattered  $\gamma$  rays with respect to the polarization plane of the incident photon beam can be used to deduce transition multipolarity, *i.e.*, parity quantum

numbers of resonant states. The azimuthal angular distribution of dipole transitions is known as

$$W(\theta, \phi) = W(\theta) \mp \frac{3}{4} (1 - \cos^2\theta) \cos\phi$$

where  $\theta$  is the scattering angle between the incoming and scattered photons and  $\phi$  is the azimuthal angle defined by the polarization plane and the reaction plane.  $W(\theta)$  is the angular correlation function for unpolarized radiation [5]. Here, the minus (plus) sign is for E1 (M1) transitions.

The analyzing power for parity determination is defined by using the azimuthal angular distribution of  $W(90^\circ, 0^\circ)$  and  $W(90^\circ, 90^\circ)$  as

$$\Sigma = \frac{W(90^\circ, 0^\circ) - W(90^\circ, 90^\circ)}{W(90^\circ, 0^\circ) + W(90^\circ, 90^\circ)}$$

The analyzing power equals to +1 for M1 transitions and -1 for E1 transitions under the 100% linear polarization of the incident photon beam. On the other hand, the measured intensity asymmetry is given by

$$A = \frac{N_{\parallel} - N_{\perp}}{N_{\parallel} + N_{\perp}} = q\Sigma$$

where  $N_{\parallel}$  ( $N_{\perp}$ ) is the measured intensity of scattered  $\gamma$  rays detected at  $\theta = 90^\circ$  in the plane parallel (perpendicular) to the polarization plane. Here,  $q$  is the measurement sensitivity of the detection system which is estimated to be 0.8 for the present case by using the Monte Carlo simulation code. Therefore, the azimuthal intensity asymmetry is expected to be +0.8 for M1 transitions and -0.8 for E1 transitions. Figure 2 shows the measured intensity asymmetry for the scattered  $\gamma$  rays. The data are clearly separated on the multipolarities (E1 or M1) of the transitions.

The energy integrated scattering cross sections  $I_s$  were deduced from the measured intensity of the transitions to the ground states. Here,  $I_s$  is defined using the partial decay width of the ground state transition  $\Gamma_0$  as

$$I_s = \frac{2J + 1}{2J_0 + 1} \left( \frac{\pi\hbar c}{E} \right)^2 \frac{\Gamma_0^2}{\Gamma}$$

where  $J$ ,  $E$ , and  $\Gamma$  are the spin, energy, and total decay width of the excited state, respectively, and  $J_0$  is the spin of the ground state. From the present measurement, a total ground state decay width of

## References

- [1] A. Tonchev *et al.*, Phys. Rev. Lett. **104**, 072501 (2010).
- [2] K. Heyde *et al.*, Rev. Mod. Phys. **82**, 2365 (2000).
- [3] A. Richter, Prog. Part. Nucl. Phys. **34**, 261 (1995).
- [4] W.R. Nelson *et al.*, SLAC National Accelerator Laboratory, Report No. SLAC-R-

35.6(1.1) eV was obtained at energy region between 7.5 and 12 MeV.

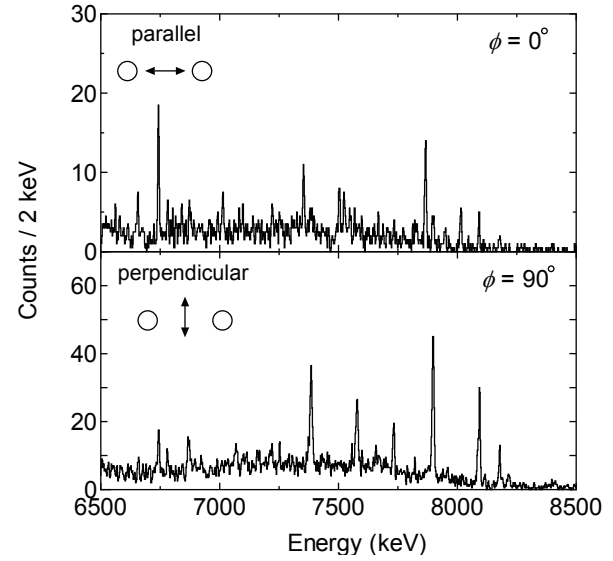


**Figure 1** Typical NRF  $\gamma$ -ray spectra observed at the polar and azimuthal angles of  $(\theta, \phi) = (90^\circ, 0^\circ)$  and  $(90^\circ, 90^\circ)$  are shown in upper panel and lower panel, respectively. In addition to the NRF  $\gamma$  rays, peaks associated with single and double escapes are seen.

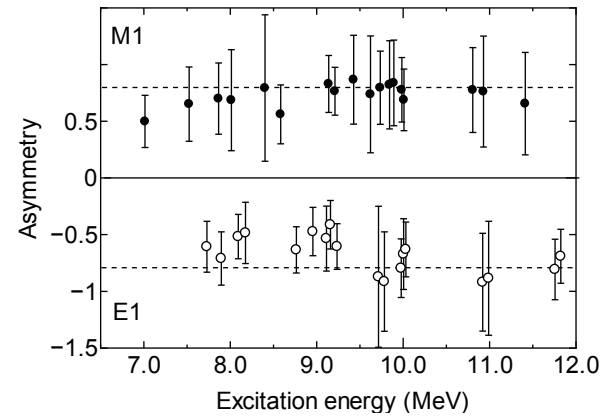


**Figure 2** Azimuthal intensity asymmetry obtained for M1 (closed circle) and E1 (open circles) transitions in  $^{52}\text{Cr}$ . The experimental sensitivity  $q$  ( $=0.8$ ) deduced from the numerical calculation is shown with dashed lines.

**265** (1985).

- [5] L.W. Fagg and S.S. Hanna, Rev. Mod. Phys. **31**, 711 (1959).

# Azimuthal anisotropy of neutrons in $^{56}\text{Fe}(\text{polarized } \gamma, n)^{55}\text{Fe}$ reaction at BL01

T. Hayakawa<sup>1</sup>, T. Shizuma<sup>1</sup>, S. Miyamoto<sup>2</sup>, S. Amano<sup>2</sup>, A. Takemoto<sup>2</sup>, M. Yamaguchi<sup>2</sup>, and K. Horikawa<sup>2</sup>,  
H. Akimune<sup>3</sup>, S. Chiba<sup>4</sup>, K. Ogata<sup>5</sup> and M. Fujiwara<sup>5</sup>

<sup>1</sup>National Institute for Quantum and Radiological Science and Technology

<sup>2</sup>LASTI, University of Hyogo

<sup>3</sup>Konan University

<sup>4</sup>Tokyo Institute of Technology

<sup>5</sup>Research Center for Nuclear Physics (RCNP), Osaka University

II

## Abstract

We have measured the azimuthal anisotropy of neutron yields emitted from the  $^{56}\text{Fe}(\gamma, n)^{55}\text{Fe}$  reaction with a linearly polarized  $\gamma$ -ray beam generated by laser Compton scattering at the beam line of BL01 in NewSUBARU. The neutron yields have been measured as a function of the azimuthal angle  $\phi$  of the linear polarization plane of the  $\gamma$  ray beam at the polar angle of  $90^\circ$ . The azimuthal anisotropy of the neutrons measured at  $\phi=0^\circ, 10^\circ, 25^\circ, 45^\circ, 60^\circ, 70^\circ,$  and  $90^\circ$  has been well reproduced by a function of  $a + b\cos(2\phi)$  predicted by Agodi in 1957.

## Introduction

In 1957, Agodi predicted theoretically that when a nucleus is excited via dipole transitions with linearly polarized  $\gamma$ -rays, the azimuthal angle distribution of nucleons emitted from  $(\gamma, n)$  and  $(\gamma, p)$  reactions at the polar angle  $\theta=90^\circ$  should follow a simple function of  $a + b \cos(2\phi)$ , where  $\phi$  is the azimuthal angle [1]. Because there was no established method to generate 100% linear polarized energy tunable  $\gamma$ -ray beam, Agodi's prediction has not been examined for nuclei in a wide mass region. Horikawa *et al.* have verified for the first time this prediction by measuring neutrons from Au, I, and Cu [2] using linear polarized laser Compton scattering  $\gamma$ -ray beams at BL01 in NewSUBARU. However, the azimuthal angle distributions were measured only in 30 degree steps. Unfortunately, since the function of  $\cos(2\phi)$  has the symmetry against  $\phi$ , only a few measured points give difference values. Therefore, in this study we measure neutron yields from the  $^{56}\text{Fe}(\text{polarized } \gamma, n)^{55}\text{Fe}$  reaction at seven angles of  $\phi=0^\circ, 10^\circ, 25^\circ, 45^\circ, 60^\circ, 70^\circ,$  and  $90^\circ$  to verify in further detail the azimuthal angle distribution predicted by Agodi [3].

## Experiments and Results

The LCS  $\gamma$  ray beam was generated by the Compton scattering of high energy electrons stored in NewSUBARU with laser photons

provided from a Q-switch Nd:YVO<sub>4</sub> laser. The maximum energy of the generated photon beam was 16.7 MeV, which was determined by the electron energy and the laser wavelength. The energy of electrons stored in NewSUBARU was 974 MeV. The wavelength of the laser was 1064 nm. In contrast, the lowest energy of the LCS beam was mainly determined by the collimator size. A collimator with a diameter of 3 mm was set before the target position. The energy spread of the  $\gamma$  rays is about 3 MeV. The diameter of the incident  $\gamma$ -ray beam was about 3 mm at the target position. The storage ring was operated by a single bunch mode with a repetition rate of 2.5 MHz to generate only one  $\gamma$ -ray pulse by one laser pulse. The time widths of the electron bunch and the laser pulse were 60 ps and 8 ns, respectively. The laser power was 3.8 W and the electron current was about 20 mA. The evaluated flux of the photons was  $(1-2)\times 10^6$  photons/s in an energy range from 14 MeV to 16.7 MeV.

Neutrons were generated by the photon-induced reaction on  $^{56}\text{Fe}$  (see Fig. 1). The neutrons were measured using the time-of-flight (TOF) method. The target was located inside of the irradiation room with a concrete shield with a thickness of 540 mm. Neutrons were led to the outside of the irradiation room through a hole with a diameter of 80 mm. The distance between the target and the detector was 970 mm. Neutrons and photons were measured using a plastic scintillator with a size of  $50 \text{ mm} \times 30 \text{ mm}$  with a 60-mm diameter photomultiplier. This detector was located at the polar angle of  $\theta=90^\circ$  outside of the irradiation room. A 2-mm thickness lead

shield was set in front of the detector to absorb low photons. However, high energy  $\gamma$ -rays scattered from the target were also observed. A time-to-amplitude converter (TAC) was used to measure the time interval between a start pulse from the detector and a stop pulse from the electron storage ring. The TAC signals were recorded using a multi-channel analyzer (MCA). A natural iron target with a size of  $\phi$  10 mm  $\times$  50 mm was used. Since the isotopic abundance of  $^{56}\text{Fe}$  is 91.7%, we assume that the neutron anisotropy from  $^{56}\text{Fe}$  is dominated in the following discussion.

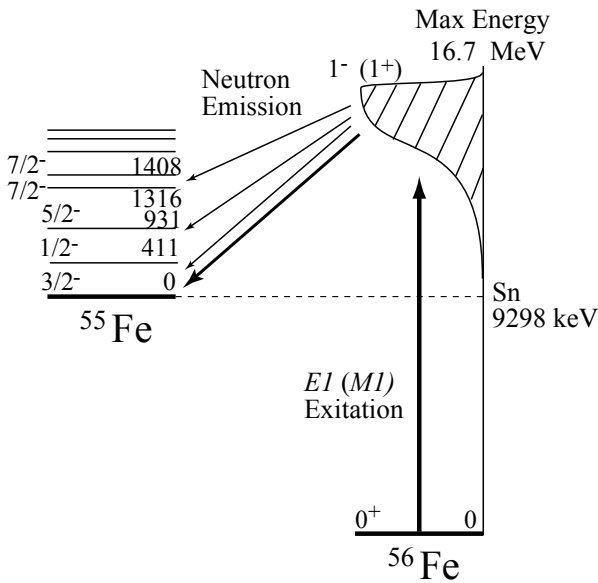


**Figure 1** Schematic figure for photodisintegration reactions on  $^{56}\text{Fe}$ . Excited states with low spin states in  $^{56}\text{Fe}$  are populated by the absorption of a photon, and subsequently these excited states decays away to the residual nucleus  $^{55}\text{Fe}$  by the emission of a neutron.

The neutron anisotropy was measured by changing the angle of the linear polarization plane of the incident LCS ray beam at the angles of  $\phi = 0^\circ, 10^\circ, 25^\circ, 45^\circ, 60^\circ, 70^\circ,$  and  $90^\circ$ , where  $\phi = 0^\circ$  was defined as the electric wave being in the plane of the detector. The linear polarization plane angle of the LCS beam was determined by measuring the polarization plane angle of the laser since the polarization of the laser was transferred directly to the LCS-ray.

Figure 2 shows a typical TOF spectrum measured by the plastic scintillator. A broad peak for neutrons and a sharp peak for gamma-rays are observed. These two peaks are clearly separated by the TOF method. The background originated from natural radioactivities and cosmic-rays is low compared with the neutron signal. Next, we

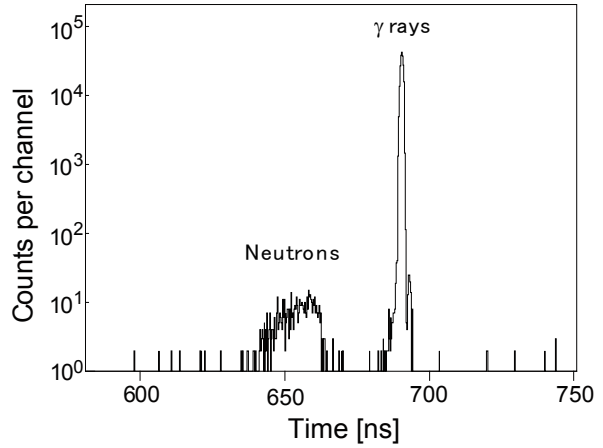


**Figure 2** Typical Time-of-Flight spectrum. The neutrons and  $\gamma$ -rays emitted from the iron target are clearly separated.

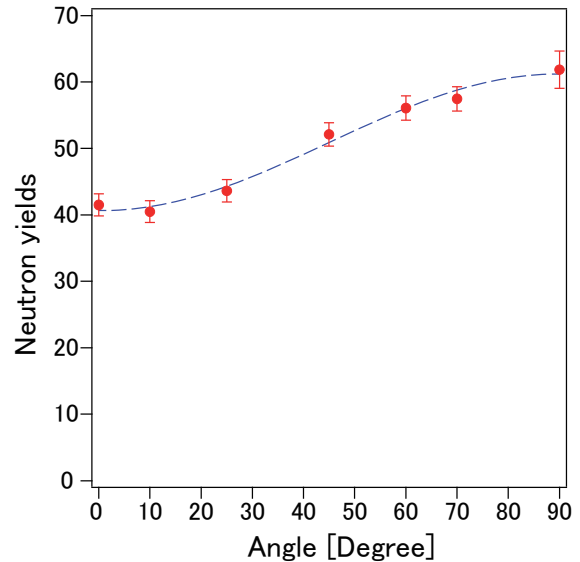


**Figure 3** Neutron yields as a function of the angle between the detector and the plain of the linear polarization. The dashed line is derived by  $\chi^2$ -fitting.

plot a neutron yields as a function of the azimuthal angle,  $\phi$ , between the detector and the plain of the linear polarization of the incident gamma-ray beam. These yields can be reproduced well by the function of  $a + b \cos(2\phi)$ , which was predicted by Agodi [3].

### References

- [1] A. Agodi, *Il Nuovo Cimento*, **5(1)**, 21 (1957).
- [2] K. Horikawa *et al.*, *Phys. Lett. B*, **737**, 109 (2014).
- [3] T. Hayakawa *et al.*, *Phys. Rev. C* **93**, 044313 (2016).

# The film modification of Si-containing hydrogenated DLC films by the soft X-ray irradiation

Shotaro TANAKA<sup>1</sup>, Ryo IMAI<sup>1</sup>, Takayuki HASEGAWA<sup>2</sup> and Kazuhiro KANDA<sup>1</sup>

1. LASTI, University of Hyogo

2. Synchrotron Analysis L. L. C.

## Abstract

The film modification of Si-containing diamond-like carbon (Si-DLC) films by the exposure to synchrotron radiation (SR) in the soft X-ray region was studied by near-edge X-ray absorption fine structure (NEXAFS) spectroscopy using SR. We found that Si oxidization layer was formed at surface of Si-DLC and this oxidization layer was deoxidized by the additional exposure to soft X-ray. Because of absorption of soft X-ray by Si oxidization layer, the Si oxidization layer protect Si-DLC films from soft X-ray exposure, and desorption of hydrogen was suppressed.

## Introduction

Diamond-like carbon (DLC) films have various useful properties such as high hardness, a low friction coefficient, high abrasion quality, a gas barrier, chemical inertness and surface lubrication. Because of these characteristics, DLC films were utilized as coating materials on automobile parts, hard disks, artificial blood vessels, edge tools and food containers. In addition, DLC films are expected to be used in outer space as a lubrication instead of oil, which cannot be used in space because it freezes in vacuums [1, 2]. But, it has been reported that hydrogenated DLC (H-DLC) films were caused desorption of hydrogen due to soft X-ray exposure [3].

Hetero elements such as Si, Ti and W were improved by several properties of DLC films such as heat-resisting property, and adhesion. We found out that desorption of hydrogen was suppressed in the soft X-ray exposure to Si doped DLC films. But  $sp^2/(sp^2+sp^3)$  ratio of C atom estimated from NEXAFS spectra was increased and film volume was decreased by soft X-ray exposure. These results are same with the results of irradiation experiments for none doped H-DLC films. Clarification of the effect of soft X-ray exposure on DLC films is important to ensure that DLC films are used in outer space safely. In this study, we investigated the modification of Si-DLC films by soft X-ray exposure by the measurement of Si-K edge NEXAFS spectra of Si-DLC films.

## Experiments

500-nm-thick Si-DLC films were deposited on Si wafers by using a plasma-enhanced CVD method. The content of H, C and Si of Si-DLC films were  $\approx 40$  at.%,  $\approx 40$  at.% and  $\approx 20$  at.% respectively. There were estimated from the combination of Rutherford backscattering spectrometry (RBS) and elastic recoil detection analysis (ERDA) techniques.

The soft X-ray irradiation of the Si-DLC films was carried out at BL06. The SR at the BL06 irradiation chamber had a continuous spectrum from IR to soft X-rays, lower than 1000 eV. This include 110 eV and 300 eV, which is the ionization energy of a silicon *L* shell and a carbon *K* shell, respectively. During this experiment, the electron energy of NewSUBARU storage ring was 1.0 GeV. The BL06 sample stage was room temperature and the pressure in the chamber was the order of  $10^{-5}$  Pa. An SR dose [mA·h] was derived from the product of the ring current [mA] and exposure time [h].

Si-K edge NEXAFS spectra were measured by total electron yield (TEY) method at BL05A of the NewSUBARU. This measurement enabled us to know information on the local structure near surface of sample. The soft X-ray exposure to sample carried out at magic angle ( $54.7^\circ$ ) with respect to the surface of the sample. The measured energy range in the experiment was 1810-1890 eV of Si-K edge.

## Result and discussion

Figure 1 shows Si-K edge NEXAFS spectra of Si-DLC films exposed to the soft X-ray, that of the Si-DLC film before exposure and that of the SiO<sub>2</sub> powder for comparing the peak of Si-DLC films. The peak of 1846.8 eV was appeared at 80 mA·h soft X-ray dose. This peak derived from SiO<sub>2</sub>. This result means that Si in Si-DLC films was oxidized by soft X-ray exposure under existence of oxygen. However, intensity of the peak of 1846.8 eV decreased at 1500 mA·h dose. Figure 2 shows Si-K edge NEXAFS spectra around 1846.8 eV. The peak of 1846.8 eV drastically increased until 800 mA·h dose. However, at 1000 mA·h dose (pink line), the intensity of peak decreased. Moreover, the intensity of peak decreased sharply at 1500 mA·h dose. On the other hand, the intensity of the energy range about 1843-1846 eV increased. This energy range derived from deoxidization of SiO<sub>2</sub> [4]. These results mean that the Si oxidization layer was formed at 200 mA·h dose. It is considered the Si was oxidized by residual oxygen at vacuum chamber. The formed Si oxidization layer was deoxidized by the additional exposure to soft X-ray. It is considered that hydrogen in Si-DLC films was desorbed by soft X-ray exposure at the dose range of 0-200 mA·h. Beyond 200 mA·h, Because of absorption of soft X-ray by Si oxidization layer, soft X-ray was not reached bulk of Si-DLC, and desorption of hydrogen was suppressed. Figure 3 shows result of dependence of soft X-ray irradiation of volume change. Comparing these results with the results of volume change, the volume was drastically decreased by desorption of hydrogen process at the dose range of 0-200 mA·h. Beyond 200 mA·h, the Si oxidization layer protect Si-DLC films from soft X-ray exposure, and desorption of hydrogen was suppressed. As a result degree of volume decrease was slowly decrease. However the Si oxidization layer was deoxidized in the region more than 800 mA·h, degree of volume change was not changed. It is considered that deoxidization of Si oxidization layer is not affected the durability against X-ray exposure. Oxidization of Si in Si-DLC caused by the irradiation of atomic oxygen was reported [5]. Thus, it is considered that these phenomena can be observed at outer space. Therefore, it was found that the Si-DLC films have durable against space environment such as soft X-ray.

## Conclusion

The film modification of Si-DLC films by the soft X-ray exposure was investigated by the measurement of Si-K edge NEXAFS spectra. Si oxidization layer was formed at surface of Si-DLC films by soft X-ray exposure under existence of oxygen. The Si oxidization layer was deoxidized by the exposure to soft X-ray. In addition, it was founded the Si oxidization layer protect Si-DLC films from soft X-ray exposure because of soft X-ray was desorbed by the Si oxidization layer. Therefore, Si-DLC films have high durable against space environment such as soft X-ray and atomic oxygen.

## Reference

- [1] C. Donnet *et al.*, Surf. Coat. Technol. 120 (1999)548.
- [2] C. Donnet *et al.*, Tribology of Diamond-like Carbon, Springer, 2008.
- [3] R. Imai *et al.*, Diamond. Relat. Matel. 44(2014)8-10.
- [4] R. Sammynaiken *et al.*, J. Appl. Phys. 92 (2002) 3000.
- [5] K. Kidena *et al.*, Trans. Mat. Res. Soc. Japan 40 (2015) 363.

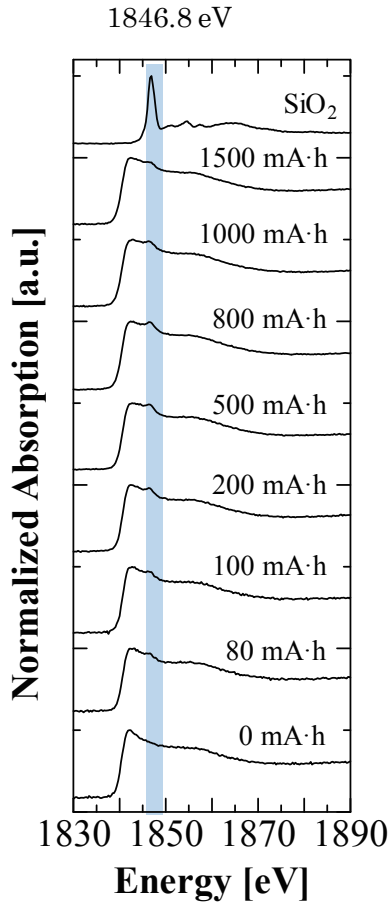


Figure 1. Si-*K* edge NEXAFS spectra of Si-DLC films before and after soft X-ray exposure and SiO<sub>2</sub> powder. The blue line is 1846.8 eV.

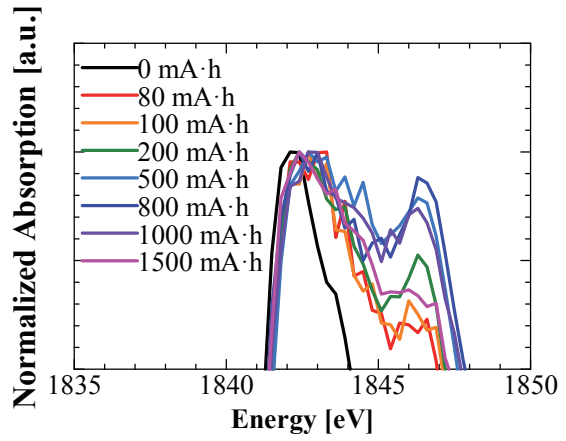


Figure 2. Si-*K* edge NEXAFS spectra around 1846.8 eV of Si-DLC films before and after soft X-ray exposure.

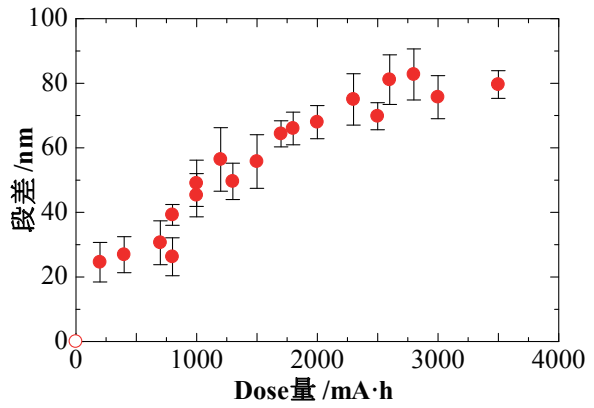


Figure 3. Dependence of soft X-ray irradiation of volume change.

# Surface Modification Processes of Highly Hydrogenated Diamond-Like Carbon Thin Films by the Soft X-ray Irradiation

Kazuhiro Kanda<sup>1</sup>, Ryo Imai<sup>1</sup>, Keiji Komatsu<sup>2</sup>, Hidetoshi Saitoh<sup>2</sup>  
<sup>1</sup> LASTI, University of Hyogo, <sup>2</sup> Nagaoka University of Technology

## Abstract

Synchrotron radiation process of a hydrogenated diamond-like carbon (H-DLC) film was investigated by the exposure of H-DLC films to white soft X-ray lower than 1000 eV. The desorbed species from the surface of H-DLC film by irradiation of soft X-ray and its dose dependence were measured using quadrupole mass spectrometer. The dose dependency of thickness and density of H-DLC film were discussed by the measurement of X-ray reflection. The film modification of H-DLC film by the SR exposure was confirmed to occur due to the desorption of hydrogen molecule from H-DLC film in the dose range of 0 - 200 mA·h.

## Introduction

Diamond-like carbon (DLC) film is amorphous carbon film, which contains  $sp^3$  hybridized carbon corresponding to a diamond structure and  $sp^2$  hybridized carbon corresponding to a graphite structure. In addition, DLC film usually contains a certain amount of hydrogen. The superlubricity of DLC film, along its low friction coefficient, high hardness, chemical inert, and high wear and corrosion resistance, make it one of the most promising coatings for applications, such as cutting tools, automobile parts, molds, computer hard disks, optical devices, food containers, and artificial blood vessels. Recently DLC film was considered to use as a lubrication material in space from its superlubricity. Oils and fats, which are used as lubricant materials on the ground, cannot be used in outer space, because they evaporated and froze in a vacuum. Hydrogenated DLC (H-DLC) film with a hydrogen content greater than 40 at.% can be expected to use as a lubrication material in space because it provides ultra-low friction (friction coefficient less than 0.001), even under vacuum conditions [1,2]. On the other hand, in the outer space, environmental tolerances unlike ground, such as ultra-high vacuum, variation in temperature from a high temperature to low temperature, collision with ionic particles and neutral atoms, and soft X-ray irradiation, are required. It has been considered that the DLC film generally had very strong tolerance for a soft X-ray [3]. However, our group has recently reported that soft X-ray exposure on H-DLC films leads to surface modification; Soft X-ray irradiation against hydrogen-rich DLC films caused desorption of hydrogen from film and film volume change [4] and rise of hardness [5]. Still, the modification processes causing by soft X-ray exposure on H-DLC films are not yet fully understood.

In order to use hydrogenated DLC films

safely in space, it is necessary to clarify the influence of soft X-ray on film properties and rate of the deterioration of H-DLC film by the soft-X ray. In the present work, for the purpose to grasp the modification processes by soft X-ray exposure on H-DLC films, we measured the desorbed species from the surface of H-DLC film by irradiation of soft X-ray and its dose dependence using quadrupole mass spectrometer (QMS). In addition, dose dependences of film density and thickness were estimated by the measurement of X-ray reflection (XRR).

## Material and methods

H-DLC films were deposited on Si wafers by using an amplitude-modulated RF plasma-enhanced CVD method. (Nippon ITF Co.) This method enables the deposition of DLC films containing a lot of hydrogen. The desired value of film thickness was 200-nm-thick. The hydrogen content of H-DLC films was estimated to be  $\approx 50$  at.% by using the combination of Rutherford backscattering spectrometry (RBS) and elastic recoil detection analysis (ERDA) techniques [5].

The SR irradiation of the H-DLC films was carried out at BL06 of the NewSUBARU synchrotron facility. The experimental apparatus at BL06 are described in detail in refs. [6,7]. The light source of BL06 was bending magnet. The SR extracted from a bending magnet was introduced to sample stage as straight light via a pair of mirror. The SR at the BL06 sample stage had a continuous spectrum from IR to soft X-rays, lower than 1 keV. This includes 300 eV, which is the ionization energy of a carbon  $K$  shell. During this experiment, the electron energy of the NewSUBARU ring was 1.0 GeV and the ring current was 300 mA in the top-up mode. Except the detection of desorbed species using quadrupole mass spectrometer, the SR was

irradiated to a sample surface perpendicularly. An SR dose [ $\text{mA}\cdot\text{h}$ ] is derived from the product of the ring current [ $\text{mA}$ ] and exposure time [ $\text{h}$ ]. In the present study, the H-DLC films were exposed to soft X-ray in the dose region to  $3000 \text{ mA}\cdot\text{h}$ . During the exposure of the H-DLC films to soft X-ray, the pressure in the irradiation chamber was the order of  $10^{-5} \text{ Pa}$  and the temperature of a sample stage was confirmed to be room temperature using a thermocouple. After the SR exposure, the modified H-DLC films were kept in the dry box.

### Result and Discussion

Dose dependences of the desorbed species from H-DLC film surface by the irradiation of soft X-ray was measured using a QMS (Anelva Co., Q-M400QA-M) equipped at irradiation chamber of BL06. A detectable mass range was from 1 to 400, and mass resolution,  $M/\Delta M \geq 2M$ . The QMS was arranged perpendicular to the advancing direction of soft X-ray beam. In this measurement, an incident soft X-ray beam was introduced to a sample at  $45^\circ$  with respect to the surface normal. The desorbed species from the sample were detected with a QMS arranged at  $45^\circ$  with respect to the surface normal of the sample in the opposite direction of the incident beam. Detected signals with QMS were considered to include not only desorbed species from sample DLC films, but residual gas species in the irradiation chamber and substrate Si wafer. Therefore, we measured the mass spectrum in the SR exposure to Si wafer without the deposition of DLC film as back-ground, and we subtracted these values from the measured mass spectrum in the SR exposure to H-DLC film. Mass spectrum just after an SR irradiation start to H-DLC film, which was obtained by such treatment described above, was showed in Fig. 1. In the mass range more than 60, the peak was not observed.

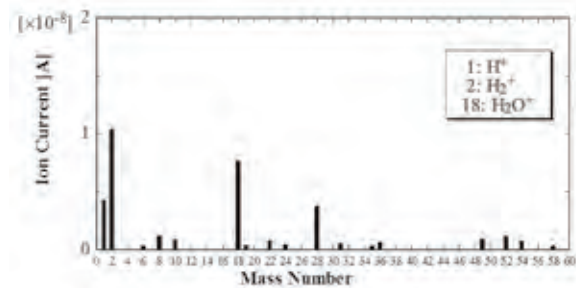


**Fig. 1** Mass spectrum of desorbed species from H-DLC film by the irradiation of SR just after start.

Peaks in Fig. 1 at mass number 18 and 28 were ascribable to water molecule and nitrogen molecule,

respectively. These are back ground species, which were not removed by above treatment, and/or species, which adhered to the surface of the H-DLC film. In tense peak at mass number 2 showed that hydrogen molecules and/or hydrogen molecule ions were desorbed from the surface of H-DLC film by SR exposure. Peak at mass number 1 is due to hydrogen ion and/or hydrogen atom, which might directly come out of a H-DLC film; and made by decoupling of hydrogen molecules in the QMS is possible. It is a noteworthy fact that the species that carbon coupled with hydrogen, such as  $\text{CH}^+$  (mass number, 13),  $\text{CH}_2^+$  (mass number, 14),  $\text{C}_2\text{H}_2^+$  (mass number 26), and etc. were not observed. In other words, desorption of carbon, namely, etching was very slower than desorption of hydrogen.

Next we studied dose dependence of quantity of desorbed species. In this experiment, we used commercial DLC film deposited with ion plating method (Nanotec) for a reference as a representative mark of typical DLC film. The hydrogen content of ion-plating DLC (IP-DLC) film was  $\approx 20\%$  estimated by using ERDA/RBS. Fig. 2 showed the dose dependence of most intense peak at mass number, 2.

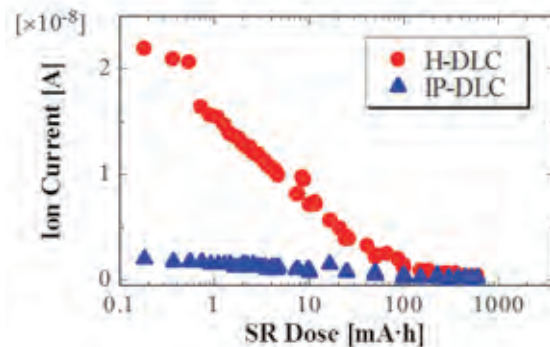


**Fig.2** SR dose dependence of  $\text{H}_2^+$  species (mass number = 2) from H-DLC film and IP-DLC film.

A large quantity of hydrogen is emitted from the H-DLC film at the same time to start irradiation of soft X-ray. Quantity of desorbed hydrogen decreased steadily with increase of SR dose and became approximately constant with a very small value in the dose range more than  $200 \text{ mA}\cdot\text{h}$ . On the other hand, desorption of hydrogen was hardly observed even if IP-DLC film was expose to soft X-ray. That to say, it was confirmed that hydrogen was not desorbed in the exposure of the DLC film with the hydrogen content less than a certain value. From these results, H-DLC film can be modified due to desorption of hydrogen by the soft X-ray exposure, while IP-DLC film has high tolerance against soft X-ray.

We performed the measurement of the X-ray reflection (XRR) to obtain a film thickness and density of the H-DLC film. The X-ray reflection was measured with XRR apparatus (Mac science, M03XHF MXP3). Fig. 3 showed the exposure dose

dependence of the film thickness estimated from XRR study.

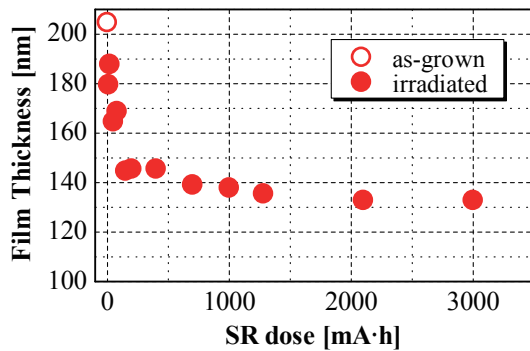


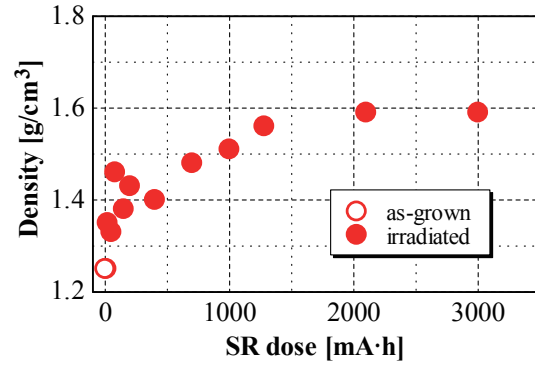
**Fig. 3** Dose dependence of thickness of H-DLC film estimated by the measurement of XRR.

The film thickness at the time of non-irradiation was according to film formation condition in  $\approx 200$  nm. Film thickness suddenly decreased from  $\approx 200$  nm to  $\approx 145$  nm by SR exposure in the dose range of 0 - 200 mA·h. In the dose range more than 200 mA·h, film thickness decreased gently and maintained the constant in 130 nm.

Fig. 4 showed the dose dependence of film density on the basis of XRR measurement.

The density of H-DLC film at the time of non-irradiation was  $1.25 \text{ g/cm}^3$ . Density of diamond and graphite are  $3.51 \text{ g/cm}^3$  and  $2.26 \text{ g/cm}^3$ . Density of DLC films almost populated in the range of 1.7-2.3  $\text{g/cm}^3$ , and that of H-DLC film used in the present study,  $1.25 \text{ g/cm}^3$  was very small. Density of H-DLC film before SR exposure,  $1.25 \text{ g/cm}^3$  increased drastically to  $1.40 \text{ g/cm}^3$  by after SR exposure with the 200 mA·h dose. In the dose range more than 200 mA·h, film density increased gradually and became constant,  $1.60 \text{ g/cm}^3$  in the dose more than 2000 mA·h. From these

**Fig. 4** Dose dependence of density of H-DLC film estimated by the measurement of XRR.



## Conclusion

In the irradiation of soft X-ray against H-DLC film, desorption of hydrogen from H-DLC film, decrease of film thickness, and increase of film density was occurred in the dose range of 0 - 200 mA·h. These dose dependences were accord with that of hydrogen content in the film which was estimated from ERDA/RBS technique in ref. [5]. From these results, modification of H-DLC film by the soft X-ray begins with desorption of hydrogen molecules from H-DLC film by the absorption of soft X-ray. It was confirmed that desorption of hydrogen caused decrease of film volume and increase of density, and other film properties.

## References

- [1] C. Donnet *et al.*, Tribology of Diamond-like Carbon, Springer (2008).
- [2] C. Donnet *et al.*, Surf. Coat. Technol. 68-69 (1994) 626.
- [3] H. Kyuragi *et al.*, Appl. Phys. Lett. 50 (1987) 1254.
- [4] K. Kanda *et al.*, Jpn. J. Appl. Phys. 50 (2011) 055801.
- [5] R. Imai *et al.*, Diamond Relat. Matter. 44 (2014) 8-10.
- [6] K. Kanda *et al.*, Jpn. J. Appl. Phys., 42 (2003) 3983-3985.
- [7] Y. Kato *et al.*, Jpn. J. Appl. Phys., 43, (2004) 3938-3940.

# Refractive-index modifications in Silica-Based Films by Undurator Radiation with a multilayer spectrometer

K. Moriwaki, G.Kimura, Graduate School of Eng., Kobe Univ.,  
K.Kanda, and S.Matsui, LASTI/Univ. Hyogo

## Abstract

Undurator radiation (UR) by the NewSUBARU (BL7A) is used for silica-based films modifications for applications of optical devices like waveguides. UR with or without a multilayer spectrometer is used for the samples, and the observed effects are compared. The modification layers are separated in two parts of the shallow and strong one and the relatively deep and moderate one without the spectrometer. The thin layers with less than 5 nm thickness from the surface show strong reduction and high refractive index changes on the order of  $10^{-2}$  depending on the UR energy. With the spectrometer, the surface reduction layer is not observed after the UR radiation, although the relatively deep and moderately modified layer is observed. The difference between the samples irradiated with and without the spectrometer may be caused by the irradiation intensity or a sample temperature effect.

## Introduction

Synchrotron radiation (SR) and undurator radiation (UR) are used for radiation-induced refractive index changes in silica-based glass for optical devices like optical waveguides<sup>1,2)</sup>. UR is a very useful tool for the materials modifications, because it can select a useful wavelength, having very high intensity. UR with a multilayer spectrometer would be more useful for the purpose because it has high intensity and the most suitable wavelength can be selected without higher order ones. In this report, modification effects are compared with or without the spectrometer.

## Experiments and Results

Thermally grown SiO<sub>2</sub> films on Si substrates and fused quartz substrates were used for the UR irradiation. UR with the first-peak energy ranging from 20 to 110eV is used without the spectrometer, and more than 80eV is used with the spectrometer. Irradiated samples were characterized by XPS (X-ray Photoelectron Spectroscopy), optical absorption spectroscopy, and refractive index measurements.

Figure 1 shows two modification layer model for the samples irradiated by UR without the

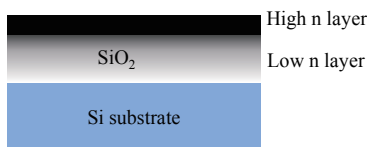


FIG.1 Two modification-layers irradiated by UR with a peak energy from 20 to 110eV without the spectrometer. Each layers show higher ( $10^{-2}$ - $10^{-1}$ ) and lower ( $10^{-2}$ ) refractive-index changes, respectively.

spectrometer<sup>1,2)</sup>. The two-layer structures have large refractive-index in the very thin surface, and have relatively low refractive-index layer in the underlying part.

For the surface layer in the two-layer structures, it was found that the refractive-index changes are increased by making the UR irradiation wavelength longer. By the results of XPS measurements, Si-Si bonds in the shallow surface layer less than 4nm thickness appeared, that means surface reduction. A correlation between an amount of the Si-Si bonds and the refractive-index changes were also found. By the results of optical absorbance measurements, defects were found to be generated by the UR irradiation. The Si-Si bonds is a major cause of the refractive index changes in the sample. Other defects are also suggested to be a cause of the refractive-index changes in both the shallow surface and the underlying layer. The refractive indices were reduced drastically by removing the surface reduction layer, but they still remain at certain level ( $10^{-3}$ ) which can be applied for some optical devices<sup>2)</sup>.

Figure2 shows that the surface reduction layer is not observed in the sample irradiated by UR with the spectrometer, as compared in the sample irradiated without the spectrometer. There is a clear difference between the two samples. The samples show also no reduction evidence as shown in Fig.3, by increasing irradiation-dose up to by 4 time as much as the one in Fig.2. The results in Fig.3 might mean that causes of the reduction are not only by the higher irradiation intensity but by the sample temperature effect, because the sample temperature is drastically decreased on the samples irradiated by UR with the spectrometer.

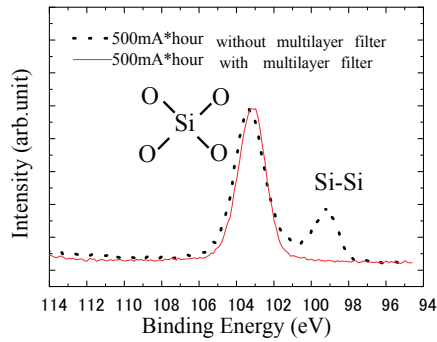


Fig2. XPS spectra of Si 2p peaks for UR irradiated samples with an energy of 80eV with and without a multilayer filter. Two peaks are those of SiO<sub>2</sub> and Si-Si bond<sup>2)</sup>.

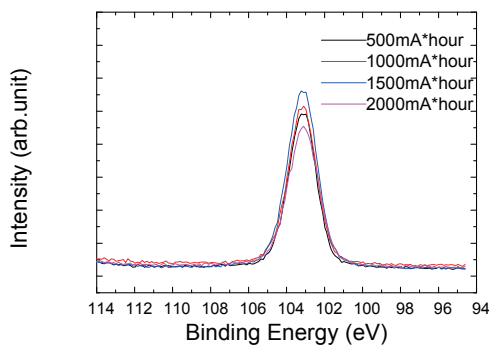


Fig3. XPS spectra of Si 2p peaks for UR irradiated samples with the spectrometer by increasing the dose from 500 to 2000 mA\*hour.

Although the surface reduction layer disappeared, refractive index changes were also found for the samples irradiated by UR with the spectrometer, as shown in Fig.4. The refractive index changes in Fig.4 are lower than the one caused by the surface reduction, but are still high enough for an application to optical devices.

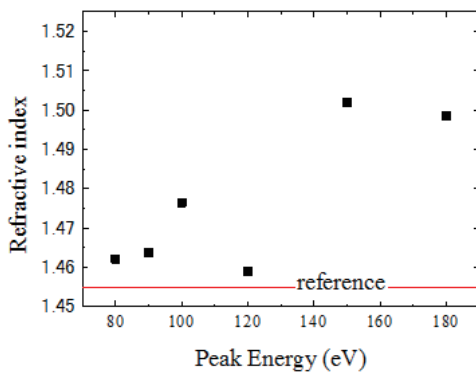


Fig4 Refractive index changes after irradiation by UR with the spectrometer.

Further investigations are needed for the measurements because of the scattered results in Fig.4.

The refractive index changes may be caused by defects in the irradiated samples, as appeared in Fig.5 and Fig.6. By using the spectrometer, the absorbance for the irradiated samples is decreased from the one without the spectrometer, but still show the certain level (Fig.5). The absorbance data were changed by the irradiated peak-energies as in Fig.6, but its reproducibility is not clear yet.

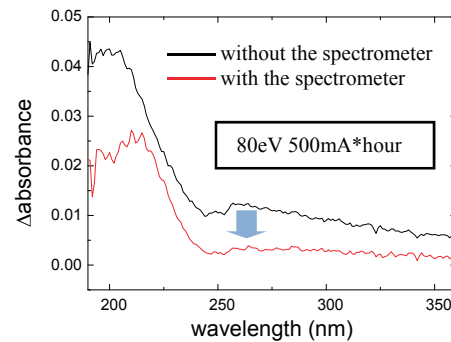


Fig5. Optical absorbance for samples irradiated by UR with and without the spectrometer.

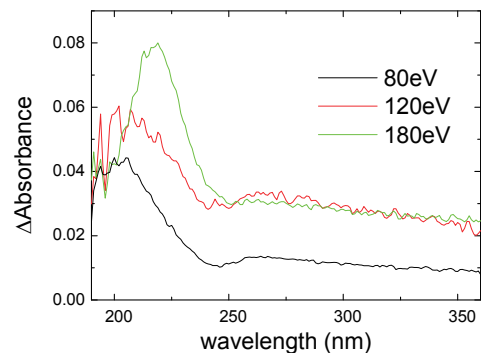


Fig6. Optical absorbance for samples irradiated by UR with the spectrometer at 3 peak-energies from 80-180 eV.

## Conclusions

UR-irradiated samples showed clear differences between by the radiation with and without the spectrometer. Those kinds of modification would be useful for silica-based glass as optical material, but further investigations are needed to determine the most effective radiation conditions

## References

- [1] K.Moriwaki et al., LASTI Annual Report vol.15 (2013).
- [2] K.Moriwaki et al., LASTI Annual Report vol.16 (2014).

# Effect of the soft X-ray on the surface of fluorinated DLC film

H. Takamatsu<sup>1</sup>, M. Okada<sup>1</sup>, M. Niibe<sup>1</sup>, K. Kanda<sup>1</sup>

<sup>1</sup>LASTI, University of Hyogo, 3-1-2 Koto, Kamigori, Ako, Hyogo 678-1205 Japan

## Abstract

The effect of the soft X-ray on the surface of the fluorinated diamond-like carbon (F-DLC) film was investigated. The studies of stylus profiler, X-ray photoelectron spectroscopy (XPS) and the near-edge X-ray absorption fine structure (NEXAFS) showed that decrease in film thickness, fluorine desorption and increase in  $sp^2/(sp^2+sp^3)$  ratio of C atom in the F-DLC film was caused by the irradiation of the soft X-ray.

## 1. Introduction

The diamond-like carbon (DLC) film is well known for its various superior properties like high hardness, wear resistance, chemical inertness, and low friction coefficients [1]. It's used in various situation such as automobile parts, electronic components, medical instrument, the space industry, etc., and the development efforts for further performance enhancements are conducted by many researchers every day now.

The several properties of the DLC film were improved by doping of hetero elements such as Si, Ti and W. Especially, the fluorinated diamond-like carbon (F-DLC), which contains fluorine atom in the DLC film has some excellent properties, such as low surface energy, low-dielectric constant, chemical inertness, etc., while keeping the high hardness of the DLC film [2].

It has been reported that hydrogen was desorbed from the hydrogenated DLC (H-DLC) film due to the soft X-ray irradiation [3]. In this study, we investigated the effect of the soft X-ray on surface of the F-DLC film. The steps between irradiation parts and unirradiation parts, the element composition ratio at the film surface and the  $sp^2/(sp^2+sp^3)$  ratio of C atom in the film were measured with stylus profiler, X-ray photoelectron spectroscopy (XPS) and the C-K edge near edge X-ray absorption fine structure (NEXAFS) spectra, respectively.

## 2. Experiments

The 210-nm-thick F-DLC film was deposited on Si wafers by using a plasma-enhanced CVD method. The hydrogen content and the fluorine content of the F-DLC film were estimated, respectively, to be  $\approx 2$  at.% and  $\approx 40$  at.% with the combination of Rutherford backscattering spectrometry (RBS) and elastic recoil detection analysis (ERDA) techniques.

The soft X-ray irradiation of the F-DLC film was

carried out at BL06 of the NewSUBARU synchrotron facility. The SR at the BL06 irradiation chamber had a continuous spectrum from IR to soft X-ray, lower than 1000 eV. This includes the ionization energy of a carbon K shell at 300 eV and the ionization energy of a fluorine K shell at 690 eV. As a result, the K shell electrons of the C and F atoms could be excited by SR at BL06. During this experiment, the electron energy of the NewSUBARU storage ring was 1.0 GeV. The BL06 sample stage was room temperature and the pressure in the chamber was the order of  $10^{-5}$  Pa. An SR dose [mA·h] was derived from the product of the ring current [mA] and irradiation time [h].

## Result and discussion

Fig.1 shows the film thickness change by the soft X-ray irradiation. Red points indicate film thicknesses which were estimated using stylus profiler from the step depth between irradiation part and unirradiation part on the F-DLC film surface. The step was created by putting an Au mesh on the F-DLC film surface, during irradiation of the soft X-ray. The film thickness decreased precipitously from 210 nm to 160 nm, in the SR dose range of 0-300 mA·h, and became constant in about 150 nm over 500 mA·h. Blue points show the film thickness which estimated from the section images of irradiated F-DLC without an Au mesh with the scanning electron microscope (SEM). The results of stylus profiler and SEM show the stop of the film thickness decrease. In addition, the difference of the film thickness between the sample with Au mesh and the sample without Au mesh did not appear. Therefore it can be understood that stop of the film thickness decrease is an end of the reaction not a limit of the aspect ratio.

Fig.2 shows change of the elementary composition ratio in the soft X-ray irradiated F-DLC estimated with XPS. Red points, blue points and green points

show fluorine content, oxygen content, and carbon content, respectively. The fluorine content decreased precipitously from 0.8 to 0.2, in the SR dose range of 0-300 mA·h, and became constant in about 0.1 over 500 mA·h. The carbon content relatively increased with a decrease in fluorine. As these results, it is clear that fluorine is desorbed from the F-DLC film surface by the soft X-ray irradiation. The oxygen content increased from 0 to 0.15, the range of 0-300 mA·h, and became constant about 0.2 over 500 mA·h. It is understood that the nonpair electron of carbon which created by fluorine desorption is stabilized by combination with oxygen in residual atmosphere.

Fig.3 shows the  $sp^2/(sp^2+sp^3)$  ratio change of carbon in F-DLC by the soft X-ray irradiation. The  $sp^2/(sp^2+sp^3)$  ratio was estimated from the C-K NEXAFS spectrum by comparison with the highly ordered pyrolytic graphite (HOPG) as a standard sample. The  $sp^2/(sp^2+sp^3)$  ratio increased precipitously from 0.4 to 0.6, in the range of 0-300 mA·h, and became constant in about 0.6 over 500 mA·h. In other words, the bonding state of carbon varied from diamond-like to graphite-like by irradiation of SR dose with 300 mA·h. It is understood that the dangling bond of carbon which created by fluorine desorption and dissociation of carbon single bonding formed carbon double bonding by recombination.

### Conclusion

The effect of the soft X-ray on surface of F-DLC film was investigated by the measurements of the film thickness with stylus profiler, the element composition ratio at the film surface with XPS and the  $sp^2/(sp^2+sp^3)$  ratio of C atom with C-K edge NEXAFS. In the range of 0-300 mA·h, the film thickness decreased precipitously from 210 nm to 160 nm, the fluorine content decreased precipitously from 0.8 to 0.2, and the  $sp^2/(sp^2+sp^3)$  ratio increased precipitously from 0.4 to 0.6. In the dose region more than 500 mA·h, the effect of the soft X-ray on surface of F-DLC film was not observed.

### References

- [1] A. Grill, *Diamond Relat. Mater.*, 8 (1999) 428.
- [2] S. Miyake *et al.*, *J. Tribol.*, 1991
- [3] R. Imai *et al.*, *Diamond. Relat. Matel.* 44(2014)8-10.

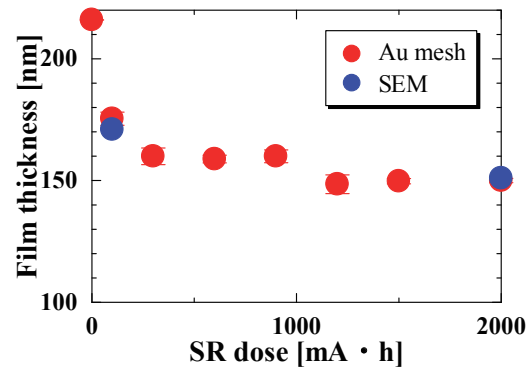


Fig.1 The soft X-ray irradiation dose dependence of the film thickness with Stylus profiler and SEM

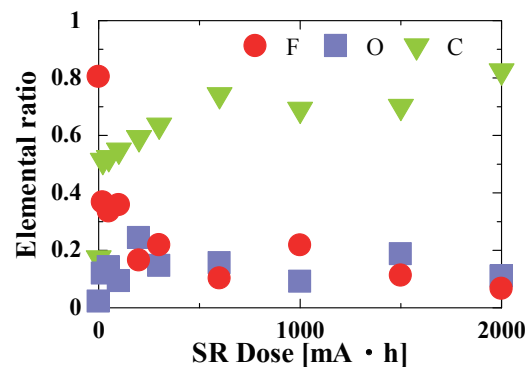


Fig.2 The soft X-ray irradiation dose dependence of the element composition ratio with XPS

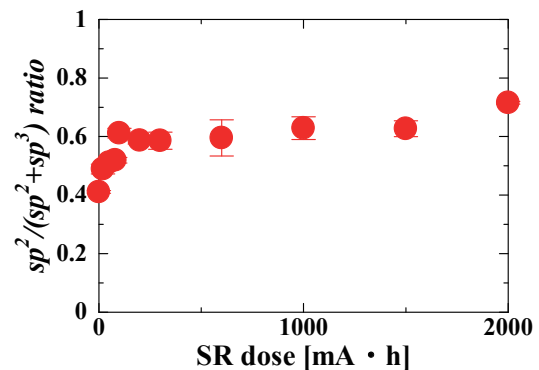


Fig.3 The soft X-ray irradiation dose dependence of the  $sp^2/(sp^2+sp^3)$  ratio with NEXAFS

# Evaluation of damage in an organic thin film with cluster ion sputtering

S. Fujita<sup>1</sup>, Y. Nohara<sup>1</sup>, M. Ohno<sup>1</sup>, Y. Haruyama<sup>2</sup>

<sup>1</sup>Nissan Chemical Industries, Ltd, Chiba, Japan

<sup>2</sup>LASTI, University of Hyogo, Hyogo, Japan

II

## Abstract

We investigated the changes of surface morphology and chemical bonding state of cluster ion sputtered PMMA thin film to evaluate sputtering damage in an organic thin film. By measuring the atomic force microscope (AFM) image of sputtered PMMA, it was confirmed that the surface roughness of PMMA increased with increasing incident cluster ion energy. On the other hand, the near-edge X-ray absorption fine structure (NEXAFS) spectra at the carbon K-edge region, suggested that the amount of C=C and C=O bonds in sputtered PMMA was influenced by the ion species and incident energy of ion.

## Introduction

Ion sputter depth profiling has been widely used with X-ray photoelectron spectroscopy (XPS) or time-of-flight secondary ion mass spectrometry (TOF-SIMS) for the characterization of thin film structures. However, the monomer ion sputtering causes significant damage to the structure of organic materials. Therefore, in case of sputtering polymeric thin films, those chemical bonding state or composition ratio are changed from original state. In order to improve this problem, the cluster ion sputtering method has been attracting attention in recent years. The cluster ion is a collection of atomic or molecule ions, it has been reported that it is possible to sputter organic materials at lower damage than monomer ions. In the previous studies, it was reported that cluster ions do not penetrate deeply into target materials because incident energy of each constituent ion was very low, therefore, the energy of their impact was deposited within the few nanometers of the surface [1]. However, the mechanism has not been completely clarified yet. Therefore, we investigated changes of surface morphology and chemical bonding state of cluster ion sputtered PMMA thin film to evaluate sputtering damage in an organic thin film.

## Experiments

PMMA (Sigma-Aldrich, Mw = 120,000) was dissolved in toluene as a 4 wt% solution. PMMA thin films were prepared by spin coating on an ITO/glass substrate with a thickness of about 150 nm. PMMA were sputtered with an ion gun attached to the XPS (PHI 5000 VersaProbe and PHI Quantera) instrument. In sputtering, Ar gas cluster ion beam (Ar-GCIB) with a mean size of about 2500 atoms/cluster and C<sub>60</sub> cluster beam were used. Moreover, Ar monomer ion was also

used for the purpose of comparison with those cluster ions. The sputtering rate of each ion species for PMMA was evaluated by XPS. Table 1 shows the sputtering condition at each ion species. After sputtering, the surface roughness was measured by AFM (Bruker Dimension Icon) and the chemical bonding state was measured by XPS and NEXAFS. For XPS measurements, a monochromatic Al K $\alpha$  (hv = 1486.6 eV) X-ray source was used. The NEXAFS measurements were performed at NewSUBARU synchrotron radiation (SR) facility on beamline 7B. NEXAFS spectra were simultaneously measured by the Auger electron yield (AEY), total electron yield (TEY) and fluorescence yield (FY) methods. To reduce the SR irradiation damage of the samples during measurements, the samples were cooled at about 80 K and NEXAFS spectra were recorded at this temperature.

## Results and discussion

Fig.1 shows AFM images of each PMMA surface after sputtering. Scanned area was all 10  $\times$  10  $\mu$ m. The value of average surface roughness (Ra) obtained from the AFM was described at the bottom of each image. It was confirmed that the each surface roughness of PMMA after sputtering increased as compared with that before sputtering. At the surface after the Ar monomer sputtering, a lot of hole with diameter of about 150-200 nm were observed. Meanwhile, at the surface after each cluster ion sputtering, the granular structure was observed. Moreover, it was confirmed that the surface roughness after Ar-GCIB sputtering increased with increasing

Table.1 The sputtering condition at each ion species

Ion species	Incident ion energy	Sputtering area	Sputtering rate
Ar monomer	1.0 keV	2×2 mm	7.4 nm/min
C <sub>60</sub>	10 keV	2×2 mm	32 nm/min
① Ar-GCIB(Ar <sub>2500</sub> )	5.0 keV	3×3 mm	9.2 nm/min
② Ar-GCIB(Ar <sub>2500</sub> )	7.0 keV	3×3 mm	22 nm/min
③ Ar-GCIB(Ar <sub>2500</sub> )	10 keV	3×3 mm	73 nm/min

incident ion energy. This was considered to be due to the energy of each constituent ion in Ar-GCIB increased. These results suggest that ion species and incident energy have a significant effect on PMMA surface morphology.

Fig.2 shows the C 1s and O 1s XPS spectra of the PMMA after sputtering. Three peaks were observed at 288.6, 286.4, and 285 eV in C 1s spectrum. These peaks were assigned as C=O, C-O, and C=C from PMMA, respectively. Furthermore, two peaks were observed at 533.5 and 532 eV in O 1s spectrum. These peaks were assigned as O-C, O=C from PMMA, respectively [2]. After Ar monomer sputtering, the intensities of C-O and C=O peaks decreased while that of C-C peak increased. Therefore, it was confirmed that the chemical bonding state of PMMA surface

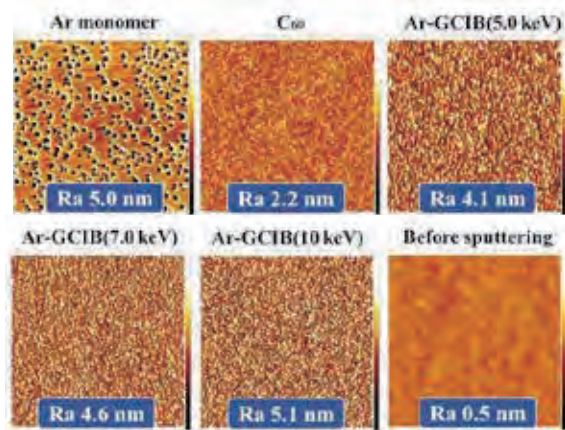


Fig.1 AFM images of PMMA surface after sputtering

after Ar monomer sputtering was significantly changed compared with that before sputtering. Meanwhile, there was no significant change in the cluster ion sputtered surface.

Fig.3 shows the C K-edge NEXAFS spectra of the PMMA after sputtering. The NEXAFS spectra were normalized by the edge-jump intensity. Two peaks were observed at 285 and 289 eV. These peaks were assigned as a transition from a carbon 1s to  $\pi^*$  orbital of C=C, and to  $\pi^*$  of C=O, respectively [3]. It is considered that the

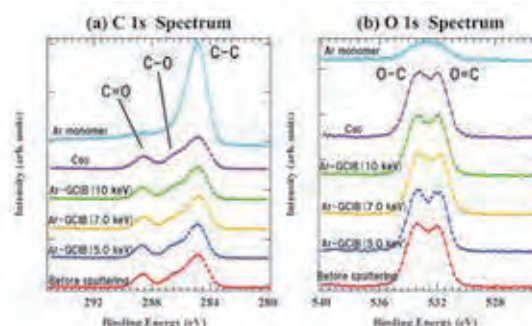


Fig.2 XPS spectra of PMMA after sputtering

C=C peak is derived from sputtering damage, and the C=O peak from PMMA [3,4]. Next, we estimated the ratio of each bond intensity from the NEXAFS spectra for comparison. As shown in Fig.4, the amount of C=C was largest at Ar monomer, followed in order by C<sub>60</sub>, Ar-GCIB and before sputtering. Here, the amount of C=C after cluster ion sputtering was not significantly changed compared with that before sputtering. On the other hand, the amount of C=O bond was smallest at Ar monomer sputtering. The amount of C=O bond by the AEY and TEY methods indicated opposite trend against C=C. Furthermore, FY spectra showed that the Ar-GCIB sputtering did not change in the chemical bonding state in PMMA thin film.

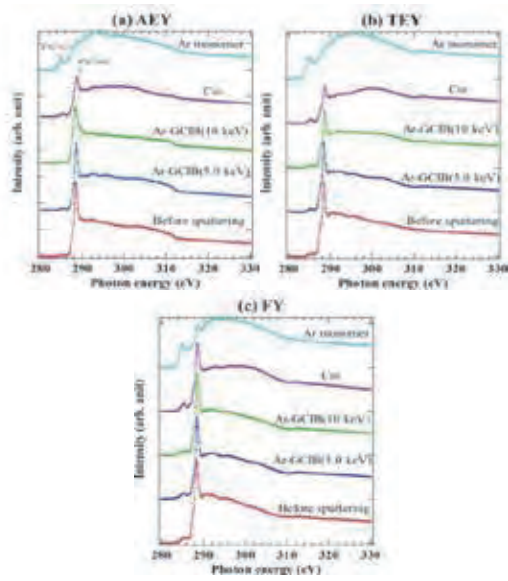


Fig.3 C K-edge NEXAFS spectra of PMMA after sputtering

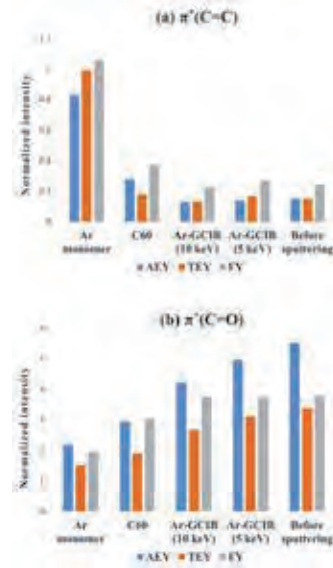


Fig.4 The ratio of each bond intensity

**References**

[1] G. Gillen *et al.*, Rapid. Commun. Mass Spectrom. **12**, 1303, (1998)  
 [2] C. Ton-That *et al.*, Polymer. **42**, 1121, (2001)  
 [3] O. Dhez *et al.*, J. Electron Spectrosc. Relat. Phenom. **128**, 85, (2003)  
 [4] B. Pignataro *et al.*, Nucl. Instrum. Methods Phys. Res. B. **131**, 141, (1997)

# Molecular orientation in photoreactive liquid crystalline polymer films observed by NEXAFS

Y. Haruyama<sup>1</sup>, Y. Taniguchi<sup>2</sup>, M. Kondo<sup>2</sup>, N. Kawatsuki<sup>2</sup>, M. Okada<sup>1</sup>, and S. Matsui<sup>1</sup>  
<sup>1</sup>Laboratory of Advanced Science and Technology for Industry, University of Hyogo  
<sup>2</sup>Graduate School of Engineering, University of Hyogo

## Abstract

The molecular orientation of the pre-aligned photoreactive liquid crystalline polymer PMCB10M films has been investigated using the near-edge X-ray absorption fine structure (NEXAFS) at the C K-edge region. By combining the thickness dependence of PMCB10M films and three types of simultaneous detection methods of NEXAFS measurements, the molecular orientations of PMCB10M films at the near-surface (<2 nm), at the inner-surface (~10 nm) and in the bulk (>10 nm) were evaluated. In addition, it was found that the orientation of the liquid crystalline molecules near the surface was parallel to the surface irrespective of the thickness of PMCB10M films.

## Introduction

The studies on the photoinduced molecular orientation of the polymeric films have attracted significant attention for a potentially wide range of applications such as birefringent optical devices, the photo alignment layer of liquid crystal displays, and optical memories. The polymethacrylate comprised of 4-methoxycinnamolybiphenyl (MCB) side groups connected via decylene spacers (PMCB10M) is one of photoreactive liquid crystalline polymers [1, 2]. It was reported that the molecular orientation of photoreactive liquid crystalline polymer controlled by the linearly polarized UV radiation and the subsequent annealing procedure [1, 2]. However, the molecular orientation of photoreactive liquid crystalline polymer near the surface and the interface between the film and the substrate is not clear. To investigate the molecular orientation of PMCB10M films, NEXAFS spectra at the C K-edge region were measured by three types of simultaneous detection methods with the different probing depth.

## Experiments

PMCB10M was synthesized as described in a previous paper [1]. PMCB10M films of 15-150 nm thickness were prepared by spin-coating a tetrahydrofuran (THF) solution of the polymers onto ITO coated glasses. The pre-aligned PMCB10M films were prepared by irradiating the linearly polarized UV light to the films and by subsequently annealing at 120-240 °C for 10 minutes.

NEXAFS experiments were performed at a beamline 7B of the NewSUBARU synchrotron radiation (SR) facility, the University of Hyogo. NEXAFS spectra were simultaneously measured by Auger electron yield (AEY), total electron yield (TEY) and fluorescence yield (FY) methods.

The sample could be rotated around a vertical axis to change the incidence angle of the SR to the sample surface. The direction of the linear polarization in the SR was horizontal. To evaluate the molecular orientation of PMCB10M films, NEXAFS spectra were recorded in parallel and perpendicular configurations, where the direction of linearly polarized UV light irradiated to the films was parallel and perpendicular to that of the linear polarization in the SR, respectively.

## Experiments and Results

Figures 1(a) and 1(b) show the C K-edge NEXAFS spectra of pre-aligned PMCB10M films, measured by the AEY method, as a function of incidence angle of the SR in parallel and perpendicular configurations, respectively. The thickness of PMCB10M films was 150 nm. A sharp peak at 284.8 eV, which was assigned to transitions from the C 1s orbital to the unoccupied  $\pi^*$  orbitals originating from aromatic ring sites, was observed [2, 3]. With increasing the incidence angle, the intensity of the peak at 284.8 eV decreased remarkably in the parallel configuration while it was almost unchanged in the perpendicular configuration. This indicates that the orientation of the liquid crystalline molecules in PMCB10M at the near-surface is parallel to the polarization direction of the UV light. On the other hand, the angular dependence of the intensity at 284.8 eV in the TEY method became smaller than that in the AEY method as shown in figure 1(c). In addition, the angular dependence of the intensity at 284.8 eV in the FY method (not shown) had the similar angular dependence to that in the TEY. These results indicate that the orientations of the liquid crystalline molecules in pre-aligned PMCB10M films at the inner-surface and in the bulk are

different from that at the near-surface.

NEXAFS spectra of pre-aligned PMCB10M films in the thickness of 15 and 55 nm were also measured in parallel and perpendicular configurations. In the case, the angular dependence of the intensity at 284.8 eV in the

AEY method showed the similar behaviour to that in the thickness of 150 nm. Therefore, it was found that the orientation of liquid crystalline molecules near the surface was parallel to the surface irrespective of the thickness of PMCB10M films.

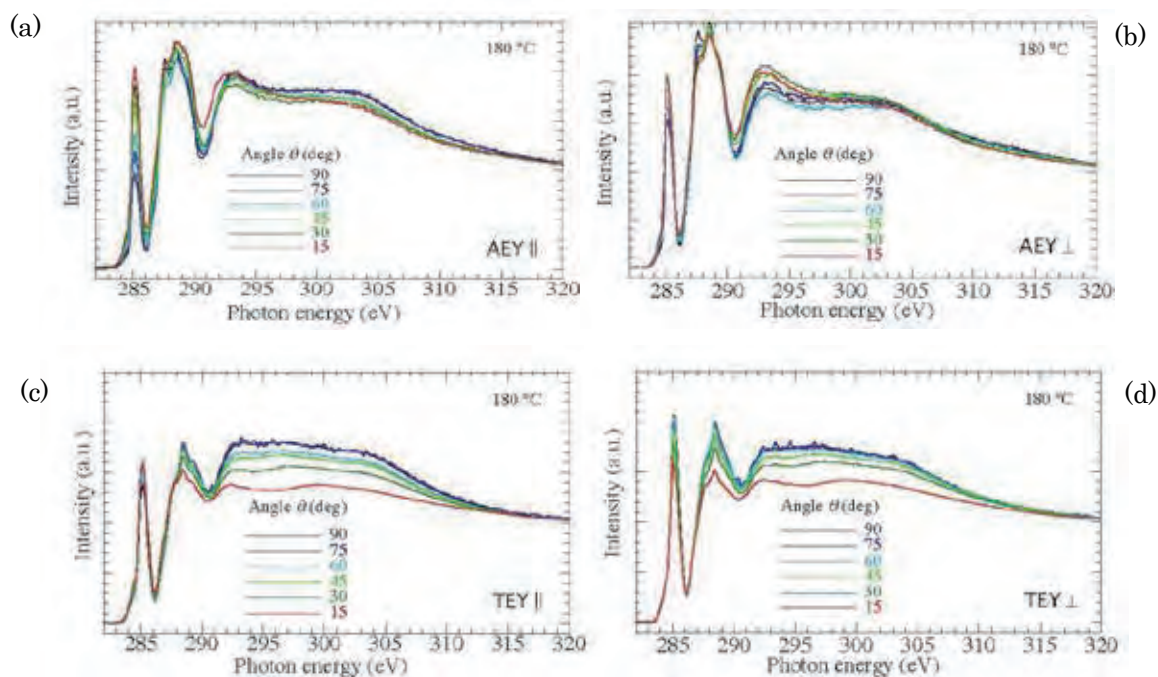


Fig. 1 C K-edge NEXAFS spectra of pre-aligned PMCB10M films, measured by the AEY and the TEY methods, as a function of incidence angle of the SR in parallel (a), (c) and perpendicular (b), (d) configurations, respectively..

## References

- [1] N. Kawatsuki and J. Horii: *Mol. Cryst. Liq. Cryst.* **498**, 49-58, (2009).
- [2] N. Kawatsuki, Y. Taniguchi, M. Kondo, Y. Haruyama, and S. Matsui: *Macromolecules* **48**, 2203, (2015).
- [3] N. Kawatsuki, Y. Inada, M. Kondo, Y. Haruyama, and S. Matsui: *Macromolecules* **47**, 2080, (2014).

# A large takeoff-angle dependence of C-K emission spectra observed in highly oriented pyrolytic graphite

Noritaka Takehira,<sup>1</sup> Masahito Niibe,<sup>1</sup> Yuma Araki,<sup>1</sup> and Takashi Tokushima,<sup>2,1</sup>

<sup>1</sup>Laboratory of Advanced Science and Technology for Industry, University of Hyogo,

<sup>2</sup>Spring-8 Center, RIKEN

II

## Abstract

We observed a large takeoff-angle dependence of C-K emissions in highly oriented pyrolytic graphite (HOPG). The dependence changes by mosaic spread in HOPG samples and X-ray excitation energy. At the excitation energy of 310 eV, far from the absorption edge, we observed a large takeoff-angle dependence of  $\pi \rightarrow 1s$  emission, which has never been reported. According to the band calculation for HOPG, the large angle dependency could be attributed to the resonant transition of 1s electrons to  $\pi^*$  state at the 25 eV higher than the Fermi level.

## Introduction

The soft x-ray spectroscopy using highly brilliant synchrotron radiation is a capable tool for analyzing the local structure around an atom. In particular, high-resolution x-ray emission spectroscopy and x-ray absorption spectroscopy in the soft x-ray region are well suited for analyzing the local and electronic structures of light-element materials because these spectroscopies can provide high-resolution elemental orbital information. Additionally, the combination of soft x-ray emission and absorption spectroscopies can investigate bandgap structure, because they directly reflect the valence and conduction bands, respectively.

A number of studies [1-10] of the electron structure of graphite has been studied in detail, especially with the absorption and emission spectra of the soft X-rays. The layered structure of graphite leads the separation of electron orbitals:  $\sigma$  orbitals spread in the basal plane, while  $\pi$  orbitals are perpendicular to the plane. This difference in the polarization of  $\pi$  and  $\sigma$  electrons is clarified by the dependence of X-ray emission and absorption spectra of graphite on the angle of incidence to the sample surface.

We measured the takeoff-angle dependence of the C-K emission spectra of an HOPG with the newly constructed soft X-ray emission spectrometer (SXES) at the NewSUBARU SR facility [11]. As a result, we observed a large take-off-angle dependence of C-K emissions that has not been previously reported. Also the mosaic spread of HOPG and excitation energy dependence of emission spectra is distinguished clearly.

## Experiment

Table 1 shows four type of commercially-available HOPG crystal samples and their mosaic spread (Union Carbide Co. and Optigraph Inc.). The SXES experiments were performed at the beamline BL-09A [12] at the NewSUBARU SR facility. The samples are fixed in a copper holder to measure the C-K emission spectra. The angle between the directions of the incident beam and the take-out of the emission spectrum is fixed to 90°. The takeoff-angle dependence of the emission spectra was measured by rotating the sample varying from 15° to 75° around a vertical axis.

Table 1. Four type of commercially-available HOPG crystal samples and their mosaic spread.

sample	mosaic spread	
AGraphZ	$0.4 \pm 0.1$ °	Optigraph Inc.
ZYA	$0.4 \pm 0.1$ °	Union Carbide Co.
ZYB	$0.8 \pm 0.2$ °	Union Carbide Co.
ZYH	$3.5 \pm 1.5$ °	Union Carbide Co.

## Results and Discussion

Figure 1 shows the takeoff-angle dependence of the C-K emission spectra measured for the AGraphZ-HOPG. The excitation energy of the soft X-rays used in this measurement was 310 eV. Because the incident X-ray intensity changes upon rotation of the sample, all the emission spectra were normalized to unity for the emission peak intensity of the  $\sigma \rightarrow 1s$  transition at around 276 eV. The peak around the energy 282 eV is found to have a large

angle dependence, and it is identified as light emission due to  $\pi \rightarrow 1s$  transitions.

In previous reports [1-10], the intensities of  $\pi$  emission were at most comparable or less to the  $\sigma$  emission intensity. We are the first to report the observation that the  $\pi$  emission intensity is much higher than the  $\sigma$  emission.

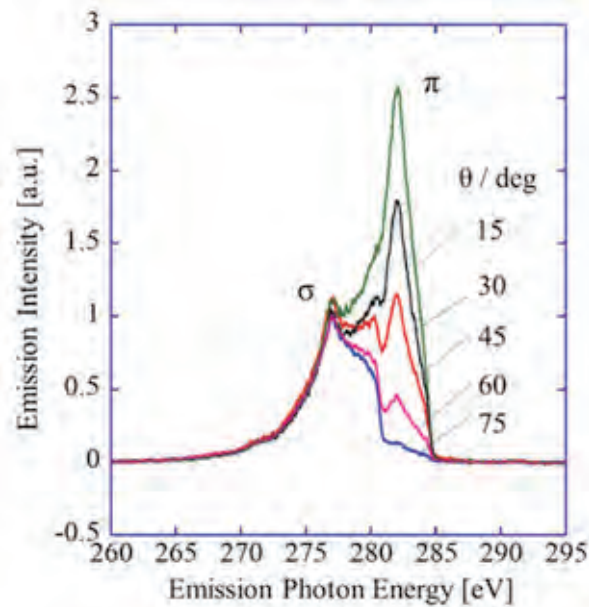


Figure 1. Takeoff-angle dependence of C-K emission spectra for AGraphZ-HOPG at the excitation energy of 310 eV.

Figure 2 shows the takeoff-angle dependence of the intensity of  $\pi$  emission for four type of HOPG samples at the excitation energy of 310 eV, and the curves denote the calculated value using model of ideal graphite structure [13,14]. Because of mosaic spread of HOPG samples, takeoff-angle dependence were found to varied significantly. It is found that as the quality of the crystal structure of the graphite become better, the takeoff-angle dependence of  $\pi$  emission increases.

Figure 3 shows the excitation energy dependence of the integrated intensity of  $\pi$  emission ratio ( $\pi_0 / \pi_{75}$ ) and C-K absorption spectra measured for the AGraphZ-HOPG. It is found from the figure that the integrated intensity of  $\pi$  emission exhibits a large value at 284.5 eV where the sharp  $\pi^*$  absorption occurs and 291.8 eV where a  $\sigma^*$  absorption indicates an increase. Moreover, the integrated intensity of  $\pi$  emission ratio was also found to increase with a gradual curve at the excitation energy of around 310 eV, as reported in Figure 1.

As shown in Figure 3, the large takeoff-angle dependence was observed at 284.5 eV and 291.8 eV, where the large resonant absorptions were also observed. When viewing only the C-K absorption spectra, particularly strong resonant absorption does not appear at 310 eV. However, in the band structure of the fairly high-energy side of the graphite calculated by R.F. Willis et al. [15], there is a portion of the high density of states named “ $\pi_2$ ” at 310 eV (25 eV higher than the Fermi level). The large takeoff-angle dependence of the  $\pi$  emission observed at 310 eV is believed to be related to the resonant photon absorption by the  $C1s \rightarrow \pi_2$  transition.

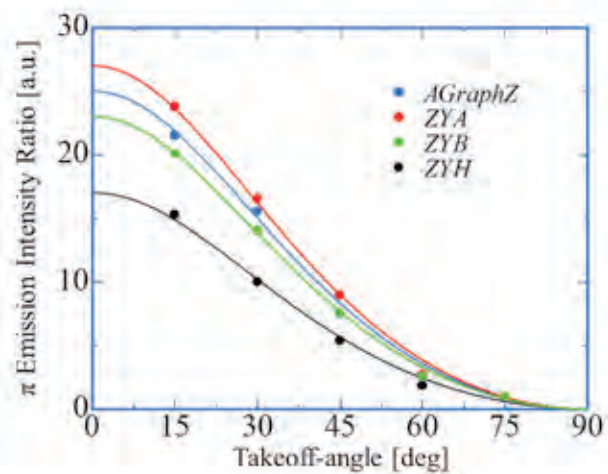


Figure 2. Intensity of  $\pi$  emission ratio ( $\pi_0 / \pi_{75}$ ), for various samples and calculated curve at the excitation energy of 310 eV.

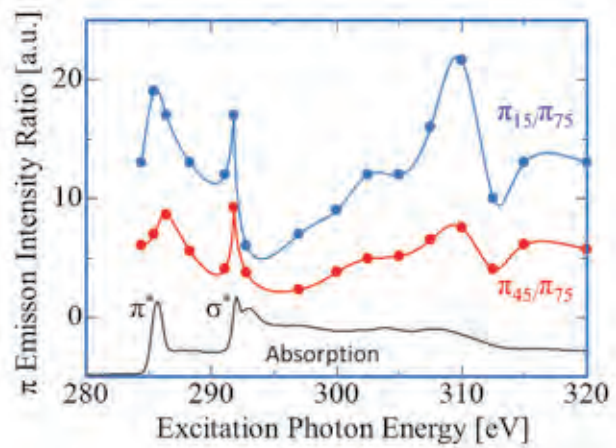


Figure 3. Excitation energy dependence of integrated intensity of  $\pi$  emission ratio ( $\pi_0 / \pi_{75}$ ) for AGraphZ-HOPG.

## Acknowledgments

This work was performed under the auspices of MEXT (Ministry of Education, Culture, Science and Technology, Japan) under the contract subject "Project for Creation of Research Platforms and Sharing of Advanced Research Infrastructure."

## References

- [1] - R. A. Rosenberg, P. J. Love et al., Phys. Rev. B. 33, 4034 (1986).
- [2] - Y. Ma, N. Wassdahl et al., Phys. Rev. Lett. 69, 2598 (1992).
- [3] - Y. Ma, P. Skytt et al., Phys. Rev. Lett. 71, 3725 (1993).
- [4] - P. Skytt, J. Nordgren et al., Phys. Rev. B 50, 10457 (1994).
- [5] - J. A. Carlisle, E.L. Shirley et al., Phys. Rev. Lett. 74, 1234 (1995).
- [6] – J. H. Guo and J. Nordgren, J. Elec. Spectra. Rel. 110, 105 (2000).
- [7] – E. L. Shirley., J. Elec. Spectra. Rel. 110, 305 (2000).
- [8] – A. V. Sokolov, E. Z. Kurmaev et al., J. Exp. Theor. Phys. 77, 108 (2003).
- [9] – V. V. Belavin, A. V. Okotrub et al., J. Exp. Theor. Phys. 103, 604 (2006).
- [10] - L. Zhang, N. Schwertfager et al., Phys. Rev. B. 86, 245430 (2012).
- [11] - M. Niibe and T. Tokushima, AIP Conf. Proc. (SRI2015), in press.
- [12] - M. Niibe et al., Synchrotron Radiation Instrumentation, AIP Conf. Proc. 705, 576 (2004).
- [13] – A.Mansour, S.E.Schnatterly et al., Phys. Rev. B 31, 6521 (1985).
- [14] – A.Mansour, S.E.Schnatterly et al., Phys. Rev. B 36, 9234 (1987).
- [15] - R.F. Willis, B. Fitton, and G. S. Painter, Phys. Rev. B 9, 1926 (1974).

# Irradiation Effect of Oxygen Plasma to TiO<sub>2</sub> Thin Films

Yuma Araki<sup>1</sup>, Masahito Niibe<sup>1</sup>, Retsuo Kawakami<sup>2</sup>, Noritaka Takehira<sup>1</sup>, Yoshitaka Nakano<sup>3</sup>

(Univ. Hyogo<sup>1</sup>, Tokushima Univ.<sup>2</sup>, Chubu Univ<sup>3</sup>)

## Abstract

In our previous study, we found that the TiO<sub>2</sub> thin film prepared by sputtering deposition had oxygen deficiency. Therefore, we irradiated oxygen plasma to the TiO<sub>2</sub> film to decrease oxygen deficiency and improve photocatalytic activity. Photocatalytic activity of the TiO<sub>2</sub> thin films was evaluated by measuring the decomposition rate of organic dye (brilliant blue FCF) with UV irradiation. Composition of the film and irradiation damage were analyzed with X-ray photoelectron spectroscopy (XPS) and near edge X-ray absorption fine structure (NEXAFS) methods, respectively. As a result, O/Ti ratio at the surface of TiO<sub>2</sub> thin films increased when oxygen plasma was irradiated. And there is a high correlation between photocatalytic activity and O/Ti ratio at the surface.

## Introduction

TiO<sub>2</sub> is known as photocatalytic material and used for many products. Therefore, it has been required to improve the photocatalytic performance. In general, TiO<sub>2</sub> are used as powder. However, using it as thin film is superior in transparency and uniformity. In our previous study, we succeeded to produce anatase type TiO<sub>2</sub> thin films by sputtering on a glass substrate<sup>(1)</sup>, and it had photocatalytic activity. However, we found that the sample had less activity than original single-crystal because of oxygen deficiency<sup>(2)</sup>. Therefore, we irradiated TiO<sub>2</sub> thin films with oxygen plasma for intending to decrease oxygen vacancy density and to improve photocatalytic activity.

## Experiment

TiO<sub>2</sub> thin film was coated on a glass substrate using the facing target type magnetron sputtering equipment<sup>(1)</sup>. Then oxygen plasma was irradiated to the films by dielectric barrier discharge system. The flow rate of oxygen gas was 15 ml/min and gas pressure and irradiation time were changed from 10 to 1000 hPa and 60 to 180 min, respectively. In this study, substrate temperature was risen by plasma irradiation. Therefore, to clarify the effect of substrate temperature, we made another sample in which oxygen plasma was irradiated to the films for a short time while heating the substrate by a heater. Oxygen plasma was irradiated with five minutes at gas pressure 1,000 hPa and substrate temperature was changed from 30 to 200 °C.

O/Ti concentration ratio at the surface of TiO<sub>2</sub> thin films was evaluated by X-ray photoelectron

spectroscopy (XPS, Shimadzu ESCA-1000). Etching damage was analyzed by near edge X-ray absorption fine structure (NEXAFS) of the Ti-L absorption edge at the New SUBARU BL-09A. To evaluate photocatalytic activity, TiO<sub>2</sub> sample was soaked in brilliant blue solution and irradiated ultraviolet rays using a black light and measured the dye decomposition rate.

## Result

The treatment time dependence of dye decomposition rate and the O/Ti ratio at the surface of TiO<sub>2</sub> thin film were shown in Fig.1 (a) and Fig.1 (b), respectively. The dye decomposition rate and the O/Ti ratio at the surface of TiO<sub>2</sub> thin films shows good correlation. Photocatalytic activity and O/Ti ratio at the surface of TiO<sub>2</sub> thin films improved when oxygen plasma was irradiated until 60 minutes. However, the O/Ti ratio decreased when the oxygen plasma was irradiated more than 60 minutes. We thought that it was caused by a rise in substrate temperature by the oxygen plasma irradiation.

The heater temperature dependency of dye decomposition rate and O/Ti ratio at the surface of TiO<sub>2</sub> thin film were shown in Fig.2 (a) and Fig.2 (b), respectively. The dye decomposition rate and the O/Ti ratio at the surface of TiO<sub>2</sub> thin films shows good correlation. However, the temperature of substrate increased more than 30 degrees, photocatalytic activity and O/Ti ratio at the surface of TiO<sub>2</sub> thin films decreased. Because diffusivity coefficient increased by substrate temperature rose, oxygen could be diffused.

NEXAFS spectra of the  $\text{TiO}_2$  thin films were shown in Fig 3. Etching damage was not observed in less than 1,000 hPa and at high temperature. Therefore, photocatalytic activity of the  $\text{TiO}_2$  thin films had little influence by etching damage. As a result, we succeeded to control an oxygen deficiency under a certain condition. To improve the photocatalytic activity, we have to suppress the rise in substrate temperature by controlling irradiation of the plasma and need to try further development.

#### 【References】

- 1) K. Tominaga, K. Okada, Y. Miyamoto, S. Ohkuma, K. Shiraishi, K. Kusaka, and T. Hanabusa, *J. Surf. Sci. nanotechnol.* 7, 290 (2009)
- 2) R. Kawakami et al. *submitted to J. Vac. Sci. Technol. A* (2015)

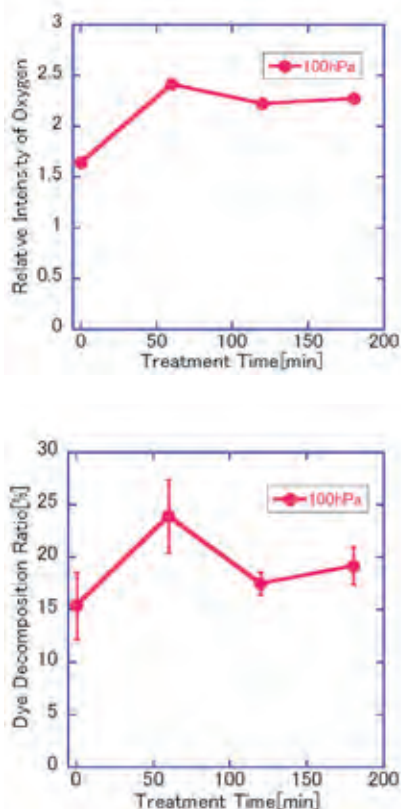


Fig.1 dye decomposition rate (a) and O/Ti ratio (b) at the surface of  $\text{TiO}_2$  thin films

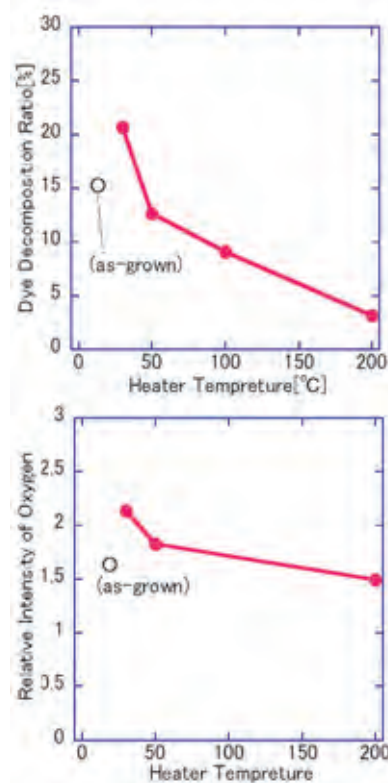


Fig.2 dye decomposition rate (a) and O/Ti ratio (b) of  $\text{TiO}_2$  thin film treated with increasing temperature at the surface

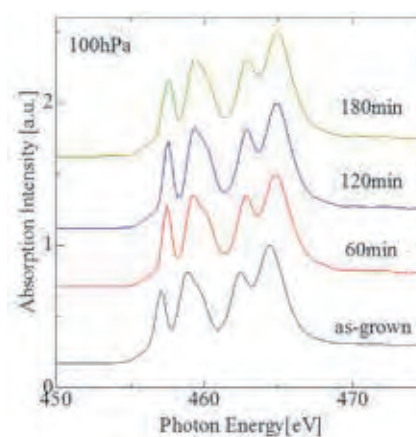


Fig.3 Ti-L NEXAFS spectra of  $\text{TiO}_2$  thin films treated at 100 hPa and various treatment time

# Modification of horizontally aligned multi-walled carbon nanotube films by Ar ion beam irradiation and its characterization by soft x-ray spectroscopy

S. Honda<sup>1,7</sup>, M. Niibe<sup>2</sup>, M. Terasawa<sup>2,7</sup>, R. Hirase<sup>3</sup>, H. Yoshioka<sup>3</sup>, H. Izumi<sup>3</sup>, K. Niwase<sup>4</sup>, E. Taguchi<sup>5</sup>, T. Harada<sup>2</sup>, Y. Muramatsu<sup>1</sup>, K.-Y. Lee<sup>6</sup> and M. Oura<sup>7</sup>

<sup>1</sup>Graduate School of Engineering, University of Hyogo, 2167 Shosha, Himeji, Hyogo 671-2280, Japan

<sup>2</sup>Laboratory of Advanced Science and Technology for Industry, University of Hyogo, 3-1-2 Kouto, Kamigori, Ako, Hyogo 678-1205, Japan

<sup>3</sup>Hyogo Prefectural Institute of Technology, Kobe 654-0037, Japan

<sup>4</sup>Hyogo University of Teacher Education, Kato, Hyogo 673-1494, Japan

<sup>5</sup>Osaka University, Ibaraki, Osaka 567-0047, Japan

<sup>6</sup>Department of Electronic Engineering, National Taiwan University of Science and Technology, No. 43, Sec. 4, Keelung Rd., Taipei 106, Taiwan

<sup>7</sup>RIKEN SPring-8 Center, Sayo, Hyogo 679-5148, Japan

## Abstract

Low energy Ar ions were irradiated to horizontally aligned multi-walled carbon nanotube (HA-MWCNT) films using an electron cyclotron resonance ion source at SPring-8 BL17SU. Soft X-ray photoelectron spectroscopy (XPS) and soft X-ray absorption spectroscopy (XAS) measurements were performed to characterize electronic states of the irradiated HA-MWCNT films at BL17SU of SPring-8 and BL10 of NewSUBARU.

## Introduction

Nanostructured carbon materials such as carbon nanotubes (CNTs) and graphenes have been extensively studied toward realization of next-generation nanodevice applications. The morphology of the CNTs strongly relates to the device performance. For example, horizontally aligned multi-walled CNTs (HA-MWCNTs) have been demonstrated to be applicable to the nanodevices such as sensors, and LSI interconnects. On the other hand, irradiating nanostructured carbon materials with energetic charged particles, such as ions and electrons, is thought to be capable of tailoring their structure and properties, and can be applied to process of nanodevice fabrication. It was reported that the electrical transport properties and structural properties of the individual CNT were modified by the electron irradiation. Thus, many researches were focused on the charged particle irradiated individual CNT. However effects of ion irradiation on the structural properties and/or electronic states of ensembles of HA-MWCNT films have not been fully understood.

## Experimental

HA-MWCNT films were grown by catalytic thermal chemical vapor deposition. Electron cyclotron resonance ion source at SPring-8 BL17SU [1] was employed for irradiation of singly charged Ar ions with a energy of 5.0 keV. The structural properties of irradiated HA-

MWCNT films were characterized by scanning electron microscopy (SEM), Raman spectroscopy and transmission electron microscopy (TEM). In addition, soft X-ray photoelectron spectroscopy (XPS) and soft X-ray absorption spectroscopy (XAS) measurements were performed at BL17SU at SPring-8 [2] and BL10 at NewSUBARU [3], respectively.

## Results and Discussion

Figure 1 shows the C K-edge XAS spectra of the HA-MWCNT films as-prepared and irradiated by Ar ions of different fluences. The intensity was normalized using the  $\sigma^*$  peak height at 292 eV. The incident angle ( $\alpha$ ) of the SR beam to the sample plane was varied from 45° to 90° (normal incidence). As shown in Fig. 1(a), it is apparent that as-prepared HA-MWCNT films shows an inverse dependence of the  $\pi^*$  peak height at 285 eV with increasing  $\alpha$ . On the other hand, for the irradiated HA-MWCNT films, there is no  $\alpha$  dependence of the  $\pi^*$  peak height with increasing Ar ion fluence. These results indicate the amorphization of the MWCNTs after Ar ion irradiation.

Figure 2 shows the C 1s XPS spectra of the HA-MWCNT films as-prepared and irradiated by

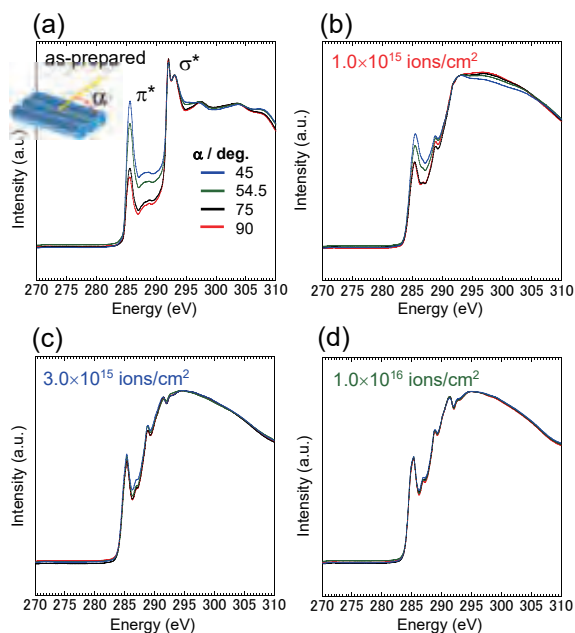


Fig. 1 C K-edge XAS spectra of the irradiated HA-MWCNT films.

Ar ions of different fluencies, with HOPG and carbon black (CB, N330) as references. It was found that the shape of C 1s XPS spectra of HA-MWCNT films was changed from asymmetry to near symmetry after Ar ion irradiation. The spectra of carbon black (amorphous carbon) are similar to those of the irradiated HA-MWCNT films. Since carbon black is composed of  $sp^2$ -hybridized carbon crystallites,  $sp^2$ -hybridized carbon hexagonal ring network in the MWCNT may be destroyed and nonbenzenoid rings and edge carbon atoms may be formed after the irradiation [4].

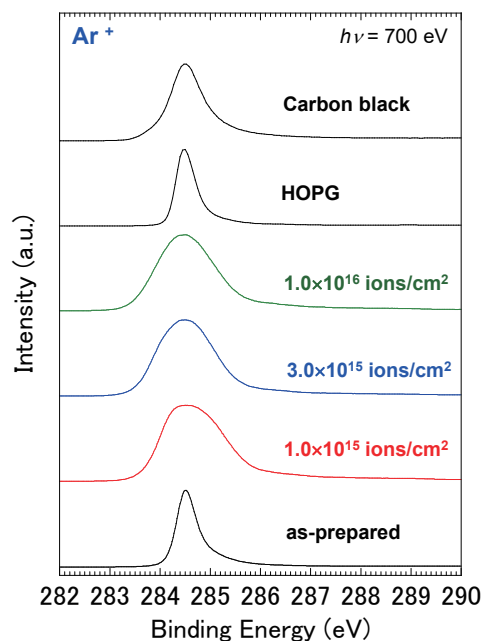


Fig. 2 C 1s XPS spectra of the irradiated HA-MWCNT films.

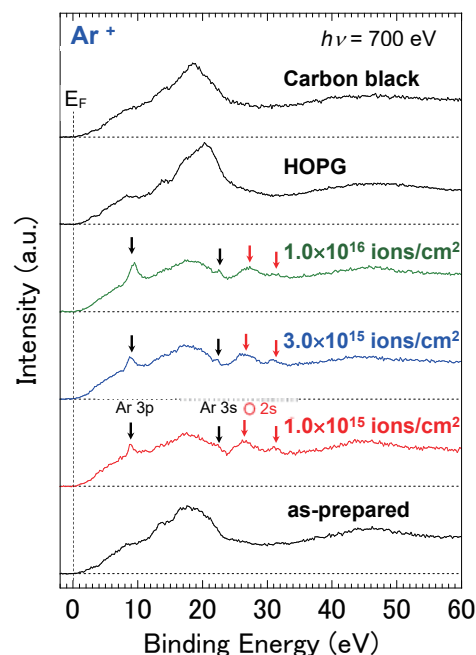


Fig. 3 C valence band XPS spectra of the irradiated HA-MWCNT films

Moreover, as shown in Fig.3, additional peaks appeared in C valence band XPS spectra after the irradiation. It is also worth noting that C valence band XPS spectra in the vicinity of the Fermi level of as-prepared and irradiated HA-MWCNT films have different features. These peaks in Fig. 3 can be assigned to O 2s electrons [5]. Compared with C 1s spectra, valence band spectra were more sensitive to chemical environment. The valence band spectra showed that there were two different chemical states of oxygen. The oxidation of C atoms may be attributed to the defect on the MWCNT surface induced by the irradiation. Furthermore, C K-edge and O K-edge XAS spectra of the irradiated HA-MWCNT films were compared with standard aromatic compounds having various oxygenated functional groups (fingerprint method [6]). As a result, carboxyl groups are considered to be introduced onto the MWCNTs after the irradiation.

#### References

- [1] M. Oura *et al.*, *J. Synchrotron Radiat.* **5**, 1058 (1998).
- [2] K. Horiba *et al.*, *J. Electron Spectrosc. Relat. Phenom.* **144–147**, 1027 (2005).
- [3] Y. Muramatsu *et al.*, *Adv. X-Ray Chem. Anal.*, Japan **43**, 407 (2012).
- [4] R. D. Heidenreich *et al.*, *J. Appl. Cryst.* **1**, 1 (1968).
- [5] Y. Xie *et al.*, *Surf. Sci. Spectra* **1**, 271 (1993).
- [6] Y. Muramatsu *et al.*, *Surf. Rev. Lett.* **9**, 267 (2002).

# Development of High-Reflective W/Si-multilayer Diffraction Grating for the Analysis of Fluorine Materials

°Masaki Kuki<sup>1</sup>, Tomoyuki Uemura<sup>2</sup>, Masato Yamaguchi<sup>1</sup>, Tetsuo Harada<sup>1</sup>,  
Takeo Watanabe<sup>1</sup>, Yasuji Muramatsu<sup>2</sup>, and Hiroo Kinoshita<sup>1</sup>

<sup>1</sup>Center for EUV Lithography, LASTI, University of Hyogo,  
1-1-2 Kouto, Kamigori, Ako-gun, Hyogo, Japan

<sup>2</sup>Graduate School of Engineering, University of Hyogo,  
2167 Shosha, Himeji, Hyogo, Japan  
kuki@lasti.u-hyogo.ac.jp

For the analysis of fluorine materials and 3d transition metals by soft-x-ray absorption spectroscopy, A new diffraction grating with multilayer coating was installed at the BL-10 beamline of the NewSUBARU synchrotron light source. The target photon energy range of this grating is from 500 eV to 1,000 eV, which includes absorption edges of fluorine and 3d transition metals. The beam intensity of BL-10 in this range was very low due to low reflectance of the diffraction grating for the usage of monochromator. In order to obtaining high reflectance, we developed wideband W/Si multilayer and this multilayer was coated on a new diffraction grating. The reflectance of this multilayer was approximately 13-times higher than that of previous Ni single layer at the fluorine absorption energy edge of 697 eV. The beam intensity at the energy of 697 eV using the new diffraction grating was over 40 times stronger than that using the previous Ni-coated diffraction grating. As the result, using the new diffraction grating, it can be observed that the high-quality absorption spectrum of EUV resist at the absorption edge of fluorine and standard materials of 3d transition metals. The results show that the W/Si multilayer coating significantly improved the performance of the grating at the target energy range.

**Keywords:** W/Si multilayer, wideband multilayer grating, synchrotron light, soft x-ray absorption spectroscopy

## 1. Introduction

Soft-x-ray absorption spectroscopy (XAS) is widely used for the analysis of light element materials, which measures absorption spectrum near the absorption edges. The XAS system at BL10 beamline of NewSUBARU synchrotron light source [1-4]. For example, deterioration mechanism of tire rubber and engine oil were analyzed [2, 3]. In addition, we analyzed the chemical reaction of the extreme ultraviolet (EUV) chemically amplified (CA) resist using BL-7 XAS system [5]. We measured XAS spectrum around the fluorine absorption energy edge of 697 eV to evaluate the decomposition reaction of photoacid generator (PAG) of CA EUV resist during EUV exposure. However, this previous result had large noise due to

low photon intensity in this energy region. In order to develop of high-sensitive EUV resist, it is necessary to measure the fluorine energy regions with low noise in and sufficient energy resolution. The main reason of the poor intensity own to the low reflectance of the diffraction grating in BL-7 and BL-10 beamlines, which had a small deviation angle of 168° for the diffraction grating.

Since in general, a CA resist is easy to deteriorate, it is important to analyze the resist by XAS near the resist process equipment for resist coating, baking, developing spin coater, developer, and hot plate in the clean room. Thus a new diffraction grating which had high reflectance on 697 eV for the usage of XAS at BL-10 beamline of NewSUBARU should be installed. For considering general usage of

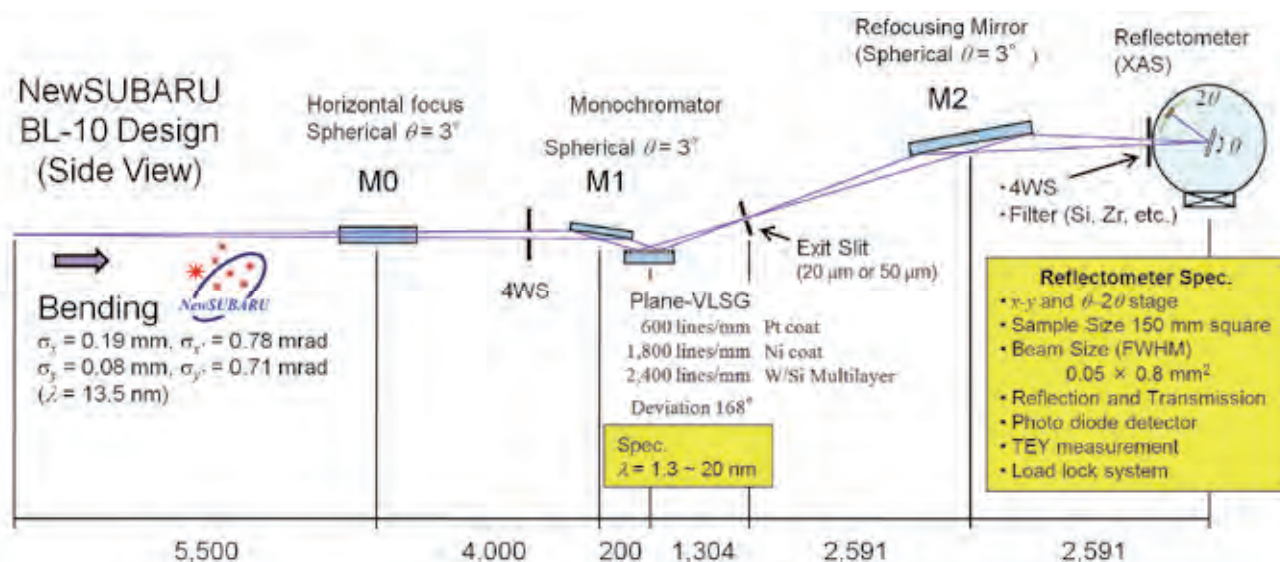


Fig.1. Schematic layout of BL-10 of NewSUBARU.

BL-10, target energy of the new grating was set from 500 eV to 1,000 eV, which includes absorption edges of fluorine and 3d transition materials. High reflectance of the new grating is essential for the precise reaction mechanism analysis of the resist for the semiconductor devices.

The platinum coated grating would have not enough reflectance due to the small deviation angle of the grating for BL-10. For example in the soft-x-ray emission spectroscopy, wideband multilayer coating significantly improved reflectance of a grating [6]. Thus, we developed a multilayer coating and it was coated on the grating in this study to enhance the reflectance in the target energy region. The beam intensity and XAS spectrum were evaluated with the new multilayer-coated grating.

## 2. Experimental

### 2.1 Design of beamline BL-10

The optical layout of BL-10 of NewSUBARU is shown in Fig.1. This beamline was originally designed for reflectometry of EUV optics, where a reflectometer is located at the end of the beamline. The vacuum chamber for the reflectometer was used for the XAS measurement. The entrance slit design is slitless. The M0 mirror is a concave mirror with a grazing angle of incidence (GAOI) of 3°, which horizontally focuses on the sample which was settled in the XAS chamber with magnification of three. The acceptance angle of the M0 is 5 mrad in

the horizontal direction. The monochromator type which was utilized for BL-10 beamline is the plane varied line-space grating (VLSG), and it was described the paper written by Hettrick and Underwood [7]. The reflected light by the spherical concave M0 mirror focused on the exit slit in the vertical direction by M1 concave mirror and diffraction grating. Two gratings were installed in the monochromator, which had groove densities of 600 mm<sup>-1</sup> (G1) and 1,800 mm<sup>-1</sup> (G2). The deviation angle of the grating is small as 168°, because BL-10 was originally designed for low-energy use of the research for EUVL energy region. The G1 grating was originally installed for the EUV research. The G2 grating was installed for XAS measurement in 2009. In this study, a new grating with groove density of 2400 mm<sup>-1</sup> (G3) was installed. The exit slit is relayed up to 5.2 m downstream at unity magnification by a vertical refocusing mirror, where the focusing size is approximately 0.05 × 0.8 mm<sup>2</sup> on a sample. The all GAOI of the three glancing spherical mirrors such as M0, M1, and M2 is 3°. The mirrors were coated with single layer of platinum with the thickness of 50 nm. The deviation angle of the grating is 168°, and was corresponded to GAOI of 6° with specular-reflection condition. The G2 grating was coated with single layer of Ni with the thickness of 100 nm. The calculated reflectance of the glancing mirrors and G2 grating are shown in Fig.2. These two data were calculated value using the IMD software [8] in this paper. The

surface roughness was assumed to be 1 nm. Since the reflectance of the glancing mirrors was approximately 30% at the photon energy of 697 eV, the reflectance of the grating requires higher than 10% in the target energy region. However, since the reflectance of the G2 grating was less than 1% in the energy range higher 700 eV, the beam intensity becomes very low at the sample surface for XAS experiment. Thus, the high reflective coating is needed to increase the light intensity. And, the groove height of 4.2 nm for the G3 grating was optimized to achieve high diffraction efficiency at the photo energy of 697 eV.

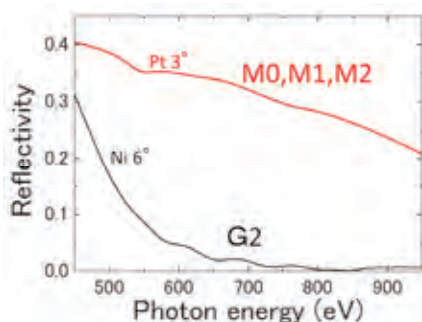


Fig.2. Calculated reflectance of BL-10 optical components of the mirrors and the grating (G2).

### 2.2. Design of multilayer coating

In this study, a W/Si-multilayer coating was developed for the G3 grating to enhance the reflectance in the target photo energy region. The material pair of the multilayer was chosen to W/Si because of high optical contrast and low absorption to achieve high reflectance. Figure 3 shows the calculated reflectance of aperiodic W/Si multilayer, periodic W/Si multilayer, Pt single layer, and Ni single layer, with GAOI of 6°. Platinum is generally used for mirror coating of glancing mirrors for the beamline of the synchrotron. Surface roughness of the single layer was assumed to be 1 nm with the thickness of 50 nm. Roughness of the multilayer interface was assumed to 0.5 nm. The periodic W/Si multilayer film had 10 periods of 3.0-nm-thick W layer and 7.0-nm-thick Si layer. Reflectance of this periodic W/Si multilayer was approximately 30% at the photon energy of 697 eV, and has more than 20% in the target photo energy region. As a results, an aperiodic design had wideband reflectance as shown in Fig. 3, and the structural design of the

W/Si multilayer is shown in Fig. 4. As a results, it was achieved that high reflectance the diffraction grating of over 10% in the whole target energy region by coating an aperiodic-designed W/Si multilayer.

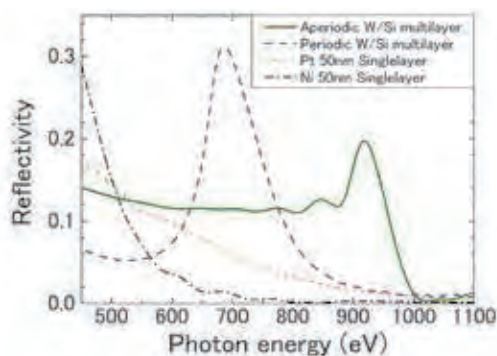


Fig. 3. Calculated reflectance of single metal layers and W/Si multilayers for the grating coating.

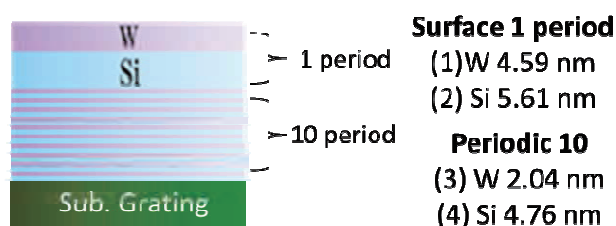


Fig.4. Structural design of the wideband W/Si multilayer.

The multilayer had aperiodic structure which consisted of one periodic multilayer coated on ten periodic multilayer. And the multilayer thickness was optimized to obtain the high reflectance in the photon energy target region. The periodic structure reflects well in energy region from 800 to 1,000 eV, where the period thickness was optimized to reflect this region. And, the top two layers widely reflects low-energy beam below 800 eV, because reflectance of tungsten single layer was enough high in this low energy region. Thicknesses of the two top layers were optimized to make positive interference of the reflections from the top surfaces (vacuum/W, W/Si, Si/W and W/Si). Further, the thickness of this multilayer was easy to control in deposition because the thickness of the period structure was able to measure with high accuracy by x-ray reflectivity (XRR) measurement.

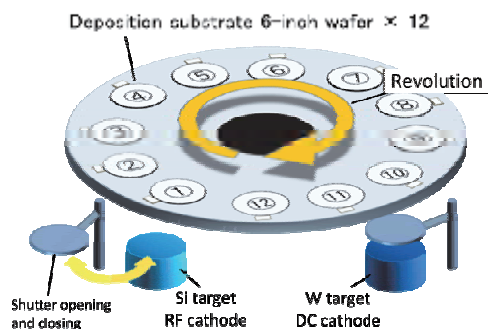


Fig.5. Schematic view of the magnetron-sputtering deposition system.

### 2.3 Deposition system

The W/Si multilayers were prepared by a magnetron-sputtering deposition system as shown in Fig. 5. A 6-inch RF cathode was used for Si layer deposition, and a 6-inch DC cathode was used for W layer deposition. Twelve samples of 6-inch Si wafer were usually settled by large holding plate with 830 mm in diameter. Each 6-inch-wafer sample was settled at the distance of 300 mm from the rotation center on the holding plate. For each deposition layer, the deposition layer thickness was controlled by the rotation speed of the holding plate. The deposition system was pumped down to the vacuum pressure higher than  $1.5 \times 10^{-4}$  Pa, and typically the deposition was carried out at the Ar pressure of 1.7 Pa. When W/Si multilayer was deposited on a Si wafer at the Ar pressure of 0.17 Pa, the film was peeled off due to high film stress. The Ar gas pressure was chosen to 1.7 Pa to reduce the film stress. At this Ar pressure condition, the deposited multilayer did not peel off.

For the development of the multilayer, a Si wafer was used as a substrate. The grating substrate is 150 mm in length, 30 mm in width, and 25 mm in thickness. And the groves were patterned in the region of 130 mm (L)  $\times$  22 mm (W). In deposition, the grating substrate was set the groove region parallel to the rotation direction of the holding plate.

### 2.4. Measurement condition of reflectance

Reflectance of W/Si multilayer on a Si wafer was measured at the reflectometer of BL-10. Reflectance of a 76.5-nm-thick Ni and 52.9-nm-thick Pt single layers were also measured. The G2 grating was chosen. When the width of the exit slit was set to be 50  $\mu$ m, the monochromated photon energy

resolution of 600 can be achieved around the photo energy of 700 eV. A photodiode (IRD SXUV-100) was used as a detector to measure the beam intensity. GAOI was  $6^\circ$ . A 1- $\mu$ m-thick Cu filter was installed to cut the high order light from the grating. The reflectance in photon energy range from 500 to 930 eV, because absorption edge of the Cu filter was around 930 eV.

### 2.5. XAS measurement of EUV resist

The sample was poly hydroxyl styrene-co-tert-butylacrylate (PHS-TBA) resist with a photoacid generator of tri-phenyl sulfonium nonaflate (TPS-nonaflate), which measured in previous paper [5]. The resist film thickness of 50 nm was spin-coated on a wafer. EUV light of 91.8 eV with the G1 grating was exposed on the sample with seven exposure dose condition from 0 to 98 mJ/cm<sup>2</sup>. XAS spectrum was measured by total electron yield (TEY) method. The seven exposed position was measured around fluorine absorption edge of 650 to 730 eV with the G3 grating. The exit-slit width was 20  $\mu$ m, where the energy resolution was 1,300 around 700 eV.

## 3. Results and discussions

Figure 6 shows the measurement result of the reflectance. At the photon energy of 697 eV for the fluorine 1s core level absorption edge, the reflectance of the Ni single layer, the Pt single layer and the wideband W/Si multilayer were about 0.7%, 2.7% and 13.4%, respectively. The reflectance of the W/Si multilayer is 13 times higher than that of Ni single layer. And since the W/Si multilayer had high reflectance of more than 10% for the photon energy region from 500 to 930 eV, this multilayer was coated on the G3 grating substrate and it was installed in BL-10 for the soft x-ray absorption spectroscopy.

Figure 7 shows the beam intensity measured by the photodiode with the G2 and the G3 grating without filters. The exit-slit width was 10  $\mu$ m. The electron current measured by the photodiode with the G3 diffraction grating at the photon energy of 697 eV was 69 nA and the photodiode current was 40 times larger than that with the G2 diffraction grating. In addition, the photon energy region from 500 to 1,000 eV, the photodiode current was

significantly improved and was more than 50 nA. This result shows the largest photon number can be obtained using the G3 diffraction grating in the target photon energy region.

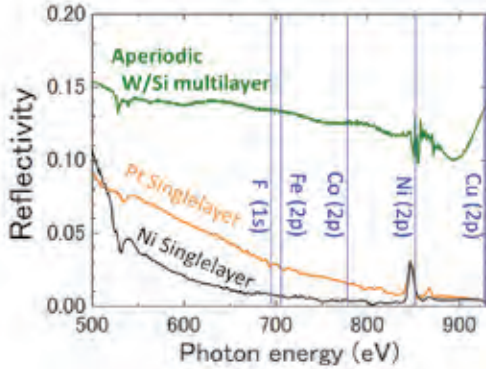


Fig.6. Reflectance of the wideband W/Si-multilayer, the Ni single-layer, the Pt single-layer samples

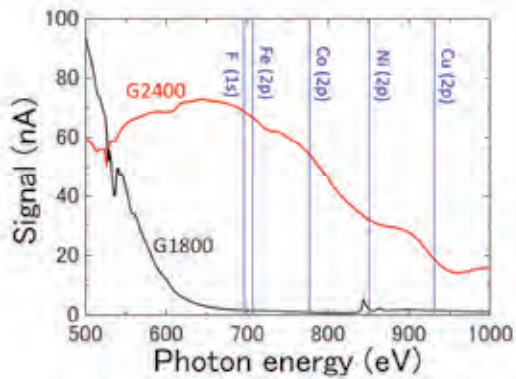


Fig.7. Beam intensity with G2 and G3 gratings

Figure 8 shows the result of TEY-XAS measurement of the EUV CA resist material. The absorption structure of fluorine 1s core level was measured with a high signal-to-noise ratio. We successfully observed the peak height of the absorption spectra decreased slightly with increasing the EUV exposure dose. This is indicated that the fluorine 1s core level of the anion of photo acid generator in the EUV CA resist decomposed during EUV exposure. Figure 9 shows the 1s core level absorption spectra measured by TEY-XAS method for the fluorine of the anion of PAG in the EUV resist and 3d-transition-metal compounds. All the spectra were measured with a high signal-to-noise ratio. The monochromator had enough energy resolution to evaluate the chemical bonding for the compounds. In addition to the target energy region, the absorption spectrum of Zn 1s core level around

the photo energy of 1,020 eV was clearly resolved. The TEY-XAS method using BL-10 beamline has a good capability to measure the absorption spectra to evaluate chemical bonding in the photon energy region from 500 to 1100 eV.

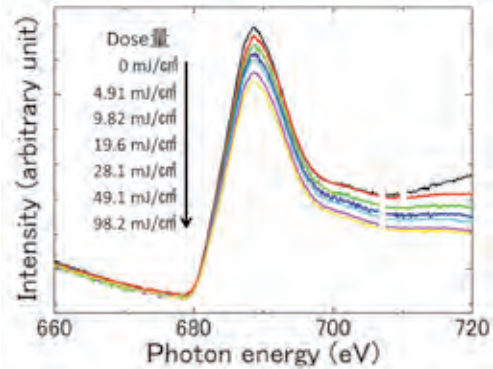


Fig.8. TEY-XAS measurement result of the resist at fluorine absorption edge

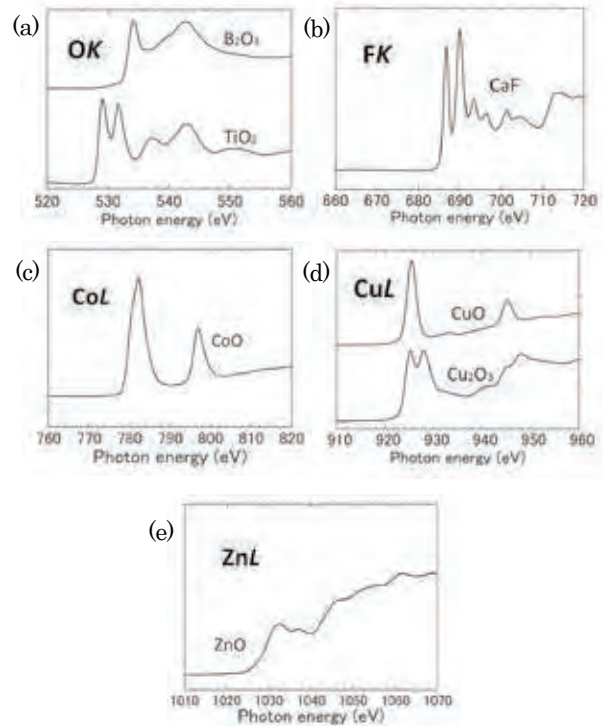


Fig.9. TEY-XAS measurement result of the standard samples such as (a)  $B_2O_3$  and  $TiO_2$ , (b)  $CaF$ , (c)  $CoO$ , (d)  $CuO$  and  $Cu_2O_3$ , and (e)  $ZnO$  compounds.

#### 4. Conclusions

We developed high reflective and wideband multilayer coating for the photon energy from 500 to 1,100 eV. This coating had aperiodic structure of W/Si with 11 periods. The reflectance of this coating

was 13 times higher than the previous Ni single layer coating, and was over 10% in the target photon energy region. We deposited the wideband multilayer on the grating substrate of G3, which was employed as a monochromator of BL-10 beamline for the TEY-XAS measurement method. The beam intensity was significantly improved more than 40 times at the absorption edge energy of fluorine 1s core level. And, high photon intensity can be achieved in the target photon energy region. We measured the resist sample using TEY-XAS method. The fluorine decomposition reaction of the resist was clearly measured with good signal-to-noise ratio. And, the absorption structures of standard  $3d$  transition metal compounds were also resolved clearly. This result shows BL-10 beamline had high capability of XAS measurement in the photon energy region from 500 to 1100 eV with a sufficient energy resolution and high beam intensity. In addition, the reflectometer of BL-10 can measure the reflectance of the metal coatings on an optical element in this photo energy region, and it can be strongly contributed the development of soft x-ray optics. The well-developed W/Si aperiodic multilayer diffraction grating can provide significant improvement of beamline performance for the high energy photon region.

## References

1. Y. Muramatsu, A. Tsueda, T. Harada, and H. Kinoshita, *Adv. X-Ray Chem. Anal. Jpn.* **43**, 407 (2012) (in Japanese).
2. Y. Muramatsu, A. Tsueda, T. Uemura, T. Harada, and H. Kinoshita, *Adv. X-Ray Chem. Anal. Jpn.* **44** (2013) 243 (in Japanese).
3. T. Uemura, Y. Muramatsu, K. Nanbu, T. Harada, and H. Kinoshita, *Adv. X-Ray Chem. Anal. Jpn.* **45** (2014) 269 (in Japanese).
4. T. Uemura, Y. Muramatsu, K. Nanbu, D. Fukuyama, M. Kuki, T. Harada, T. Watanabe, and H. Kinoshita, *Adv. X-Ray Chem. Anal. Jpn.* **46** (2015) (in Japanese, in printing).
5. K. Emura, T. Watanabe, M. Yamaguchi, H. Tanino, T. Fukui, D. Shiono, Y. Haruyama, Y. Muramatsu, K. Ohmori, K. Sato, T. Harada, and H. Kinoshita, *J. Photopolym. Sci. Technol.* **27** (2014) 631.
6. T. Imazono, M. Koike, N. Hasegawa, M. Koeda, T. Nagano, H. Sasai, Y. Oue, Z. Yonezawa, S. Kuramoto, M. Terauchi, H. Takahashi, N. Handa, and T. Murano, *J. Phys: Conference Series* **425** (2013) 152008.
7. M. C. Hettrick and J. H. Underwood, *AIP Conf. Proc.* **147** (1986) 237.
8. D. L. Windt, *Comput. Phys.* **12** (1998) 360.

# Development of the molecular orientation analysis by soft X-ray absorption spectroscopy (soft XAS)

Eiji Takahashi<sup>1</sup>, Katsuya Imanishi<sup>1</sup>, Shogo Suehiro<sup>1</sup>, Yoshiyuki Suzuri<sup>2</sup>,  
Yuki Ota<sup>3</sup>, Yasuji Muramatsu<sup>3</sup>

<sup>1</sup> Sumika Chemical Analysis Service, Ltd.,  
1-135, Kasugade-Naka 3-chome, Konohana-ku, Osaka 554-0022, Japan

<sup>2</sup> Innovation Center for Organic Electronics, Yamagata University,  
1-808-48 Arcadia, Yonezawa, Yamagata 992-0119 Japan

<sup>3</sup> Graduate School of Engineering, University of Hyogo,  
2167, Shosha, Himeji, Hyogo 671-2280 Japan

## Abstract

Soft X-ray absorption spectroscopy (soft XAS) can detect light elements at high sensitivity. In this study, about a material used for organic light-emitting diodes, was analyzed for its molecular orientation by using XAS. We were able to determine the orientation angle by confirming horizontal orientation of the molecules from the measurement results using XAS. As a result, we have developed the analysis method of organic thin films with depth information, which will contribute to the optimization of manufacturing process.

## Introduction

Organic multilayered thin films are used for organic light-emitting diodes and organic solar cells. In the manufacturing process of these films, it is important to control accurately the thickness of each layer in nm because the mixing ratio between the constituents and their states affect the performance of these films. Controlling of their molecular orientation has recently gaining attention as it would lead to the improvement of thin film properties<sup>[1, 2]</sup>. Spectroscopic ellipsometry is known as a handy and effective method for determining the molecular orientation of single-layer thin films<sup>[1]</sup>. For thin films of several tens of nm in thickness, multilayered structure or mixed layers, whose analysis is more difficult due to detection sensitivity and effects from multiple elements, new evaluation methods are required.

Soft X-ray absorption spectroscopy (soft XAS) can detect light elements at high sensitivity. A spectrum generated by this method reflects the electronic state of each element. Based on this spectrum, mixture ratio can be calculated by using a standard spectrum for each compound and molecular orientation can be determined by measuring incident angle dependence<sup>[3, 4]</sup>. The information depth is expected to be shallow because soft X-rays have lower penetrabilities.

In this study, B3PyMPM (4,6-bis(3,5-di-3-pyridylphenyl)-2-methylpyrimidine), a material used for electron transport layer, was analyzed for its molecular orientation by using XAS.

## Experiment

Fig. 1 shows the organic materials used and the molecular structure. The molecular orientation was analyzed using a thin film prepared by vapor deposition of B3PyMPM on a silicon wafer (Fig. 1a).

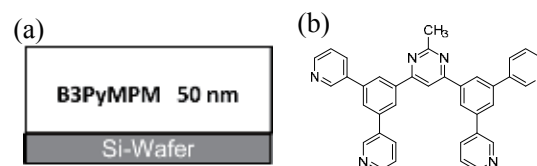


Fig. 1 (a) The structure of thin films, and (b) Molecular structure of the B3PyMPM

XAS measurements were conducted at BL10 in the New SUBARU. The specimen surfaces were irradiated with microbeam X-ray to obtain spectra by measuring the photoelectric current in the specimens with an ammeter (Total electron yield). The measurements were performed across the nitrogen k-edge and carbon k-edge (N K and C K). Each signal intensity was normalized by the intensity of peaks ( $\sigma^*$ ) generated by nitrogen (or carbon)  $\sigma$  bonds.

## Results and Discussion

Fig. 2 shows the XAS spectra of B3PyMPM thin film obtained for different incident angles ( $\theta$ ) of soft X-ray to the substrate.

At the N K edge of the spectra, the ratio of signal intensity to the peak intensity generated by  $\pi$  bonds between nitrogen and carbon became higher as the

incident angle of X-ray decreased (smaller  $\theta$ ). This was because the polarization direction of X-ray coincided with the direction of  $\pi$  orbital, indicating that the main skeleton, pyrimidine, as well as the four pyridine rings at molecular ends composing B3PyMPM were oriented horizontally to the substrate.

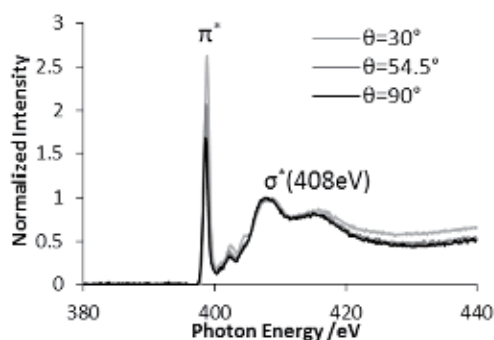


Fig. 2 XAS spectra of B3PyMPM thin film for different X-ray incident angles(N K edge)

These molecular orientations are in agreement with the results of spectroscopic ellipsometry [2].

Fig. 3 shows the signal intensity ratio of  $\pi^*$  to  $\sigma^*$  plotted against the soft X-ray incident angles. We referred to a method explained in a previous study [3] in calculating the angle ( $\alpha$ ) between the normal vector to the substrate surface and the  $\pi^*$  orbital that is perpendicular to the molecular plane, assuming that all aromatic rings of B3PyMPM were on the same plane. In this calculation, molecular orientation to the substrate surface would be horizontal if  $\alpha < 54.7^\circ$  (the magic angle), perpendicular if  $\alpha > 54.7^\circ$ , and non-oriented if  $\alpha = 54.7^\circ$ .

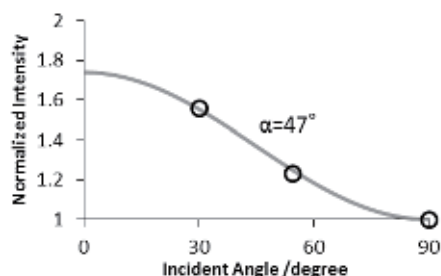


Fig. 3 Molecular orientation of B3PyMPM thin film(N K edge)

The calculation results were  $\alpha = 47^\circ$  for N K edge, confirming horizontal orientation of the

molecules.

## Conclusions

Up until now, there has been only few methods available for accurate assessment of organic thin film's molecule orientation. In this study, XAS proved to be capable of analyzing materials used for organic light-emitting diodes. Also, calculations of information depth enabled the analysis of organic thin films with depth information, which will contribute to the optimization of manufacturing process.

## References

- [1] D. Yokoyama: J. Mater. Chem., 21, 19187 (2011).
- [2] D. Yokoyama, H. Sasabe, Y. Furukawa, C. Adachi, J. Kido: Adv. Funct. Mater., 21, 1375 (2011).
- [3] F. Zheng, B.-N. Park, S. Seo, P. G. Evans, F. J. Himpsel: J. Chem. Phys., 126, 154702 (2007).
- [4] Y. Muramatsu, E. M. Gullikson: 'Advances in X-Ray Chemical Analysis, Japan' (in Japanese), 42, 267 (2011).

# Local structure analysis of graphitic carbon materials by X-ray absorption spectroscopy

Kentaro Murayama<sup>1</sup>, Taizo Haruyama<sup>1</sup>, Rie Kazihara<sup>1</sup>, Yasuji Muramatsu<sup>2</sup>  
<sup>1</sup>MIKUNI COLOR, Ltd., <sup>2</sup>University of Hyogo

## Abstract

To characterize graphitic carbon materials by soft X-ray absorption spectroscopy, XANES of many graphitic carbon samples were measured in BL10 at the NewSUBARU. It has been found that the relationship between the  $\pi^*$  peak width and height in C *K*-XANES provides information on local structure of hexagonal carbon layers. Hence, we have proposed the relationship which is named as “ $\pi^*$  peak map” for the significant index of local structure analysis of graphitic carbon materials.

## Introduction

Graphitic carbons have attracted much attention for energy and transparent electrode materials because of their superior electrical conductivity and low cost. The electrical conductivity is dependent on the  $\pi$  electron states of  $sp^2$ -carbon atoms in hexagonal carbon layers. It is therefore required to develop a measurement technique for obtaining some information of local structure. We have previously found that X-ray absorption near-edge structure (XANES) in the C *K* region provides information of edge carbon atoms and/or nonbenzenoid rings in the hexagonal carbon layers [1]. In this study, we have measured C *K*-XANES of many industrial graphitic carbon materials and deeply discuss the  $\pi^*$  profiles.

## Experiments

Samples were commercially available graphite, carbon nanotube (CNT), and carbon black (CB) of furnace carbon black, acetylene black, and Ketchen black. Physical properties of them are listed in Table 1. XANES measurements were carried out at BL10 in the NewSUBARU SR facility. Powder samples of the carbon materials were pressed and held on indium substrates, and total electron yield (TEY) was measured by monitoring the sample photocurrent in the C *K* region. Incident angle of SR beam to the sample plane was turned at the magic angle of  $54.5^\circ$ . A  $1800\text{ mm}^{-1}$  grating and a  $20\text{ }\mu\text{m}$  slit were used for the C *K*-XANES measurements.

## Results and Discussion

Figure 1 shows the C *K*-XANES of the carbon samples and the highly oriented pyrolytic graphite (HOPG) as a reference. Compared to HOPG, the  $\pi^*$  peak profile of carbon samples is generally broader. Such the broader  $\pi^*$  peak profile should reflect the  $\pi$  electron state variation of carbon atoms in hexagonal carbon

layers. To clearly display the broader portion in  $\pi^*$  peak of carbon samples, subtracted spectra between each carbon sample and HOPG are plotted on XANES with bold lines. The broader portion can be shown as two peaks at 284.5 eV and 286.2 eV which are named as peak *a* and *b*, respectively. From our previous spectral analyses by using the first-principle calculation code, CASTEP, such the peaks *a* and *b* can be explained by edge carbon atoms in hexagonal carbon layers [2].

To further discuss the  $\pi^*$  peak profile, we have plotted the relationship between the  $\pi^*$  peak height ( $\pi^*/\sigma^*$  peak height ratio) and width (peak *a*) in Figure 2, which is named as “ $\pi^*$  peak map” [3]. In the map, carbon samples take characteristic distribution dependent on the kind of samples. The samples of graphite (denoted by GRA in the figure) distribute near HOPG, which

Table 1. Details of the graphitic carbon samples.

Sample name	Surface area / $\text{m}^2\text{g}^{-1}$	Particle size / nm	DBP absorption / $\text{cm}^3 100\text{g}^{-1}$
FB1	250	15	52
FB2	12	122	41
FB3	220	16	105
FB4	560	13	91
FB5	350	11	
FB6	125	20	115
FB7	79	24	150
FB8	370	13	77
FB9	260	16	69
FB10	180	18	55
FB11	290	14	98
FB12	290	14	98
FB13	25	225	155
FB14	142	18	130
FB15	244	16	80
FB16	119	22	144
FB17	79	28	101
FB18	56	38	158
AB1	39	48	140
AB2	69	35	160
AB3	370	12	250
AB4	156	26	220
AB5	380		282
AB6	63		234
AB7	58		218
KB1	800	40	360
KB2	377		300
GRA1	258.4		
GRA2	9.9		
GRA3	7.9		
GRA4			
GRA5			
GRA6			
GRA7			
CNT1			
CNT2			

is rational because graphite particles should hold large hexagonal carbon layers. Samples of CNT also distribute near HOPG, because CNT consists of hexagonal carbon structures. Acetylene black (AB) and Ketchen black (KB) distribute on left side of furnace carbon (FB). Such the distribution seems to reflect the electrical conductivity dependent on local structures; electrical conductivities of AB and KB are higher than those of FB. From these results, it can be considered that samples which distribute on left side in  $\pi^*$  peak map hold larger hexagonal carbon layers and higher crystalline structures. On the contrary, the samples which have some structural defects like edge carbon atoms and/or nonbenzenoid rings are distributed on right side in the map. This consideration from the  $\pi^*$  peak map can not be obtained by the physical properties shown in Table 1.

It is therefore concluded that the proposed  $\pi^*$  peak map is useful for characterization of graphitic carbons from the view point of local structures.

### References

- [1] Y. Muramatsu, R. Harada, M. Motoyama, and E. M. Gullikson, TANSO, 236, 2-8 (2009).
- [2] Y. Muramatsu, T. Ooe, T. Okada, and E. M. Gullikson, Proc. of the 9th International Symposium on Atomic Level Characterizations for New Materials and Devices '13, ALC'13, 516-518 (2013).
- [3] Y. Muramatsu, K. Murayama, and T. Okada, Proc. of the 10th International Symposium on Atomic Level Characterizations for New Materials and Devices '15, ALC'15, 27p-P-38 (2015).

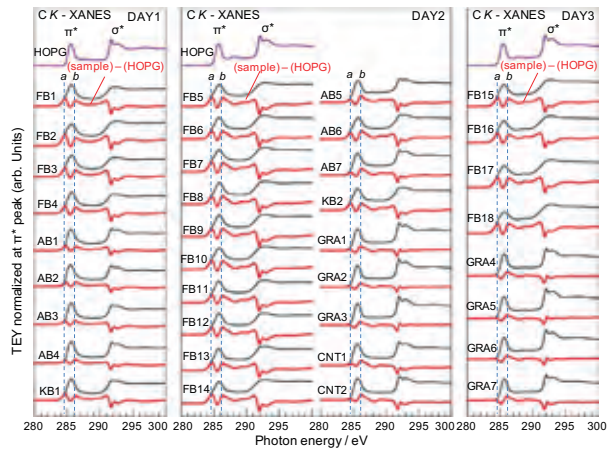


Fig. 1 C K - XANES spectra of HOPG and graphitic carbon samples.

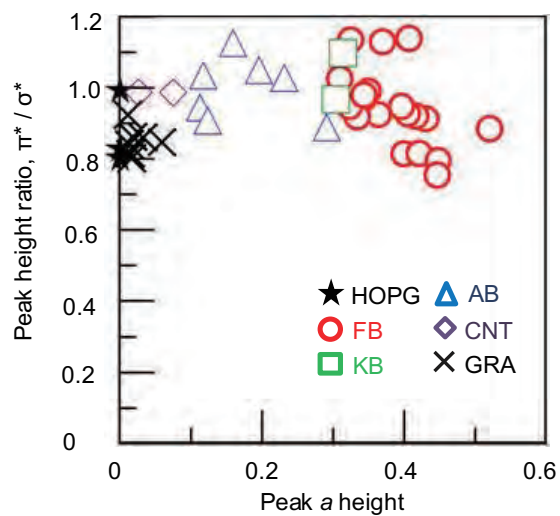


Fig. 2 Relationship between the  $\pi^*/\sigma^*$  peak height ratio and peak  $a$  height ( $\pi^*$  peak map).

# Soft X-Ray Absorption Spectroscopy of Oxygen in Rubber - Brass adhesive layer

Takashi Kakubo <sup>1</sup>, Naoya Amino <sup>1</sup>, Keita Nanbu <sup>2</sup>, Yasuji Muramatsu <sup>2</sup>,

<sup>1</sup> Yokohama rubber Co., Ltd., 2-1 Oiwake, Hiratsuka, Kanagawa 254-8601, Japan

<sup>2</sup> Graduate School of Engineering, University of Hyogo, 2167 Shosha, Himeji, Hyogo 671-2201, Japan

## Abstract

The chemical state of oxygen in the rubber and brass adhesion layer was evaluated by using total-electron-yield soft X-ray absorption spectroscopy (TEY-XAS). Fatty acids including in rubber compounds are influence to the adhesion of rubber and brass. Oxygen including in fatty acid on rubber surface was estimated. After adhering rubber compound and brass plate by curing, the adhesion layer was sliced. Each of the surfaces was measured by TEY-XAS at NewSUBARU and Advanced Light Source (ALS). The quantitative analysis of oxygen can be obtained from the peak height ratio  $O\sigma^*/C\sigma^*$  in the TEY-XAS.

## Introduction

The adhesion of rubber and steel in tire is quite important for safety driving of automobile. If the adhesion systems do not work, the tire will be break soon. So some analysis for the adhesion system was evaluated [1, 2]. Fatty acids including the rubber compounds affect to decrease adhesive force of rubber and metal. Fatty acids are including in natural rubber, compounding agent or cobalt salt. To evaluate the chemical state of surface oxygen in the rubber and brass adhesion layer, TEY-XAS was used. After adhering rubber compound to brass plate by curing, the rubber layer was sliced. Each of the surfaces was measured by TEY-XAS at NewSUBARU and at Advanced Light Source (ALS). The quantitative analysis of oxygen can be obtained from the peak height ratio  $O\sigma^*/C\sigma^*$  from the results of TEY-XAS.

## Experiments and Results

Rubber compound including natural rubber, carbon black, Zinc oxide, sulfur and rubber agents was mixed and prepared. After putting the uncured rubber on the brass plate, the rubber was cured at 170 °C for 10min. To make it easier to peel off, only 0.5phr sulfur was mixed to the rubber compound. The adhesion layer was sliced by cutting knife after curing as shown in Figure 1. Each of the surfaces was measured by XAS.

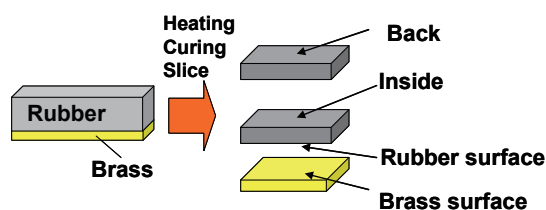


Fig.1 Adhesive samples for XAS measurement.

Soft x-ray absorption spectra of the samples were measured with the total-electron-yield (TEY) in beamline BL-10 at the NewSUBARU and in beamline BL-6.3.2 at the Advanced Light Source (ALS). Same samples were used for both measurements, and both XAS results were compared.

Figure 2 shows the results of XAS in the CK and OK region of adhesion sample. Stearic acid was used for standard sample of fatty acid. Acetone extracted brass plate was used for Normal brass sample.

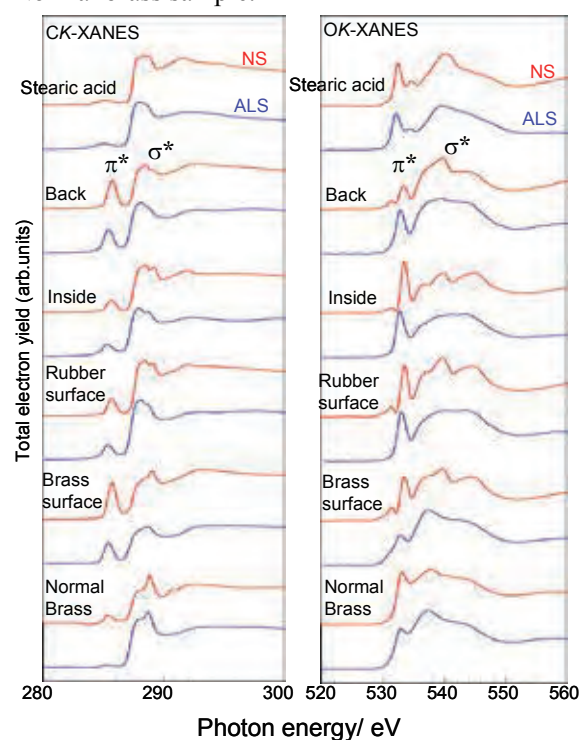


Fig.2 Soft x-ray absorption spectra in the CK and the OK region of Rubber and Brass adhesion sample.

For rubber samples,  $\pi^*$  bonding in the CK region were observed at 285eV. Some impurities on the brass were observed from the result of Normal brass. The peak of  $\sigma^*$  bonding of ZnO in the OK was shown at 538 eV. The peak of  $\sigma^*$  bonding of carboxyl group in the OK was shown at 540 eV. ZnO was mixed in the rubber, so the ZnO component was detected by XAS measurement.

Figure 3 shows that the peak height ratio  $O\sigma^* / C\sigma^*$ . The peak height ratio of Rubber surface and Brass surface are higher than that of Back or Inside. The ratio in the rubber increases as close to the brass. Oxygen including in fatty acid on rubber surface was estimated. In addition, the ratio of Brass surface and Normal brass are higher. Brass is originally stabilized by ZnO because of ZnO is formed on the brass surface. Thereby ZnO is detected strongly on brass surface by XAS measurement. The amount of oxygen derived ZnO on brass surface is common to be reduced by vulcanization of rubber.

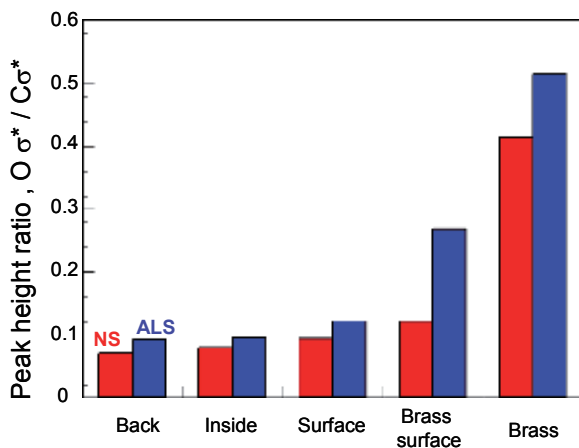


Fig.3 Peak height ratio  $O\sigma^*/C\sigma^*$  of each parts in adhesion layer.

The peak height ratios measured at ALS were higher than that measured at NewSUBARU. The tendency of oxygen content in each layer is similar.

### Conclusions

The quantitative analysis of oxygen derived fatty acid or ZnO can be obtained from the peak height ratio  $O\sigma^*/C\sigma^*$  in the TEY-XAS. Oxygen content of the rubber close to the brass is increased. This result is due to fatty acids in the rubber. It is possible to know the tendency of the oxygen component in the rubber and brass adhesion layer.

### References

[1] T. Hotaka et al., Nippon Gomu Kyokaishi., 77,7, pp.244-249 (2004).

[2] K. Ozawa et al., Applied Surface Science., 264, pp.297-304 (2013).

# Analyses of surface state of detonation nanodiamond

Masahiro Nishikawa<sup>1</sup>, Ming Liu<sup>1</sup>, Akira Yamakawa<sup>1</sup>, and Yasuji Muramatsu<sup>2</sup>

<sup>1</sup> Daicel Corporation, <sup>2</sup> University of Hyogo

## Abstract

Detonation nanodiamond (DND) is a carbon nanomaterial promising for various applications, and controlling its surface state is very important to express its functionality. For this purpose, we have started X-ray absorption near edge structure (XANES) measurements at BL-10 in the NewSUBARU SR facility.

## Introduction

Detonation nanodiamond (DND) is nano-sized synthetic diamond with 4 ~ 5 nm in average diameter of primary particle (Fig.1) [1]. It is a kind of “carbon nanomaterial” and greatly expected for wide range of applications by taking advantage of physical properties of diamond in combination with the characteristics of nanoparticles. DND is produced from explosives by detonation process followed by purification and dispersion processes (Fig.2). Daicel Corporation has installed a test facility for detonation process in Harima Plant (Hyogo, Japan).

Due to small particle size, DND has large specific surface area more than 300 m<sup>2</sup>/g. 10 ~ 20% of all atoms making up particles are exposed on the surface, where oxygen functional groups like carboxylate or hydroxyl group exist (Fig.3). The state of functional groups is affected by detonation and purification conditions, and affects the dispersibility in various media in various conditions.

Analyzing surface state of DND precisely and control that properly is very important to obtain favorable dispersibility in target medium, by which the expression of distinguished functionality of DND is expected.

For this purpose, we have started analyses of DND surface state with X-ray absorption near edge structure (XANES) measurement [2, 3].

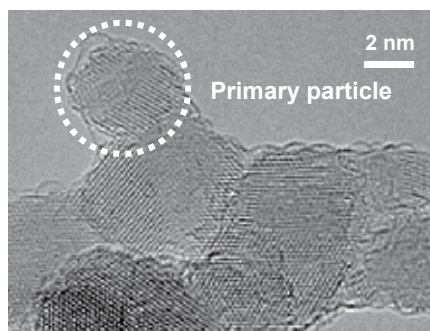


**Fig.1** Transmission electron microscope (TEM) image of nanodiamond (by the courtesy of Prof. T. Hayashi, Shinshu University).

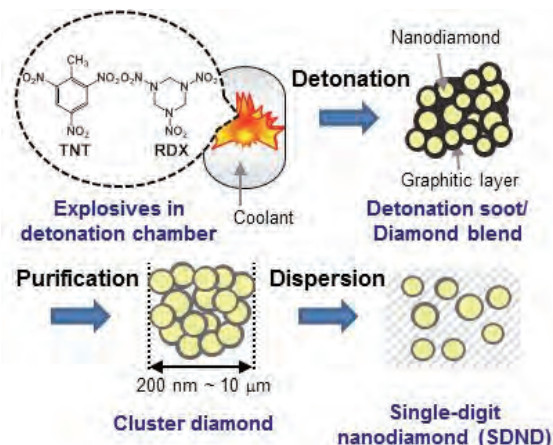


**Fig.2** Manufacturing processes of detonation nanodiamond.

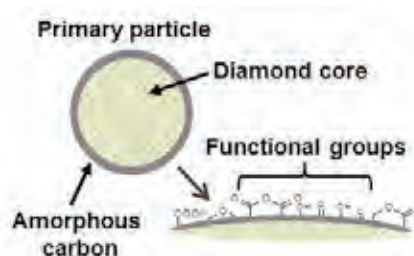


**Fig.3** Illustration of nanodiamond primary particle and its surface.

## Experiments

XANES measurements were carried out at BL-10 [4] in the NewSUBARU SR facility. CK-edge, OK-edge and NK-edge XANES were recorded by the total electron yield (TEY) method.

DND sample was manufactured by Daicel Corporation. Average primary particle diameter of the sample was determined 4.1 nm according to Sherrer's equation by HMFWD of the 111 peak of powder X-ray diffraction analysis. BET specific surface area was 341 m<sup>2</sup>/g. Oxygen content of the sample was estimated ca. 13% by elemental analysis, and nitrogen content was 2.5%.

## Results and Discussion

CK-edge XANES spectrum of DND is shown in Fig.4 together with that of highly oriented pyrolytic graphite (HOPG).

Absorption peak at 285.1 eV is presumably the peak from  $\pi^*$  of  $sp^2$  carbon on the DND surface. The photon energy is slightly lower than that of HOPG (285.5 eV). It is supposed that  $sp^2$  carbon of DND would be less ordered than graphitic carbon like HOPG. Further investigation for the exact structure is needed. Assuming that the intensity of  $\pi^*$  peak is liner to the  $sp^2$  carbon content and that of HOPG is 100%,  $sp^2$  carbon content of the DND sample is estimated 8.5% from the relative intensity of  $\pi^*$  peak for DND, with standardized at 293 eV (Table 1). The peak at 286.7 eV is supposed to come from hydroxylated  $sp^2$  carbon. It has been observed that intensities of those peaks vary, sometimes with subtle shift of photon energy, by manufacturing processes and treatment conditions (data not shown).

OK-edge and NK-edge XANES spectra are shown as Fig. 5. We are presuming that the peak intensity of OK-edge XANES and that at 286.7 eV of CK-edge XANES, and oxygen content by elemental analysis correlate one another. On the other hand, peak shape and intensity of NK-edge XANES is unchanged among various samples. Nitrogen in DND is derived from nitro group of explosives and nitrogen content in DND is almost the same among samples unless nitrogen containing group is introduced by additional treatment.

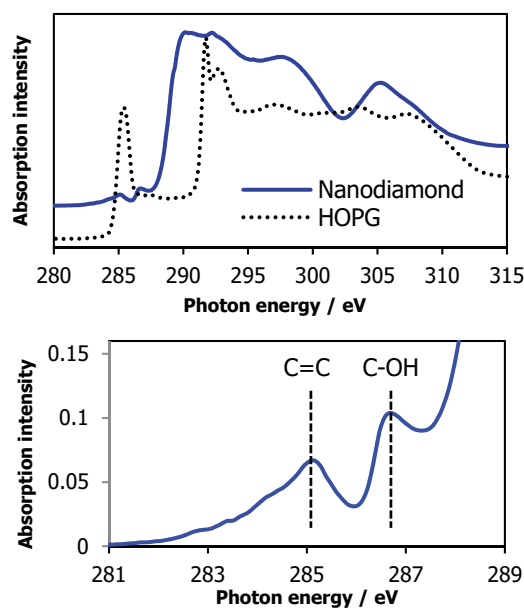
We are working for various samples with different sources, processes and treatments for further elucidation.

**Table 1** Peak intensities of DND (standardized at 293 eV of CK-edge XANES)

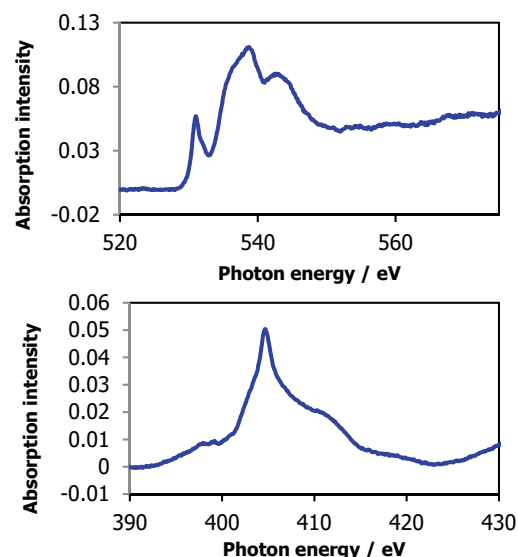
CK-edge XANES		
$\pi^*$ (C=C)	Relative intensity to	$\pi^*$ (C-OH)
285.1 eV	HOPG $\pi^*$	286.7 eV
0.067	0.085	0.103

OK-edge XANES	
$\pi^*$ (C=O)	$\sigma^*$ (OH)
530.9 eV	538.7 eV
0.057	0.111



**Fig. 4** CK-edge XANES spectrum of DND



**Fig. 5** OK-edge XANES (upper) and NK-edge XANES (lower) spectra of DND

## References

- [1] V. N. Mochalin, O. Shenderova, D. Ho and Y. Gogotsi, *Nature Nanotechnology*, **7**, 11-23 (2012).
- [2] S. Osswald, G. Yushin, V. Mochalin, S. O. Kucheyev, and Y. Gogotsi, *J. Am. Chem. Soc.*, **128**, 11635-11642 (2006).
- [3] E. M. Zagrebina, A. V. Generalov, A. Y. Klyushin, K. A. Simonov, N. A. Vinogradov, M. Dubois, L. Frezet, N. Mårtensson, A. B. Preobrajenski, and A. S. Vinogradov, *J. Phys. Chem. C*, **119**, 835-844 (2015).
- [4] T. Uemura, Y. Muramatsu, K. Nambu, D. Fukuyama, M. Kuki, T. Harada, T. Watanabe, and H. Kinoshita, *Adv. X-ray Chem. Anal., Japan*, **46**, 317-325 (2015).

# Analysis of the carbon black by soft X-ray absorption spectroscopy

Atsusyoshi Inoue<sup>1</sup>, Masaya Fujisue<sup>2</sup>, Takeshi Hattori<sup>1</sup>, Tsuyoshi Takakura<sup>1</sup>,  
Tomohiko Inoue<sup>1</sup>, Kentarou Murayama<sup>3</sup>, Yasuji Muramatsu<sup>3</sup>

<sup>1</sup>Mitsubishi Chemical Corporation, <sup>2</sup>Mitsubishi Rayon Co. LTD, <sup>3</sup>University of Hyogo

## Abstract

Soft X-ray absorption spectroscopy (XAS) is effective analysis method for characterizing chemical bonding state of carbon materials. For example, in the case of nano-graphite, we have obtained information of edge carbon atoms in hexagonal carbon layer by analyzing the XAS spectra in the CK region. In this study, we have evaluated variety of furnace carbon blacks (CB) by the XAS measurement. As a result, we have found the inverse correlation between the intensity of the peak attributed to edge carbon in hexagonal carbon layer and the nitrogen absorption specific surface area (N<sub>2</sub>SA), Di-butyl phthalate oil absorption (DBP), respectively. Furthermore, we have confirmed the difference of the local structure during the graphitization.

## Introduction

As a raw material of tires and rubber products, CB is wildly used. In order to satisfy the customer's requirements, variety of CBs are produced. For further understanding of chemical and physical bonding between CB and rubber, it is important to investigate the fundamental structure, especially, the chemical bonding state of hexagonal carbon layer. XAS measurement is a powerful tool to identify carbon double bond and single bond, in addition, the edge carbon atoms in hexagonal carbon layer. In this report, we have focused on the chemical bonding state change of hexagonal carbon layer in CBs from XAS measurements by changing the physical properties (N<sub>2</sub>SA, DBP, and graphitization) of CBs, and those results are issued.

## Experiments

XAS measurements by total electron yield (TEY) were performed using synchrotron radiation in BL-10 at the NewSUBARU [1]. CBs provided from Mitsubishi Chemical Corporation have been measured. Those samples have N<sub>2</sub>SA in the range of 28-374(m<sup>2</sup>/g) and DBP in the range of 46-137 (ml/100g). Graphitized CBs (Sample1 and Sample2) are also included.

We have considered the chemical bonding state of carbon by using two parameters,  $\pi^*/\sigma^*$  and the normalized peak-*a* height.  $\pi^*/\sigma^*$  is peak intensity ratios between the  $\pi^*$  peak and the  $\sigma^*$  peak. Normalized peak-*a* height was obtained by subtracting the measured spectrum from the highly oriented pyrolytic graphite (HOPG) spectrum as a reference [2,3]. Peak-*a*, attributed to the edge carbon atoms in hexagonal carbon layer, appears approximately at 284 eV in the subtracted spectrum. For a reference, nano-graphites obtained by mechanically grinding HOPG under Ar atmosphere were measured.

## Results

Fig.1 shows the relationship between the  $\pi^*/\sigma^*$  ratio and normalized peak-*a* height (CB(●), nano-graphite (Δ)). Dotted line is the primary approximation line of nano-graphite.

Plot of grinded nano-graphite shifted towards the lower right as we extend the grinding time. This shows that the grinding time increases the number of defect in hexagonal carbon layer.

In case of CB,  $\pi^*/\sigma^*$  and normalized peak-*a* height are in the range of 0.7-0.9 and 0.3-0.5, respectively. These plots are distributed along the dotted line.

Focusing on Sample1 and Sample2, plot shifted towards upper left compared to Sample0. Since graphitized temperature is higher in Sample2 than in Sample1, the number of defect in hexagonal carbon layer is expected to be lower in Sample2. Therefore, XAS could confirm the rearrangement of crystallite during the graphitization.

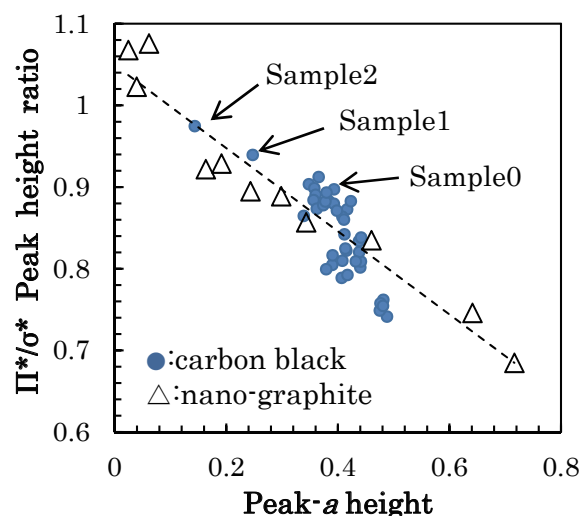


Fig.1 Relationship between peak height ratio ( $\pi^*/\sigma^*$ ) and peak-*a* height (CB(●) and nano-graphite (Δ)).

Fig.2 shows the relationship between  $N_2SA$  and normalized peak-*a* height (2a), along with relation between DBP and normalized peak-*a* height (2b). Normalized peak-*a* height of CB linearly decrease as  $N_2SA$  increase. Similar relation is observed for DBP. It is new to know that the number of defect in hexagonal carbon layer is affected by DBP, although it may take a little more time to identify the cause of observed results.

Interestingly however, Sample1 and Sample2 show totally different balance. This result suggested that we can produce CB with different chemical bonding state, independent of  $N_2SA$  and DBP.

As described above, XAS measurement is useful in comparing the chemical bonding state of hexagonal carbon layer of CB. In our future work, we would like to identify the effect of oxygen at the edge of hexagonal carbon layer by analyzing oxidized CBs.

### References

- [1] T. Uemura, Y. Muramatsu, K. Nambu, D. Fukuyama, M. Kuki, T. Harada, T. Watanabe, and H. Kinoshita, *Adv. X-ray Chem. Anal., Japan*, 46, 317-325 (2015).
- [2] Y. Muramatsu, T. Ooe, T. Okada, and E.M. Gullikson, *Proc. 9th International Symposium on Atomic Level Characterization for New Material and Devices*, 516-518 (2013).
- [3] Y. Muramatsu, K. Murayama, and T. Okada, *Proc. 10th International Symposium on Atomic Level Characterization for New Material and Devices' 15*, 27p-P-38 (2015).

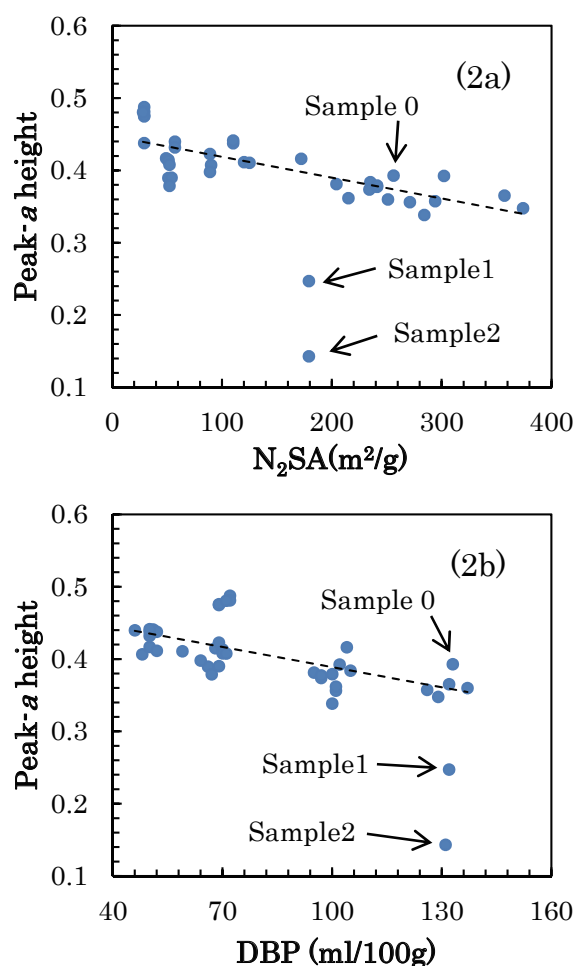


Fig.2 Upper panel (2a) shows the relationship between peak-*a* height and  $N_2SA$  ( $m^2/g$ ). Lower panel (2b) shows the relationship between peak-*a* height and DBP (ml/100g).

# Development of Transmission Grating for EUV Interference Lithography of 1X nm HP

Tsubasa Fukui, Hirohito Tanino, Yuki Fukuda, Masaki Kuki, Takeo Watanabe, Hiroo Kinoshita, and Tetsuo Harada

*Laboratory of Advanced Science and Technology for Industry, University of Hyogo  
3-1-2 Koto, Kamigori, Ako-gun, Hyogo, 687-1205, Japan  
tfukui@lasti.u-hyogo.ac.jp*

The advanced feature size patterning process of semiconductor conductor devices was being charged with the important role with development of an information-technology oriented society. Extreme ultraviolet lithography (EUVL) is expected as a leading candidate of the next generation lithography for semiconductor electronic devices. The development of EUV resist which has high resolution, high sensitivity, low LWR, and low out gassing is a second critical issue of the EUVL. Development of the two-beam interference exposure tool using the EUV light has been upgraded for the critical dimension of 10-nm-order in EUV resist patterning process. This tool was installed at the 10.8-nm-long undulator beamline BL09B of NewSUBARU synchrotron radiation facility. Using this EUV interference lithographic method, 15 nm hp resist pattern had been replicated on a silicon wafer. The transmission grating fabrication is the most significant key technology in the EUV interference lithography. The advanced fabrication process is applied for the transmission-grating fabrication for the EUV resist patterning beyond the feature size of 15 nm, such as 12.5 and 10 nm.

**Keywords:** EUV lithography, interference lithography, transmission diffraction grating

## 1. Introduction

EUVL [1] will be used in the semiconductor electronic device high volume manufacturing for the patterning in the 16 nm feature size around 2016. The top three issues of the EUVL are the development of 1) source, 2) resist, and 3) mask. The critical issues of EUV resist are the simultaneous achievement of the high resolution, sensitivity, low LER, and low out gassing [2]. Currently, on Feb. 25, 2015, ASML press release announced that using ASML NXE-3300B exposure beta tool, the EUV-light-source power increased to 90 W at the intermediate focus position, and TSMC semiconductor chip manufacturer exposed 1022 wafers in 24 hours. 10-nm-feature-size-patterning technology is required in 2020 for the high volume manufacturing listed in the international technology roadmap for semiconductor (ITRS) [3].

The resolution specification of ASML NXE3300B EUV exposure tool is 22 nm. Thus it cannot reach to the resolution of 10-nm order. To accelerate the EUV resist development of 10-nm order, it is very significant to develop the EUV interference lithographic exposure tool for the resolution achievement of 10-nm order [4]. The EUV interference lithography had been developed and replicated 15 nm line and space (L/S) resist pattern by using two window-type transmission-diffraction grating

(TDG) on which has 30 nm L/S grating pattern. In addition, 28-nm-diameter-hole resist pattern had been replicated by four window-type TDG which has 40 nm L/S grating pattern [5, 6, 7]. The replicated 15 nm L/S and 28 nm hole resist patterns on a silicon wafer are shown in Fig. 1(a) and (b), respectively.

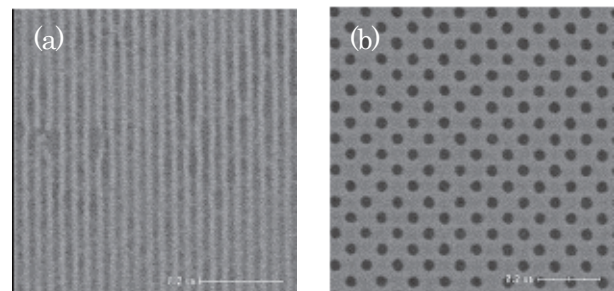


Fig. 1 (a) 15-nm-L/S inorganic-resist pattern, and (b) 28-nm-diameter hole organic-resist pattern using EUV-IL

The reduction of the vibration amplitude from a dry pump is a significant factor for the resist patterning of a small feature size in the EUV-IL exposure. The displacement of the vibration amplitude between the TDG and wafer should be reduced to approximately 1/3 of the target resolution of 10 nm in EUV-IL [8]. The vibration amplitude displacement of the frequency range from 0 to 50 Hz has been suppressed less than 3 nm.

However, with taking care of the vibration suppression, since the TDG fabrication for 10-nm-order EUV resist patterning is most significant, this paper focused on the fabrication of the TDG for the EUV resist patterning of 10-nm-order resolution achievement using EUV-IL.

## 2. Experiment

### 2.1. Interference lithography

A schematic view of the interference lithography which was installed is shown in Fig. 2. An experimental chamber was installed at 10.8-m-long undulator beamline BL09C. The 1.0 GeV electron linear accelerator of the large synchrotron radiation facility of SPring-8 is used as an injector for the New SUBARU electron beam storage ring which is a medium scale light source. The circumference of this ring is approximately 118.9 m and the schematic view of this facility was shown in Fig. 3.

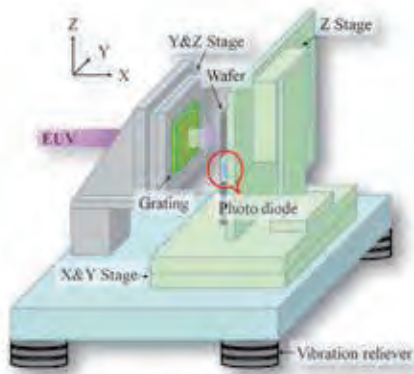


Fig.2 A schematic view of the interference lithography which was installed

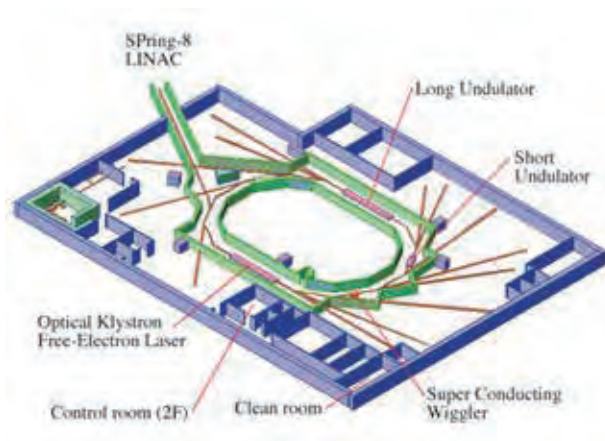


Fig. 3 The schematics view of NewSUBARU synchrotron light facility

Configuration of the two beam interference exposure tool using the coherent EUV light is shown in Fig. 4 [9].

The TDG has two window. In general, the coherent light is diffracted into the  $0^{\text{th}}$ ,  $\pm 1^{\text{st}}$ ,  $\pm 2^{\text{st}}$ , ... -orders lights from a diffraction grating. The interference fringe is generated by interfering with the  $+1^{\text{st}}$  order light from one window of TDG and  $-1^{\text{st}}$  order light from another window of TDG, and the generated-fringe pitch has a half pitch of the TDG grating pattern. As a result, resist pattern pitch of the 1/2 pattern pitch of the TDG can be replicated on a wafer when settle at the interference position. For example, a TDG with 20 nm L/S grating pattern can form a resist pattern of 10 nm L/S on a wafer at the interference position.

In the resolution region of 10 nm and below, since the replicated pattern is easy to be affected by the flare of the imaging optics, the flare control of the optics is very significant. However, since in the case of EUV-IL, EUV-IL need not to use optics, there is no flare to be affected to the fine pattern replication. Thus EUV-IL is a powerful exposure tool to evaluate resist resolution and LWR performance for the development of EUV resist material.

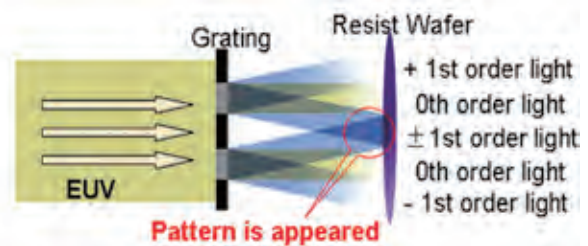


Fig. 4 Principle of interference exposure

### 2.2 Transmission-diffraction gratings

A TDG is the significant key element of EUV-IL for the advanced fine resist patterning. A schematic view of a fabrication process of a TDG is shown in Fig. 5 [10]. Diffraction efficiency strongly depends on the absorber material and its thickness. TaN material was selected to employ as an absorber grating of the TDG because of the high diffraction efficiency, the good sputtering and dry-etching performance.

First, 25 nm TDG tried to fabricate. And then 20 nm TDG process was evaluated. To achieve the advanced fine patterning for these TDGs, the following three specified process should be employed.

- 1) The  $\text{SiO}_2$  hard mask process should be employed for the patterning of the TaN layer with aspect ratio of approximately 3.
- 2) The low stress sputtering of the TaN and  $\text{SiO}_2$  layers was required.
- 3) The center stop process was employed to cut off the incident light for the interference patterning.

The transmission fabrication flow is listed as followings.

- 1) The low stress 100-nm thick  $\text{Si}_3\text{N}_4$  double coated 4-inches Si substrate was performed as the TDG substrate.
- 2) The TaN and  $\text{SiO}_2$  layers which employed as an absorber grating and hard mask respectively were sputtered on the substrate.
- 3) Electron beam resist was coated.
- 4) The resist was patterned by 50-keV-electron-direct-writing tool.
- 5) The EB resist pattern was transformed to the  $\text{SiO}_2$  hard mask layer by dry etching process.
- 6) The hard mask pattern was transformed to the TaN absorber grating by dry etching process.
- 7) The back side  $\text{Si}_3\text{N}_4$  layer was dry etched.
- 8) The back side Si was removed by the KOH wet etching process at the temperature of 90 °C to perform the  $\text{Si}_3\text{N}_4$  membrane.
- 9) A 2  $\mu\text{m}$  thick EB resist was coated to perform the center stop layer to cut off the direct incident EUV light.
- 10) The center stop resist on the window area was exposed by EB, and development and rinse processing were carried out.
- 11) The remained resist was removed by  $\text{O}_2$  ashing process.

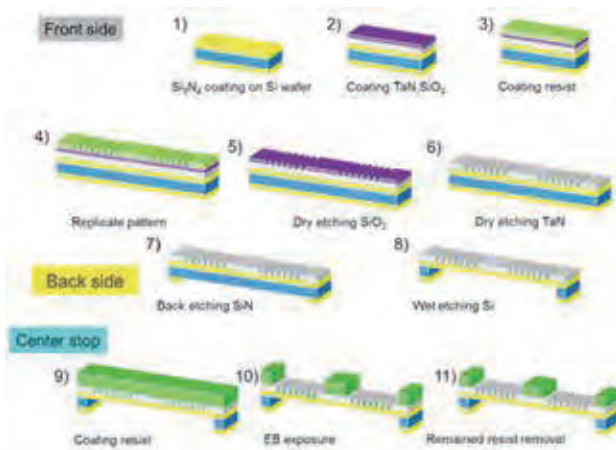


Fig. 5 Fabrication process flow of TDG

### 2.3 Resist processing

In this fabrication process of TDG, the electron beam lithography plays an important role to form a grating pattern with a small feature size. ZEP520A (Nihon Zeon) resist had been employed as the EB patterning of the TDG. However this resist resolution limit was 25 nm in the EB direct writing. A higher resolution EB resist is required to

fabricate a TDG with 25 and 20 nm L/S. In addition, resist with higher etching tolerance is needed.

gL3002T (Gluon Lab.) resist which is a revised version of ZEP520A resist and HSQ resist (XR-1541-002, Toray Dow Corning) were tried to use in the fabrication process of the TDG. The averaged molecular weight of gL3002T resist is 10 times larger than that of ZEP520A resist and also has higher resolution and process stability comparison to the organic positive type resist.

HSQ resist is a negative type resist of on the basis of the silicon containing resist and has a resolution of 6 nm. However, the sensitivity of HSQ resist is approximately 10 times lower than that of ZEP520A resist.

As results, gL3002T and HSQ resists were employed for the fabrication of the TDG with a feature size of 25 and 20 nm L/S grating pattern.

## 3. Results and Discussions

### 3.1 gL3002T resist process

The resist was spin coated on a  $\text{SiO}_2$  layer to be the thickness of 50 nm. Prebake was carried out at the temperature of 180 °C in 180 s. O-xylene and 2-propanol was employed as a developer and rinse solutions, respectively. A SEM image of the cross sectional view of the replicated gL3002T resist pattern is shown in Fig. 6. Both scanning electron microscope (SEM) images of 25 and 20 nm L/S resist patterns were replicated on a  $\text{SiO}_2$  layer as shown in Fig. 6(a) and (b), respectively.

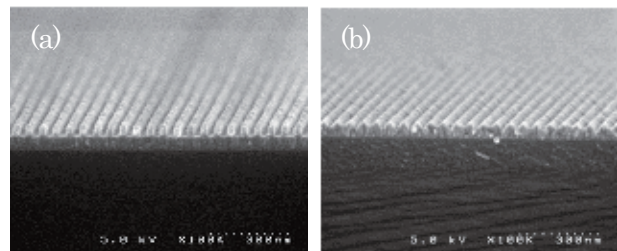


Fig. 6 SEM images of (a) 25 nm and (b) 20 nm L/S gL3002T resist pattern on  $\text{SiO}_2$  layer

A fine rectangular cross sectional shape of 25 nm L/S gL3002T resist pattern was formed. However, since it couldn't be formed in the case of 20 nm L/S resist pattern, gL3002T was employed in the fabrication of TDG with a feature size of 25 nm.

$\text{SiO}_2$  25 nm L/S pattern was formed by dry etching using the 25 nm L/S gL3002T resist pattern as a mask. The cross sectional SEM image of  $\text{SiO}_2$  25 nm L/S pattern is shown

in Fig. 7(a). For this  $\text{CF}_4$  etching process, RF and bias power were 100 W and 25 W, respectively. And chamber vacuum pressure was 1.3 Pa, and the  $\text{CF}_4$  gas flow rate was 60 sccm.

TaN 25 nm L/S pattern was formed by dry etching using the 25 nm L/S  $\text{SiO}_2$  pattern as a mask. The cross sectional SEM image of TaN 25 nm L/S pattern is shown in Fig. 7(b). For this  $\text{Cl}_2$  etching process, RF and bias power were 100 W and 25 W, respectively. And chamber vacuum pressure was 1.3 Pa, and  $\text{Cl}_2$  gas flow rate was 25 sccm.

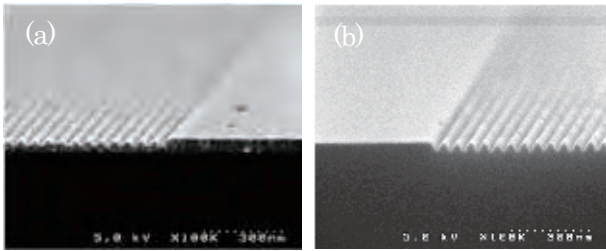


Fig. 7 Cross sectional SEM images of (a)  $\text{SiO}_2$  and (b) TaN 25 nm L/S patterns formed after dry etching

After the Si substrate back side etching and formulation of the center stop processes, 25 nm L/S TDG was succeeded to fabricate. Using TDG, 12.5 nm L/S resist pattern will be replicated in the EUV-IL exposure.

### 3.2 HSQ resist process

Replicated 20 nm L/S HSQ resist pattern on a bare Si wafer using 50 keV EB direct writing tool is shown in Fig. 8(a). However, HSQ resist pattern with a waving shape was replicated because of charging up in EB lithography. Since the exposure sensitivity of HSQ resist has approximately 10 times lower than that of ZEP520 resist, large amount of negative electric charges are accumulated on the resist surface during EB exposure. It is easier to occur this charging up phenomenon using low sensitivity EB resist material. Thus Espacer (Showa Denko) was employed as a top coating material to avoid charging up phenomenon. Espacer is water soluble and has a large conductivity. Fig. 8(b) shows the CD-SEM image of 20 nm L/S HSQ resist pattern applied Espacer top-coating process before the EB exposure. As shown in this figure, the waving shape disappeared and 20 nm L/S HSQ pattern was succeeded to replicate. The top-coating condition was 2,500 rpm in 60 s using spin coater, after the HSQ resist coating on the substrate. For HSQ resist process condition, spin-coating condition was 2,500 rpm in 60 s and prebake was carried out at the temperature of 80 °C in 80 s. And

the initial HSQ resist thickness was 36 nm. The 2.38% TMAH alkali aqueous solution and deionized water were employed as a developer and rinse solution.

Development and rinse conditions were at the temperature of 22 °C in the period of 30 s, and at the room temperature in the period of 30 s, respectively.

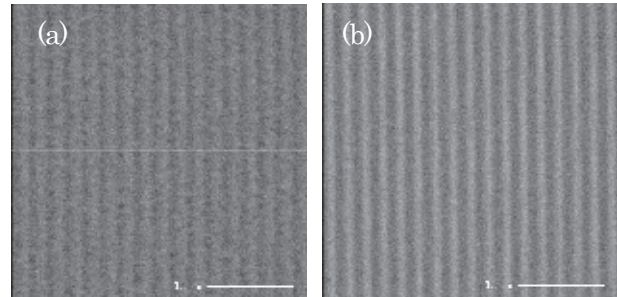


Fig. 8 20 nm L/S pattern (a) affected by charging up on Si substrate and (b) to stop the effect of charging up Espacer was employed

In the case of a TDG fabrication, resist pattern should be replicate  $\text{SiO}_2$  layer for the hard mask process. Figure 9 shows cross sectional SEM image of 20 nm L/S HSQ pattern on a  $\text{SiO}_2$  layer.

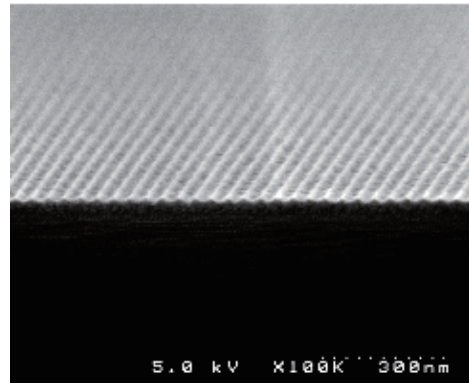


Fig. 9 20 nm L/S pattern with Espacer process

2.38% TMAH alkali aqueous solution was employed for the development. The cross sectional resist pattern shape is not a rectangular. To obtain the rectangular cross sectional shape of HSQ resist pattern, the alkaline strong NaOH aqueous solution was employed. To raise osmosis of NaOH into the HSQ resist material, NaCl was added. Finally, mixture aqueous solution of 1% NaOH and 4% NaCl was employed as a developer. As a result, 20 nm L/S HSQ resist pattern with a rectangle-cross-sectional shape was replicated with employing the mixture developer solution of NaOH/NaCl. This cross sectional SEM image is shown in Fig. 10(a). The thickness was 36 nm.

$\text{SiO}_2$  20 nm L/S pattern was formed by dry etching using

the 20 nm L/S HSQ resist pattern as a mask. The cross sectional SEM image of SiO<sub>2</sub> 20 nm L/S pattern is shown in Fig. 10(b). Thickness was 20 nm. For this CF<sub>4</sub> etching process, RF power, Bias power, chamber pressure, CF<sub>4</sub> gas flow rate were 100 W, 25 W, 1.3 Pa, and 60 sccm, respectively.

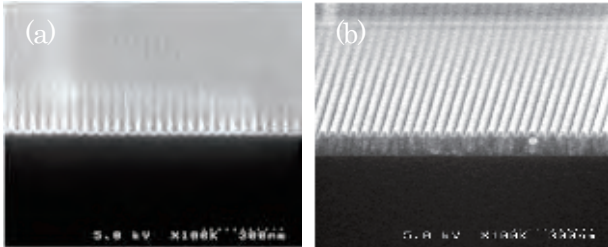


Fig. 10 Cross sectional SEM images of 20 nm L/S (a) HSQ resist pattern, and (b) SiO<sub>2</sub> pattern after CF<sub>4</sub> dry etching

As shown in this figure, the cross sectional shape of 20 nm SiO<sub>2</sub> pattern is rectangle. TaN 20 nm L/S grating pattern could be replicate employing this SiO<sub>2</sub> pattern as a mask in dry etching in Cl<sub>2</sub> gas.

#### 4. Conclusions

25 nm L/S gL3002T resist pattern with a rectangular cross sectional shape was formed. TaN grating pattern was formed by CF<sub>4</sub> and Cl<sub>2</sub> gas dry etching. Fabrication of a TDG which has 25 nm L/S grating pattern was completed by forming the back side etching of Si substrate and the center stop process.

HSQ resist with 20 nm L/S rectangular cross sectional pattern was formed by employing mixture aqueous solution of 1 % NaOH and 4 % NaCl as a developer. 20 nm L/S of SiO<sub>2</sub> was formed by CF<sub>4</sub> gas dry etching. 20 nm L/S of a TaN grating pattern can be transform by SiO<sub>2</sub> 20 nm L/S pattern as a Cl<sub>2</sub> dry-etching mask. Using the TDG with 20 nm L/S grating pattern, EUV resist will be evaluated in EUV-IL exposure.

#### References

1. H. H. Solak, C. David, J. Gobrecht, V. Golovkina, F. Cerrina, S.O. Kim, P.F. Nealey / *Microelectronic Engineering* **67** (2003) 56.
2. The summaries of the International Symposium of Extreme Ultraviolet Lithography 2010
3. ITRS Roadmap [<http://www.itrs.net/>].
4. Yasuyuki Fukushima, Naoki Sakagami, Teruhiko Kimura, Kamaji Yoshito, Takafumi Iguchi, Yuya Yamaguchi, Masaki Tada, Tetsuo Harada, Takeo Watanabe, and Hiroo Kinoshita : "Development of Extreme Ultraviolet Interference Lithography System," *Jpn. J. Appl. Phys.* **49** (2010) 06GD06-1 .
5. Y. Fukushima, Y. Yamaguchi, T. Kimura, T. Iguchi, T. Harada, T. Watanabe and H. Kinoshita: "EUV Interference Lithography for 22 nm Node and Below," *J. Photopolym. Sci. Technol.* **23** (2011) 673.
6. T. Urayama, T. Watanabe, Y. Yamaguchi, N. Matsuda, Y. Fukushima, T. Iguchi, T. Harada, H. Kinoshita : "EUV Interference Lithography for 1X nm," *J. Photopolym. Sci. Technol.* **24** (2011) 153.
7. Y. Yamaguchi, Y. Fukushima, T. Harada, T. Watanabe and H. Kinoshita: "Transmission grating fabrication for replicating resist pattern of 20 nm and below," *Jpn. J. Appl. Phys.* **50** (2011) 06GB10-1.
8. Hirohito Tanino, Tsubasa Fukui, Kazuya Emura, Yuta Hayashi, Yuki Fukuda, Masaki Kuki, Masato Yamaguchi, Tetsuo Harada, Takeo Watanabe, Hiroo Kinoshita: "Development of EUV interference lithography system for evaluation of EUV resist with hp 10 nm," *I. E. E. Jpn.* (2014) 7.
9. S. Suzuki, Y. Fukushima, R. Ohnishi, T. Watanabe, and H. Kinoshita, "Pattern Replication in EUV Interference Lithography," *J. Photopolym. Sci. Technol.* **21** (2008) 435.
10. Y. Yamaguchi, Y. Fukushima, T. Iguchi, H. Kinoshita T. Harada and T. Watanabe "Fabrication Process of EUV-IL Transmission Grating," *J. Photopolym. Sci. Technol.* **23**(2010) 681.

# Trial fabrication of PTFE-filled E-plane waveguide coupler using SR etching process

Mitsuyoshi Kishihara<sup>1</sup>, Akinobu Yamaguchi<sup>2</sup>, Yuichi Utsumi<sup>2</sup>, and Isao Ohta<sup>3</sup>

<sup>1</sup>Faculty of Computer Science & System Engineering, Okayama Prefectural University

<sup>2</sup>Laboratory of Advanced Science and Technology, University of Hyogo

<sup>3</sup>University of Hyogo

## Abstract

We report a trial fabrication of the PTFE-filled E-plane waveguide coupler for short millimeter-wave based on the SR etching process of PTFE, with the aim of developing integrated waveguide circuits. In this report, an integrated PTFE pattern, in which the two 3-dB couplers are cascaded, is fabricated. Then, the frequency characteristics of the fabricated coupler are measured.

## Introduction

The metal-covered waveguide circuits such as H- and E-plane waveguide circuits suit with the millimeter-wave and submillimeter-wave applications requiring refined configurations, because the structures are very simple and various desired performances are realized by optimization of the contour of circuit structure.

Recently, various micromachining technologies such as laser cutting, lithography, etc. have been applied to the development of components in the field of microwave and millimeter-wave engineering as well as in the field of mechatronics, optics, and fluidics. Trial fabrications of a hollow waveguide horn antenna at W-band based on the fabrication process using SU-8 photoresist, a coplanar transmission line and its filter at microwave band based on the LIGA process, etc. have been reported. Also, it has been reported that PTFE (Polytetrafluoro-ethylene) microstructures can be fabricated by direct exposure to synchrotron radiation (SR) [1]. The SR direct etching process has been applied to the fabrication of various PTFE-filled waveguide circuits [2]. The fabrication process is considered useful to construct the components for millimeter-wave and submillimeter-wave frequencies.

In this report, a PTFE-filled E-plane waveguide coupler for short millimeter-wave is fabricated based on the SR direct etching process of PTFE, sputter deposition of metal, and electroplating, with the aim of developing integrated waveguide circuits [3]. First, a cavity-type 3-dB directional coupler is designed at 180 GHz. Then, an integrated PTFE pattern, in which the two 3-dB couplers are cascaded, is fabricated. For the measurement, a frequency tripler is used to obtain the G-band (140-220 GHz) signals from a V-band (50-75 GHz) source, and only the transmitted power is detected. The

frequency characteristics of the PTFE-filled E-plane waveguide coupler are measured, and the validity of the fabrication process is verified.

## PTFE-Filled Waveguide Coupler

Figure 1 illustrates a structure of PTFE-filled E-plane waveguide 3-dB coupler. It consists of a rectangular cavity ( $a \times b \times d$ ) and four E-plane waveguides ( $w \times d$ ). The dimensions of the PTFE-filled waveguide were determined as 0.40 mm  $\times$  0.80 mm ( $w \times d$ ) for the 180 GHz operation. The dimensions  $a$ ,  $b$  of the cavity and the position  $t$  were optimized to realize the 3-dB coupler, and  $a = 1.77$  mm,  $b = 1.42$  mm, and  $t = 0.27$  mm were obtained.

In this report, an integrated PTFE pattern that the two 3-dB couplers are cascaded is fabricated, and the transmitted characteristics of the circuit are measured.

## Fabrication

A trial fabrication of the PTFE-filled E-plane waveguide coupler for 180 GHz operation was performed based on the SR direct etching process, sputter deposition of metal, and electroplating. Figure 2 illustrates the experimental situation of the SR etching process. A stencil mask representing circuit pattern is put on the PTFE sheet (thickness: 0.80 mm). Then X-ray is irradiated to obtain the PTFE pattern.

Figure 3 displays the integrated PTFE pattern

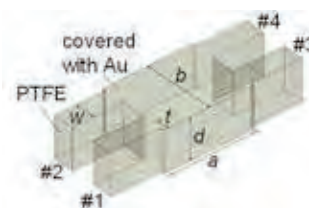


Fig.1 Structure of PTFE-filled E-plane waveguide coupler.

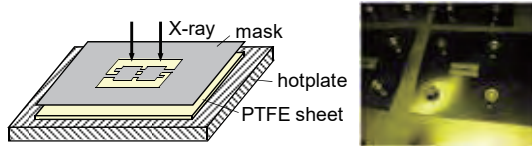


Fig.2 PTFE sheet is etched by direct exposure to SR.



Fig.3 Integrated PTFE pattern obtained by the SR direct etching process. Two 3-dB couplers are cascaded.



Fig.4 Integrated PTFE pattern covered with Au film by the sputter deposition and electroplating.

of the two 3-dB couplers obtained by the SR direct etching process. The amount of X-rays exposed is 1700 Asec. It takes about 1.6 hours to obtain the PTFE pattern. The fabrication accuracy is within errors of  $\pm 7.5\mu\text{m}$ , which depends on the accuracy of the mask. Note that the stepped ( $\lambda/4$ ) transformers for impedance matching are also embedded in the pattern in Fig. 3.

After etching the PTFE pattern, the waveguide structure covered with thin metal film can be realized by sputtering Au all over the surface of the PTFE pattern as shown in Fig.4. The PTFE pattern is exposed to Ar plasma for several minutes to perform surface modification. Then, Au is deposited on the entire surface. In this report, the Au film of about 500 nm in thickness is formed. To increase the thickness of the Au film, electroplating process is used. In this work, Au film is increased up to 5  $\mu\text{m}$ . After forming the Au film, the integrated pattern of the PTFE-filled E-plane waveguide couplers is obtained by removing the unnecessary frame.

### Measurement

A measurement system is prepared using a frequency tripler (VDI WR5.1 $\times$ 3 Broadband Tripler, 140 GHz - 220 GHz) and a detector (VDI WR5.1 Zero-Bias Detector, 140 GHz - 220 GHz) to measure the frequency characteristics of the 180 GHz PTFE-filled



Fig.5 Frequency characteristics of the integrated cavity-type 3-dB couplers.

waveguides. A vector network analyzer (Agilent E8361C) is used for the V-band source (50 GHz - 70 GHz). The V-band signal is inputted to the tripler, and only the transmitted power is observed as DC-voltage.

Figure 5 shows the frequency characteristics of the integrated cavity-type 3-dB couplers constructed of PTFE-filled E-plane waveguide. Solid red line indicates the measured transmission characteristics of the couplers. The frequency characteristics of the  $S$ -parameters using a high frequency structure simulator (HFSS) are plotted for comparison. It is found that the measured curve  $S_{21}$  shows similar tendency to the simulated  $S_{21}$  except in the proximity of 176 GHz and 183 GHz. Although the causes of the two falls of the transmission characteristics must be made clear, the combined output signal of the 3-dB couplers can be observed in the G-band.

### Conclusion

Trial fabrication of the cascaded PTFE-filled E-plane waveguide 3-dB couplers for short millimeter-wave was demonstrated, and the transmission characteristics were measured. The fabrication process is considered applicable for the development of integrated waveguide circuits.

### Acknowledgement

This work was supported by JSPS KAKENHI Grant Number 26420314.

### References

- [1] Y. Zhang, T. Katoh, M. Washio, H. Yamada, and S. Hamada, Applied Physics Letters, vol.67, no.6, pp.872-874, Aug. 1995.
- [2] M. Kishihara, H. Ikeuchi, Y. Utsumi, T. Kawai, and I. Ohta, IEICE Trans. Electron. vol.E95-C, no.1, pp. 122-129, Jan. 2012.
- [3] M. Kishihara, H. Ikeuchi, Y. Utsumi, T. Kawai, and I. Ohta, IEICE Trans. Electron. vol.E95-C, no.1, pp. 122-129, Jan. 2012.

# Lab-on-a-CD to implement high precise unit chemical operation for Immunoassay

Masaya Takeuchi<sup>1</sup>, Yasuto Arisue<sup>1</sup>, Yoshiaki Ukita<sup>2</sup>, Chiwa Kataoka<sup>3</sup>,  
Toshiro Kobayashi<sup>4</sup>, Akinobu Yamaguchi<sup>1</sup>, Yuichi Utsumi<sup>1</sup>

<sup>1</sup>University of Hyogo, <sup>2</sup>University of Yamanashi,

<sup>3</sup> Carbuncle Bio ScienTech LLC, <sup>4</sup>National Institute of Technology Tsuyama College

## Abstract

The Lab-on-a-CD is a kind of micro analysis system that implement unit chemical operations such as cleaning, mixing and so on. This device is circular and it manipulate solution by utilizing centrifugal force when rotated. As an application of device, ELISA is effective. ELISA is immunoassay that enable quantitative analysis by utilizing Antigen-antibody reaction. In this study, we fabricate Lab-on-a-CD using capillary, siphon valve and attempt high accuracy of sequential sending solution assumed ELISA.

## Introduction

In Clinical Examination, ELISA is famous method that examine pestilence maker such as protein and peptide and so on. ELISA enable quantitative analysis by utilizing antigen-antibody-reaction with enzyme. This is several types and explains sandwiches method for example. First, we uniformly fix primary-antibody to solid phase surface (Fig.1(a)) and inject antigen (Fig.1(b)). Then part of antigen adhere Primary-antibody. After washing extra antigen (Fig.1(c)), we inject secondary antibody fixing enzyme (Fig.1(d)) and likewise wash it (Fig.1(e)). Finally, substrate is injected (Fig.1(f)). Then substrate reacts with enzyme and varies

its spectrum of absorbance. Thus, quantitative analysis is possible to measure the absorbance. The reaction-stop-solution is actually injected because of suppressing excess reaction of substrate and Enzyme.

For way realized this ELISA, there is method that use micro titer plates. But this method take long period of time and reduce reliability. Also, the method using robot is very expensive. This prevents development to Clinic. For a means solving these problem, micro analysis system is attracted attention.

Micro analysis system is device that integrate unit chemical operation such as mixing, washing and so on by using fine flow-path. It is expected miniaturization of device, reduction of reagent, shortening of examination time and high precision.

There is Lab-on-a-CD in a kind of device that utilize micro analysis system. This device is disk-shaped and is formed Flow-path from center to outside. Centrifugal force is generated by rotated this and can send a liquid from center to outside. We can realize unit chemical operation by this.

In this study, we fabricate Lab-on-a-CD for ELISA utilizing capillary valve, siphon valve, mixing structure and attempt high efficiency and high accuracy.

## Design of Lab-on-a-CD

Material of device uses PDMS. One of two PDMS cut into a circle is dug Flow-path by Rapid-typing-method[1].

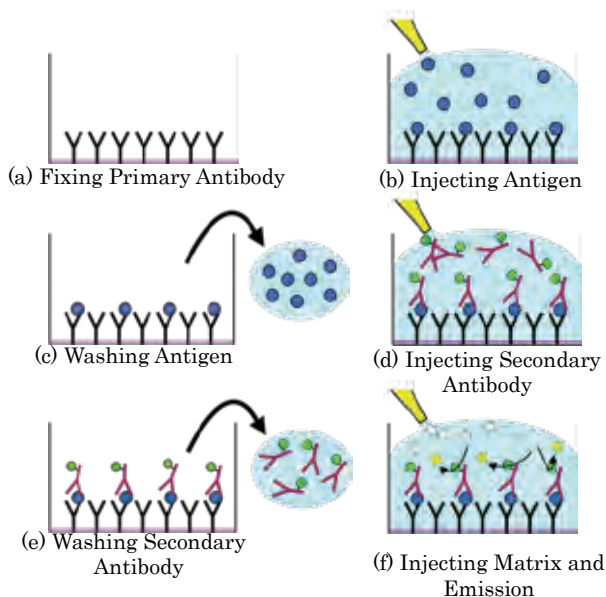


Fig.1 Sandwiches method

The other is smooth. The Lab-on-a-CD complete by pasting two PDMS. However, the PDMS is applied Hydrophilic treatment beforehand.

Lab-on-a-CD using Capillary valve, Siphon valve, mixing structure is operated while the rotational speed up and down and realize protocol that need to analyze in low rotation speed.

Fig.2 shows concept figure of capillary valve. Capillary valve is designed more thin than flow-path[2]. Liquid can stay by surface tension between Capillary valve and flow-path(Fig.2(b)). Design of Break-rotation-speed become possible by adjusting width of capillary valve because strength of surface tension depends on that of capillary valve, where Break-rotation-speed is rotation speed that solution of reserver flow out by Centrifugal force. Relation of break-rotation-speed  $f_{cb}$  and width of capillary valve is expressed by following equation.

$$f_{cb} = \sqrt{\frac{\gamma \cdot \sin\theta}{\pi^2 \rho \Delta R \bar{R} d_H}} \quad (1)$$

Where  $\gamma$  is surface tension of liquid,  $\theta$  is contact angle,  $\rho$  is density of liquid,  $d_H$  is width of valve,

$$\Delta R = R_2 - R_1, \quad \bar{R} = (R_2 + R_1)/2.$$

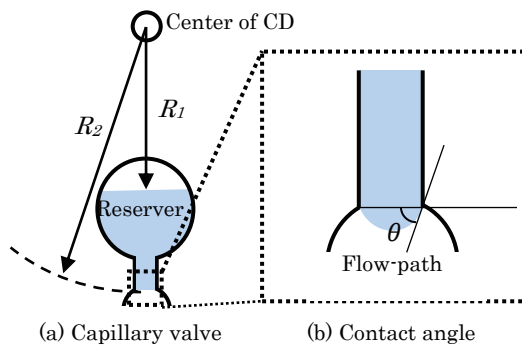


Fig. 2. Structure of Capillary valve

Siphon valve utilize capillarity and the principle of the siphon(Fig.3)[3]. Liquid of reserver enter flow-path by capillarity and fulfill valve. Next, by increasing rotation speed, strengthen centrifugal force and send liquid by the principle of the siphon. Break rotation speed of Siphon valve is expressed following equation.

$$f_{cb} = \sqrt{\frac{\gamma \cdot \cos\theta}{\pi^2 \rho \Delta R \bar{R} d_H}} \quad (2)$$

Design of break rotation speed become possible. Proposed Lab-on-a-CD need operation mixing Substrate and reaction-stop-solution. But quantity of solution dealt with micro analysis system is micro scale and the nature of the fluid is difference compared with macro scale.

There is two state of laminar flow and turbulence. Laminar flow is regular flow

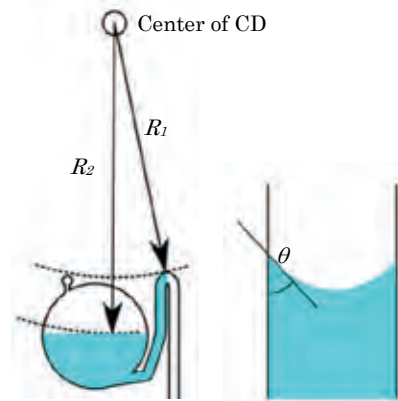


Fig. 3. Concept of siphon

that the flow line of the fluid is parallel. Turbulence is irregular flow that the flow line proceeds while crossing. Reynolds number  $R_e$  express the nature of the fluid.

$$R_e = \frac{\rho v d}{\mu} \quad (3)$$

Where  $v$  is flow velocity,  $d$  is inner diameter of Flow-path,  $\mu$  is viscosity. Fluid that Reynolds number equals shows hydrodynamically the equivalent nature. Fluid becomes more irregular if this number is large. It switches from Laminar flow to turbulence at about  $R_e = 2000$ . In micro analysis system, Reynolds number becomes comparatively small numerical number and the nature of laminar flow notably appear. In other words, the mix of solution is almost not occur in flow path in case of using Y-type-micro-mixer(Fig.4). Thus, we must wait mix of solution a few

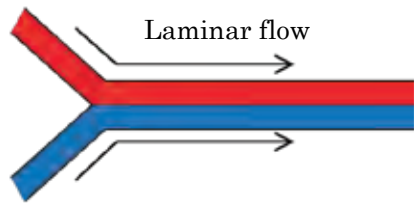


Fig. 4. Y-type-micro-mixer

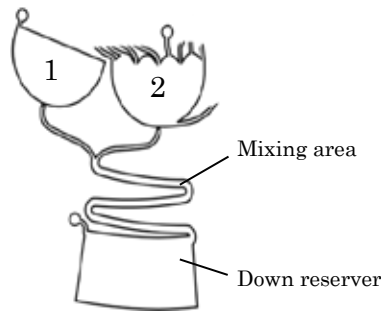


Fig. 5. Mixing structure

minutes in reservoir. We propose mixing structure to solve this problem. Fig.5 shows the concept of device used verification experiment. Mixing area is formed between 1,2-reservoir and down reservoir. When the solution runs Flow-path, it yield vortex by using mixing-structure, which is explained as below. Velocity of fluid running pipe interior center is faster than pipe interior surface because of

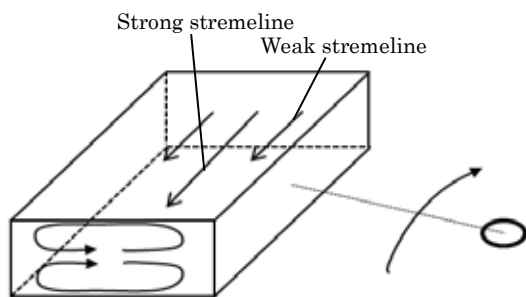


Fig. 6. Formation of Coriolis force

surface tension. Thus, Coriolis's force occurring when rotating CD is different pipe interior center and surface. The vortex occur by this action(Fig.6). Thus, liquid is easier to mix.

**Experiments and Results**

We fabricate Lab-on-a-CD utilizing Capillary

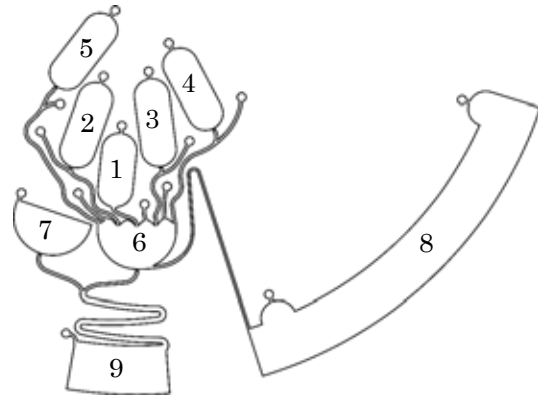


Fig. 7. Concept of proposed Lab-on-a-CD

valve, Siphon valve, mixing structure and perform "Sequential-selection-solution-sending-experiment" assumed ELISA. Fig.7. shows concept of fabricated device. The capillary valve's width of 1-6 reservoirs becomes thin as the capillary number is large. 6, 7-reservoir is the same width. Thus, Break rotation speed increase as the capillary number is large. Also 6, 7-reservoir is the same Break rotation speed. Fig.8 shows the relation between break rotation speed calculated by actual width flow-path and measured by experiment. Measured value of respective break rotation speed is smaller than that calculated. As this reason, we consider that hydrophilic process of PDMS is not enough. Next, we perform the experiments assuming actual ELISA carried out by the sequential unit chemical operation. Respective reservoir is

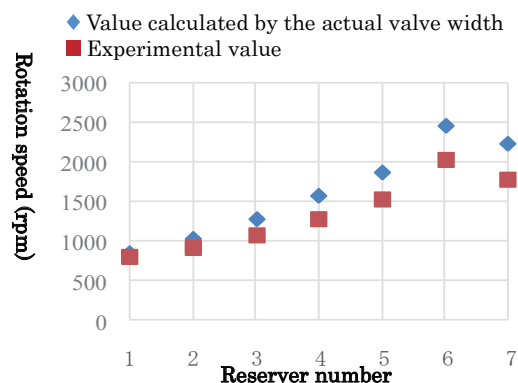


Fig. 8. Relation of Break rotation speed and Reservoir number

fulfilled with solution and rise rotation speed by 1000 rpm per second. We verify whether assumed experiment is possible or not. 1-reservoir(antigen) valve is open as rising rotation speed and solution is injected 6-reservoir(reaction field). This solution is sent

to 8-reserver(Waste-solution-reserver) using siphon valve. These operation is likewise performed 3-reserver(Primary-Antibody) and 2, 4-reserver (Washing-solution). Next, solution of 5-reserver(Substrate) is sent to 6-reserver. Capillary valve of 6,7-reserver is broken by rotation speed further, the solution is sent to 9-reserver(inspection reserver) through the mixing area. Fig.9 shows the experimental result. Capillary valve, Siphon valve operate as designed and the solution is mixed and can be sent to inspection reserver. Thus we can realize Sequential-selection-solution-sending assuming ELISA.

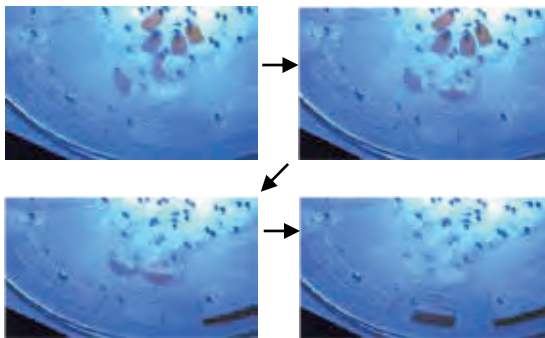


Fig.9. Mixing structure

- [1] J. Cooper McDonald, et al., : “Fabrication of Microfluidic system in poly”, *Electrophoresis*, Vol.21, pp.27-40(2000)
- [2] Siyi Lai, Shengnian, et al., : “Design of a Compact Disk-like Microfluidic Platform for Enzyme-Linked Immunosorbent Assay” , *Anal. Chem*, Vol.76, pp. 1832-1837 (2004)
- [3] Jens Ducree, et al., : “The centrifugal microfluidic Bio- Disk platform”, *Journal of Micromechanics and Micro Engineering*, Vol.17, pp.103-115 (2007)

# Proposal of Direct Digital Manufacturing Approach for Production of Microfluidic Devices

Yoshiaki Ukita<sup>1</sup>, Akinobu Yamaguchi<sup>2</sup>, and Yuichi Utsumi<sup>2</sup>

<sup>1</sup>University of Yamanashi

<sup>2</sup>Laboratory of Advanced Science and Technology, University of Hyogo

## Abstract

We propose and discuss direct digital manufacturing (or three-dimensional printing technology) for the low-cost manufacturing of microfluidic devices. The difficulty of commercialization of microfluidic product and advantage of direct digital manufacturing are briefly discussed. Then some example of microfluidics manufacturing using direct digital manufacturing and flow pumping in the developed microfluidic chips using centrifugal pumping are introduced.

## Introduction

It has been widely shared problem that the development cost of microfluidic system for chemical and analytical system is too high to realize product with reasonable amount of initial investment, since beginning size of the market is niche or too small to compare to the investment while it have to be grown in future. Direct digital manufacturing (or 3D printing technology) is becoming popular style in industry for production of final product. Especially in the case of small volume production of complex resin structure in niche market, it is advantageous since it does not require the production of expensive mold or molding facilities. In this report we would like to propose and discuss the potential of direct digital manufacturing for the production of microfluidic devices.

## Concept

Figure 1 depicts the difference of microfluidic device production by conventional manner and direct digital manufacturing. In the case of conventional manner, the microfluidic system is developed in research and development process using small volume production method that typically utilized in research such as photolithography for the manufacturing of microfluidic chips. Afterward when the prototype of the product is developed the development phase shifts to scaling up. In this shift of the phase it is forced to change the way of manufacturing since typical research technology is not suitable mass production of product therefore there is great gap between research and scaling-up and there require great amount of investment, time, and patience. On the other hand, in the case of direct digital manufacturing, the

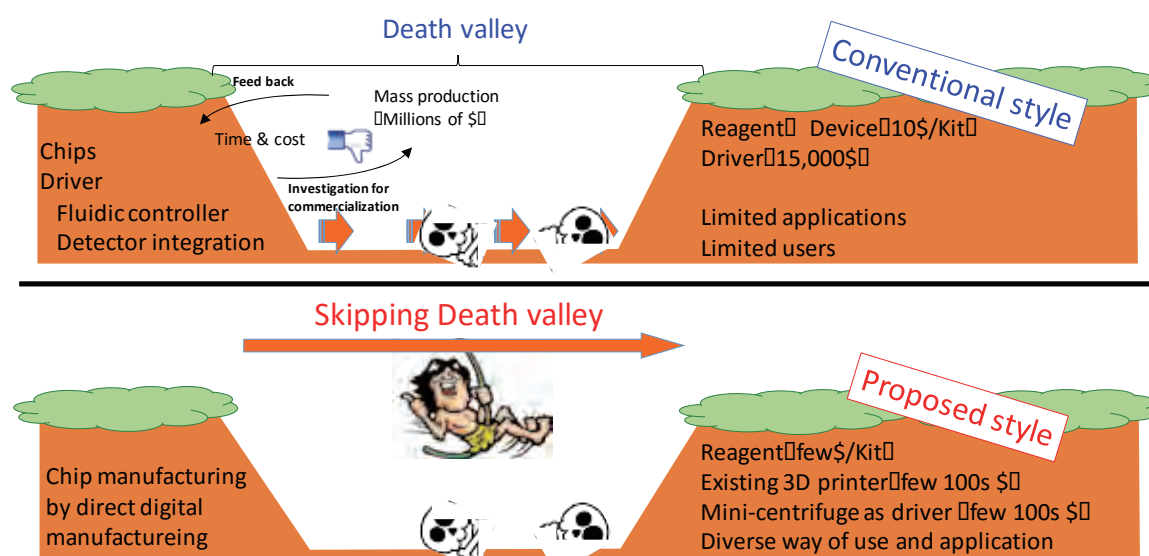


Fig. 1 Comparison of conventional way of commercialization and proposed way of commercialization by direct digital manufacturing approach.

development of the research can be driven using the 3D printer that potentially used by end-user therefore once the product is developed in the research phase the product can be directly introduced to market since the product can be supplied with the style of electronic data. Therefore direct digital manufacturing of microchip is advantageous to greatly reduce the cost of initial investment for commercialization of microfluidic products [1].

### Demonstration of direct digital manufacturing of microfluidic chips and centrifugal flow control

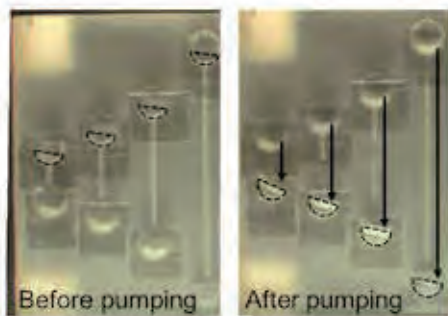


Fig. 2 Demonstration of centrifugal microfluidic pumping in monolithic microfluidic chip with  $500 \times 500 \mu\text{m}^2$  embedded microchannel.

Figure 2 shows the demonstration of centrifugal microfluidic pumping in monolithic microfluidic chip. Square shaped microchannels with  $500 \times 500 \mu\text{m}^2$  and  $250 \times 250 \mu\text{m}^2$  are successfully embedded while some channels cannot flow through the liquid due to clogging of the microchannel due to residual resin in the microchannel [2]. We also attempt autonomous

flow sequencing using water clock concept and successfully demonstrated four step flow injection at steadily rotating device that manufactured by the use of existing three dimensional printer [2, 3]. (data not shown) Refer the references for further detail of the research and development [1-3].

### Summary

In this report we discussed the potential advantage of the use of direct digital manufacturing concept for the production of microfluidic product. Moreover the demonstration of microfluidic manufacturing and centrifugal flow control are introduced. Owing the concept of centrifugal microfluidic pumping is also advantageous since it is possible to utilize the mini-centrifuge, which already commercially available and cheap, as device driver.

### References

- [1] Y. Ukita, Y. Utsumi, Y. Takamura, Direct digital manufacturing of a mini-centrifuge-driven centrifugal microfluidic device and demonstration of a smartphone-based colorimetric enzyme-linked immunosorbent assay, *Analytical Methods*, 8, 256-262, 2016 DOI: 10.1039/C5AY01969A
- [2] Y. Ukita, Y. Takamura, Y. Utsumi, Direct Digital Manufacturing of Autonomous Centrifugal Microfluidic Device, *Japanese Journal of Applied Physics*, 55, 06GN02, 2016, DOI: 10.7567/JJAP.55.06GN02
- [3] Y. Ukita, Y. Takamura, Y. Utsumi, Water-clock-based autonomous flow sequencing in steadily rotating centrifugal microfluidic device, *Sensors and Actuators B*, 220, 180-183., 2015

# Synthesis of particles extracted from aqueous solution induced by X-ray radiolysis using synchrotron radiation

Akinobu Yamaguchi<sup>1</sup>, Ikuo Okada<sup>2</sup>, Takao Fukuoka<sup>1</sup>, and Yuichi Utsumi<sup>1</sup>

<sup>1</sup>Laboratory of Advanced Science and Technology, University of Hyogo

<sup>2</sup>Synchrotron Radiation Research Center, Nagoya University

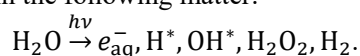
## Abstract

We report the synthesis of metallic nano- and micro- particles from the corresponding liquid solution [gold(I) trisodium disulphite solution, electrical plating solution, including  $\text{Na}_3\text{Au}(\text{SO}_3)_2$  and  $\text{NH}_2\text{CH}_2\text{CH}_2\text{NH}_2$  etc.] by X-ray radiolysis using synchrotron radiation. These results demonstrate the behavior of three-dimensional printers, enabling us to build composite material structure with metallic and other materials.

## Introduction

The potential to fabricate metallic nano- and micro materials on silicon substrates or other substrates from liquid solutions is ideal for three-dimensional lithography systems, drug delivery materials. Many methods are currently available for the synthesis of such particles. For example, synthesis of these particles has been successfully demonstrated by sonochemical reaction, chemical reduction of metallic ions in aqueous solutions, and laser ablation and laser-induced photochemical reactions, etc.

X- or  $\gamma$ -ray irradiation has also been investigated as a radiation-assisted synthesis of gold particles on a silicon substrate was reported by Rosenberg and coworkers [1] and Yamaguchi et al.[2] The method for synthesizing nano- and micro-particles. Other groups also demonstrated the synthesis of gold and nickel colloidal particles induced by synchrotron radiation (SR) X-ray irradiation. The formation of such particles was also performed using a laboratory X-ray source, however the synthesis rate was very slow. The physical and chemical mechanisms of particle formation through X- or  $\gamma$ -ray radiolysis have been investigated by X-ray photoelectron spectroscopy and optical spectroscopy. As a result, the metallic particles are essentially produced by a redox reaction induced by X- or  $\gamma$ -ray irradiation within the solution. The X- or  $\gamma$ -ray exposure enables us to easily induce chemical reactions to obtain metallic particles, as the irradiation provides hydrogen and hydroxyl radicals in the following matter:



In this report, we demonstrate the synthesis of metallic particles from corresponding aqueous solutions by X-ray radiolysis. We reported the formation of gold, copper and iron particles. In the case of gold particles, the prepared substrate

enabled the measurement of molecule through the surface enhanced Raman spectroscopy.

## Experiments and Results

Various metallic particles were directly synthesized from appropriate solutions through X-ray irradiation using the SR. [2] The deposition experiment setup is schematically shown in Fig. 1. After SR X-ray exposure, the specimen was washed with deionized water to remove residual materials. All experiments were

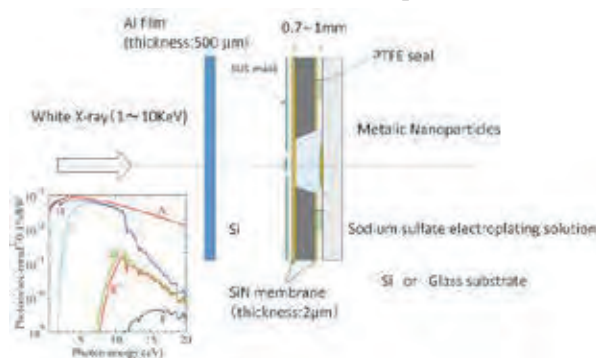


Fig. 1 Experimental setup for the X-ray irradiation of the  $\text{Na}_3\text{Au}(\text{SO}_3)_2$  electroplating solution. Photon intensity obtained from A: synchrotron radiation, B: mirror, C: Be film, D: Al film, E: metallic solution and F: Stainless steel mask.

performed in air and at room temperature.

First, gold nanoparticles were prepared by X-ray irradiation of electroplating solutions consisted of a gold (I) trisodium disulphite 2 – 3 %  $\text{Na}_3\text{Au}(\text{SO}_3)_2$  and 1.4 – 1.9 %  $\text{NH}_2\text{CH}_2\text{CH}_2\text{NH}_2$  etc. The solution was deposited on a 10 mm<sup>2</sup> silicon substrate sealed by a SiN membrane protected silicon and polytetrafluoroethylene (PTFE) plates. This assembly was covered by stainless steel frame holder. The PTFE plate between SiN membrane and Si substrate protects the solution seeping from the stainless steel frame

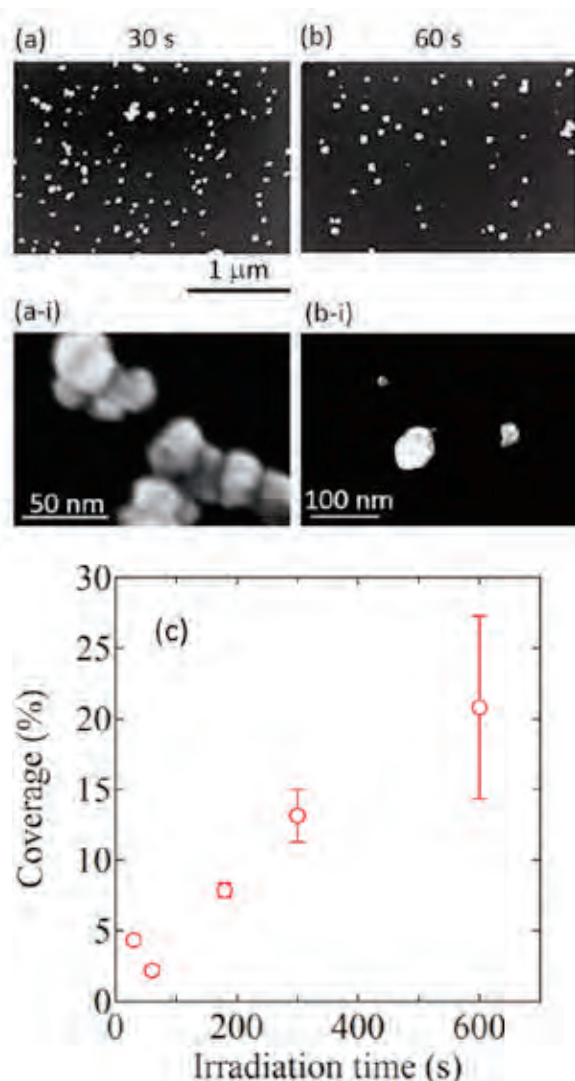
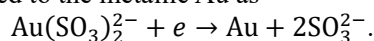


Fig. 2 SEM images of Au nanoparticles acquired after X-ray irradiation times of (a) 30 and (b) 60 s. Corresponding high-resolution SEM images are shown in (a-i) and (b-i). (c) Substrate surface coverage by Au nanoparticles as a function of X-ray irradiation time.

holder as shown in Fig. 1.

Figure 2 shows SEM images of Au nanoparticles deposited on Si substrate in (a) 30 and (b) 60 s by X-ray irradiation. As shown in the SEM images, quasi-spherical particles exhibiting almost uniform nanometric sizes were created in the irradiated area. In the electroplating solution, the radial reaction is induced and Au ion is reduced to the metallic Au as



The grains become denser and their interconnections remained random with increasing irradiation time. We found that elementary particles ranging from a few to several tens of nanometers gradually aggregated into larger particles and clusters. The surface roughness increase considerably up to a few

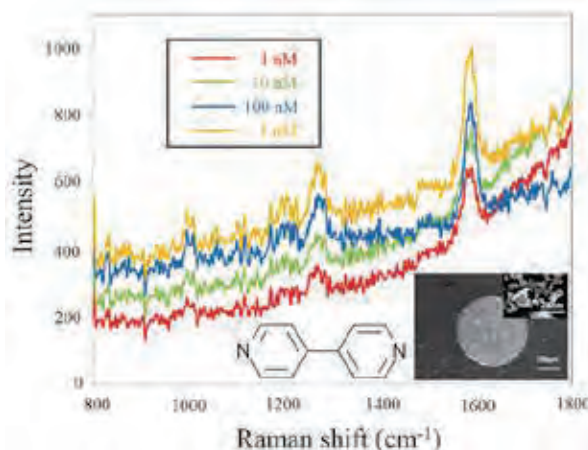


Fig. 3 Surface-enhanced Raman scattering (SERS) spectra of 4bpy for different densities. The insets show molecular formula of 4bpy and an SEM image of Au nanoparticles.

hundreds of nanometers with increasing irradiation time. However, the film appeared discontinuous. The surface coverage was plotted as a function of the irradiation time as shown in Fig. 2(c).

Next, the surface enhanced Raman scattering (SERS) of 4, 4'-bipyridine was measured using the Si substrate on which gold nanoparticles and clusters was deposited. The SERS measurement was performed using a simple Raman spectrometer without any microscope (RAM-100S, Lambda Vision Inc.) equipped with a 785 nm laser (100 mW) with  $2 \times 2 \text{ mm}^2$  squared laser spot area. Figure 3 shows the density dependence of SERS spectra of 4bpy using the substrate prepared by 600 s of X-ray irradiation. Characteristic Raman peaks for 4bpy were visible at 1000, 1200, 1280 and  $1580 \text{ cm}^{-1}$ . Some SERS-active structures known as 'hot-spot' may exist on the Si substrate.

In conclusion, Au nanoparticles were synthesized by direct X-ray synchrotron radiation of an electroplating solution. Au cluster grew and aggregated to generate SERS-active structure 'hot-spots' as the X-ray irradiation density increased. This direct X-ray irradiation induced metallic nanoparticles can also provide novel lithography process to construct the additional nanostructures onto the previously patterned area. This convenient and high-sensitivity in situ SERS platform can be used in Lab-on-a-Chip.

#### References

- [1] R. A. Rosenberg *et al.*, *J. Vac. Sci. Technol. B* **16**, 3535 (1998); Q. Ma *et al.*, *Appl. Phys. Lett.* **76**, 2014 (2000).
- [2] A. Yamaguchi *et al.*, *Mater. Chem. Phys.* **160**, 205 (2015); A. Yamaguchi *et al.*, *Jpn. J. Appl. Phys.* **55**, 055502 (2016).

# Negative tone 50 nm line and space pattern fabrication by electron beam lithography using NEB-22

Makoto Okada and Shinji Matsui  
LASTI, Univ. of Hyogo

## Abstract

Electron beam lithography (EBL) is an important technology as a nanofabrication process. To delineate a high-resolution pattern with a short EB exposure time, EB resists are being developed. NEB-22 is one of negative-tone chemically amplified EB resist. So far, it was difficult to fabricate less than 100 nm line-and-space (L&S) pattern of NEB-22. We attempted a 50 nm scale L&S pattern fabrication by EBL using a diluted NEB-22.

## Introduction

Nanoimprint lithography (NIL) [1, 2] is a one of the nanofabrication technologies, and nanoimprint mold with a high resolution pattern is usually fabricated by electron beam lithography (EBL). The reversal pattern of the mold pattern is imprinted on the resin because NIL is a contact process. Hence, it is important to choose the positive- or negative-tone mold patterns depending on the intended use.

NEB-22 (Sumitomo Chemical Co., NEB-22A2) [3] is one of the negative-tone EB CARs [4] and has potential in the fabrication of less than 50 nm line and space (L&S) pattern because a 36 nm isolated line was delineated by EBL [5]. If we can fabricate 50 nm scale L&S pattern by EBL using NEB-22 with a low dose, NEB-22 becomes a workable choice for fabricating negative-tone less than 100 nm L&S pattern. We therefore attempted EBL using NEB-22 for negative-tone high-resolution L&S patterning.

This study is published from Jpn. J. Appl. Phys. **54** (2015) 118004.

## Experiments and Results

A direct-write EBL was carried out by Elionix ELS-7500 system. The acceleration voltage and beam current were 50 kV and 50 pA, respectively. The exposed area was  $300 \times 1200 \mu\text{m}^2$ . The exposure dose was  $40 \mu\text{C}/\text{cm}^2$ . We diluted NEB-22 with 1-methoxy-2-propyl acetate (propyleneglycol monomethyl ether acetate, PGMEA), which is the solvent of NEB-22, at a weight ratio of 2:1. The NEB-22 film spin-coated at 4000 rpm was about 100-nm thickness, which was measured by using JEOL JSM-6700F SEM apparatus. A hexamethyldisilazane (HMDS) treated Si substrate was used to increase adhesion between the resist and the substrate. We carried out post-apply bake (PAB) and post-exposure bake (PEB) for 2 min. PAB and PEB temperatures were 90 and 95°C, respectively. A cold development was carried out for fabricating the high-resolution NEB-22 pattern [6]. The exposed

NEB-22 substrate was soaked in 2.38% tetramethylammonium hydroxide (TMAH) at 10 °C for 20 s. The rinse was done in deionized water at room temperature for 30 s. We observed the fabricated NEB-22 pattern by SEM.

We first carried out EBL using undiluted NEB-22 for delineating the high-resolution pattern. Figures 1(a) and 1(b) show the SEM image of top-view and cross-sectional SEM images of the fabricated pattern. We confirmed from the cross-sectional SEM image that the pattern was developed, but it was collapsed because the pattern height was about 200 nm. This result shows that the low height NEB-22 pattern fabrication is necessary to achieve the high-resolution pattern by EBL.

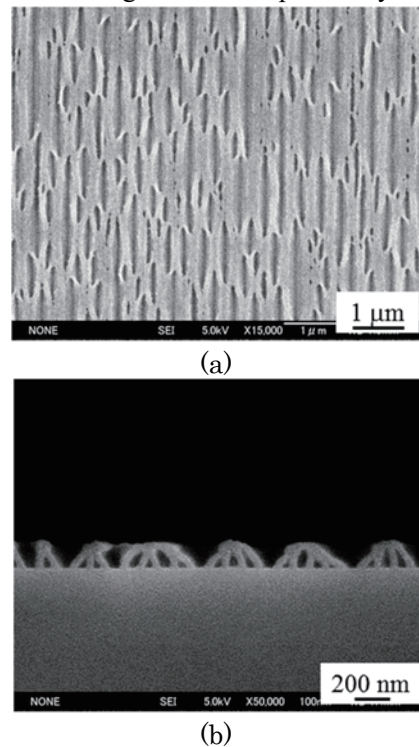
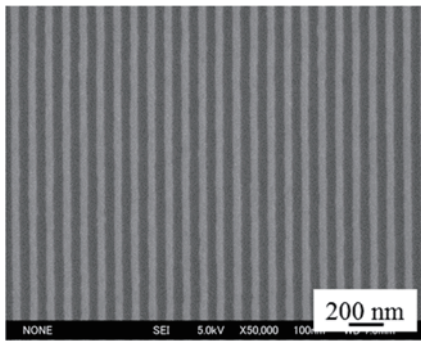


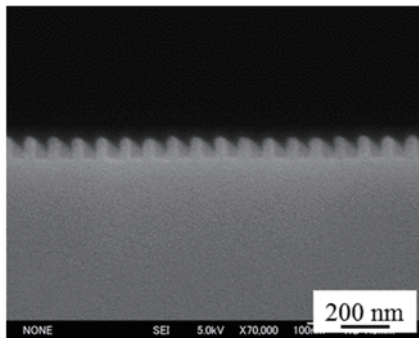
Fig. 1 (a) Top-view and (b) cross-sectional SEM images of the fabricated pattern by EBL using undiluted NEB-22.

We next used the diluted NEB-22. Figures 2(a) and 2(b) show the top-view and cross-sectional SEM

images of the NEB-22 pattern. The negative-tone NEB-22 pattern was clearly fabricated. The line- and space-widths were 40 nm and 60 nm, respectively. In addition, the pattern height was about 90 nm. We then calculated the resist contrast from the contrast curve in Fig. 3, as the slope of the linear portion of the rising section of the curve and obtained 2.9. These results indicate that we succeeded in the negative-tone fine pattern fabrication by EBL using diluted NEB-22.



(a)



(b)

Fig. 2 (a) Top-view and (b) cross-sectional SEM images of the fabricated pattern by EBL using diluted NEB-22 [7]. Copyright (2015) The Japan society of Applied Physics.

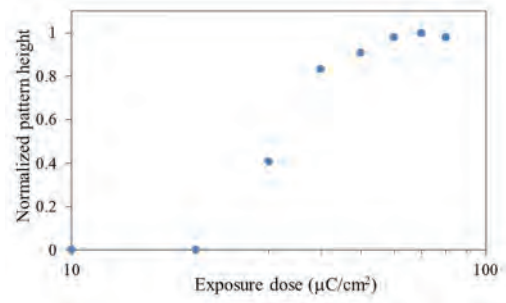


Fig. 3 Relationship between normalized fine pattern height and exposure dose. [7]. Copyright (2015) The Japan society of Applied Physics.

### Conclusion

We challenged to fabricate the fine negative-tone L&S pattern by EBL using diluted NEB-22. The NEB-22 film thickness was about 100 nm before EBL. The negative-tone pattern fabrication of 40-nm-line, 60-nm-space, and 90-nm-height was succeeded. NEB-22 has a resolution capability to fabricate 30 nm scale pattern. We further continue the research to achieve the 30 nm L&S patterning of NEB-22.

### Acknowledgements

This work was partially supported by adaptable & seamless Technology Transfer Program through Target-driven R&D (A-STEP) (Research No. AS2615023M) funded by Japan Science and Technology Agency.

### References

- [1] S. Y. Chou, P. R. Krauss, and P. J. Renstrom, *Appl. Phys. Lett.* **67**, 3144 (1995).
- [2] S. Y. Chou, P. R. Krauss, and P. J. Renstrom, *Science* **272**, 85 (1996).
- [3] Y. Uetani, R&D Rep. Sumitomo Chemical Co. 2000-I, p. 4 (2000) [in Japanese].
- [4] H. Ito, C. G. Willson, and J. M. J. Frechet, *Dig. Tech. Pap. Symp. VLSI Technology*, 1982, p. 86.
- [5] L. E. Ocola, C. J. Biddick, D. M. Tennant, W. K. Waskiewicz, and A. E. Novembre, *J. Vac. Sci. Technol. B* **16**, 3705 (1998).
- [6] L. E. Ocola, D. Tennant, G. Timp, and A. Novembre, *J. Vac. Sci. Technol. B* **17**, 3164 (1999).
- [7] M. Okada and S. Matsui, *Jpn. J. Appl. Phys.* **54**, 118004 (2015).



## Part 3. List of Publications



Retirement memorial lecture of Prof. Shinji Matsui



## List of publications

### (1) Papers

1. **"Photoneutron cross sections for neodymium isotopes: Toward a unified understanding of ( $\gamma$ ,n) and (n, $\gamma$ ) reactions in the rare earth region"**  
H.-T. Nyhus, T. Renstrøm, H. Utsunomiya, S. Goriely, D. M. Filipescu, I. Gheorghe, O. Tesileanu, T. Glodariu, T. Shima, K. Takahisa, S. Miyamoto, Y.-W. Lui, S. Hilaire, S. Péru, M. Martini, L. Siess, and A. J. Koning  
Physical Review C, **91**, 015808-1-7 (2015).
2. **"ニュースバル放射光施設における放射光利用の新展開"**  
宮本修治  
シリーズ「共用施設活用のススメ」第5回  
OPTRONICS, Vol.**34**, No.5, pp.121-127 (2015). ISSN 0286-9659
3. **"レーザーコンプトン散乱  $\gamma$  線を用いた光核反応"**  
早川岳人, 宮本修治  
展望, Isotope News, No.**734**, pp. 12-16 (2015).
4. **"Photoneutron Reactions in Nuclear Astrophysics"**  
H. Utsunomiya, S. Goriely, D.M. Filipescu, O. Tesileanu, I. Gheorghe, T. Glodariu, H.-T. Nyhus, T. Renstrøm, Y.-W. Lui, T. Shima, K. Takahisa, S. Miyamoto  
Journal of Physics: Conference Series **590**, 012023 (2015).
5. **"The  $\gamma$ -Ray Beam-Line at NewSUBARU"**  
H. Utsunomiya, S. Hashimoto, S. Miyamoto  
Nuclear Physics News, vol.**25**, Issue 3, pp.25-29, July-September (2015). DOI:10.1080/10619127.2015.1067539
6. **"Photodisintegration of  $^9\text{Be}$  through the  $1/2^+$  state and cluster dipole resonance"**  
H. Utsunomiya, S. Katayama, I. Gheorghe, S. Imai, H. Yamaguchi, D. Kahl, Y. Sakaguchi, T. Shima, K. Takahisa, S. Miyamoto  
Physical Review C, **92**, pp. 064323-1-8 (2015).
7. **"Dispersion, spatial growth rate, and start current of a Cherenkov free-electron laser with negative-index material"**  
Y. Wang, Y. Wei, D. Li, K. Takano, Ma. Nakajima, X. Jiang, X. Tang, X. Shi, Y. Gong, J. Feng, and S. Miyamoto  
Physics of Plasmas, **22**, 083111-1-7 (2015).
8. **"HARPO, a gaseous TPC as a gamma telescope and polarimeter: first measurement in a polarised photon beam between 1.7 and 74 MeV"**  
Delbart, S. Amano, D. Attié, D. Bernard, P. Bruec, D. Calvet, P. Colas, S. Daté, M. Frodin, Y. Geerebaert, B. Giebels, D. Götz, P. Gros, S. Hashimoto, D. Horan, T. Kotaka, M. Louzir, Y. Minamiyama, S. Miyamoto, H. Ohkuma, P. Poilleux, I. Semeniouk, P. Sizun, A. Takemoto, S. Wang, M. Yamaguchi  
The 34th International Cosmic Ray Conference, 30 July- 6 August, 2015  
The Hague, The Netherlands, Proceedings of Science (POS)
9. **"HARPO: beam characterization of a TPC for gamma-ray polarimetry and high angular-resolution astronomy in the MeV-GeV range"**  
S. Wang, D. Bernard, P. Bruec, M. Frodin, Y. Geerebaert, B. Giebels, P. Gros, D. Horan, M. Louzir, P. Poilleux, I. Semeniouk, D. Attié, D. Calvet, P. Colas, A. Delbart, P. Sizun, D. Götz, S. Amano, T. Kotaka, S. Hashimoto, Y. Minamiyama, A. Takemoto, M. Yamaguchi, S. Miyamoto, S. Daté, H. Ohkuma  
7th International Symposium on Large TPCs for Low-Energy Rare Event Detection  
Journal of Physics: Conference Series **650**, 012016 (2015). doi:10.1088/1742-6596/650/1/012016

10. **"Damage Characteristics of n-GaN Crystal Etched with N<sub>2</sub> Plasma by Soft X-ray Absorption Spectroscopy"**  
Masahito Niibe, Takuya Kotaka, Retsuo Kawakami, Yoshitaka Nakano, Takashi Mukai  
*e-J. Surf. Sci. Nanotech*, **14**, 9-13 (2016).
11. **"Surface Analysis of AlGa<sub>N</sub> Treated with CF<sub>4</sub> and Ar Plasma Etching"**  
Shodai Hirai, Masahito Niibe, Retsuo Kawakami, Tatsuo Shirahama, Yoshitaka Nakano, Takashi Mukai  
*e-J. Surf. Sci. Nanotech*, **13**, 481-487 (2015).
12. **"Resistance of Hydrogenated Titanium-doped Diamond-Like-Carbon Film to Hyperthermal Atomic Oxygen"**  
Kengo Kidena, Minami Endo, Hiroki Takamatsu, Masahito Niibe, Masahito Tagawa, Kumiko Yokota, Yuichi Furuyama, Keiji Komatsu, Hidetoshi Saitoh and Kazuhiro Kanda  
*Metals*, **5**, 1957-1970 (2015).
13. **"Hyperthermal Atomic Oxygen Beam Irradiation Effect on the Hydrogenated Si-doped DLC Film"**  
Kengo Kidena, Minami Endo, Hiroki Takamatsu, Ryo Imai, Masahito Niibe, Kumiko Yokota, Masahito Tagawa, Yuichi Furuyama, Keiji Komatsu, Hidetoshi Saitoh and Kazuhiro Kanda  
*Trans Mat. Res. Soc. Jpn.* **40**, 353-358 (2015).
14. **"Structural dependence of corrosion resistance of amorphous carbon films against nitric acid"**  
Atsuyuki Takarada, Tsuneo Suzuki, Kazuhiro Kanda, Masahito Niibe, Masayuki Nakano, Naoto Ohtake, Hiroki Akasaka  
*Diamond and Related Materials*, **51**, 49-54 (2015)
15. **"Study of Synchrotron Radiation Near-Edge X-Ray Absorption Fine-Structure of Amorphous Hydrogenated Carbon Films at Various Thicknesses"**  
Sarayut Tunmee, Ratchadaporn Supruangnet, Hideki Nakajima, XiaoLong Zhou, Satoru Arakawa, Tsuneo Suzuki, Kazuhiro Kanda, Haruhiko Ito, Kenji Komatsu, and Hidetoshi Saitoh  
*Journal of Nanomaterials*, **2015**, Article ID 276790 (2015).
16. **"Surface functionalization of Diamond-like carbon film by the irradiation of soft X-ray"**  
Kazuhiro Kanda  
*CERAMICS JAPAN*, **50**, 46-52 (2015). (in Japanese)
17. **"Comparison between AlGa<sub>N</sub> surfaces etched by carbon tetrafluoride and argon plasma: Effect of the fluorine impurities incorporated in the surface"**  
Retsuo Kawakami, Masahito Niibe, Yoshitaka Nakano, Tatsuo Shirahama, Shodai Hirai, Takashi Mukai  
*Vacuum*, **119**, 264-269 (2015).
18. **"Ar<sup>+</sup>-irradiation-induced damage in hydride vapor-phase epitaxy GaN films"**  
Yoshitaka Nakano, Daisuke Ogawa, Keiji Nakamura, Retsuo Kawakami, and Masahito Niibe  
*J. Vac. Sci. Technol. A* **33**, 043002 (2015).
19. **"Recovery of x-ray absorption spectral profile in etched TiO<sub>2</sub> thin films"**  
Keiji Sano, Masahito Niibe, Retsuo Kawakami and Yoshitaka Nakano  
*J. Vac. Sci. Technol. A* **33**, 031403 (2015).
20. **"Electrical Investigation of Deep-Level Defects Induced in AlGa<sub>N</sub>/Ga<sub>N</sub> Heterostructures by CF<sub>4</sub> Plasma Treatments"**  
R. Kawakami, Y. Nakano, M. Niibe, T. Shirahama, and T. Mukai  
*ECS Solid State Letters*, **4**, 36-38 (2015).

21. **"Three-dimensional hydrogen silsesquioxane nanostructure fabrication by reversal room-temperature nanoimprint using poly(dimethylsiloxane) mold"**  
N. Sugano, M. Okada, Y. Haruyama, and S. Matsui  
Jpn. J. Appl. Phys. **54**, 06FM05-1-06FM05-4 (2015).
22. **"Evaluation of the fluorinated antisticking layer by using photoemission and NEXAFS spectroscopies"**  
Y. Haruyama, Y. Nakai, and S. Matsui  
Applied Physics A **121**, pp. 437–441 (2015).
23. **"Electronic structure of fluorinated self-assembled monolayer investigated by photoelectron spectroscopy in the valence band region"**  
Y. Haruyama and S. Matsui  
Jpn. J. Appl. Phys. **54**, 075202-1-075202-4 (2015).
24. **"High-resolution line and space pattern fabrication by electron beam lithography using NEB-22 resist"**  
M. Okada and S. Matsui  
Jpn. J. Appl. Phys. **54**, 118004-1-118004-2 (2015).
25. **"Influence of film thickness on the reorientation structure of photoalignable liquid crystalline polymer films"**  
N. Kawatsuki, Y. Taniguchi, M. Kondo, Y. Haruyama, S. Matsui  
Polymer **90**, pp. 290-294 (2016).
26. **"Phase Imaging Results of Phase Defect Using Micro Coherent EUV Scatterometry Microscope"**  
Tetsuo Harada, Hiraku Hashimoto, Tsuyoshi Amano, Hiroo Kinoshita, and Takeo Watanabe  
J. Micro-Nanolith. Mem. **15**, 021007 (2016).
27. **"Actual defect observation results of an extreme ultraviolet blank mask by coherent diffraction imaging"**  
Tetsuo Harada, Hiraku Hashimoto, Tsuyoshi Amano, Hiroo Kinoshita, and Takeo Watanabe  
Appl. Phys. Express **9**, 035202 (2016).
28. **"Phase Imaging Results of Phase Defect Using Micro Coherent EUV Scatterometry Microscope"**  
Tetsuo Harada, Hiraku Hashimoto, Tsuyoshi Amano, Hiroo Kinoshita, and Takeo Watanabe  
Proc. SPIE 9635 96351E (2015).
29. **"Development of element technologies for EUVL"**  
Hiroo Kinoshita, Takeo Watanabe and Tetsuo Harada  
Adv. Opt. Techn. **4**, pp. 319-331 (2015).
30. **"Development of High-Reflective W/Si-multilayer Diffraction Grating for the Analysis of Fluorine Materials"**  
Masaki Kuki, Tomoyuki Uemura, Masato Yamaguchi, Tetsuo Harada, Takeo Watanabe, Yasuji Muramatsu, and Hiroo Kinoshita  
J. Photopolym. Sci. Technol., **28**, pp. 531-536 (2015).
31. **"Development of Transmission Grating for EUV Interference Lithography of 1X nm HP"**  
Tsubasa Fukui, Hirohito Tanino, Yuki Fukuda, Masaki Kuki, Takeo Watanabe, Hiroo Kinoshita, and Tetsuo Harada  
J. Photopolym. Sci. Technol., **28**, pp. 525-529 (2015).

32. **"Effective EUV Resist Outgassing Barrier Using a Novel Top Coat Material"**  
Xiaowei Wang, Georg Pawlowski, Tetsuo Okayasu, Masato Suzuki, Yusuke Hama, Takeo Watanabe, Tetsuo Harada, and Hiroo Kinoshita  
J. Photopolym. Sci. Technol., **28**, pp. 111-117 (2015).
33. **"Recent Progress in EUV Resist Outgas Research at EIDEC"**  
Eishi Shiobara, Isamu Takagi, Yukiko Kikuchi, Takeshi Sasami, Shinya Minegishi, Toru Fujimori, Takeo Watanabe, Tetsuo Harada, Hiroo Kinoshita, and Soichi Inoue  
J. Photopolym. Sci. Technol., **28**, pp. 103-110 (2015).
34. **"Development of a reflectometer for a large EUV mirror in NewSUBARU"**  
Haruki Iguchi, Hiraku Hashimoto, Masaki Kuki, Tetsuo Harada, Takeo Watanabe, and Hiroo Kinoshita  
Proc. SPIE 9658, 965819 (2015).
35. **"EUV mask observations using a coherent EUV scatterometry microscope with a high-harmonic-generation source"**  
Takahiro Fujino, Yusuke Tanaka, Tetsuo Harada, Yutaka Nagata, Takeo Watanabe, and Hiroo Kinoshita  
Proc. SPIE 9658, 965818 (2015).
36. **"Quantitative phase imaging of a small phase structure on an extreme-ultraviolet mask by coherent diffraction imaging"**  
Tetsuo Harada, Hiraku Hashimoto, Yusuke Tanaka, Tsuyoshi Amano, Takeo Watanabe, Hiroo Kinoshita  
Appl. Phys. Express **8**, 055202 (2015).
37. **"Extreme ultraviolet mask observations using a coherent extreme ultraviolet scatterometry microscope with a high-harmonic-generation source"**  
Takahiro Fujino, Yusuke Tanaka, Tetsuo Harada, Yutaka Nagata, Takeo Watanabe, and Hiroo Kinoshita  
Jpn. J. Appl. Phys. **54**, 06FC01 (2015).
38. **"Analysis of EUV Resist Outgassing Depended on the Dosage"**  
E. Shiobara, I. Takagi, Y. Kikuchi, T. Sasami, S. Minegishi, T. Fujimori, T. Watanabe, T. Harada, H. Kinoshita, S. Inoue  
SPIE Proc. 9422, 942210 (2015).
39. **"Study of Dill's B parameter measurement of EUV resist"**  
Atsushi Sekiguchi, Yoko Matsumoto, Tetsuo Harada, Takeo Watanabe, and Hiroo Kinoshita  
SPIE Proc. 9422, 94222L (2015).
40. **"ニュースバル多目的ビームライン BL10 における軟 X 線吸収分析 (4) ; 軟 X 線吸収分析装置の導入と有機薄膜試料の軟 X 線吸収・反射率分析"**  
植村智之, 村松康司, 南部啓太, 福山大輝, 九鬼真輝, 原田哲男, 渡邊健夫, 木下博雄  
X線分析の進歩第 **46** 集, pp. 317-325 (2015).
41. **"Surface-enhanced Raman Scattering active metallic nanostructure fabricated by photochemical reaction of synchrotron radiation"**  
A. Yamaguchi, T. Matsumoto, I. Okada, I. Sakurai and Y. Utsumi  
Materials Chemistry and Physics **160**, 205-211 (2015).

42. **"On-chip integration of novel Au electrode with a higher order three-dimensional layer stack nanostructure for surface-enhanced Raman spectroscopy"**  
Akinobu Yamaguchi, Takao Fukuoka, Ryohei Hara, Kazuhisa Kuroda, Ryo Takahashi and Yuichi Utsumi  
RSC Advances, **5**, 73194-73201 (2015).
43. **"Fabrication of Dihedral Corner Reflector Array for Floating Image Manufactured by X-ray Lithography using Synchrotron Radiation"**  
A. Yamaguchi, S. Maekawa, T. Yamane, I. Okada and Y. Utsumi  
Transactions of the Japan Institute of Electronics Packaging **8**(1), 23-28 (2015).
44. **"Water-clock-based autonomous flow sequencing in steadily rotating centrifugal microfluidic device"**  
Yoshiaki Ukita, Yuzuru Takamura, Yuichi Utsumi  
Sensors and Actuators B: Chemical, **220**, 180-183 (2015).
45. **"Proposal of Minicentrifuge-Compatible Centrifugal Microfluidic Device"**  
Yoshiaki Ukita, Yuichi Utsumi, Yuzuru Takamura  
Sensors and Materials, **27**, 5, 391-402 (2015).
46. **"Fabrication of SERS Active Noble Metallic Nanostructure by Synchrotron Radiation Induced Photochemical Reaction"**  
T. Matsumoto, I. Okada, I. Sakurai, Y. Utsumi and A. Yamaguchi  
IEEE Xplore (Electronic Packaging and iMAPS All Asia Conference (ICEP-IACC), 2015 International Conference on, Kyoto 2015), pp866-869 (2015).
47. **"Fabrication and evaluation of dihedral corner reflector array for floating image manufactured by synchrotron radiation"**  
T. Yamane, S. Maekawa, Y. Utsumi, I. Okada and A. Yamaguchi  
IEEE Xplore (Electronic Packaging and iMAPS All Asia Conference (ICEP-IACC), 2015 International Conference on, Kyoto 2015), pp436-439 (2015).
48. **"Application of Gold Nanoparticles Self-assemblies to Unclonable Anti-counterfeiting Technology"**  
T. Fukuoka, A. Yamaguchi, R. Hara, T. Matsumoto, Y. Utsumi and Y. Mori  
IEEE Xplore (Electronic Packaging and iMAPS All Asia Conference (ICEP-IACC), 2015 International Conference on, Kyoto 2015), pp432-435 (2015).
49. **"X線励起液相反応による金属ナノ粒子生成と応用 (Synthesis and application of gold nanoparticles using photochemical reaction induced by X-ray irradiation)"**  
山口明啓, 岡田育夫, 福岡隆夫, 村上元規, 内海裕一  
MES 2015, pp265-268 (2015). (in Japanese)
50. **"微量分子検出のための高次ナノ構造体の創製と実装 (Fabrication and Assembly of Higher Order Nanostructure for Surface Enhanced Raman Scattering)"**  
山口明啓, 福岡隆夫, 内海裕一  
Mate 2016, pp281-284 (2015). (in Japanese)
51. **"放射光光化学反応による金属ナノ粒子生成 (Synthesis of metallic nanoparticles in liquid solution using X-ray photochemical reaction)"**  
山口明啓, 岡田育夫, 櫻井郁也, 福岡隆夫, 石原マリ, 内海裕一  
Mate 2016, pp457-458 (2016). (in Japanese)

## (2) International meetings

1. **"Measurement of a Polarized Gamma Ray Beam from 1.7 to 74 MeV with the HARPO TPC"**  
P.Gros, D. Bernard, Ph. Bruel, M. Frodin, Y. Geerebaert, B. Giebels, Ph. Gros, D. Horan, M. Louzir, P. Poilleux, I. Semeniouk, S. Wang, D. Calvet, D. Attié, P. Colas, A. Delbart, P. Sizun, Diego Götz, S. Amano, T. Kotaka, S. Hashimoto, Y. Minamiyama, A. Takemoto, S. Miyamoto, M. Yamaguchi, S. Daté, H. Ohkuma  
13th Pisa Meeting on Advanced Detectors, 24-, May (2015).
2. **"NewSUBARU LCS Gamma-ray Source"**  
Shuji Miyamoto  
International Workshop of Laser Compton Scattering Gamma Ray Sources and Their Applications, NewSUBARU, Kouto, Japan, Nov. 11 - 12, 2015.
3. Hold International Workshop 国際ワークショップ開催  
International Workshop of Laser Compton Scattering Gamma Ray Sources and Their Applications, NewSUBARU, Kouto, Japan, Nov. 11 - 12, 2015
4. **"Low-Temperature Crystallization of Si, Ge and Si-Nanocrystal by Soft X-Ray Irradiation"**  
N. Matsuo, A. Heya, S. Miyamoto, T. Mochizuki, K. Kanda, K. Kohama, M. Takahashi, K. Itoh  
Collaborative Conference on 3D and Materials Research 2015, 15-19 June 2015, Busan, South Korea.
5. **"Development of DLC cone for fast ignition experiment"**  
Mayuko Koga, Takuma Ono, Takuma Tokunaga, Hayato Kadota, Takashi Hashimoto, Kazuhiro Kanda, Takayoshi Norimatsu  
9th International Conference on Reactive Plasmas (ICRP-9) October 12-16, 2015.
6. **"Double Crystal Monochromator Controlled by Integrated Computing on BL07A in New SUBARU, Japan"**  
Masato Okui, Naoki Yato, Akinobu Watanabe, Baiming Lin, Norio Murayama, Sei Fukushima and Kazuhiro Kanda  
12th International Conference on Synchrotron Radiation Instrumentation(SRI2015) July 6-10, 2015, Marriott Marquis Times Square New York City, NY United States.
7. **"Continuous Generation of Laser Plasma x-ray using Solid Rare Gas Targets"**  
S.Amano  
The 4<sup>th</sup> Advanced Lasers and Photon Source Conference (ALPS'15), Yokohama, Apr.22-24, 2015.
8. **"Anatase TiO<sub>2</sub> Thin Films Grown by Facing-Target Reactive Sputtering and Its Impact on Photocatalytic Activity"**  
Retsuo Kawakami, Masahito Niibe, Yoshitaka Nakano, Chisato Azuma and Takashi Mukai  
Proceedings of International Symposium of Dry Process 2015, pp.125--126, Nov. 2015, Awaji Japan.
9. **"A Relation between Pinch-Off Voltages and Deep-Level Defects in AlGaIn/GaN Hetero-Structures Treated by CF<sub>4</sub> Plasma"**  
Yoshitaka Nakano, Retsuo Kawakami, Masahito Niibe, Tatsuo Shirahama and Takashi Mukai  
11th International Conference on Nitride Semiconductors (ICNS-11), Beijing, Sep. 2015.

10. **"Low energy soft X-ray Emission Spectrometer at BL-09A in NewSUBARU"**  
Masahito Niibe and Takashi Tokushima  
The 12th inter'l conf. on Synchrotron Radiation Instrumentation (SRI2015) 6-10 July 2015, New York, USA.
11. **"Development of the Surface-sensitive Soft X-ray Absorption Fine Structure Measurement Technique for the Bulk Insulator"**  
Takumi Yonemura, Junji Iihara, Shigeaki Uemura, Koji Yamaguchi, Masahito Niibe  
The 12th inter'l conf. on Synchrotron Radiation Instrumentation (SRI2015) 6-10 July 2015, New York, USA.
12. **"Comparison between Surface Characteristics of Titanium Oxide Thin Films Treated with N<sub>2</sub> Dielectric Barrier Discharge Plasma and Annealed in N<sub>2</sub> Gas"**  
Retsuo Kawakami, Masahito Niibe, Yoshitaka Nakano and Takashi Mukai  
Proc. 13th International Symposium of Sputtering & Plasma Processes (ISSP), pp.63--66, Kyoto, Jul. 2015.
13. **"Temperature dependence of molecular orientation of liquid crystalline polymer induced by nanoimprint-graphoepitaxy"**  
M. Okada, Y. Haruyama, S. Matsui, R. Hosoda, Y. Taniguchi, N. Kawatsuki and H. Ono  
59th International Conference on electron, ion, photon beam technology and fabrication(EIPBN2015), San Diego, USA, 2015/5/27
14. **"Upgrade of a Vacuum Ultraviolet and Soft X-ray Undulator Beamline BL07B in NewSUBARU"**  
Y. Haruyama and S. Matsui  
12th International Conference on Synchrotron Radiation Instrumentation (SRI 2015), Newyork, USA, 2015/7/7
15. **"Surface Evaluation of HSQ containing PDMS Additive after Room-temperature Nanoimprinting"**  
N. Sugano, M. Okada, Y. Haruyama, and S. Matsui  
32nd International Conference of Photopolymer Science and Technology(ICPST-32), Chiba, Japan, 2015/7/25
16. **"Toward Less Than 50 nm-Line and Space Negative Tone Pattern Fabrication by Electron Beam Lithography using NEB-22"**  
M. Okada and S. Matsui  
41th International Conference on Micro and Nano Engineering (MNE2015), The Netherlands, 2015/9/22
17. **"Localized liquid crystalline molecular orientation in line and space pattern fabricated by double nanoimprint-graphoepitaxy"**  
M. Okada, Y. Taniguchi, Y. Haruyama, H. Ono, N. Kawatsuki, and S. Matsui  
41th International Conference on Micro and Nano Engineering (MNE2015), The Netherlands, 2015/9/23
18. **"Negative tone high resolution line and space pattern mold fabrication by electron beam lithography using NEB-22"**  
M. Okada and S. Matsui  
The 14th International Conference on Nanoimprint and Nanoprint Technology 2015 (NNT2015), Napa, USA, 10/23

19. **"Double nanoimprint-graphoepitaxy for localized liquid crystalline molecular orientation in imprinted pattern"**  
M. Okada, Y. Taniguchi, Y. Haruyama, H. Ono, N. Kawatsuki, and S. Matsui  
The 14th International Conference on Nanoimprint and Nanoprint Technology 2015 (NNT2015), Napa, USA, 10/23
20. **"Resin Concentration Dependence of Residual Layer Thickness in UV Reversal Nanoimprinting"**  
N. Sugano, M. Okada, Y. Haruyama and S. Matsui  
28th International Microprocesses and Nanotechnology Conference (MNC2015), Toyama, Japan, 2015/11/12
21. **"Negative Tone 40 nm-Line and 60 nm-Space Pattern Fabrication by Electron Beam Lithography Using NEB-22"**  
M. Okada and S. Matsui  
28th International Microprocesses and Nanotechnology Conference (MNC2015), Toyama, Japan, 2015/11/12
22. **"Study of the Durability of Antisticking Layer against Repeated Ultra Violet Nanoimprinting"**  
S. Iyoshi, M. Okada, Y. Haruyama and S. Matsui  
28th International Microprocesses and Nanotechnology Conference (MNC2015), Toyama, Japan, 2015/11/13
23. **"Evaluation of Molecular Orientation of Photo-Cross-Linkable Liquid Crystalline Polymer in 200 nm-Line and Space Pattern by Measuring Diffraction Efficiency"**  
M. Okada, Y. Taniguchi, Y. Haruyama, H. Ono, N. Kawatsuki, and S. Matsui  
28th International Microprocesses and Nanotechnology Conference (MNC2015), Toyama, Japan, 2015/11/13
24. **"Observation Result of Actual Phase Defects on an EUV Mask Using Micro Coherent EUV Scatterometry Microscope"**  
H. Hashimoto, T. Harada, T. Amano, H. Kinoshita and T. Watanabe  
Micronano conference 2015, Toyama, Japan, Nov.10-13, 2015.
25. **"Measurement Result of an EUV Collector Mirror Using a Large Reflectometer at NewSUBARU"**  
H. Iguchi, H. Hashimoto, M. Kuki, T. Harada, H. Kinoshita, T. Watanabe, Y.Y. Platonov, M.D. Kriese and J.R. Rodriguez  
Micronano conference 2015, Toyama, Japan, Nov.10-13, 2015.
26. **"Soft X-ray Absorption Spectroscopy using SR for EUV Resist Chemical Reaction Analysis (Invited talk) "**  
Takeo Watanabe  
TWG EUV Resist Workshop, Maastricht, Netherland, Oct. 4, 2015.
27. **"Extreme ultraviolet mask observations using a coherent extreme ultraviolet scatterometry microscope with a high-harmonic-generation source"**  
Takahiro Fujino, Yusuke Tanaka, Tetsuo Harada, Yutaka Nagata, Takeo Watanabe, Hiroo Kinoshita  
Photomask Technology 2015, Monterey, USA, 2015/9/29.

28. **"Development of Transmission Grating for EUV Interference Lithography of 1X nm HP"**  
Tsubasa Fukui, Hirohito Tanino, Yuki Fukuda, Masaki Kuki, Takeo Watanabe, Hiroo Kinoshita, and Tetsuo Harada  
The 32nd International Conference of Photopolymer Science and Technology, Makuhari Messe, Chiba, Japan, June 24 - 26, 2015.
29. **"Development of High-Reflective W/Si-multilayer Diffraction Grating for the Analysis of Fluorine Materials"**  
Masaki Kuki, Tomoyuki Uemura, Masato Yamaguchi, Tetsuo Harada, Takeo Watanabe, Yasuji Muramatsu, and Hiroo Kinoshita  
The 32nd International Conference of Photopolymer Science and Technology, Makuhari Messe, Chiba, Japan, June 24 - 26, 2015.
30. **"Recent Progress in EUV Resist Outgas Research at EIDEC"**  
Eishi Shiobara, Isamu Takagi, Yukiko Kikuchi, Takeshi Sasami, Shinya Minegishi, Toru Fujimori, Takeo Watanabe, Tetsuo Harada, Hiroo Kinoshita, and Soichi Inoue  
The 32nd International Conference of Photopolymer Science and Technology, Makuhari Messe, Chiba, Japan, June 24 - 26, 2015.
31. **"Effective EUV Resist Outgassing Barrier Using a Novel Top Coat Material"**  
Xiaowei Wang, Georg Pawlowski, Tetsuo Okayasu, Masato Suzuki, Yusuke Hama, Takeo Watanabe, Tetsuo Harada, and Hiroo Kinoshita  
The 32nd International Conference of Photopolymer Science and Technology, Makuhari Messe, Chiba, Japan, June 24 - 26, 2015.
32. **"EUV resist outgassing analysis for the new platform resists at EIDEC"**  
Eishi Shiobara, Yukiko Kikuchi, Shinji Mikami, Takeshi Sasami, Takashi Kamizono, Shinya Minegishi, Takakazu Kimoto, Toru Fujimori, Takeo Watanabe, Tetsuo Harada, Hiroo Kinoshita, Satoshi Tanaka  
SPIE advanced Lithography 2016, San Jose USA, Feb. 23-24, 2016.
33. **"FABRICATION OF TRANSMISSION GRATING OF EUV INTERFERENCE LITHOGRAPHY FOR 1X NM HP EUV RESIST EVALUATION"**  
Takeo Watanabe, Tsubasa Fukui, Hirohito Tanino, Yuki Fukuda, Masaki Kuki, Masato Yamaguchi, Tetsuo Harada  
EUV International Symposium 2015, Masstricht, Netherland, Oct. 6-8, 2015.
34. **"QUANTITATIVE PHASE-CONTRAST IMAGING OF A PHASE DEFECT USING A LENSLESS MICROSCOPE"**  
Tetsuo Harada, Hiraku Hashimoto, Tsuyoshi Amano, Hiroo Kinoshita, Takeo Watanabe  
EUV International Symposium 2015, Masstricht, Netherland, Oct. 6-8, 2015.
35. **"A Study of EUV Resist Sensitivity by Using Metal materials"**  
Atsushi Sekiguchi, Yoko Matsumoto, Tadashi Yamanouchi, Takeo Watanabe, Tetsuo Harada, Hiroto Kudo  
EUV International Symposium 2015, Masstricht, Netherland, Oct. 6-8, 2015.
36. **"Comparison of EUV Resist Outgassing between Organic and Inorganic Materials"**  
Yukiko Kikuchi, Takeshi Sasami, Shinya Minegishi, Shinji Mikami, Takashi Kamizono, Toru Fujimori, Takeo Watanabe, Tetsuo Harada, Eishi Shiobara  
EUV International Symposium 2015, Masstricht, Netherland, Oct. 6-8, 2015.

37. **"Phase Imaging Results of Phase Defect Using Micro Coherent EUV Scatterometry Microscope"**  
Tetsuo Harada, Hiraku Hashimoto, Tsuyoshi Amano, Hiroo Kinoshita, and Takeo Watanabe  
Photomask Technology 2015, Monterey, USA, Sep.29 - Oct.1, 2015.
38. **"Development of Micro Coherent EUV Scatterometry Microscope for Phase Defect Characterization"**  
Hiraku Hashimoto, Yusuke Tanaka, Tetsuo Harada, Takeo Watanabe, Hiroo Kinoshita  
Photomask Japan 2015, Yokohama, Japan, Apr. 20-22, 2015.
39. **"Development of a reflectometer for a large EUV mirror in NewSUBARU"**  
Haruki Iguchi, Hiraku Hashimoto, Masaki Kuki, Tetsuo Harada, Takeo Watanabe, and Hiroo Kinoshita  
Photomask Japan 2015, Yokohama, Japan, Apr. 20-22, 2015.
40. **"EUV mask observations using a coherent EUV scatterometry microscope with a high-harmonic-generation source"**  
Takahiro Fujino, Yusuke Tanaka, Tetsuo Harada, Yutaka Nagata, Takeo Watanabe, and Hiroo Kinoshita  
Photomask Japan 2015, Yokohama, Japan, Apr. 20-22, 2015
41. **"Fabrication of SERS Active Noble Metallic Nanostructure by Synchrotron Radiation Induced Photochemical Reaction"**  
T. Matsumoto, I. Okada, I. Sakurai, Y. Utsumi and A. Yamaguchi  
International Conference on Electronics Packaging (ICEP2015), April 14-17 (2015), Kyoto, Japan
42. **"Fabrication and evaluation of dihedral corner reflector array for floating image manufactured by synchrotron radiation"**  
T. Yamane, S. Maekawa, Y. Utsumi, I. Okada and A. Yamaguchi  
International Conference on Electronics Packaging (ICEP2015), April 14-17 (2015), Kyoto, Japan
43. **"Application of Gold Nanoparticles Self-assemblies to Unclonable Anti-counterfeiting Technology"**  
T. Fukuoka, A. Yamaguchi, R. Hara, T. Matsumoto, Y. Utsumi and Y. Mori  
International Conference on Electronics Packaging (ICEP2015), April 14-17 (2015), Kyoto, Japan
44. **"Optofluidic devices implemented 3D gold nanostructure enabling surface enhanced Raman scattering"**  
Akinobu Yamaguchi, Takao Fukuoka, Ryo Takahashi, and Yuichi Utsumi  
The International Chemical Congress of Pacific Basin Societies 2015, December 15-20 (2015), Honolulu, Hawaii, USA
45. **"SERS active gold nanostructure by synchrotron radiation induced photochemical reaction"**  
Takeshi Matsumoto, Ikuo Okada, Ikuya Sakurai, Yuichi Utsumi, Akinobu Yamaguchi  
The International Chemical Congress of Pacific Basin Societies 2015, December 15-20 (2015), Honolulu, Hawaii, USA
46. **"Surface enhanced Raman scattering sensing using a coffee-ring-type 3D silver nanostructure self-assembled on glass substrates"**  
Akinobu Yamaguchi, Takao Fukuoka, Ryohei Hara, Yuichi Utsumi  
The International Chemical Congress of Pacific Basin Societies 2015, December 15-20 (2015), Honolulu, Hawaii, USA

47. **"Gold nanoparticle self-assemblies for on-dose-authentication of medical tablets"**  
Takao Fukuoka, Akinobu Yamaguchi, Yuichi Utsumi, Yasushige Mori  
The International Chemical Congress of Pacific Basin Societies 2015, December 15-20 (2015), Honolulu, Hawaii, USA
48. **"Sterically-bulky self assemblies of gold nanoparticles"**  
Takao Fukuoka, Ryo Takahashi, Yuichi Utsumi, Akinobu Yamaguchi  
The International Chemical Congress of Pacific Basin Societies 2015, December 15-20 (2015), Honolulu, Hawaii, USA
49. **"Fundamental study of a microwave irradiation structure using transparent post-wall waveguide"**  
Mitsuyoshi Kishihara, Yasuhito Minamiyama, Akinobu Yamaguchi, Yuichi Utsumi  
The International Chemical Congress of Pacific Basin Societies 2015, December 15-20 (2015), Honolulu, Hawaii, USA

### (3) Academic degrees

#### 1. Master of Engineering

Shodai Hirai (University of Hyogo)

"Surface analysis of AlGaN films etched with Ar, CF<sub>4</sub> and UV-assisted CF<sub>4</sub> plasmas"

Tsubasa Fukui (University of Hyogo)

10 nm 領域の EUV 干渉露光用透過型回折格子の製作

"Fabrication of an EUV interference-lithography grating for 1x-nm pattern replication"

Masato Yamaguchi (University of Hyogo)

軟 X 線吸収分光法による EUV フォトレジスト分析手法の開発

"Chemical reaction analysis of EUV photoresist using soft x-ray absorption spectroscopy"

Hirohito Tanino (University of Hyogo)

EUV 干渉露光装置の高度化

"Improvement of EUV interference-lithography system"

Takahiro Fujino (University of Hyogo)

高次高調波を用いた回折顕微鏡による EUV マスクの欠陥観察手法の開発

"Defect observation of EUV mask using an EUV diffraction microscope with a high harmonic generation EUV source"

Masaki Kuki (University of Hyogo)

500~1,100 eV 領域用の高反射 W/Si 多層膜回折格子の開発

"Development of a high-reflective W/Si-multilayer coating on a diffraction grating for 500 - 1,100 eV region"

Takeshi Matsumoto (University of Hyogo)

"Study on detection of mouse IgG through ELISA using Lab-on-a-CD"

Motoki Murakami (University of Hyogo)

"Study on fabrication of microfluidic chip and micro-total analysis system made of PTFE"

#### 2. Master of Science

Karin Kobayashi (University of Hyogo)

"Study of LEENA Electron Beam Monitor and Tuning of Accelerator"

Takuya Matsumoto (University of Hyogo)

"Simulation Study of Laser Compton Gamma-ray Beam Source"

Norihiro Sugano (University of Hyogo)

"ナノインプリント用 PDMS 離型剤含有 HSQ レプリカモールドに関する研究"



# **LASTI Annual Report Vol.17 (2015)**

---

September 2016, Published by  
Laboratory of Advanced Science and Technology for Industry  
University of Hyogo  
3-1-2 Kouto, Kamigori-Cho, Ako-gun, Hyogo 678-1205, JAPAN  
Phone: +81-791-58-0249 / FAX: +81-791-58-0242

## **Editorial board**

NIIBE Masahito (Editor in Chief)

SHOJI Yoshihiko

HARUYAMA Yuichi

YAMAGUCHI Akinobu

HARADA Tetsuo

---

Laboratory of Advanced Science and Technology for Industry  
University of Hyogo

3-1-2 Kouto, Kamigori, Ako-gun, Hyogo 678-1205 Japan

兵庫県立大学 高度産業科学技術研究所

〒678-1205 兵庫県赤穂郡上郡町光都 3-1-2

